

# Geological and Geochemical Explorations of the Salitre Formation Phosphorite, Eastern Brazil

Thesis by  
Cecilia Brooke Sanders

In Partial Fulfillment of the Requirements for the  
Degree of  
Doctor of Philosophy

The logo for the California Institute of Technology (Caltech), featuring the word "Caltech" in a bold, orange, sans-serif font.

CALIFORNIA INSTITUTE OF TECHNOLOGY  
Pasadena, California

2023  
Defended July 1, 2022

© 2023

Cecilia Brooke Sanders  
ORCID: 0000-0002-2663-164X

All rights reserved except where otherwise noted

## ACKNOWLEDGEMENTS

The gratitude I feel for my family and community is a boundless, global ocean. I will never be able to thank them enough.

To my parents, Lisa and Norman Sanders. . . You brought me into this world, and from the second I opened my eyes you placed wonders in front of them. Thank you for every book you read to me, every song you sang to me, and every trip to the museum. Thank you for every insightful and thoughtful conversation. Thank you for encouraging me to be bold and take up space. Thank you for loving me even when I was mad with fear and self-doubt. Thank you for being the brilliant, incisive, creative, passionate, and extraordinarily good and loving people that you are.

To Mammaw. . . You have been my third parent, all my life – feeding me, clothing me, cheering me on. You came up in a world that did everything it could to keep you down, but you rose up and raised your family and community up with you. Thank you for your strength and your love, and for instilling in your descendants the value of education and justice.

To my siblings, Samantha and Cedric Sanders. . . Your encouragement, your belief in me, has meant all the world. You are both such fiercely intelligent, talented, and intimidatingly cool people, and I consider myself incredibly lucky to be your sister and your friend. Thank you for all of the joy, silliness, solidarity and strength you have given me.

To Grandma Jane. . . It was on your bookshelves and in your garden that I learned to believe it was possible to make the world a better place than we found it. Your letters and essays on nature and politics were bold, insightful, inspirational. Your love of and respect for the intellect and innate kindness of children were world-changing. I'm sorry I couldn't finish this degree sooner, and spend more time reveling in nature with you.

To my Aunts, Uncles, and Cousins, near and far. . . I am beyond lucky to have such smart, kind, passionate people in my life. Thank you for your love and support, and for believing in me.

To my best friend, Dustin “Dune” Morris. . . You're a fantastic geologist, a thoughtful and creative educator, and a phenomenal storyteller — an absolute inspiration. Thank you for the last 5 years of field geology, worldbuilding, dreaming, self-discovery, joy, silliness, and being unapologetically ourselves: from field partners

to lifelong friends. I am so excited to build a better world together as friends and colleagues.

To my dear friends Morgan Hooper and Nicole Wallack. . . I couldn't have made it through the past 6 years without you. You are both such brilliant scientists, and such interesting, creative delightful people, and truly wonderful friends. Thank you for every late night of problem sets, ridiculous tv shows, and delicious food. Thank you for letting me cry on your shoulders, for the sharing of burdens. Thank you for believing in me even when I was at my lowest.

To Johnathan Sorrentino. . . I'm so blessed to have met you and become your friend. I can't wait for the next chapter of our lives, collaborating on taphonomy experiments, canoeing around Canada with you and Morgan, playing tabletop games. . . You rock.

To my brilliant, insightful, and deeply kind colleagues and kindred spirits. . . Ted Present, Selva Marroquin, Kelsey Moore, Sean Mullin, Kyle Metcalfe, Judy Pu, Tessa Browne, and so many more. . . Thank you for all of your advice, empathy, and so many joyful moments. And to Sarah Zeichner, Usha Farey-Lingappa, Emma Sosa, and Daniela Osorio-Rodriguez – thank you for being such inspirations as artists, scientists, educators, and activists.

To Janice Grancich, Julie Lee, Mark Garcia, and so many other GPS staff. . . Thank you for everything you do, to help us graduate students learn and grow and have so many life-changing experiences. And thank you for your kindness and empathy over the last 6 years.

To Bethany Ehlmann, Robin Wordsworth, Fred Ciesla, Terry Hurford, Geronimo Villanueva, John Johnson, David Johnston, Ann Pearson, Andy Knoll, David Charbonneau, Chi Chi Nnakwe, the researchers at PERL, the educators at ChesPax, and so, so many others. . . Thank you for teaching and mentoring me as a K-12 student, an undergraduate, and a baby grad student, for introducing me to the world of scientific research, and for believing in my abilities. . . It really takes a village.

To the students, professors, and researchers of the Laboratório de Análises de Minerais e Rochas (LAMIR) e Laboratório de Análises de Bacias (LABAP) da Universidade Federal do Paraná, as well as our collaborators from the Universidade Federal do Bahia, thank you for making this thesis possible — for welcoming me into the Brazilian geology community, for teaching me Portuguese, for traveling with me all over Brazil from the highest plateaus to the deepest caves. . . Thank you, thank you, thank you for a life-changing experience.

To the farmers, miners, educators, and conservationists of the Chapada Diamantina and Cavernas do Peruaçu regions, thank you for the gift of your time and knowledge.

To my thesis committee members Victoria Orphan, John Eiler, Woody Fischer, and Dianne Newman. . . Thank you for your truly heroic patience, kindness, and persistence in teaching me how to be a geologist and geochemist. Thank you for not giving up on me even when I wanted to give up on myself. Thank you for being such incredible, inspirational thinkers and educators. One couldn't ask for better role models.

To John Grotzinger, my thesis adviser. . . You are a legendary figure in the worlds of geology and planetary science, and being able to work with you these past 6 years has been the greatest honor and privilege. I have learned so much from you, as a scientist and an educator, and if one day I can become even half the professor you are I will have achieved greatness. Thank you for your patience and thoughtfulness, for allowing me to be my raw, vulnerable self. Thank you for your empathy. Thank you for your support. Thank you for believing in me. And of course, thank you for the most incredible field experiences and campfire concerts.

To Ponyo. . . I know that you are a dog, and I know that you can't read. But gosh, I love you, and you have been the most incredible emotional support pup. Thank you for all your kisses and stretchy paws and snuggles. Thank you for being the Best Baby.

To Eduardo Cabral, my partner and soon-to-be spouse. . . I could write a whole other dissertation about all of the ways you have loved me, supported me, inspired me, and filled my life with joy and meaning in the past 6 years — and it still wouldn't cover the half of it. You have been my closest, dearest friend and confidante. You cared for me and loved me when I was in the darkest depths of my depression, you supported me and listened to me and made me feel seen and understood. You made me feel strong and smart and capable, and turned my lowest lows into triumphs. You are so wildly smart and clever and funny, but your infinite capacity for kindness and compassion are just. . . Extraordinary. I love you so much, Eduardo, and I am so grateful for everything you do and everything you are. I can't wait to start the next chapter of our lives together.

## ABSTRACT

This thesis documents my explorations of an ancient seafloor environment through sedimentary geology and stable isotope geochemistry. The geologic record of this seafloor — its life, environmental conditions, lithification, burial and exposure — consists of hundreds of meters of sedimentary rock, outcropping across Bahia and Minas Gerais, Brazil. Though it consists primarily of carbonate grains surrounded by carbonate cements, such as might be found forming in any shallow carbonate platform, this record also contains one of Brazil's most extensive sedimentary phosphate deposits. In these deposits, phosphate is concentrated as carbonate fluorapatite cements (CFA) in digitate stromatolites, distinctively finger-like, branching accretionary structures likely formed by the accumulation of sediment by microbial mats and biofilms. Chapter 1 introduces the broader motivations of this kind of paleoenvironmental and paleoecological research, for understanding the record of life on Earth and other worlds. Chapter 2 presents new sedimentological and stratigraphic data which interpret the depositional setting of a seafloor 600 million years ago on the rending supercontinent of Gondwana. Chapter 3 presents new carbon and oxygen isotopic measurements and clumped isotope measurements of structural carbonate in phosphatic and non-phosphatic textures of the rock, and uses them to constrain the alteration history of the rock and its effect on the record of primary depositional conditions. Chapter 4 presents new data on the sulfur isotope composition of specific minerals in the rock, combining several disparate analytical methods to draw conclusions about the metabolism of the stromatolites' microbial architects. Chapter 5 describes the distribution of organic material and style of fossilization, and presents preliminary data which suggest a possible mechanism by which microbial activity may have facilitated phosphate concentration and mineralization. As a whole, this thesis demonstrates the value of multidisciplinary analyses in the reconstruction and understanding of sedimentary phosphorite deposits throughout Earth history, improving our understanding of how and to what extent phosphorites may record the history of life and the environment.

## PUBLISHED CONTENT AND CONTRIBUTIONS

Sanders, C. B. and J. P. Grotzinger (2021). “Sedimentological and stratigraphic constraints on depositional environment for Ediacaran carbonate rocks of the São Francisco Craton: Implications for phosphogenesis and paleoecology”. In: *Pre-cambrian Research* 363, p. 106328. DOI: <https://doi.org/10.1016/j.precamres.2021.106328>.

C.B.S participated in the conception of the project, execution of the field work, collection of samples, elemental and mineralogical analysis of samples, organization/analysis/presentation of data, and writing of the manuscript.

## TABLE OF CONTENTS

Acknowledgements . . . . .	iii
Abstract . . . . .	vi
Published Content and Contributions . . . . .	vii
Table of Contents . . . . .	vii
List of Illustrations . . . . .	x
List of Tables . . . . .	xxvi
Chapter I: Introduction . . . . .	1
Chapter II: Sedimentological and stratigraphic constraints on depositional environment for Ediacaran carbonate rocks of the São Francisco Craton: Implications for phosphogenesis and paleoecology . . . . .	14
2.1 Abstract . . . . .	14
2.2 Introduction and geologic context . . . . .	15
2.3 Methods . . . . .	19
2.4 Depositional environments: Salitre and Sete Lagoas formations . . . . .	20
2.5 Paragenesis . . . . .	32
2.6 Discussion: Phosphogenesis on a wave-swept, high energy carbonate platform . . . . .	39
2.7 Conclusions and future work . . . . .	46
2.8 Acknowledgements . . . . .	47
2.9 Figures and tables . . . . .	59
Chapter III: Paragenesis of an Ediacaran carbonate-platform phosphorite: Constraints from optical petrography and texture-specific clumped isotope paleothermometry . . . . .	84
3.1 Abstract . . . . .	84
3.2 Introduction . . . . .	85
3.3 Geologic and stratigraphic framework . . . . .	87
3.4 Sedimentary context and origin of phosphate mineralization in the Salitre Fm. . . . .	89
3.5 $\Delta_{47}$ , $\delta^{18}O$ , and $\delta^{13}C$ values of carbonate in calcite, dolomite, and CFA . . . . .	94
3.6 Discussion and conclusions . . . . .	100
3.7 Methods . . . . .	106
3.8 Acknowledgements . . . . .	113
3.9 Figures and tables . . . . .	124
Chapter IV: Sulfur geochemistry of the Salitre Formation phosphorites: Im- plications for the role of sulfur cycling in phosphogenesis on an Ediacaran carbonate platform . . . . .	132
4.1 Abstract . . . . .	132
4.2 Introduction and background . . . . .	133
4.3 Geologic context . . . . .	136

4.4	Methods . . . . .	137
4.5	Results . . . . .	146
4.6	Discussion and conclusions . . . . .	151
4.7	Future work . . . . .	156
4.8	Acknowledgements . . . . .	156
4.9	Figures and tables . . . . .	165
	Appendix A: Overlarge tables from chapter 2 . . . . .	171
	Appendix B: Preliminary evaluation of cation bridging as a mechanism of organic matter preservation in phosphatic microbialites of the Salitre For- mation, Northeastern Brazil . . . . .	172
B.1	Abstract . . . . .	172
B.2	Introduction . . . . .	173
B.3	Geologic context . . . . .	174
B.4	Methods . . . . .	176
B.5	Results . . . . .	177
B.6	Discussion and conclusions . . . . .	180
B.7	Acknowledgements . . . . .	184
B.8	Figures . . . . .	187
	Appendix C: Questionnaire . . . . .	192
	Appendix D: Consent Form . . . . .	193

## LIST OF ILLUSTRATIONS

<i>Number</i>	<i>Page</i>
1.1 600 million years ago, a wave-tossed sea. . . . .	1
1.2 Sunken palaces. . . . .	9
1.3 The sunken palaces sunk further still, not just beneath the waves but beneath the sea floor. . . . .	10
1.4 The ancient, sunken cities were laid bare and desiccated – alien ruins on a planet made anew... Then, I arrived. . . . .	11
1.5 What information could these ruins hold about the world as it was when their miniscule bricks were first laid and cemented? . . . . .	12
1.6 I immersed myself in the reconstruction of the paleoenvironment and paleoecology that had produced these structures, determined their composition, and sealed the fate of the remains of the organisms that lived on them. . . . .	13
2.1 Geographic position and regional geologic context for Salitre and Sete Lagoas formations. (a) Location of São Francisco Craton and remnants of adjacent cratons on the South American continent (modi- fied after Umberto G. Cordani and Sato, 1999), as well as distribution of Ediacaran and late Cryogenian lithostratigraphic units. Map of São Francisco Craton modified after Reis, Suss, et al., 2017 and Alkmim and Marcelo A. Martins-Neto, 2012. Blue rectangles represent the locations of the more magnified insets in (c-e). 0 corresponds to Locality 0 ( <i>Fazenda Arrecife</i> , Table 1). (b) Lithostratigraphic units relevant to this study and their putative stratigraphic correlation, with absolute age constraints in red. (c) Northern Irecê paleobasin. Field sites for this study are marked by pink circles and crosses, and those locations discussed in the text are numbered in black (Table 1). (d) Southern Irecê paleobasin (near Iraquara, MG, Brazil). Scale is the same as (c). (e) Januária area (near Cavernas do Peruaçu National Park, MG, Brazil). (f) Sete Lagoas area. Maps are modified after those published by the Geologic Survey of Brazil or CPRM (Dalton de Souza et al., 2003; Fonseca et al., 2014). . . . .	60

2.2 Depositional facies model illustration, featuring 9 distinct lithofacies and their spatial relationships. (a) Illustration of depositional settings for 9 identified lithofacies. Red color denotes authigenic or early diagenetic CFA cements. (b) Illustration of phosphatic (CFA-cemented) and non-phosphatic (carbonate-cemented) textures, as they occur in study area: associated with laminated cross-stratified carbonate grainstone/rudstone. (c) Illustration of symmetric wave-rippled limestone lithofacies. . . . . 61

2.3 Lithofacies of the Salitre and Sete Lagoas formations. (a-c) Lithofacies 1, laminated cross-stratified carbonate grainstone/rudstone. (d-e) Lithofacies 2, tabular intraclast conglomerate. (f) Lithofacies 3, planar laminated very fine-grained limestone/dolostone, interbedded with examples of Lithofacies 4, nodular limestone, and Lithofacies 5, crinkly laminite. (g-h) Lithofacies 4, nodular limestone, interbedded with Lithofacies 5, crinkly laminite. | (a) Laminated, cross-stratified carbonate grainstone, preserving possible asymmetric wave ripples, climbing ripples, and troughs. Section broadly coarsens upward, with the coarsest intervals being replete with ooids and aggregate grains (e.g., grapestones). Salitre Fm, Locality 4 (Fig. 1c), Io 4. (b) Finer-grained lenses within laminated, cross-stratified grainstones. Salitre Fm, Locality 11 (Fig. 1c), Vila Morro Grande. (c) Irregular trough cross-stratification. Salitre Formation, Locality 4 (Fig. 1c), Io 4. (Caption continues on next page.) . . . . . 62

- 2.4 Continued from previous page... (d) Tabular intraclast conglomerate below and among cross-stratified grainstone. Salitre Fm, Locality 15 (Fig. 1d), Cabbage Patch. (e) Intraclast conglomerate among cross-stratified, oolitic dolostone, where pebble- and cobble-scale intraclasts abut a boulder. Salitre Fm, Locality 11 (Fig. 1c), Vila Morro Grande. (f) Crinkly and undulating beds of laminated limestone. Centimeter-scale mounds near middle of image appear to be nodular hardgrounds draped by fine laminated sediment. Salitre Fm, Locality 14 (Fig. 1d), Coxinha Antiga. (g) Nodular limestone, where cohesive mounds are draped by fine sediment. Salitre Fm, Locality 19 (Fig. 1e), Levinópolis. (h) Nodular limestone over fine, planar laminated limestone, with bedding plane visible. Sete Lagoas Fm, Locality 19 (Fig. 1e), Levinópolis. Note: finger is 1.5 centimeter wide, pen is 1 centimeter wide and 11 centimeter long, hammer handles are 4-5 centimeter wide. Otherwise, scale is indicated in the frame. . . . . 63
- 2.5 Digitate stromatolite-bearing lithofacies of the Salitre Formation (Lithofacies 6). (a) Bedding-plane view of phosphatic digitate stromatolite biostrome, showing merging and dividing growth habit. This biostrome is between 1 and 2 meters thick with a lateral extent of perhaps 10 meters. Locality 3 (Fig. 1c), Fazenda Nova Canãa. (b) Bedding-plane view of phosphatic digitate stromatolite biostrome of similar dimension to (a), showing elongation of stromatolites. Locality 9 (Fig. 1c), Lonely Road. (c) Digitate stromatolite biostrome in Locality 7 (Fig. 1c), Cerberus. This biostrome was perhaps 20 meters in lateral extent with vertical thickness that varied between 1 and 20 centimeters. Stromatolites are predominately composed of CFA, though there is sometimes some late, patchy silicification, while contemporaneous and vertically bounding cross-stratified grainstones are dolomite. (Caption continues on next page.) . . . . . 64

2.6 Continued from previous page. (d) Incipient digitate stromatolites from the same interval photographed in (c). (e) Stromatolite mound at Locality 5 (Fig. 1c), Aristeia, where phosphatic digitate stromatolites merge over several decimeters of growth to form laminated, but internally disordered and irregular, mounds. Also pictured is cross-stratified grainstone onlapping the stromatolitic mound. (f) Cut face of a hand sample from a depth of 33.3 meters in CBPM Core 010 (Fig. 1c). Darkest gray/black regions are finely laminated digitate stromatolites in oblique cross section, and intraclasts thereof. Lightest gray regions are the very fine matrix of recrystallized and micritized, but originally well-rounded, well-sorted, calcite grains against which the stromatolites grew. (g) Cut face of a hand sample from a depth of 8.6 meters in CBPM Core 011 (Fig. 1c). Mottled dark grey and light gray regions are finely laminated limestone, while pale orange and tan regions are mostly CFA. Note: finger is 1.5 centimeters wide, pen is 1 centimeter wide and 11 centimeter long, hammer handles are 4-5 centimeter wide. Otherwise, scale is indicated in the frame. . 65

- 2.7 Domal and columnar stromatolite bioherm (Lithofacies 7) and associated grainstone facies (Lithofacies 1) in the Salitre and Sete Lagoas formations. (a) Photograph of a columnar stromatolite bioherm. The bioherm appears to have had at least half a meter of synoptic relief on the seafloor during its growth, with a maximum diameter approaching 6 meters. Stromatolites near the center of the bioherm appear more stratiform, while they are more distinctly columnar and elongate near the margins. Locality 0 (Fig. 1a), Fazenda Arrecife. (b) Plan view of two adjacent stromatolite bioherms at Locality 0 (Fig. 1a). In this locality, bioherms have elliptical footprints with 0.8-3.6 m semi-minor axes and 1.3-6.3 m semi-major axes (based on a survey of 25 such bioherms over an area of  $1e4m^2$ ). Bioherms universally appear to have 10-30 centimeter-thick laminated “carapaces” or envelopes of roughly even width around their entire perimeter. Stromatolites within bioherms are closely, polygonally packed, with stromatolites near these envelopes being the most elongate. Channels between bioherms are filled variously with tabular intraclast conglomerate, medium-to-coarse grainstones with abundant cross-stratification. Bioherm carapaces are picked out in white. Measuring tape in frame shows 0.7 m. (Caption continues on next page.) . . . . . 66

- 2.8 Continued from previous page. (c) Red arrows indicate thin layers of very coarse lime grainstone, partially silicified, within finer laminated sediments on the margins of one of the stromatolite bioherm. Locality 0 (Fig. 1c), Fazenda Arrecife. The grainstones pictured here contain primary phosphatic intraclasts, with roughly 5% of all intraclasts/reworked grains being phosphatic (CFA) and 95% being calcitic. (d) Calcitic digitate stromatolites merged into a disordered/irregular stromatolite mass (bottom third of image), gradually merging to form a domal stromatolite with 7-10 centimeter of synoptic relief. (Boundaries between irregular/disordered mass and large, domal stromatolite are picked out in white.) The darkest region (top third of image) is comprised of medium-to-coarse, oolitic lime grainstone, featuring abundant 5-40 centimeter cross-sets describing assymetric wave ripples and some possible swaley cross-stratification. São Francisco Riverbank Locality (Table 1). Card is 9 centimeters tall and 4.5 centimeter wide. Hammer handles are 4-5 centimeter wide. Otherwise, scale is indicated in the frame. . . . . 67
- 2.9 Illustrations of columnar stromatolite bioherms and associated intraclast conglomerate and cross-stratified lime grainstone, depicted in plan view and bedding-perpendicular cross sections. Upper illustration represents sketches from an outcrop in Locality 0 (Fig. 1a, Table 1), Fazenda Arrecife. Lower illustration is a schematic representation of the facies (based on a survey of 25 bioherms over an area of  $1e4m^2$ ). 68

- 2.10 Annotated field photographs and depositional model for symmetric wave-rippled limestone (Lithofacies 8). (a) Wave-rippled limestone. Salitre Formation, Locality 6, Fazenda Catavento. Pencil is 13 centimeter length, <1 centimeter width. (b) Wave-rippled limestone in same location as (a). Dotted lines indicate location of ripple crests for a 20-centimeter-scale interval of vertical section. (c) Wave-rippled limestone in same location as (a-b). Hammer handle is 5 centimeter wide and 15 centimeters long. (d) Depositional model for wave-rippled limestone lithofacies: (i) Oscillatory flow in high-energy, shallow platform environment organizes sediment into symmetric ripples. (ii) Variations in carbonate sediment supply and flow energy result in chevron-style overlapping of laminae, with ripple crest location migrating back and forth. Ripple crests may be stabilized by early cementation. (iii) Period of lower-energy flow and high sediment supply fills ripple troughs, dampens relief. (Continues on next page.) . . . . . 69
- 2.11 Continued from previous page. (iv) Another generation of symmetric ripple formation. (v) Period of lower-energy flow and low sediment supply allows colonization of seafloor locally by microbial mats or biofilms. These biofilms stabilize the morphology of the ripple crests and may contribute locally to partial cementation of uppermost laminae. (vi) Resumption of higher-energy oscillatory flow disrupts and fragments laminae that are partially cemented or otherwise stabilized by mats. (vii) Period of lower-energy flow allows fragments to settle, being redeposited over cemented, stabilized ripple structures. Sediment fills troughs and dampens relief of ripple structures. (viii) Cycle repeats. (e) Inset from (d)(viii), demonstrating the effect of compaction (force indicated by black arrow) and later pressure solution on the appearance of ripples' internal structure: suturing of laminae boundaries, loss of definition of individual laminae, variation in laminae thickness, and stylolites. . . . . 70
- 2.12 Calcite pseudomorphs after aragonite crystal fans (Lithofacies 9) among planar-laminated and asymmetric ripple cross-stratified mudstone to very fine grainstone (Lithofacies 1 and 3). (a) Semi-isolated fans at Locality 17, Gruto do Janelão. (b) Laterally extensive (10s of meters) beds of crystal fans at Locality 22, Riacho do Campo. . . . . 71

- 2.13 Stromatolite bioherm comprised of both phosphatic digitate stromatolites and merged, irregular calcitic stromatolites. Locality 5 (Fig. 1c, Table 1), Aristeia. (a) Outcrop photo. (b) Annotation of (a), where laminae are traced in white. Carbonate fluorapatite (CFA) cements are shaded in red. Calcite cements are shaded in gray. Grains are calcitic peloids and ooids. More isolated digitate stromatolites branch and merge upsection, transitioning into bioherm with centimeters to decimeters of synoptic relief. Cross-stratified oolitic grainstone (Lithofacies 1) forms the initiation surface of the bioherm, onlapping it upsection. . . . . 72
- 2.14 Representative stratigraphic columns and textural sketches of the Salitre and Sete Lagoas formations, with approximate location on the São Francisco Craton (inset from Fig. 1a). Colors correspond to lithofacies 1-9, as defined in 3.2, Table 2, and Fig. 2. Pie charts superimposed on map of São Francisco Craton show proportion of measured stratigraphic section in each region represented by each lithofacies categorization. \*Since Lithofacies 9 (crystal fans) represents a negligible proportion of stratigraphic thickness, it is excluded from color blocks. . . . . 73
- 2.15 Generalized timing of mineral phases and fabrics observed in the Salitre and Sete Lagoas formations. Time proceeds from left to right: earliest textures related to the depositional environments are farthest left, and features of latest diagenesis are farthest right. 1Feature observed only in the Sete Lagoas Formation. 2Feature observed only in the Salitre Formation. Pale gray features are considered “later diagenetic,” and therefore not directly relevant to the processes of authigenic and early diagenetic phosphogenesis. . . . . 74

- 2.16 Thin section photomicrographs, taken in plane-polarized light, capturing representative microtextures within grainstone/rudstone and digitate stromatolite facies of the Salitre Formation. Images at right are annotated versions of images at left. Colors, as indicated in the key, represent different diagenetic phases: blue = micro-to-cryptocrystalline CFA, colorless/gray = CaCO<sub>3</sub> micrite and recrystallized xenotopic cements, orange = replacive silica/microcrystalline quartz cements pink = blocky-to-granular dolomite spar filling early porosity (Dolomite I), red = euhedral to subhedral dolomite spar nucleating at primary grain boundaries (Dolomite II), and purple = fracture-filling calcite spar. (Continues on next page.) . . . . . 75
- 2.17 Continued from previous page... (a) Ooids and peloids from grainstone facies, Locality 4 (Fig. 1c, Table 1). (b) Grainy interstromatolite fill from Locality 0 (Table 1), with CFA intraclasts, ooids, and peloids. (c) Left-hand flank of a phosphatic digitate stromatolite from Locality 5 (Fig. 1c, Table 1). (d) Laminae of a phosphatic digitate stromatolite from CBPM Core 011 (Fig. 1c), cross-cut by a fracture filled with calcite spar. . . . . 76
- 2.18 Back-scattered electron (BSE) images of a phosphatic digitate stromatolite from Locality 5 (Fig. 1c, Table 1), where white/lightest gray indicates CFA, medium gray indicates low-Mg calcite, and dark gray indicates high-Mg calcite. (a) A view of the CFA- and calcite-cemented laminae near core of stromatolite. (b) Margin of the same stromatolite as (a), where the contact between stromatolite and associated crinkly laminite is defined by the transition from CFA cement to calcite cement. (c) Higher-magnification view of the area indicated by the orange box in (b), emphasizing the rim of isopachous CFA cement around rounded calcite grains near the stromatolite margin. 77
- 2.19 XRF images of cut, unpolished slabs of phosphatic and non-phosphatic digitate stromatolites of the Salitre Fm, where specified colors indicate fluorescence intensity of P, Fe, S, Ca, and Mg (from left to right). Far right images are reflected white light photographs. Dotted lines demarcate boundary between stromatolites and grainy interstromatolite fill. Arrows indicate stratigraphic up. (a) Branching and merging digitate stromatolites from Locality 5 (Fig. 1c, Table 1). (b) Digitate stromatolites from CBPM Core 011 (Fig. 1c). . . . . 78

- 2.20 Early-to-mid-stage diagenesis of phosphatic textures. Small arrows indicate stratigraphic up. (a) XRF image of cut, unpolished slab from CBPM Core 011 (Fig. 1c), featuring phosphatic digitate stromatolites and phosphatic intraclasts derived from said stromatolites near margin of stromatolitic buildup (Lithofacies 6). Color yellow indicates fluorescence intensity of P. (b) XRF image of cut, unpolished slab from Locality 0 (Fig. 1a, Table 1), featuring phosphatic intraclasts within carbonate grainstone facies near margins of columnar and digitate stromatolite buildups. Such intraclasts are interpreted as more distally and/or energetically transported derivatives of intraclasts like those pictured in (a). (c) Annotated thin section photomicrograph from within the white circled area in (b), featuring an altered phosphatic intraclast. This is a representative example of the extent of fabric-destructive diagenesis of phosphatic facies observed within the Salitre Fm. . . . . 79
- 2.21 X-ray fluorescence (XRF) images of cut, unpolished slabs of phosphatic and non-phosphatic textures of the Salitre Fm, where specified colors indicate fluorescence intensity of the indicated elements. Far right images are reflected white light photographs. Dotted lines demarcate boundaries between stromatolites and grainy, interstromatolite fill. Arrows indicate stratigraphic up. (a) Branching and merging digitate stromatolites from Locality 5 (Fig. 1c, Table 1). (b) Digitate stromatolites from CBPM Core 011 (Fig. 1c). (c) Phosphatic digitate stromatolites and phosphatic intraclasts derived from said stromatolites near margin of stromatolitic buildup (Lithofacies 6). Billet from CBPM Core 011 (Fig. 1c). (d) Calcitic, dolomitic, and phosphatic intraclasts within carbonate grainstone facies near margins of columnar and digitate stromatolite buildups. Locality 0 (Fig. 1a, Table 1). . . . . 80

- 2.22 Thin section photomicrographs, taken in plane-polarized light, capturing representative microtextures within grainstone/rudstone and digitate stromatolite facies of the Salitre Formation. Images at right are annotated versions of images at left. White outlines highlight primary grain boundaries. Colors, as indicated in the key, represent different diagenetic phases: pink = blocky-to-granular dolomite spar, green = Fe-sulfides and oxidized pseudomorphs thereof, blue = CFA, and colorless/tan = CaCO<sub>3</sub> micrite and recrystallized xenotopic cements. (a) Grainy inter-stromatolite fill from Locality 5 (Fig. 1c, Table 1), with blocky dolomite spar filling early porosity. (b) Right-hand flank of a phosphatic digitate stromatolite from Locality 5 (Fig. 1c, Table 1). (c) Later fractures filled with calcite spar and associated with Fe-sulfides, cross-cutting phosphatic digitate stromatolite laminae, Locality 5 (Fig. 1c, Table 1). (d) Recrystallized ooid grainstone from Locality 4 (Fig. 1c, Table 1), featuring Fe-associated stylolite. . . . . 81
- 2.23 Thin section photomicrographs, taken in plane-polarized light, capturing representative examples of microtextures that exhibit features of late-stage hydrothermal diagenesis within grainstone/rudstone and digitate stromatolite facies of the Salitre Formation. Images at right are annotated versions of images at left. Red arrows indicate examples of Fe-sulfides and oxidized pseudomorphs thereof. (a-c) Replacive fluorite among recrystallized and partially dolomitized sparry cements, showing spatial relationships to Fe-sulfide minerals. Sample from Core 011 (Fig. 1c). (Continues on next page.) . . . . . 82
- 2.24 Continued from previous page. (d) Blocky dolomite spar (Dolomite I) filling early porosity within inter-stromatolite grainstone, with margins of individual crystals recrystallized to murky, more finely crystalline dolomite spar (Dolomite II). Dolomite II associated with fluorite cement, and Fe-sulfide-bearing veins. Sample from CBPM Core 010 (Fig. 1c). (e) Same microfacies shown in D from CBPM Core 010 (Fig. 1c), but showing internally laminated CFA-cemented intraclast derived from digitate stromatolite afloat in recrystallized CaCO<sub>3</sub> cements. . . . . 83

- 3.1 Geographical and stratigraphic context of presented geochemical measurements. (a) Map depicting the location of the São Francisco craton relative to nearby cratonic remnants (modified after Sanders and Grotzinger, 2021; Umberto G. Cordani and Sato, 1999; Reis, Suss, et al., 2017; Alkmim and Marcelo A. Martins-Neto, 2012). (b) Geologic map of region indicated in (a), and stratigraphy of the Una Group. (Dalton de Souza et al., 2003; Fonseca et al., 2014). (c) Simplified stratigraphic columns from the Aristeia locality (indicated in (b), see also TABLE), with inset previously published in Sanders and Grotzinger (2021) depicting digitate stromatolite buildup in which CFA cements – colored red – are prevalent at the base/core of the buildup, and are less common in the more merged/disordered laminated textures. (d) Simplified stratigraphic columns from the Cerberus, Minotaur, and Io localities (indicated in (b)). Shapes adjacent to the columns indicate the location in each stratigraphic column from which geochemical samples and their corresponding thin sections and slabs were collected. . . . . 127
- 3.2 Sedimentological characterization of CBPM drill cores. Colored shapes adjacent to the columns indicate the location in each stratigraphic column from which geochemical samples and their corresponding thin sections and slabs were collected, according to the same key as Fig. 3.1. Location of drill cores in Fig. 3.1b. . . . . 128
- 3.3 Measured  $\Delta_{47}$ ,  $\delta^{13}C_{mineral}$ ,  $\delta^{18}O_{mineral}$ , and calculated  $\delta^{18}O_{water}$  data for sample powders extracted by micro-scale drilling of earliest cement fabrics in syndepositional phosphatic and non-phosphatic facies. Error bars represent  $\pm 1$  S.E. (standard error). (a)  $\Delta_{47}$ -derived temperature vs.  $\delta^{18}O_{mineral}$ . Contours indicate  $\delta^{18}O_{water}$  based on equilibrium fractionation models. (b)  $\Delta_{47}$ -derived temperature vs. calculated  $\delta^{18}O_{water}$ . Contours indicate  $\delta^{18}O_{mineral}$  based on equilibrium fractionation models. (c)  $\delta^{18}O$  vs.  $\delta^{13}C$ . Labels indicate where multiple measurements overlap. In (a-c), circles indicate measurement of calcite sample, triangles dolomite, and squares CFA. Like colors indicate samples collected from the same locality and/or stratigraphic context. See Figs.3.1-3.2 for sample locations and facies associations. . . . . 129

- 3.4 Annotated illustration of the formation and diagenesis of a digitate stromatolite and adjacent carbonate grainstone, representative of the phosphatic members of the Salitre Formation. Illustration is schematic and combines in several slides true features observed in dozens of petrographic thin sections and slabs. (a) Illustration of a stromatolite in active formation amidst carbonate ooid and peloid sedimentation. (b-c) Insets indicated in (a), depicting the stages of diagenesis as interpreted from petrographic imagery and geochemical data in this and previous work (Sanders and Grotzinger, 2021). At far left, thin section photomicrographs (plane polarized light) of the illustrated features. See text. . . . . 130
- 3.5 Additional photomicrographs of the major mineral phases identified within the digitate stromatolite and grainstone facies of the Salitre Formation. At left, transmitted plane-polarized light photomicrographs, at right annotated versions of the same. (a) Carbonate peloids and ooids within the grainstone/rudstone lithofacies, with varying levels of fabric-retentive to partially fabric-destructive micritization. Cements are a combination of anhedral mosaic calcite spar and micrite and more euhedral dolomite spar — which, as illustrated in Fig. 3.4, is likely the result of recrystallization of primary calcite or aragonite cements in equilibrium with a different generation of diagenetic fluids. (b) Carbonate peloids and ooids, in a photomicrograph showing the spatial relationships between the different cement mineralogies. (c) Right-hand flank of a digitate stromatolite, showing the sharp distinction between cryptocrystalline CFA cement in the laminated interior of the stromatolite and calcite micrite and calcite/dolomite spar cements in the grainstone immediately adjacent to the stromatolite. A vein containing lateritic blocky calcite spar is also visible. (d) Example of a later-stage stylolite, cross-cutting recrystallized carbonate ooids and peloids. In all panels, Fe-sulfides (pyrite, and oxidized pseudomorphs thereafter) are a minor, sparsely distributed phase. . . . . 131
- 4.1 Histogram of  $\delta^{34}S_{\text{mineral}}$  values. CAS and PYR represent  $\delta^{34}S_{\text{calcite/dolomite}}$  measured via ICP-MS and  $\delta^{34}S_{\text{pyrite}}$  measured via SIMS, respectively. PAS represents  $\delta^{34}S_{\text{PAS}}$  measured via EA-IRMS. CRS represents  $\delta^{34}S_{\text{pyrite,CRS}}$  measured via EA-IRMS. . . . . 166

- 4.2 Geographical and stratigraphic context of presented geochemical measurements, modified after previous study Sanders, J. Eiler, and Grotzinger, 2022. (a) Map depicting the location of the São Francisco craton relative to nearby cratonic remnants (modified after Sanders and Grotzinger, 2021; Cordani and Sato, 1999; Reis, Suss, et al., 2017; Alkmim and Marcelo A. Martins-Neto, 2012). (b) Geologic map of region indicated in (a), and stratigraphy of the Una Group. Dalton de Souza et al., 2003; Fonseca et al., 2014. (c) Simplified stratigraphic columns from the Aristeia locality (indicated in *b*), with inset previously published in Sanders and Grotzinger, 2021, depicting digitate stromatolite buildup in which CFA cements – colored red – which are prevalent at the base/core of the buildup, and are less common in the more merged/disordered laminated textures. (d) Simplified stratigraphic columns from the Cerberus, and Minotaur localities. (e) Simplified stratigraphic columns from CBPM Cores 5 and 10. Shapes adjacent to the columns indicate the location in each stratigraphic column from which geochemical samples and their corresponding thin sections were collected. . . . . 167
- 4.3 Illustration of distinct microtextural associations ("microfacies") examined in this study, and example thin section photomicrographs thereof. Microfacies A = carbonate-cemented grainstone, B = carbonate-cemented grainstone adjacent to phosphatic digitate stromatolite buildup, C = carbonate-cemented grainy inter-stromatolite fill, D = carbonate-cemented laminated mudstone, E = carbonate-cemented stromatolite laminae, and F = CFA-cemented stromatolite laminae. Blue shading indicates spatial distribution of phosphatic cements (i.e., Microfacies F). Colored boxes indicate textural associations of each microfacies at the outcrop/hand sample scale and example thin section photomicrographs of mineral fabrics therein. Red boxes = C and F, yellow boxes = A and B, and green boxes = C and E. D is not pictured, due to its similarity to A and B (yellow boxes). . . . . 168
- 4.4 Summary of sample preparation and methods. . . . . 169

- 4.5 Reflected light photomicrographs and Raman spectra of a representative subset of individual and aggregate Fe-sulfide crystals in thin section, whose  $\delta^{34}\text{S}$  compositions were measured via SIMS. (a,d, and g) Annotated photomicrographs of target crystals in their microfacies context. (b,e,h, and j) Magnified insets of crystals and crystal aggregates. Dotted white lines demarcate the area sputtered by the primary ion beam, and numbers indicate the order in which measurements were made in each pictured area. (c,f,i, and k) Raman spectra collected from crystals within the sputtered areas, and the mineralogies with which they are associated. . . . . 170
- B.1 Thin section photomicrographs with of CFA-cemented laminae in digitate stromatolites of the Salitre Formation, featuring organic matter concentrated in filamentous microfossils, with and without annotation. In annotated lower panels, pink lines indicate individual and bundled filamentous structures within the plane of focus. Dotted pink lines indicate filamentous structures outside of the plane of focus. (a) Randomly oriented filaments, folded back on themselves and tangled. (b) Filaments preferentially oriented parallel to stromatolite laminae. . . . . 188
- B.2 Thin section photomicrographs of CFA-cemented laminae featuring diffuse inclusions of amorphous organic matter, with blue arrows indicating orientation of subvertical striations suggestive of microbial mat structure. . . . . 188
- B.3 Back-scattered electron images annotated with locations of point energy spectra (EDS), and plotted spectra. Energies of characteristic  $K\alpha$  X-Ray emission for major elements are indicated by vertical lines. (a-b) Representative images and spectra of digitate stromatolite laminae containing carbonate grains and minor carbonate cements in a cement matrix of carbonate fluorapatite (CFA). (c) Magnified inset from panel (b) and associated energy spectra. In all back-scattered electron images: lightest gray corresponds to cryptocrystalline CFA cement, medium gray corresponds to carbonate minerals including calcite and dolomite, and darkest gray/charcoal corresponds to native organic material. . . . . 189

- B.4 Continuation of Fig. B.3. Back-scattered electron images annotated with locations of point energy spectra (EDS), and plotted spectra. Energies of characteristic  $K\alpha$  X-Ray emission for major elements are indicated by vertical lines. (d-e) Representative images and spectra of digitate stromatolite laminae containing carbonate grains and minor carbonate cements in a cement matrix of carbonate fluorapatite (CFA). 190
- B.5 (a) Back-scattered electron image and (b-f) corresponding maps of EDS spectra intensity for characteristic  $K\alpha$  emissions of major elements, featuring organic matter, carbonate grains, and minor carbonate cements within CFA-cemented laminae of a phosphatic digitate stromatolite from the Salitre Formation. . . . . 191

## LIST OF TABLES

<i>Number</i>	<i>Page</i>
2.1 See Appendix A for Table 2.1 and caption. . . . .	59
2.2 See Appendix A for Table 2.2 and caption. . . . .	59
3.1 Isotopic data. . . . .	125
3.2 Isotopic data, continued. . . . .	126
4.1 Measured $\delta^{34}S$ of CAS, PAS, CRS, and pyrite in phosphatic and non-phosphatic microfacies of the Salitre Formation. . . . .	165

*Chapter 1*

## INTRODUCTION

I.

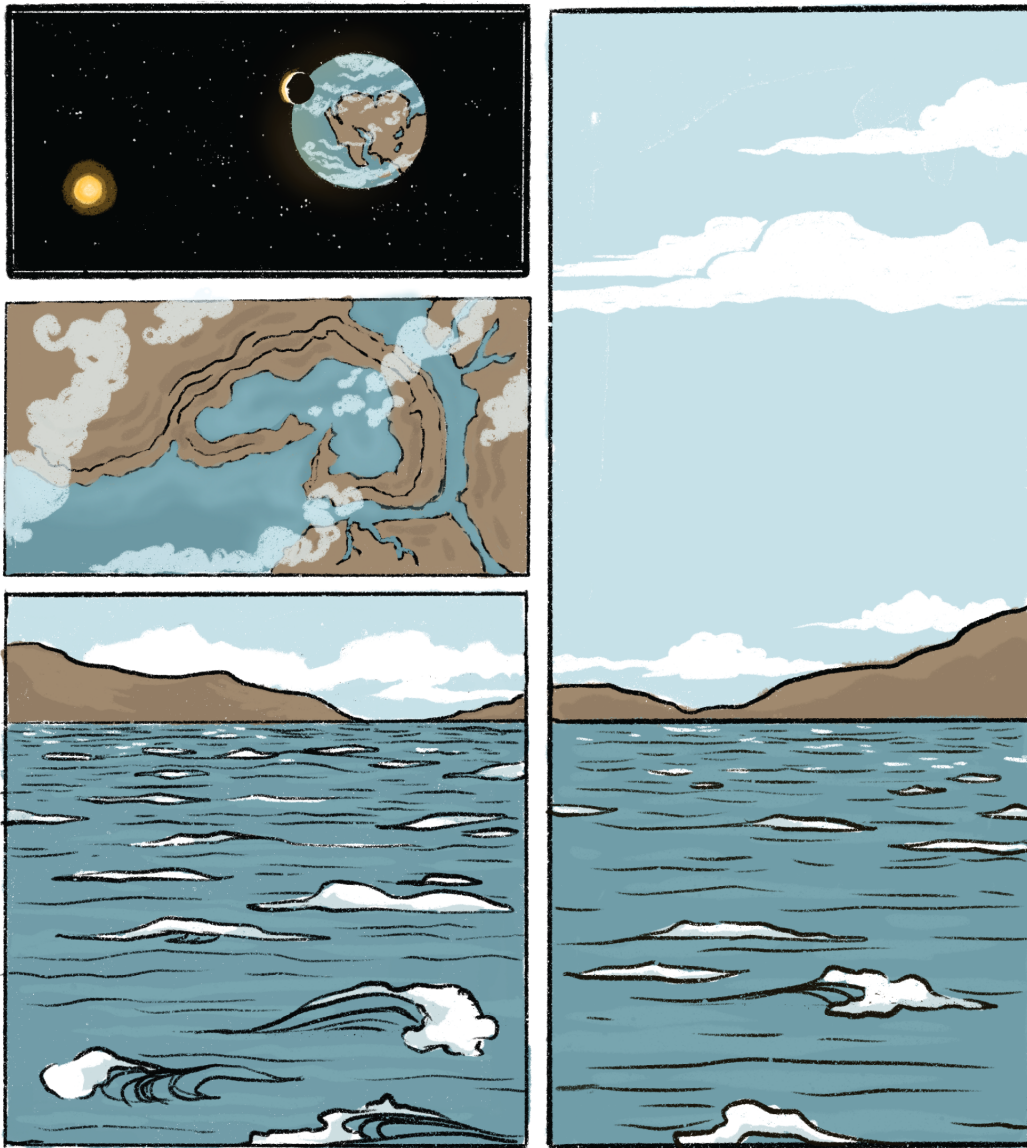


Figure 1.1: 600 million years ago, a wave-tossed sea.

600 million years ago, the continents that we call Africa, South America, Eurasia, and Australia were one. They formed a “supercontinent” comprised of dozens of thick rocky plates sutured together, named Gondwana after the Gondi people who

would one day settle upon its mangled remnants. At 600 Ma, much of Gondwana was warm and tropical. Where once there had been massive glaciers, there were now shallow wave-tossed seas.

Their only inhabitants: quietly persistent, single-celled organisms, blue-green, olive, reddish-brown, translucent, gelatinous, and aggregated in films and mats — filaments waving in the shifting currents like so many microscopic strands of grass in a breeze. These simple, persistent lifeforms clung to each other and to the rain of carbonate sediment falling from the water column, forming pillars, domes, and great mounds of intricate latticework corridors — mindless, but astonishingly complex architectures — like so many sunken palaces among the shifting pearl-white shoals.

The sunken palaces sunk further still, not just beneath the waves but beneath the sea floor, under hundreds of meters, even kilometers, of carbonate grains and mud and later siliciclastic sands. Beneath and around them, Gondwana shifted and split, its component cratons crashing into or straining apart from one another. Hundreds of millions of years of now-rock cracked, tilted, and then wore into wild new topographies under water, wind, roots, talons, paws, hoofs, and eventually feet. The ancient, sunken cities were laid bare and desiccated — alien ruins on a planet made anew.

6 years ago, I arrived in the Division of Geological and Planetary Sciences as a new graduate student. I was mad for aliens, determined to find and study life on a different planet. What would an alien fossil look like? How would we distinguish it from the million other abiogenic rocks? Are we alone in the solar system? I was ready, I told my advisers, to hike down into Gusev crater and kick apart clods of rusty dirt with my space boots yelling, “anybody home?” if that’s what it would take.

My advisers pointed out, tactfully, that this was perhaps not the best approach, and probably not plausible on the timescale of a graduate degree. My interest in life on other worlds had grown from my interest in life on Earth, hadn’t it? Perhaps, they suggested, you should study life somewhere we know it has been: the ancient Earth. This did not sound much like alien hunting, but I liked field geology and paleontology and I was intrigued. On a 2018 trip to Bahia, Brazil, I encountered the ruins of an alien city in a ditch on the side of the road. These were the sunken palaces, with their honeycomb galleries of pearly carbonate and delicately mauve calcium phosphate, the work of a million billion microbial architects a long time ago in an ocean far far away from the world I knew. How did these structures

form, and were the microbes that formed them truly architects, actively guiding the construction of their own tombs? Or passive bystanders? How different did the chemistry of the water, and the interplay of living and non-living elements, have to be from one patch of seafloor to the next to determine whether a palace could grow or not? What information could these ruins hold about the world as it was when their minuscule bricks were first laid and cemented?

I immersed myself in the reconstruction of the paleoenvironment and paleoecology that had produced these structures, determined their composition, and sealed the fate of the remains of the organisms that lived on them.

## **Chapter 2**

I measured, described, and sketched hundreds of meters of stratigraphy across the São Francisco Craton, the remnant of Gondwana which had played host to the palace-builders' ancient sea. I used these to develop a depositional facies model: a picture of the depositional setting in which both phosphate- and carbonate-cemented microbialites formed as islands among wave-tossed carbonate sediments.

## **Chapter 3**

I took slivers of rock from among the measured strata, and examined at micrometer scales their mineral fabrics, by observing and measuring the interaction of the slivers with white light, green light, X-Rays, streams of electric current, and beams of ionized particles. These data allowed me to develop a relative timeline of the formation and recrystallization of different components of the rocks within and surrounding the microbialite buildups. I then collected powders of the earliest cement minerals I could identify, dissolved them in acids, and measured their oxygen and carbon isotopic compositions, and tendency of certain isotopes to bind together therein. These data allowed me to constrain the temperatures which the rocks had experienced, and the nature and origin of fluids that flowed through and interacted with the rock throughout its existence.

## **Chapter 4**

I identified targets for further isotopic analysis among well characterized slivers of rock in which early cements of phosphatic and non-phosphatic compositions could be identified and separated from one another. On our own planet — modern Earth — structures of similar composition to the Sao Francisco's ancient phosphatic microbialites actively form in select environments. Their formation being tied to the

activity of certain community structures among sulfur-metabolizing microorganisms, I wished to examine the ancient structures for geochemical evidence of the same. I measured the sulfur isotopic composition of structural sulfate and sulfide in the cement-forming minerals within the target samples, and compared them — finding values consistent with the activity of such microbial metabolisms as are seen in modern analog environments.

### **Appendix B — Preliminary Results**

I explored possible relationships between organic matter from decaying microorganisms and the cementation and lithification of the rock itself. As with my sulfur isotope investigation, I took inspiration from analogous systems in the modern world to develop a hypothesis for the role of organic material in facilitating its own preservation: accumulation of cations around organic matter, enabling the formation of complexes between organic matter and the negatively charged components of precursor cement minerals. I used electron microscopy to look for geochemical evidence of cation-enrichment in well-characterized slivers of rock from my ancient phosphatic microbialites.

By interrogating the phosphatic and non-phosphatic microbialite structures — which I still think of as alien cities — I was able to develop some understanding of the lifeforms that created them and the world they inhabited. More broadly, I gained some understanding of the ecologies and the sequence and timing of environmental conditions necessary to preserve evidence of life on an alien world — and the tools that can be used to seek out that evidence.

This work has expanded the “alien” and “the unknown” and the “wondrous” for me beyond cold, remote Mars, to include even the most commonplace and next-door of subjects: gray-white heaps of stones in a ditch on the side of a rural road, etchings in sidewalk concrete, drab pebbles. In such heaps, we found ruined palaces. In such etchings, we might find vibrant communities of microorganisms tracing out a record of their lives that might last for hundreds of millions of years to come. In such drab pebbles, we find that we are not alone.

### **Why phosphogenesis?**

So, (to quote the late, great storyteller Seamus Heaney). Some 730 million years ago, the Earth — whose vast global oceans and barren land masses had been doing much the same thing for the first several billion years of their existence — underwent a rapid and astonishing change. The microorganisms who had been

quietly learning to harness the energy of the sun to fix inorganic carbon for 2 billion years had exceeded much of the oceans' reducing capacity, and oxygen was rapidly accumulating in the atmosphere and surface waters (Canfield, Poulton, and Narbonne, 2007; Fike et al., 2006). The Earth was cooling, its land masses continuing to drink up  $CO_2$  via silicate weathering even as glaciers encroached on the tropics and bound them in ice (Kendall et al., 2004).  $CO_2$  and other gases leaking from the world's volcanoes may have absorbed and re-emitted enough of the sun's light that they melted the ice again. Repeatedly, the world froze and thawed. The ocean churned and drew down the atmosphere's carbon into its waters. Living organisms devoured it, primary production of biomass bloomed, carbonate precipitated readily. The warm waters encroached on the land. And at last, some combination of all of these changes to the sea, the sky, and their biogeochemical cycles facilitated the emergence of complex, multicellular life (Xiao and Laflamme, 2009; Narbonne and Gehling, 2003; Narbonne, 2005). This is the globally averaged story of the Precambrian-Cambrian (PЄ-Є) Boundary; but at finer spatial scales, it is a longer and more complicated tale by far.

Variations in depositional environment and ecology beget variations in response to global change in sea level, temperature, and nutrient budgets. They also beget variations in the creation of the sedimentary record itself and its preservational biases. In order to develop a more complete picture of global change at the PЄ-Є Boundary, it is therefore vital to compare and contrast time-equivalent records of different depositional and diagenetic settings which were subject to the same global systems.

One remarkable feature of the PЄ-Є geologic record ripe for such comparative study are the abundant and often fossil-rich phosphate-rich sedimentary deposits of the Ediacaran and Early Cambrian periods. Such phosphorite deposits are uncommon in earlier Earth history, and uncommon again until the late Paleozoic Era. Ediacaran and Early Cambrian phosphorites are geographically widespread, being observed in Algeria, China, Eastern Brazil, Australia, India and Mongolia, among other localities (Peter J. Cook and Shergold, 1984; P. J. Cook, 1992; Brasier and Callow, 2007; Sheldon, 1981). This ubiquity across time-equivalent sedimentary deposits has led researchers to infer a perturbation of the global phosphorus cycle in connection with the global climate and ecological changes poeticized above (Laakso et al., 2020; Papineau, 2010; Donnelly et al., 1990). The style of phosphate mineralization, however, and the depositional facies in which it seems to have occurred, are quite

different not only between continents but between kilometer-scale subbasins, meter-scale reefs, and even sub-centimeter scale fabrics (Sanders and Grotzinger, 2021; Okubo et al., 2018; Pruss et al., 2019). Local complexities are superimposed upon the effects of global processes. These complexities appear to affect not only the distribution of phosphate minerals, but the likelihood that those minerals can facilitate high-fidelity preservation of microbial and early animal fossils, or preserve details of the aqueous chemistry of primary seawater and sediment porewaters. Indeed, phosphorites are host to some of the most well-preserved microbial and early animal fossil assemblages in the geologic record (Xiao, Zhang, and Knoll, 1998; Brasier and Callow, 2007; Anderson et al., 2017; Chin et al., 2003; Wacey et al., 2019; Bengtson et al., 2017), but what ecological niches do they represent, and were they representative of global or local systems change?

The range of biogeochemical conditions sedimentary phosphorites may represent, and their consequences for taphonomy and the creation of a paleobiological record, has been the subject of lively debate for decades. There are several categories of hypotheses:

1. Global changes in the biogeochemical P, S, and C cycles resulting from the rise of atmospheric oxygen → rise of seawater sulfate → rise of remineralization of P-bearing organic matter by sulfate-reducing microorganisms and associated microbial communities (Laakso et al., 2020; Papineau, 2010; Donnelly et al., 1990),
2. Regional and local sedimentological and biological influences on phosphate accumulation, retention, and early lithification in shallow sediments (Arning et al., 2009; Alsenz et al., 2015; H. N. Schulz and H. D. Schulz, 2005; Brock and Schulz-Vogt, 2011; J. V. Bailey et al., 2013; Lepland et al., 2014), or
3. Some combination thereof.

Most hypotheses endeavor to explain how phosphate, calcium, and carbonate ion concentrations become sufficiently high in a given setting to overcome thermodynamic barriers to rapid, early phosphate mineralization; likewise, for kinetic barriers. However, they do not explain why the invoked processes — so common through geologic time and space — so often fail to produce phosphorite. A comprehensive formation model must explain the spatial distribution of phosphorite: i.e., why phosphate mineralization might occur in one place and not another.

It may be possible to test and discriminate among models of phosphorite formation, or phosphogenesis, by comparing proxies for paleoenvironmental and paleoecological conditions between contemporaneous phosphatic and non-phosphatic facies. Ideally, these comparisons would be made among phosphatic and non-phosphatic facies within the same regions and formations, for which the impacts of mid-to-late-stage diagenesis on depositional signal preservation can be controlled.

Phosphogenesis requires the confluence of environmental conditions favorable to the precipitation of phosphate minerals like fluorapatite and carbonate-rich fluorapatite (CFA). These conditions include relatively high concentrations of dissolved inorganic phosphate ( $HPO_4^{2-}$ ,  $PO_4^{3-}$ , and  $H_2PO_4^-$ ), comparable molar concentrations of  $Ca^{2+}$  ions, relatively low concentrations of kinetic inhibitors to phosphate mineral precipitation, and the prevalence of a limited range of pH, alkalinity, and temperature conditions (Föllmi, 1996; Defforey and Paytan, 2018; Filippelli, 2011; Filippelli and Delaney, 1996). These conditions occur in some modern marine settings, mainly upwelling zones such as the coasts of Namibia, South Africa, and Peru (H. N. Schulz and H. D. Schulz, 2005; Crosby and Jake V. Bailey, 2012; Arning et al., 2009; J. V. Bailey et al., 2013). The reason for this spatial distribution may be that in upwelling zones, remineralized organic matter from deep marine settings is transported into shallower photic zones, fueling primary production and thus the flux of phosphorus-bearing organic material to the seafloor (Dale et al., 2009; Küster-Heins et al., 2010). Organically-bound and associated phosphate is liberated during the oxidation of organic matter by heterotrophic organisms throughout the water column and down past the sediment-water interface. Upwelling is only one mechanism of increasing phosphorus flux to the seafloor, however, as evidenced by the occurrence of ancient phosphorites formed in carbonate platforms, lagoons, and even lakes (Peter J. Cook and Shergold, 1984; P. J. Cook, 1992). Nevertheless, modern phosphogenetic environments are foundational to models of ancient phosphorite formation, providing examples of settings where inorganic phosphate is not only generated, but accumulated in sediments, and guarded against dilution by seawater. Mechanisms of phosphate retention and accumulation in modern and ancient phosphogenetic environments may include:

- The "iron curtain," or the shuttling of inorganic phosphate below the sediment-water interface via the burial of Fe- and Mn-(oxy)hydroxide minerals under an oxic water column, to which inorganic phosphate readily adsorbs (Föllmi, 1996; Chambers et al., 1990; Anschutz et al., 1998; Slomp et al., 1996; Sundby

et al., 1992). Phosphate is desorbed during the reduction of these minerals below the microbially-generated oxycline in sediments, but re-sorbed and re-buried if it is ever transported by advection or diffusion above that oxycline.

- Lack of exchange between reducing sediment porewaters (where remineralized phosphate is generated) and overlying seawater because of low rates of advection and/or diffusion, enabled by thick microbial mats, rapid burial, or topographical sheltering from wave action (Caird et al., 2017; D M Banerjee, Basu, and Srivastava, 1980; D. M. Banerjee, 1971).
- Microbial communities in sediments capable of producing episodes of extremely high inorganic phosphate concentrations alongside conditions of low carbonate mineral saturation; specifically, phosphate-accumulating sulfide-oxidizing bacteria migrating across the oxycline and co-occurring with anaerobic sulfate reducing bacteria (Arning et al., 2009; Brock and Schulz-Vogt, 2011; J. V. Bailey et al., 2013; Crosby and Jake V. Bailey, 2012; H. N. Schulz and H. D. Schulz, 2005).

However, *not* all of these mechanisms of phosphate retention and accumulation in marine sediments are observed in all modern phosphogenetic environments; and all *have* been observed in non-phosphogenetic environments. So which of these proposed mechanism(s) actually controls the distribution and taphonomic potential of sedimentary phosphorite through geologic time?

In some ancient phosphorites, microbial fossils comparable in size and form to modern phosphate-accumulating sulfide-oxidizing bacteria and sulfate-reducing bacteria have been identified in what seem to be authigenic phosphate cements specifically carbonate fluorapatite or CFA (Crosby and Jake V. Bailey, 2012; J. V. Bailey et al., 2013). In others, some iron-sulfide minerals, likely the result of microbial sulfate reduction in reducing porewaters, are observed to be syngenetic with apatite cements (Okubo et al., 2018). However, similar fossils and similar reduced sulfur-bearing minerals occur in non-phosphatic textures as well, e.g. Sanders and Grotzinger, 2021. Spatial associations between primary phosphatic mineral phases and microfossils, sulfide, or other proxies for paleocological conditions are not sufficient proof of causality. However, a careful accounting of associations and dissociations between phosphate and paleoenvironmental indicators in the geologic record could help constrain cause and effect relationships. The thesis presented here is an examination of the sedimentary record for just such associations.

II.

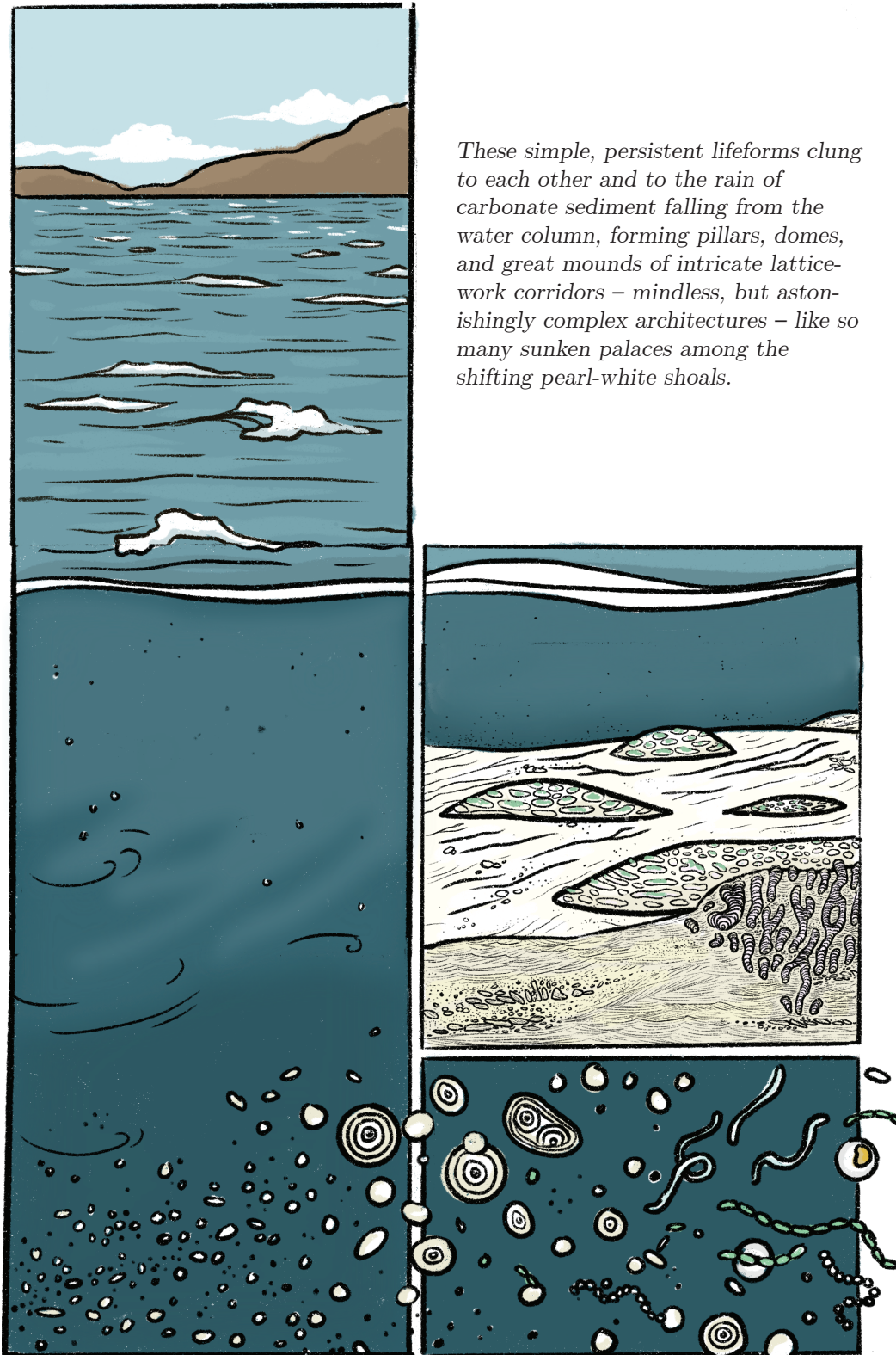


Figure 1.2: Sunken palaces.

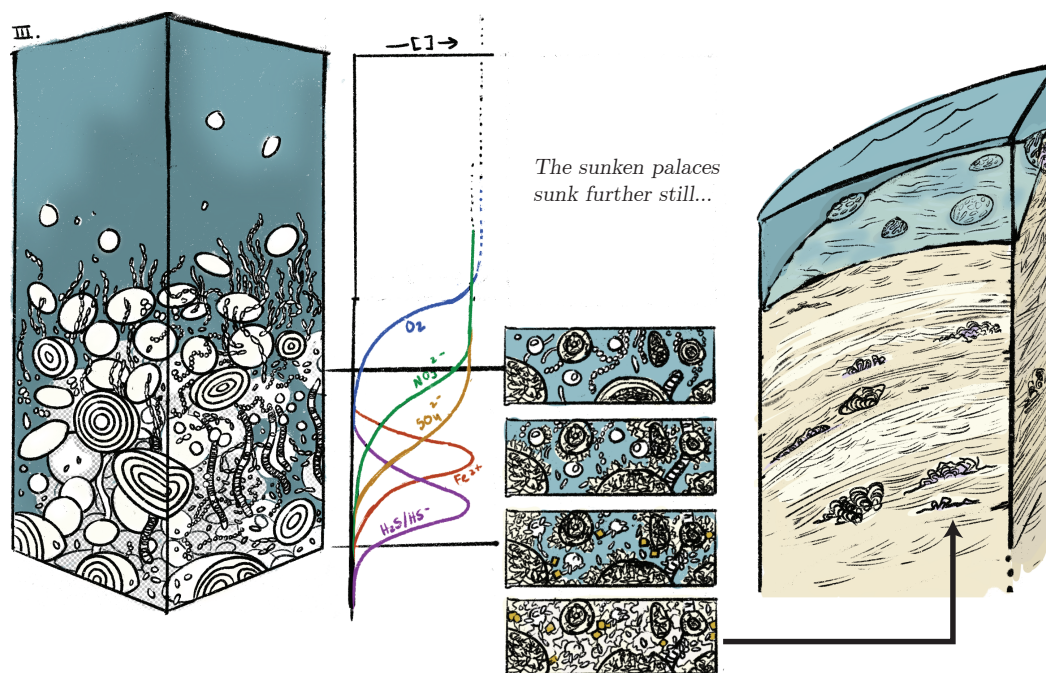


Figure 1.3: The sunken palaces sunk further still, not just beneath the waves but beneath the sea floor.



Figure 1.4: The ancient, sunken cities were laid bare and desiccated – alien ruins on a planet made anew... Then, I arrived.



Figure 1.5: What information could these ruins hold about the world as it was when their miniscule bricks were first laid and cemented?

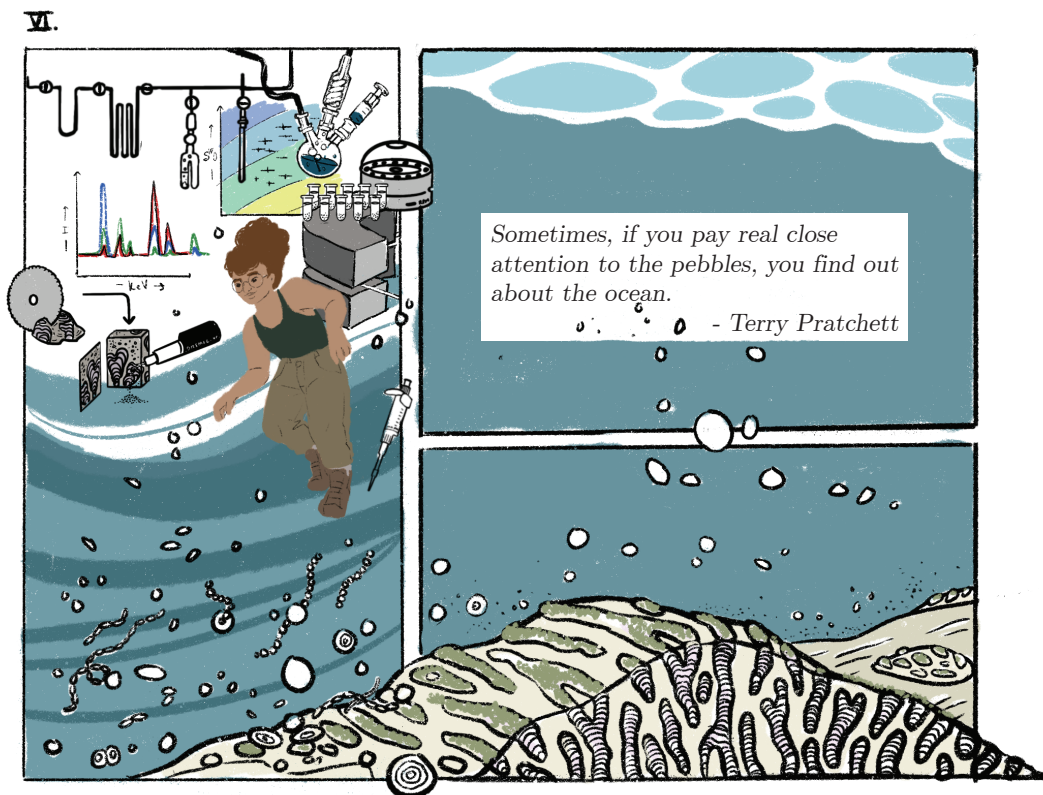


Figure 1.6: I immersed myself in the reconstruction of the paleoenvironment and paleoecology that had produced these structures, determined their composition, and sealed the fate of the remains of the organisms that lived on them.

*Chapter 2*

SEDIMENTOLOGICAL AND STRATIGRAPHIC  
CONSTRAINTS ON DEPOSITIONAL ENVIRONMENT FOR  
EDIACARAN CARBONATE ROCKS OF THE SÃO FRANCISCO  
CRATON: IMPLICATIONS FOR PHOSPHOGENESIS AND  
PALEOECOLOGY

Cecilia Sanders and John Grotzinger<sup>1</sup>

*'Rocks! Why am I messing around with lumps of stone? When did they ever tell anyone anything?' said Ponder. 'You know, sir, sometimes I think there's a great ocean of truth out there and I'm just sitting on the beach playing with. . . With stones.'* — Terry Pratchett, *Lords and Ladies*

## 2.1 Abstract

The Una and Bambuí Groups of northeastern and central Brazil are remnants of a vast intracratonic carbonate platform formed on the São Francisco Craton during the Ediacaran Period. Their basal stratigraphic units contain early phosphatic cements and phosphatic intraclasts in association with elongate digitate stromatolites in the more northern Irecê and Salitre paleobasins (Salitre Formation), and microbial laminites and aragonite crystal fan pseudomorphs in the more southern São Francisco paleobasin (Sete Lagoas Formation). Previous studies have drawn comparisons to other Precambrian phosphorites, as well as modern phosphogenetic environments, suggesting mechanisms of phosphogenesis dependent on the accumulation of porewater phosphate via microbial activity in low flow velocity environments, such as relatively quiescent tidal flats, where an absence of wave-driven advection and porewater refreshment could have allowed oversaturation with respect to carbonate fluorapatite. Here, we present new sedimentological data that characterize the depositional setting of the Salitre and Sete Lagoas formations as a shallow, wave-swept carbonate platform notable for its extensive high-energy lithofacies. In this setting, phosphatic and non-phosphatic stromatolite buildups formed within the same depositional facies, often in close (meter- and decimeter-scale) spatial associ-

---

<sup>1</sup>Division of Geological and Planetary Sciences, California Institute of Technology, Pasadena, CA 91125, USA

ation with one another. These data suggest that early phosphate mineralization of the Salitre and Sete Lagoas formations was likely not a function of low porewater advection in paleogeographically sheltered regions, but rather highly local processes of phosphate enrichment on a high-energy, wave-swept platform environment.

## 2.2 Introduction and geologic context

### Introduction

The history of life on Earth is known through diverse records: from the fossiliferous strata of sedimentary rock to the genomes of modern organisms. The records preserved in rocks have limited temporal and spatial resolution, depending on how they were formed and the history of diagenesis or alteration they have experienced. Phosphate minerals such as carbonate fluorapatite (CFA or francolite) may preserve cellular structure in the fossil record with exquisite detail and fidelity when they crystallize before or during the decay of the original organisms (e.g., Bengtson et al., 2017; Brasier and Callow, 2007; Chin et al., 2003; Muscente, Hawkins, and Xiao, 2015; Sallstedt et al., 2018; Wacey et al., 2019; Xiao, Zhang, and Andrew H. Knoll, 1998), but the particular conditions for early CFA formation or “phosphogenesis” today and in the past are not well constrained. It is generally inferred that calcium phosphate minerals will precipitate from fluids supersaturated with respect to  $Ca^{2+}$  and  $PO_4^{3-}$ , when kinetic barriers to nucleation and transport of ions to the surfaces of growing crystals, including high  $Mg^{2+}$  concentrations, high  $SO_4^{2-}$  concentrations, high alkalinity, fluctuating pH, and other factors, are overcome (Föllmi, 1996; Harouiya et al., 2007; Kramer, 1964; Martens and Harriss, 1970). But what environments and ecologies actually create these conditions? And what is the diagenetic fate of authigenic phosphate minerals once formed?

Prevailing theories cite the role of redox-stratified microbial communities in perpetuating redox gradients in sediments under oxic bottom waters, allowing phosphate to accumulate in sediment porewaters as it is released from decaying organic matter and desorbed from iron minerals (e.g., Arning et al., 2009; Brock and Schulz-Vogt, 2011; Lepland et al., 2014; H. N. Schulz and H. D. Schulz, 2005). In addition, the loss of porewater phosphate through advective exchange with bottom waters may influence the spatial extent of authigenic phosphate mineralization in environments where wave energy and sedimentation rate vary in space and time (e.g., D M Banerjee, Basu, and Srivastava, 1980; D. M. Banerjee, 1971; Caird et al., 2017).

Ancient phosphorite deposits permit tests of these formation models, particularly

when they occur in close association with non-phosphatic deposits in the same locality and depositional facies. Indeed, phosphorite deposits are geographically widespread during several periods of Earth history. This includes the Ediacaran Period, a time of significant climate upheaval involving the rise of atmospheric oxygen (Canfield, Poulton, and Narbonne, 2007; Fike et al., 2006), the end of widespread marine glaciation (e.g., B. S. Kendall et al., 2004), and the appearance of the first animal life in the geologic record (Narbonne, 2005; Narbonne and Gehling, 2003; Xiao and Laflamme, 2009). The relationship between primary phosphogenesis and the ecological transitions that characterize the Precambrian-Cambrian boundary is the subject of much debate, particularly with respect to the paleoecological constraints and taphonomic potential phosphorite itself may represent (P. J. Cook, 1992; Donnelly et al., 1990; Papineau, 2010; Sheldon, 1981; Peter J. Cook and Shergold, 1984).

The Una and Bambuí groups of Northeastern and Central Brazil preserve some record of the formation and diagenesis of chemical phosphorite during the Cryogenian and Ediacaran periods between 635 and 541 Ma. These strata span the transition at low- latitudes from the Marinoan glaciation to warmer oceans saturated with respect to calcium carbonate and experiencing the re-ignition of the biological pump in the global carbon cycle (Caird et al., 2017; Caxito et al., 2012; Delisle, 2015; Drummond et al., 2015; Iglesias and A. Uhlein, 2009; Aroldo Misi and Veizer, 1998; Paula-Santos et al., 2015; Shiraishi et al., 2019; L. C. Vieira et al., 2015). Phosphorite-bearing members of the Una and Bambuí groups are referred to, respectively, as the Salitre and Sete Lagoas formations and consist of carbonate platform deposits contemporaneous with globally distributed end-Cryogenian “cap” carbonate sequences. Variations exist among cap carbonate deposits globally with respect to water depth, wave energy regime, and terrigenous input, suggesting that the post-glacial coastlines and their biota were not universally experiencing marine transgression (Allen and Etienne, 2008; Creveling, Bergmann, and John P Grotzinger, 2016). This is critical context for models of phosphogenesis in coastal and carbonate ramp environments at the Precambrian-Cambrian boundary, where sea level change and intermittent subaerial exposure may influence redox state and ionic concentrations.

In this work, we present new sedimentological and stratigraphic data and analyses in support of a revised depositional facies model for the Salitre and Sete Lagoas formations. This in turn informs a revised consideration of models for phosphate

mineralization on the São Francisco Craton during the Ediacaran, evidence of which is preserved in distinctive digitate stromatolite buildups in the Salitre Formation (Caird et al., 2017; Delisle, 2015; J. Richard Kyle and Aroldo Misi, 1997; Aroldo Misi, Kaufman, et al., 2007; Shiraishi et al., 2019) and early cements associated with aragonite crystal fan facies in the Sete Lagoas Formation (Drummond et al., 2015; Okubo et al., 2018).

## **Geologic context**

### **Tectonic context**

The São Francisco Craton comprises a large portion of Eastern and Central Brazil (Fig. 1a). It is bounded on its northwestern margin by the Amazonia Craton and on its southwestern margin by the Paranapanema Block and Río de la Plata Craton (Heilbron, Umberto Giuseppe Cordani, and Alkmim, 2017; Reis, Alkmim, et al., 2016). During the Late Neoproterozoic, the São Francisco Craton is thought to have been sutured at its eastern margin to the West Congo Craton, a complex that collided between approximately 600 and 500 Ma with the Paranapanema Block (Alkmim, Marshak, et al., 2006). This collision culminated in the Brasília and West African orogenies, coincident with the closure of the Macaúbas seaway to the southeast, the inversion of the Paleoproterozoic-age rift deposits of the Paramirim and Pirapora corridors, and the downflexure of the craton interior (Alkmim, Marshak, et al., 2006; Reis, Suss, et al., 2017; Guimarães et al., 2011). The intracratonic and foreland sedimentary basins formed during this downflexure are referred to as the São Francisco, Irecê, and Salitre paleobasins (Reis, Alkmim, et al., 2016; Reis, Suss, et al., 2017). These were filled with generations of sediment related to the partial rifting of the craton, followed by deep-water glaciogenic deposits, and ultimately a thick succession of carbonate platform deposits (south, Bambuí Group; north, Una Group) (Alkmim and Marcelo A. Martins-Neto, 2012; M. A. Martins-Neto, Pedrosa-Soares, and Lima, 2001; Pedrosa-Soares et al., 2008). Today, the Una and Bambuí groups ride on a shallowly dipping putative detachment over Archean and Paleoproterozoic crystalline basement and Meso- and earlier Neoproterozoic metasedimentary rock (Reis, Alkmim, et al., 2016). Most faulting and tilting of the Una and Bambuí rocks result from interfering fold-thrust belts initiated during the collision of the São Francisco and Amazonian cratons in the early Cambrian, related to the Rio Preto mountain belt on the Northwestern Margin of the São Francisco Craton. The deformation of the Salitre formation is concentrated inside the Irecê paleobasin, where imbricated thrust blocks of the Salitre formation dip to the north

by 70-90° (this study, Cruz and Alkmim, 2006; M. A. Martins-Neto, Pedrosa-Soares, and Lima, 2001). The Sete Lagoas Formation is deformed closest to the margins of the São Francisco Craton, but is dominantly flat-lying in the interior. Continuous sections of both formations are abundant, though the stratigraphy of the Salitre Formation is complicated by the deformation of strata in repeated fold-thrust blocks. For this study, stratigraphic columns within the Salitre Formation were collected wherever continuous section was available within a given fault block.

### **Stratigraphy**

The Una Group consists of the Bebedouro Formation and the overlying Salitre Formation (Fig.1b). The Bebedouro Formation, less than 200 meters in thickness, is a diamictite consisting of a fine to medium-grained matrix with granule to boulder-scale clasts, both of mixed carbonate and siliciclastic composition, and inferred to be of glaciogenic origin (Guimarães et al., 2011). The Salitre Formation, having a thickness of roughly 300 to 400 meters, is typically divided into four members of roughly equal thicknesses: basal Nova America, Gabriel, Jussara, and topmost Irecê (Aroldo Misi, Kaufman, et al., 2007; A. Misi and J. R. Kyle, 1994; Aroldo Misi and Veizer, 1998). The upper three members (Gabriel, Jussara, and Irecê) are comprised of cross-stratified and wavy laminated carbonate grainstone with laterally discontinuous tabular intraclast conglomerate beds and lenses. The Nova America Member also is composed of cross-stratified grainstone (Fig. 3a-c) and intraclast conglomerate beds (Fig. 3d-e), though it is broadly coarser, with more abundant intraclast conglomerates and oolitic intervals. Laterally discontinuous digitate stromatolite and columnar stromatolite buildups occur within these cross-stratified facies (Fig. 4). Elongation of stromatolites is common (e.g., Fig. 4b). Primary francolite appears specifically as an early cement in digitate stromatolites and occasionally as well-rounded intraclasts in medium to very coarse cross-stratified carbonate grainstone adjacent to the stromatolites. The Salitre Formation has an absolute age constraint of  $616 \pm 31$  Ma, from U-Pb dating of primary francolite cements in the upper Nova America Member (Shiraishi et al., 2019). The Bambuí Group, about 350 meters in thickness, includes the basal Jequitaiá Formation ( 40 meters), the Sete Lagoas Formation ( 30-meter Lower Member, 60-meter Middle Member, and 30-meter Upper Member), the Serra do Santa Helena Formation ( 60 meters), the Lagoa do Jacaré Formation ( 50 meters), the Serra do Saudade ( 60 meters) Formation, and in some locations the Três Marias Formation ( 50 meters) (Alkmim and Marcelo A. Martins-Neto, 2012; Caxito et al., 2012; Drummond et al., 2015; G. J. Uhlein et al.,

2019; Paula-Santos et al., 2015; Iglesias and A. Uhlein, 2009). The uppermost formations, including Serra do Santa Helena, Lagoa do Jacaré, Serra do Saudade, and Três Marias formations, consist mostly of cross-stratified and planar laminated carbonate and an abundance of silty marls. Intercalated cross-stratified siliciclastic sandstones increase in abundance up-section, with coarse siliciclastic sandstone and conglomerate dominating the Três Marias Formation. The Sete Lagoas Formation sits unconformably atop the Jequitaí diamictite and, in places, crystalline basement. It is comprised mostly of cross-stratified carbonate grainstone, (mostly limestone) with abundant laterally discontinuous beds of tabular intraclast conglomerate (as shown in Fig. 3d, or those of the Salitre Formation, pictured in Fig. 3e), as well as significant columnar stromatolite buildups (not pictured) and nodular limestones (Fig. 3g-h). Its age is constrained by the appearance of fragments of possible Ediacaran fossils *Cloudina* and *Corumbella* in the Middle Member Warren et al., 2014, roughly 549-541 Ma. Detrital zircons from the Upper Sete Lagoas have yielded U-Pb and Pb-Pb dates of 550-610 Ma (Caxito et al., 2012; Paula-Santos et al., 2015). The Salitre and Sete Lagoas formations are considered equivalents, representing different parts of the same carbonate platform within an Ediacaran-age epeiric seaway (Aroldo Misi, Kaufman, et al., 2007). The Salitre formation has been previously interpreted as a marine transgressive systems tract, divided into 8 or more separate parasequences distinguished by exposure surfaces containing evaporite mineral pseudomorphs and tepee structures at the top of intertidal zone deposits Caird et al., 2017. In our study of the Irecê and Salitre paleobasins, we found no compelling evaporite pseudomorphs and reinterpret the putative tepee structures as wave-agitated intraclasts, suggesting a high energy platform sequence, discussed below. The Sete Lagoas Formation has also been interpreted as intertidal-zone in the past (Drummond et al., 2015), though we found no clear exposure surfaces in our study area.

## **2.3 Methods**

### **Study area and sample collection**

Our study area includes those parts of the São Francisco Craton located in central Bahia and northern Minas Gerais. We measured and characterized textures within meter- and 10s-of-meters-scale outcrops in over 169 locations, recording detailed stratigraphic columns in 29 of these. In Fig. 1, we show the locations of representative outcrops and sample collection sites, described in Section 3. Brief descriptions of these locations and their latitudes and longitudes are included in Table 1.

## **Analytical methods**

In addition to field data, we also used thin sections and cut, unpolished billets of samples collected from the field areas shown in Fig. 1. These were examined under petrographic microscopes for characterization of mineralogy and micrometer-scale fabrics. We also used the Caltech Geological and Planetary Sciences Division Analytical Facility's scanning electron microscope (ZEISS 1550VP Field Emission SEM/EDS, using 15 kV accelerating voltage, 13 mm working distance) and micro-XRF spectrometer (Bruker M4 TORNADO, using 50 KeV X-ray tube voltage) to produce spatially resolved maps of samples' elemental composition.

## **2.4 Depositional environments: Salitre and Sete Lagoas formations**

### **Depositional setting overview**

Previous studies constrain the Sete Lagoas and Salitre formations to represent sedimentation on a shallow carbonate platform on the interior of the São Francisco Craton (Caird et al., 2017; Drummond et al., 2015; Guimarães et al., 2011; Iglesias and A. Uhlein, 2009; Kuchenbecker, Luis, and Galvão, 2011; A. Misi and J. R. Kyle, 1994; Aroldo Misi and Veizer, 1998; Sanchez, 2014; G. J. Uhlein et al., 2019; Lucieth Cruz Vieira et al., 2007). The current study supports this interpretation, but with the added feature that depositional facies indicative of different water depths and flow velocities are distributed in a laterally discontinuous or mosaic pattern at similar stratigraphic levels across the craton. The scale of lateral discontinuity is on the order of 10s to several 100s of meters, significantly smaller than the scale of the study area. Vertically, these mosaic facies interfinger at 1-10-meter scales. From this, we infer that the lateral distribution of facies varies noncyclically with stratigraphic height and time. We thus propose an interpretation of the Sete Lagoas and Salitre formations as the remnants of a high-energy, wave-dominated carbonate platform with uniformly high current energies and a paucity of peritidal low energy facies. Authigenic or early diagenetic phosphate mineralization must have occurred within this framework.

In the model developed below, microbially influenced accretionary structures initiate growth at places of diminished sedimentation, often on and around intraclast conglomerate beds, among migrating shoals of peloidal and oolitic sediment. These interfingering microbial buildups and laminites and ripple cross-stratified grainstones and rudstones constitute a high-energy depositional facies association that dominates the platform. Planar laminated, very fine carbonate sediment and pseudomorphs after centimeter- and decimeter-scale aragonite crystal fans represent the

deepest, most quiescent depositional facies association. See Fig. 2.

### **Lithofacies**

We identify 9 distinct lithofacies within the Salitre and Sete Lagoas formations, most though not all of which appear in both formations, i.e. in both the northeastern and southern parts of the São Francisco Craton. These are (1) laminated, cross-stratified carbonate grainstone and rudstone (Figs. 3a-d), (2) tabular intraclast conglomerate (e.g., Sepkoski, 1982), (Figs. 3d-e), (3) planar-laminated, very fine-grained limestone- dolostone (Fig. 3f), (4) nodular limestone (Figs. 3g-h), (5) crinkly laminite (Fig. 3h), (6) digitate stromatolite buildups (Fig. 4), (7) columnar stromatolite buildups (Figs. 5-6), (8) symmetric wave-rippled limestone (Fig. 7), and (9) crystal fans (Fig. 8). Phosphatic digitate stromatolites appear only in the Salitre formation. Nodular limestone in the Salitre Formation is rare, identified only tentatively in Locality 14 (Fig. 1d, Table 1). Crystal fans appear only in the Sete Lagoas Formation, and then only in Localities 17 and 22 (Fig. 1c and f, Table 1), though they have also been identified both in place and in reworked storm deposits by Okubo et al. (2018) in the Riacho do Cruz area near Januária town. All lithofacies are summarized in Table 1, while more extensive descriptions are included in this section (3.2). Carbonate rocks are described according to the revised Dunham Classification schema (Dunham, 1962; Embry and Klovan, 1971; Lucia, 1995).

#### **Laminated, cross-stratified carbonate grainstone and rudstone**

Description: Cross-stratified carbonate grainstones form massive, meter-scale, and decimeter-scale beds, in continuous vertical sections that persist for hundreds of meters. Laterally, these beds may extend for tens to several hundred meters, as visible in outcrop. Beds are dominated by symmetric and asymmetric ripple-scale cross lamination (several-centimeter-scale to decimeter-scale wavelengths, sometimes seen aggrading over 5-10-centimeter-thick intervals), decimeter-thick trough cross-sets, decimeter-thick tabular beds of low-angle cross-sets, and hummocky cross-stratification (Figs. 3a-c). Primary grain sizes often are obscured by recrystallization, but range from very-fine to millimeter- and centimeter-scale well-rounded to sub-rounded intraclasts, ooids, and pisoids, and thin-chip intraclasts. In some areas, lenses of fine-grained carbonate sediment are visible within otherwise coarse intervals (Fig. 3b). Patches of dolomitization may overprint this facies, varying within beds and even within individual grains. In thin section, ooids and aggregate

grains (e.g., grapestones) may be micritized and variably silicified. Interpretation: This facies represents high-energy sediment transport, facilitated by both unidirectional currents and oscillatory flows in a high-energy platform environment. Such an environment is well-known in the modern Caribbean Sea, under the influence of persistent trade winds (e.g., Dravis and Wanless, 2008; Read, 1985), and on other ancient Precambrian carbonate platforms (e.g., J. P. Grotzinger, 1989b). The largest cross-sets (decimeter to meter-scale tabular beds) suggest large shoals migrating with persistent currents, consistent with the appearance of trough cross-stratification in the same intervals (Raaf, Boersma, and Gelder, 1977). Ooids and well-rounded peloids cemented by calcite suggest a wave-influenced environment (reviewed by Bathurst, 1975; Diaz and Eberli, 2019). The spatial scale of dolomitization varies considerably (meters to tens of meters, generally), with fronts cross-cutting beds and cross-sets, indicating a later, multi-step process not directly related to depositional environment.

### **Tabular intraclast conglomerate**

Description: These are clast-supported flat pebble conglomerates with a matrix of very-fine to fine carbonate sediment. Clasts range in size from 1 centimeter to several decimeters in their longest dimension (Figs. 3d-e). Clasts are typically thin (1 centimeter or less), flat, internally laminated chips or tablets of limestone or dolostone with rounded edges. Clasts may be imbricated, and in some cases may be oriented subvertically, buttressed by adjacent clasts at high angles. Intraclast beds are lenticular with flat to low-angle bases and mounded tops draped with very fine-grained, finely laminated carbonate laminite or cross-stratified grainstone. These beds may extend up to several meters laterally, with thickness varying between several centimeters and 1.5 meters. In some locations, intraclast conglomerate beds provide a nucleation and growth surface for stromatolite buildups. Interpretation: Tabular intraclast conglomerates suggest early cementation, enough to maintain sufficient cohesiveness during transport and redeposition (Mount and Kidder, 1993). The characteristic thickness of tabular clasts (1-3 centimeters) may be due to a number of physical and chemical factors: the depth and thickness of microbial mats that might have helped cohere sediments and facilitate the precipitation of calcite cements, centimeter-scale gradients in primary porosity that might have precluded reworking below some characteristic depth, etc. Given their size, high-energy flows were involved in their transport and redeposition. The episodic and laterally discontinuous nature of the observed intraclast conglomerate beds suggests

that either these high-energy flows were the result of storm events whose effects extended even below fair-weather wave-base, or that the formation of shallow crusts or hardgrounds varied locally, or perhaps a combination of these processes. Many observed intraclast conglomerate beds preserve evidence of oscillation of the flow, i.e., sub-vertical clast orientations and multidirectional imbrication as in Fig. 3d (Mount and Kidder, 1993).

### **Planar-laminated, very fine-grained limestone or dolostone**

**Description:** This lithofacies consists of very-fine-grained, planar-laminated calcarenites and dolarenites exhibiting irregular-to-wavy bedding (Fig. 3f). Laminae in this facies do not truncate one another, and waviness may be associated with soft-sediment-deformation structures and/or accentuated by later-stage pressure solution and the formation of millimeter-scale stylolites. Occasionally, this facies contains domal stromatolites with up to a centimeter of synoptic relief, and 5-20 centimeter diameter. These may aggregate in clusters, forming small mounds up to a meter in diameter and less than 50 centimeters in height. Occasionally, non-laminated centimeter-scale domal to thumb-shaped structures are observed in this facies, creating distinct “irregularities” in the lamination (Fig. 3f, center). **Interpretation:** Planer-laminated calcarenites and doloarenites imply carbonate sedimentation in a relatively quiescent and deep-water environment on the Ediacaran-age platform (e.g. Grotzinger, 1989; Read, 1985). In such a setting, sediments precipitate from the water column and are not transported by shear flows at the seafloor. Waviness of laminae may be attributed to differential compaction soon after deposition and before cementation, or to later pressure solution; there is no evidence for bedload sediment transport. The domal stromatolites and non-laminated domal and digitate structures were likely formed by the growth of microbial mats at the seafloor. Mats and biofilms growing at the seafloor trap and bind sediment and likely affect early cement precipitation, producing not just laminated stromatolites but un-laminated bumps and wrinkles that may be enhanced by differential pressure solution (J. P. Grotzinger and Al-Rawahi, 2014).

### **Nodular limestone**

**Description:** Irregular nodules, several millimeters up to 2 centimeters in diameter, are sometimes present in otherwise fine-grained calcarenite, interbedded with planar and wavy-to-crinkly laminated limestone (Figs. 3g-h). These nodules and their ma-

trix are comprised of equant grains of calcite cemented by microcrystalline calcite. Nodules often contain silica spherules near their cores; these are recrystallized from a formerly radial symmetry to a coarse, interlocking mosaic and appear to be a later replacement texture. These silica spherules engulf primary grains of calcite and almost always grow in close association with grains of pyrite, pyrrhotite, and iron oxide (possible pseudomorphs after pyrite and pyrrhotite). This nodular limestone is commonly found draped by finely laminated, very-fine-grained limestone stained red-orange by late iron-oxide growth along thin pressure- dissolution horizons (i.e., sinuous horsetale stylolites). Interpretation: Limestones nodules likely grew below the seafloor, as concretions precipitating from carbonate-supersaturated porewaters (reviewed by Flügel, 2010). The nuclei of these concretions may have been micrite grains (peloids) and/or organic material. The shape of individual nodules is likely influenced both by the geometry of the original nuclei, the geometry of permeability and porosity of primary sediments, compaction, and later-stage pressure solution. Nodular limestone alone may not imply a particular water depth, but the close association of this facies with planar-laminated calcarenite and wavy-to-crinkly laminite suggests formation in a relatively quiescent part of the carbonate platform (e.g., Möller and Kvingan, 1988).

### **Wavy-to-crinkly laminite**

Description: Laminae in this very-fine-grained limestone facies pinch and swell on a millimeter scale, occasionally merging (Fig. 3h). The individual laminae are several millimeters to several centimeters in thickness and are sometimes associated with nodular limestone. Interpretation: The crinkly, irregular lamination observed in the Salitre and Sete Lagoas formations is comparable to that in other ancient carbonates where variable thickness has been attributed to differential sediment accumulation due to the effects of trapping and binding by microbial mats on the seafloor (e.g. J. P. Grotzinger and Al-Rawahi, 2014; J. P. Grotzinger and A. H. Knoll, 1999). However, it seems likely that differential pressure dissolution during later burial and diagenesis could have caused or accentuated irregular thicknesses; boundaries between laminae often are associated with stylolite textures, late-stage pressure solution features observable in thin section.

### **Digitate stromatolite buildups**

Description: Digitate stromatolites in the Salitre Formation grow in intimate association with cross-stratified grainstones, and locally with tabular intraclast conglomerate (Fig. 4). Stromatolites appear to nucleate at a point, and grow to 1-2 centimeter diameter over 1-3 vertical centimeters. After the first few centimeters of growth, they may either widen and branch or terminate under finely laminated sediments. An individual digit's synoptic relief may be several millimeters to one centimeter. Typically, these digitate stromatolites are composed of microcrystalline to cryptocrystalline CFA, while inter-columnar fill is often finely laminated, very fine grained carbonate sediment composed of well-rounded to sub-rounded primary grains of calcite and dolomite (Figs. 4, 9, and 12), and some well-rounded grains of reworked finely microcrystalline carbonate fluorapatite (Fig. 15). In many outcrops, however, this fill is weathered to red-brown, friable dust, leaving behind a honey-comb of centimeter-wide interconnected pores that may appear as linear striations between elongate stromatolites in plan view (e.g., Fig. 4a-b). The thinnest accumulations of digitate stromatolites are only 1-5 centimeters thick, containing a single layer of stromatolites with mm-scale synoptic relief, draped and terminated by overlying grainstone facies (Fig. 4d). The thickest accumulations contain digitate stromatolites which broaden and branch in y-shaped or tuning-fork patterns after several centimeters, often merging again upsection (Fig. 4c). This pattern may repeat over and over again in an undulating, anastomosing pattern forming tabular buildups of 0.5-3 meters thickness and up to a half-meter of synoptic relief. These buildups tend to have bases that are flat along bedding planes, and extend laterally over 2-10 meters. These may reasonably be called bioherms or biostromes, depending on the ratio of their length to width and the nature of their lateral boundaries: tapering/downlapping as in Figs. 4c and 9, or more perpendicular to bedding as in Fig. 4e. Here, we favor the term "buildup," which captures both tabular (biostrome) and more mounded or bell-shaped (bioherm) structures (J. P. Grotzinger, 1989c; J. P. Grotzinger, 1989b; Pelechaty and J. P. Grotzinger, 1989; R. Riding, 2002; Semikhatov and Raaben, 2000). Where bedding planes are visible, elongation of digitate stromatolites is apparent, with single stromatolites forming extreme elliptical structures extending over tens of centimeters, sometimes bifurcating in sub-parallel lobes (Fig. 4a-b). In several locations, digitate stromatolites are seen to merge after 5-10 vertical centimeters into decimeter-scale mounds or domes with mottled surfaces and interiors that are still finely laminated but more disordered and with little definition of individual stromatolites within (Fig. 4e).

These disordered mounds often have a gradational transition from nucleus to outer laminae between phosphate minerals and later diagenetic carbonate minerals. The mounds often engulf nucleate on and grow around carbonate intraclasts. Interpretation: Digitate stromatolite buildups in the Salitre Formation are the likely result from a combination of trapping-and-binding and microbially-influenced carbonate and CFA precipitation at the seafloor (Tanja Bosak, Andrew H Knoll, and Alexander P Petroff, 2013; Castanier, Levrel-Métayer, and Perthuisot, 2000; J. P. Grotzinger and A. H. Knoll, 1999; R. E. Riding and Awramik, 2000; Seong-Joo, Browne, and Golubic, 2000)). Microbial mats existing in shallow, wave-agitated settings where carbonate sediments are being generated and transported must grow quickly in order to maintain access to the sunlight necessary for photoautotrophy. Sustained unidirectional or oscillatory flows causes elongation of the growing stromatolites parallel to the flow. Where sedimentation outpaces growth, mats and mat-accreted sediments would have been draped and smothered, i.e., ceased to grow and accrete due to lack of access to sunlight. Smaller stromatolites with elongation and bifurcation of columns are consistent with mat growth in high-energy settings with high sediment influx (reviewed in Tanja Bosak, Andrew H Knoll, and Alexander P Petroff, 2013). In the Salitre formation, digitate stromatolites exhibit all these features, and occur among trough-cross-stratified oolitic and peloidal grainstones and rudstones indicative of energetic shear flow: patch reefs competing for sunlight and solid growth substrate among shifting ooid shoals on a shallow, carbonate platform. These energetic flows may occasionally have broken and transported fragments of cemented stromatolites, as well, generating some phosphatic intraclasts (Fig. 15a-b)

### **Columnar stromatolite bioherms**

Description: Columnar stromatolites in the Salitre and Sete Lagoas Formations are characterized by decimeter-scale diameters and centimeter-scale synoptic relief, forming laminated columns that may continue without branching for tens of centimeters to 2 meters vertically (Fig. 5). Individual columns have an approximately circular bedding-plane cross section, but these often evolve into more polygonal forms with stratigraphic height. Between closely-packed stromatolites, there are thin columns of laminated, very-fine- to fine-grained carbonate sediment. More widely-spaced stromatolites and large, several-meter-scale accumulations of stromatolites (in general, domal bioherms) often are separated by channels filled with tabular intraclast conglomerate (Fig. 6). At Fazenda Arrecife (FA), several-meter-diameter bioherms often are enclosed in 3-to-10-centimeter-thick carapaces of finely

laminated, very fine carbonate sediments. These bioherms are not perfectly hemispherical in shape; at nucleation, they are only 20-30 centimeters across, widening upwards before terminating in a dome to form a bulb shape in cross section (Fig. 6). While many columns grow near-vertically and continuously for up to a meter, many appear to pinch and swell vertically and laterally, though there is no obvious branching or merging. Interpretation: Like digitate stromatolite buildups, columnar stromatolite bioherms are formed by microbial mats, trapping and binding sediment at the seafloor, which are then cemented to provide a substrate for later growth. The height of the individual stromatolites that form meter-scale bioherms is likely related to the depth-dependent availability of sunlight, as well as interactions between high-energy flows and the topography of the local seafloor and biogenic buildups (e.g., Allwood et al., 2009; Beukes and Lowe, 1989). Columnar stromatolite bioherms in the Salitre and Sete Lagoas formations occur in close association with cross-stratified grainstone and rudstone facies, as well as tabular intraclast conglomerates. These provide surfaces for the nucleation and growth of the bioherms, and later onlap, fill the interstices between, and ultimately overlay and truncate them. This suggests that the microbial communities responsible for the growth of columnar stromatolites existed in the same depositional environment as the communities responsible for the aforementioned digitate stromatolite buildups: high-energy wave-influenced, with shifting shoals of coarse carbonate sediment. This raises the question of why there are such significant differences in the shape and size of columnar stromatolite bioherms compared to digitate stromatolite buildups, despite experiencing similar flow velocities and sediment supplies. This could perhaps be explained by differences in timing and consistency of sediment influx or cementation (e.g., T. Bosak, Souza-Egipsy, and Newman, 2004; J. P. Grotzinger and A. H. Knoll, 1999; Noffke, Andrew H. Knoll, and John P. Grotzinger, 2002; Planavsky and Grey, 2008), in the structure of microbial mats or in other aspects of microbial ecology (e.g., Alexander P. Petroff et al., 2010), and fluid chemistry (e.g., Hickman-Lewis et al., 2019). Polygonal packing of stromatolites, as at the Fazenda Arrecife locality, was presumably the result of limited accommodation space for lateral growth in densely-growing mounds. The elongation of stromatolites at the edges of bioherms is indicative of the gradation in flow energy from the protected center of a bioherm to its channel-adjacent margins (e.g., Cecile and Campbell, 1978; J. P. Grotzinger, 1989c; P. Hoffman, 1969; Logan, 1961).

### **Symmetric wave-rippled limestone**

Description: This lithofacies consists predominately of limestone beds, several decimeters thick, in which roughly symmetric peaks are preserved at regular 5-15-centimeter lateral intervals. These peaks have a cusped, trochoidal shape, with each cusp typically having several centimeters to a decimeter of relief above the concave-upward troughs between adjacent peaks (Fig. 7a). Peaks are formed from continuous laminae, which may pinch, bulge, and fold over themselves (Figs. 7b-c), as well as laminae which pinch out on either side of a peak's crestal zone. There also occur, occasionally, some laterally discontinuous laminae that resemble fragments of once-continuous laminae. In the crestal zone of each peak, there is an abundance of overlapping laminae, forming chevron-like shingles. Because of this overlapping, the crestal zone is not consistently perpendicular to the bedding plane, but undulates and shifts, sometimes describing a sigmoidal pattern (Fig. 7c). Depositional lows between peaks are filled by lenses of sediment that onlap adjacent peaks and compensate for the peaks' depositional relief at the seafloor. Interpretation: These peaked structures are consistent with symmetrical ripples formed by wave oscillation (Allen and P. F. Hoffman, 2005b; Allen and P. F. Hoffman, 2005a; Raaf, Boersma, and Gelder, 1977; Lamb et al., 2012; Reineck and Singh, 1980), with laminae discontinuity locally enhanced by pressure solution. Critical to this interpretation is the observation of systematic interfingering or overlap of laminae in the axial zone of cusped peaks, which may have been generated by reversing flows (Allen and P. F. Hoffman, 2005b; Raaf, Boersma, and Gelder, 1977; Lamb et al., 2012; Reineck and Singh, 1980). The flexibility and cohesiveness of the folded and fragmented laminae under reversing flows may be explained by the influence of microbial mats and biofilms, or early partial cementation. Previous workers have interpreted these peaked structures as tepees, indicative of exposure surfaces in a tidal flat environment (e.g., Caird et al., 2017). Classical tee-pee structures are the result of crystal growth due to the evaporation of fluids from finely laminated sediments in a tidal flat, sabkha, or other intermittently subaerial environment. This crystal growth pushes apart partially cemented laminae, which themselves expand and separate. This expansion is accommodated by the breakage and upthrusting of some of these laminae, fragments of which rotate to form polygonal ridges which may look like peaks in cross-section. In contrast to structures observed in the Salitre and Sete Lagoas formations, the cores or crestal zones of true tepee structures are typically full of brecciated clasts and early pore-filling marine cements, and laminae cannot be routinely traced across the crest (Assereto and C. G. S. Kendall, 1977).

The structures seen within the Nova America Member of the Salitre Formation and within the Lower and Middle Sete Lagoas Formation lack most of these defining tepee characteristics. The structures do have approximately symmetric peaks, but rather than thin sheets that have been upthrust and brecciated, the peaks are formed from continuous laminae and sinuous, overlapping and tapering laminae that aggrade in a chevron pattern (Fig. 7c). These overlapping and tapering laminae, enhanced by pressure solution, are likely the result of variations in flow velocity and sediment supply, which result in the imperfect symmetry of laminae on opposite sides of the ripple crest. Brecciated material occupying hollows beneath or between separated plates, pore-filling cements, and cavity-filling peloidal sediment are all absent. Rather, laminae overlap and interfinger in the axial zone of each peak with no apparent primary void space preserved between them. Additionally, nowhere in our field area nor within the four examined drill cores did we observe dessication cracks, evaporite deposits, or pseudomorphs after evaporite minerals — common indicators of an intermittently subaerial tidal flat environment where tepees might form.

We thus interpret the observed structures to be the result of persistent wave energy (Fig. 7d); with oscillating flows producing continuous laminae and chevron-style overlapping laminae. Microbial films or mats may, by the trapping and binding of sediments and influence on carbonate mineral saturation states in pore waters (e.g., Noffke, Andrew H. Knoll, and John P. Grotzinger, 2002; Pflüger and Gresse, 1996; Simonson and Carney, 1999), have contributed to the cohesion and stability of laminae. This might explain the limited lateral migration of ripple crests, and the existence of thin laminae fragments capable of folding. No subaerial exposure on a tidal flat is involved in this formation mechanism, nor the development of evaporative facies, which could explain the lack of void-filling cements nucleating upon brecciated clasts that are so characteristic of tepees.

### **Crystal fans**

Description: Crystal fans in the Sete Lagoas Formation are 1-20 centimeters in height, 1 centimeter or less diameter at their nucleation point, and have diameters of 1-10 centimeters at their broadest. The fans nucleate on planar- laminated, very-fine-grained grainstone (limestone). Where nucleation was limited, individual fans are overlapped and draped by finely laminated carbonate grainstone (Fig. 8a). In some locations, however, laterally continuous beds of interlocking fans are more

common (Fig. 8b). Individual crystals within the fans show blunt-edged terminations and radiate from their fan's nucleation point, and composed of anhedral interlocking mosaic of calcite pseudospar, suggesting aragonite as their primary mineralogy (Sandberg, 1985). Many crystals within the interlocking mosaic exhibit twinning and later intergrowth of later Fe-oxide minerals. The most extensive crystal fan deposits (e.g. RdC locality) appear to contain successions of repeating fan beds and sediment drapes exhibiting ripple-cross-stratification and low-angle cross stratification, in decimeter-scale intervals that continue for 10-30 meters of vertical section. In outcrops with more isolated fans, individual fans or clusters of 3-5 fans may be draped by planar-laminated sediments that have been partially scoured and succeeded by hummocky and low-angle cross-stratified grainstone over 10s of centimeters of vertical section. Interpretation: Crystal fan nucleation and growth require supersaturation with respect to aragonite, and the presence of inhibitors to calcite micrite formation; making crystal fans indicators of aqueous chemistry at the seafloor (Sumner, 2002). Crystal fans, particularly in association with laminated carbonate muds, may also be considered indicators of quiescence since shear flow must be relatively weak to allow the fans to grow to any considerable synoptic relief above the seafloor without being abraded and reworked. The fact that the most isolated crystal fans in the Sete Lagoas Formation occur in association with higher-energy sedimentary structures (i.e., ripple-cross stratification), while the most laterally and vertically extensive crystal fans are associated with planar and draping laminae, is consistent with this idea.

### **Spatial distribution of lithofacies**

The São Francisco, Irecê and Salitre paleobasins are considered remnants of the same regional foreland basin that fringed the São Francisco Craton during the Ediacaran Period. The Salitre and Sete Lagoas Formations represent the basal members of a carbonate platform that accumulated within the basin during this period. In various locations, these unconformably overlie either Cryogenian-age glaciogenic diamictite and sandstone, or Paleoproterozoic and Archean-age crystalline basement. The Salitre Formation contains all of the lithofacies described above except crystal fan beds. The Sete Lagoas Formation contains all of the lithofacies described above except digitate stromatolite buildups. Both formations exhibit a general vertical stratigraphic trend from smaller primary grain size and decimeter-to-meter-scale bedding toward thicker bedding with coarser primary grains. These units are generally lithostratigraphic and chronostratigraphic correlatives (Aroldo Misi, Kaufman,

et al., 2007; Paula-Santos et al., 2015; Shiraishi et al., 2019). However, stacking patterns and transitions between lithofacies show considerable lateral variability locally and across the craton, precluding more precise stratigraphic correlation. Rather, the Salitre and Sete Lagoas formation appear to at best record high-frequency accommodation variations, perhaps representing a marine high-stand systems tract where terrigenous input was limited and carbonate platform growth balanced long-term accommodation. Both formations are characterized by interfingering or patchwork-like spatial distributions of cross-stratified grainstone facies with tabular intraclast conglomerate, wavy-to-crinkly laminite, and stromatolitic facies. This interfingering occurs over meter to tens-of-meters-scales distributed across the entire study area. This, as well as the structural complexity of the Irecê Paleobasin and marginal São Francisco Paleobasin areas, make it difficult to identify facies stacking patterns across the hundreds-of-kilometers-scale of the study area. Rather, the Salitre and Sete Lagoas Formations preserve a snapshot in the existence of an Ediacaran-age carbonate platform environment, where various lithofacies associated with shallow, high-energy, wave- and tidally-influenced facies coexist closely. Fig. 10 shows representative stratigraphic intervals of the Salitre and Sete Lagoas formations in Bahia and Minas Gerais states, plotted by their location on the modern São Francisco Craton. These represent the northern, central, and most southern areas of the craton's remnant Ediacaran intracratonic paleobasin. Tens- to several-hundreds-of-meters of strata are dominated by cross-stratified grainstone facies. Tabular intraclast conglomerates, crinkly laminite, and stromatolitic facies occur as laterally discontinuous meter- to several-meter-scale patches within these sections. Planar-laminated limestone, wavy-to-crinkly-laminated limestone, and nodular limestone facies also occur in both the Salitre and Sete Lagoas formations in meter-to-tens-of-meter-scale stratigraphic packages; but these interfinger with higher-energy facies at the scale of outcrop as well, in some localities. Crystal fans are observed rarely and form in mudstones that are interstratified with both planar-laminated and weakly cross-stratified grainstone facies. Thus, there are two major facies associations: (1) the higher-energy facies association, formed on the shallowest parts of the platform above fair-weather wave base, including cross-stratified grainstone, tabular intraclast conglomerates, microbial patch reefs, and wave-rippled laminated limestone, and (2) the lower-energy facies association, formed along to deeper parts of the platform at or below fair-weather wave base, including planar-laminated limestone, wavy-to-crinkly-laminated limestone, nodular limestone, and crystal fan beds. The high-energy and low-energy facies associations interfinger over meter- and tens-of-

meter scales laterally, particularly in the central and lower regions of the modern craton. The low-energy facies association is somewhat more prevalent in the central to southern regions of the modern craton. However, the high-energy facies association occurs everywhere in the study area. Relevant to the study of phosphatic microbialites of the Salitre Formation, we observe no significant difference between depositional facies associations of host phosphatic digitate stromatolite reefs and non-phosphatic digitate and columnar stromatolite reefs. Indeed, phosphatic and non-phosphatic stromatolites are sometimes observed to coexist within several meters of one another, as in the *Aristeia* locality (see Fig. 4e and Fig. 9). This suggests that the mechanism of authigenic or early diagenetic phosphate mineralization cannot be attributed solely to wave-energy regime and water depth as determined by location on the platform. In summary, a general lateral transition is observed from lower-energy to higher-energy facies associations over hundreds of kilometers, moving from the southern-most exposures of the Sete Lagoas Formation to the northernmost exposures of the Salitre Formation in the study area. Vertical transitions from lower-energy to higher-energy facies associations within some measured stratigraphic sections are difficult to interpret as indicators of relative sea level change given the closely interfingering nature of facies vertically and laterally. The higher-energy facies association (cross-stratified grainstone, intra-clast conglomerate, wave-rippled limestone, and microbial patch reefs containing elongate stromatolites), is observed to dominate the Salitre and Sete Lagoas formations everywhere in the study area. Taken together, these interpretations of the data illustrate a wave-swept and persistently submerged platform whose migrating, often oolitic, shoals moved over and between microbially-assembled reef structures. This platform had some regional variation in platform ramp geometry that enabled deeper waters to persist for some time in the lower-central part of the craton (i.e., southernmost Irecê and northernmost São Francisco paleobasins, near Grutinha and Calcario Rio Preto localities).

## 2.5 Paragenesis

The diagenetic histories of the Salitre and Sete Lagoas formations vary substantially with location on the São Francisco Craton, structural context, and style of exposure. However, not every part of this history is directly relevant to the mechanisms and timing of early phosphate mineralization that are the motivation for this work. Phosphorite was observed in only a few localities and restricted to specific lithofacies within the study area; namely, digitate stromatolite buildups and bioherms of

the Salitre Formation (Nova America Member) in the northern arm of the craton. Therefore, it is the diagenetic history of the phosphatic digitate stromatolite lithofacies, and the non-phosphatic columnar stromatolite and cross-stratified carbonate grainstone-rudstone facies syndepositional with them, that are most critical to this work (Fig. 2, Section 3). In Section 4, we describe and interpret the mineral phases and fabrics observed in this subset of lithofacies in the Nova America Member, examining their relevance to the mineralization and preservation of phosphorite therein. The phases discussed and the processes they represent include:

1. Peloids, ooids, and grapestones in various states of micritization, recrystallization and replacement, representing the basal members of the same Ediacaran-age carbonate platform, the following paragenetic sequence is observed (summarized in Fig. 11): carbonate sedimentation on the craton.
2. Amorphous organic matter and microbially-influenced macro-structures (i.e., stromatolites), representing the presence of microbial mats and their influence on sedimentation.
3. Carbonate micrite, xenotopic sparry cements, and micro-to-cryptocrystalline CFA cements in various states of recrystallization and replacement, representative of earliest cementation of sediments.
4. Iron(II, III)-sulfide minerals, including pyrite and pyrrhotite, and pseudomorphs thereafter of more oxidized iron minerals, representing the trapping of reduced iron and sulfur species at or below the chemocline in sediment porewaters during cementation.
5. Sutured grain boundaries and stylolites, indicative of early compaction and pressure solution.
6. Subhedral to anhedral dolomite spar (Dolomite I), cloudy with abundant inclusions, apparently replacing earlier cements.
7. Mosaic silica, apparently replacing earlier cements.
8. Fabric-selective euhedral-to-subhedral dolomite spar (Dolomite II), forming near boundaries of altered primary grains.
9. Stylolites associated with iron minerals in various states of oxidation, including Fe-sulfides and Fe-(oxy)hydroxides, indicative of late pressure solution.

10. Fluorite crystals, apparently replacing earlier cements and fabrics, indicative of later fluid diagenesis, possibly hydrothermal
11. Tectonic fractures, willed filled with silica or equigranular, hypidiotopic calcite cements, sometimes iron-sulfidespar or microcrystalline silica, often associated with Fe-sulfides and oxidized iron mineralspossible saddle dolomite.

The following sections provide brief descriptions and interpretations of the listed phases. Those phases most relevant to the process of authigenic phosphate mineralization and early diagenesis of phosphate minerals (1 – 4) are the focus of this work, and their discussion is further developed in Section 5. Later diagenetic features which do not elucidate the conditions of primary-to-early-diagenetic phosphogenesis are characterized insofar as they affect more primary fabrics, but a detailed assessment of the chemistry and thermal history of their parent diagenetic fluids is beyond the scope of this paper. The latest stages in the paragenesis of the Salitre Formation, including hydrothermal processes, are discussed in greater depth in previous studies (e.g., Caird et al., 2017; Delisle, 2015; J. Richard Kyle and Aroldo Misi, 1997).

#### ***CaCO<sub>3</sub>, Peloids, ooids, and grapestones***

*Description:* Rounded  $CaCO_3$  grains of variable sphericity are abundant, visible in hand samples and thin sections (Fig. 12 and Supplementary Fig. 2) with diameters ranging from tens to hundreds of micrometers, typically surrounded by  $CaCO_3$  cement fabrics. Many of these grains are partially or completely micritic, though some retain internal laminae distinguishable by subtle variation in crystal size, micrite envelopes, or crystal growth habit (e.g., acicular or bladed crystals juxtaposed with micrite or anhedral interlocking mosaic fabrics). Larger grains are more common within cross-stratified grainstone/rudstone facies, including grainy inter-stromatolite fill, while smaller grains dominate within stromatolite laminae. Grain boundaries appear to be primary, being cross-cut by other phases and stylolites.

*Interpretation:* These grains represent carbonate sedimentation on the Ediacaran-age São Francisco Craton, driven by precipitation from a water column supersaturated with respect to, variably, calcite and aragonite, and characterized by high-energy waves and currents (J. P. Grotzinger, 1989a; Flügel, 2010; Diaz and Eberli, 2019; Bathurst, 1975).

### **Amorphous organic matter**

*Description:* Within stromatolite laminae and irregular laminae spatially associated with stromatolites, amorphous organic matter of uncertain thermal maturity is common, appearing in thin section as diffuse, brown-colored streaks and clots which may be translucent-to-opaque (Fig.12c-d).

*Interpretation:* This diffuse organic matter is likely the remnant of microbial mat communities at and just below the sediment-water interface. Its interlamination with  $\text{CaCO}_3$  peloids and other allochems and concentration in stromatolitic facies supports this interpretation. Microbial mats and biofilms, likely formed by redox-stratified communities of photoautotrophic and heterotrophic bacteria, participated in the accumulation of sediments at the seafloor through physical trapping-and-binding of infalling sediment within the mats, leading to the formation of stromatolites, and in the topographic lows of stromatolite buildups and bioherms (Beukes and Lowe, 1989; J. P. Grotzinger and A. H. Knoll, 1999; Allwood et al., 2009). It is also possible that microbial metabolism might have promoted aragonite or calcite precipitation near or within microbial mats, due to the combined influence locally of oxygenic photosynthesis (Castanier, Levrel-Métayer, and Perthuisot, 2000; Knorre and Krumbein, 2000; Merz-Preiß, 2000; R. E. Riding and Awramik, 2000) and microbial sulfur metabolism (Visscher et al., 1998; Bottrell and Raiswell, 2000) on carbonate mineral saturation states, though textural evidence of directly microbially induced precipitation is not clearly preserved in rocks of the study area.

### **$\text{CaCO}_3$ micrite, sparry $\text{CaCO}_3$ cements, and micro-to-cryptocrystalline CFA cements**

*Description:*  $\text{CaCO}_3$  micrite, in addition to forming peloids, is also observed at the cores and edges of ooids and grapestones, as well as picking out their internal laminations (Fig. 12a-b). In these cases, micrite retains or enhances primary fabrics. Often, however, micrite is also observed to cross-cut the internal laminations of ooids and grapestones and cause the boundaries between grain and matrix to be poorly defined (Fig. 15c, Supplementary Fig. 2). In some instances, the original grain boundaries may be completely lost and the grain's general location is a blotch of micrite among otherwise sparry intergranular cements.  $\text{CaCO}_3$  spar, with individual crystals varying in size from the microcrystalline to 100 micrometers, is the dominant cement-forming phase. Typically,  $\text{CaCO}_3$  cements are xenotopic, with curving and interlocking faces between anhedral to subhedral crystals. They may be equigranular or inequigranular. Much of the stromatolitic

facies is composed of these mosaic  $CaCO_3$  cements interlaminated with peloidal layers; but the digitate stromatolite facies are often cemented by micro-to-cryptocrystalline CFA (Fig. 12c-d). These CFA cements are transparent in thin sections viewed in plane-polarized light, and nearly opaque under crossed nicols. Like the mosaic  $CaCO_3$  cements, CFA cements form bands between grainy, peloidal laminae in the stromatolites and stromatolite-associated laminites. The spatial extent of CFA cements is limited to the stromatolites themselves and the grainstone within several hundred micrometers of the stromatolites' margins (Fig. 12c-d, Supplementary Fig. 2b). At those margins, CFA may occur as isopachous cements around  $CaCO_3$  peloids and ooids (Fig. 13).

*Interpretation:* The presence of inclusions and absence of cavity-filling textures suggest that early  $CaCO_3$  cements precipitated from pore fluids, variously nucleating on pore-lining grain surfaces or growing without template substrate. CFA cements formed similarly, precipitating from pore fluids and incorporating organic material and some calcite grains as inclusions. However, the strict spatial correlation between early CFA cements and digitate stromatolite laminae suggests that CFA saturation state was elevated only in pore fluids influenced by processes occurring within those microbial laminae, while  $CaCO_3$  saturation states were elevated, at some point, practically everywhere in the platform's sediment pore fluids.

### **Fe(II,III)-sulfide minerals and pseudomorphs thereof**

*Description:* Iron-sulfide minerals occur as euhedral-to-subhedral crystals of 1-10 micrometers diameter or as masses of crystals hundreds of micrometers in diameter. These are suspended among  $CaCO_3$  cements in grainstone and among stromatolite laminae (Fig. 12 a, c). They are often partially altered to more oxidized iron minerals.

*Interpretation:* Iron sulfide minerals precipitate from sediment pore fluids where sulfide and iron concentrations are enhanced relative to bottom waters by microbial depletion of dissolved oxygen. The exact iron sulfide phase that was originally precipitated was likely pyrite (Hurtgen, Arthur, and Halverson, 2005; Rickard, 1975), but in some instances appears to have been altered early on (i.e., during early cementation) to pyrrhotite, possible evidence of the evolving depth of the oxic-anoxic chemocline in the sediments (Flügel, 2010; Truche et al., 2010). Early diagenetic pyrite and pyrrhotite mineralization occurred widely within stromatolitic, planar-laminated, and crinkly-laminated carbonate grainstone facies, and was not associated

with specific primary textural features (Fig. 14). This suggests that microbial sulfate reduction and the reduction of any detrital and authigenic oxidized iron minerals occurred at comparable depths below the sediment-water interface, determined by the influence of oxygen-generative and oxygen-consumptive microbial metabolic processes on pore fluid chemistry, but not on the specific footprint of mats or biofilms.

### **Sutured grain boundaries, stylolites**

*Description:* Stylolites are observed cross-cutting what appear to be primary grain boundaries. Some grains (peloids and ooids, and even among the component peloids and ooids of grapestones) also appear to be merged with one another. See Supplementary Fig. 2.

*Interpretation:* Compaction of early-cemented sediments led to pressure-solution of grains and crystalline cements alike. This led to the suturing of grain-boundaries (i.e. the loss of distinction between adjacent grains), thin-film recrystallization and the enhancement of interlocking in crystal mosaic cements, and some offset (tens-of-micrometers to millimeter-scale) of primary grain and cement boundaries. This compaction may also have produced some thin, horse-tail stylolites oriented roughly along planes of primary bedding/lamination.

### **Dolomite I**

*Description:* Dolomite appears to be a fabric-retentive, replacive mineralogy, with boundaries of dolomitization following the outlines of primary and earlier diagenetic features. However, the boundaries of late dolomitization are often observed cross-cutting bedding planes and laminae. At the micrometer scale, we observe fabric-retentive replacement of primary and earlier diagenetic features (within grain boundaries, cement boundaries, and the boundaries of pressure-sutured regions), and growth of zoned euhedral dolomite rhomboids into apparent porespace following primary fabrics such as stromatolite-associated laminae.

*Interpretation:* Dolomitization of this kind is typically associated with meteoric and marine diagenesis before deep burial, taking place in the marine phreatic zone where freshwater and seawater are driven by gravity and differential pressure to pass through porous rock and mix with one another, bathing limestones in magnesium-bearing fluids (reviewed in Bathurst, 1975; Flügel, 2010).

### **Mosaic silica**

*Description:* Late-diagenetic replacive silica (mainly as chert) is a common occurrence in both the Sete Lagoas and Salitre Formations. Silica replacement is often fabric-destructive, cross-cutting boundaries between primary grains and cement matrices (e.g., Fig. 15c). However, there are some textures that are well-preserved, such as outermost ooid cortices. Inner cortices and cores that were previously micritized are replaced by cryptocrystalline silica, while mosaic cements and outermost ooid cortices are more coarsely crystalline. Silicification is observed to postdate dolomitization in some settings and predate dolomitization in others. Early diagenetic silicification featuring dark gray chert nodules, known to preserve microfossils, is not observed in the study area.

*Interpretation:* Silicification may be attributed to interactions between limestone or dolostone and either evaporitic or hydrothermal brines, such as might occur during deep burial and uplift (Hesse, 1990; Bustillo, 2010; Flügel, 2010). Because the observed replacive chert fabrics are relatively late and unassociated with supratidal facies, it is unlikely that the chert is the result of precipitation from evaporative brines.

### **Dolomite II**

*Description:* Euhedral-to-subhedral dolomite crystals, some exhibiting internal zoning, occur as fabric-destructive rinds templating on primary grain boundaries (Fig. 12a, Supplementary Fig. 2c). These crystals cross-cut replacive silica cements, and replacive dolomite cements (Dolomite I).

*Interpretation:* This generation of euhedral dolomite crystals is likely the result of dolomitization during deeper burial, as evidenced by zonation and coarse, relatively large crystal sizes.

### **Stylolites associated with Fe minerals**

*Description:* Stylolites of all geometries, including anastomosing swarms of thin horsetails, bedding-parallel seams, and large-amplitude columnar and hummocky stylolites, are common in all observed facies. These indicators of pressure-induced dissolution, recrystallization, and dolomitization may truncate or offset primary textures (e.g., grain boundaries), or align with primary textures (e.g., laminae). In some locations, stylolites may be visually enhanced by the presence of all- or partially-oxidized iron minerals. See Supplementary Figs. 2d and 3d.

*Interpretation:* These later stylolites are distinct from those related to compaction and pressure-suturing of primary grains (Section 4.5). Their association with masses of variably oxidized iron-sulfide minerals suggests their origin is related to deep burial and deep fluid diagenesis.

### **Fluorite**

*Description:* Pale-purple fluorite crystals are abundant in the Salitre Formation, replacing primary and early diagenetic calcite and dolomite textures (Supplementary Fig. 3). These often contain inclusions of some of carbonate minerals. In some localities (e.g., Locality 3, Fazenda Nova Canãa), fluorite is visible at the outcrop-scale along structural joints and fault planes.

*Interpretation:* Previous workers have identified baroque or saddle dolomite, lead-and-zinc enrichments, and other features that, combined with fluorite observed in this study, are consistent with an episode or episodes of hydrothermal alteration, fluid diagenesis taking place at high temperatures during deep burial and tectonic uplift (Caird et al., 2017; J. Richard Kyle and Aroldo Misi, 1997). The fluorine may, in some cases, be sourced locally from nearby altered sedimentary phosphorite deposits, namely structurally deformed digitate stromatolite facies.

### **Fractures**

*Description:* Generations of fractures cross-cut one another and are typically filled by inclusion-rich mosaics of dolomite or calcite spar, or microcrystalline quartz (Fig. 12d). In some localities, fractures are also associated with optically dense masses of all- or partially-oxidized pyrite (Supplementary Fig. 2c).

*Interpretation:* The complex structural history of the São Francisco Craton (See Section 1.2.1 and Reis, Alkmim, et al., 2016), has resulted in faulting and folding and the formation of pervasive fracture networks. Carbonate and Fe-sulfide-rich vein-filling cements are likely related to meteoric diagenesis and hydrothermal fluids, respectively.

## **2.6 Discussion: Phosphogenesis on a wave-swept, high energy carbonate platform**

It is broadly established that authigenic phosphate mineralization will occur in environments where phosphate accumulates in marine sediment porewaters. Such environments will experience authigenic phosphate mineralization, provided that inhibitors to phosphate mineral nucleation and growth are critically limited. Phos-

phate accumulation requires both the delivery of phosphate ( $PO_4^{3-}$  or  $HPO_4^{2-}$ ) to the sediment and its retention therein (Defforey and Paytan, 2018; Filippelli, 2011; Filippelli and Delaney, 1996). Environments near upwelling zones may receive a high influx of phosphate from deeper, colder, and less oxic waters. Where upwelling is not prevalent, phosphate may still be enriched in sediment by the burial of phosphate-accumulating microorganisms under oxic bottom waters and their metabolism by sulfate-reducing microorganisms at increasingly anoxic depths in the sediment, yielding free phosphate to porewaters. After delivery, accumulation may be accomplished by Fe(III), and to a lesser extent Mn(III), mineral scavenging of phosphate near the sediment-water interface, preventing the transport of phosphate ions back to the water column. All of these mechanisms of phosphate accumulation, requiring only the existence of microbially redox-stratified marine sediments under oxic bottom waters, are invoked in the formation story of authigenic phosphate deposits in modern and ancient phosphogenetic systems (Peter J. Cook and Shergold, 1984; Filippelli, 2011; Föllmi, 1996). However, microbially redox-stratified marine sediments under oxic bottom waters are common in modern and ancient oceans, while authigenic phosphate deposits are not. There must be other factors that control authigenic and early diagenetic phosphate precipitation, beyond the existence of redox-stratified sediments. The phosphorite deposits of the Salitre and Sete Lagoas formations provide an opportunity for the assessment of microtextural evidence (this work, Okubo et al., 2018; Shiraishi et al., 2019) and regional sedimentological and stratigraphic evidence (this work, Caird et al., 2017) of differences in depositional conditions and paleoecology that might explain the development of phosphatic and non-phosphatic fabrics.

### **Depositional setting**

The Salitre and Sete Lagoas Formations are broadly correlated based on U-Pb and Pb-Pb radiometric dating (Caxito et al., 2012; Paula-Santos et al., 2015; Shiraishi et al., 2019), by  $^{87}Sr/^{86}Sr$  and  $\delta^{13}C$  chemostratigraphic correlation (Aroldo Misi and Veizer, 1998). In this study we emphasize a lithostratigraphic correlation, based on the refinement of facies models, to better constrain the environmental context of the Salitre Formation's phosphatic microbialites (Caird et al., 2017; A. Misi and J. R. Kyle, 1994) and the Sete Lagoas Formation's phosphatic cements (Drummond et al., 2015; Okubo et al., 2018). A. Misi and J. R. Kyle, 1994 interpreted the Salitre Formation's phosphatic stromatolite bioherm facies as evaporitic in origin, inferring that phosphate enrichment was also an evaporitic phenomenon occurring

in a supratidal environment that induced dolostone and chert precipitation. More recently, Caird et al. (Caird et al., 2017) subdivided the stratigraphy of the Salitre Formation's lower members to include as many as 8 distinct parasequences, 10-20 meters in thickness, demarcated by flooding surfaces preceded by evaporite pseudomorphs, desiccation cracks, and tepee structures, and deposited just after phosphatic stromatolite reef facies. In our study, we did not observe evaporite mineral pseudomorphs or desiccation cracks. Tepee structures reported by those authors are reinterpreted here as wave ripples since they lack the defining characteristics of tepees and evaporitic tidal flat or sabkha structures, as described above (Section 3.2.8, Fig. 7). Rather, the structures are most consistent with an interpretation as symmetric wave ripples and occasional reworked fragments of early-cemented or microbially-bound sediment. The peaked, symmetric wave structures are draped by fine sediment and compressed, such that they overlap and the original relief of the peaks is diminished. Those sediments form laminae of variable thickness draping the compressed peaks, eventually damping out and leveling the seafloor until another reworking event occurs to reform decimeter-scale ripples. The environmental setting is alternatively interpreted as a persistently submerged, shallow water, wave-dominated environment (see Section 3.2). Such an interpretation would place primary phosphogenesis in the Salitre Formation within a persistently subtidal environment, dominated by energetic wave action. A wave-swept shallow platform or shallowly dipping ramp model, characterized by shifting shoals of carbonate sediments around and over microbial buildups, is consistent with the vast lateral and vertical extent of cross-stratified grainstone and rudstone facies (Raaf, Boersma, and Gelder, 1977; Dunham, 1962; Embry and Klovan, 1971; Lucia, 1995), tabular intraclast conglomerate (Sepkoski, 1982), and stromatolite patch reefs with significant elongation perpendicular to oscillatory and combined-flow indicators (see Sections 3.2 and 3.3, Figs. 6, 10).

The wave-dominated, microbialite buildup model presented here is comparable to the depositional settings identified for many other instances of microbialite-associated authigenic phosphogenesis in the geologic record, including the Cretaceous phosphorite of Negev, Israel (reviewed by Soudry, 2000), the Paleoproterozoic phosphorites near Chitrakoot and Udaipur, India (D. Banerjee, Schidlowski, and Arneeth, 1986; Bengtson et al., 2017; Choudhuri, 1990; Sallstedt et al., 2018; Sisodia and Chauhan, 1990), and the Cambrian phosphorites of Georgina Basin, Australia (Southgate, 1980). The Paleoproterozoic Michigamme Formation contains abundant phosphatic crusts associated with both fossilized filamentous biofilms and

reworked phosphatic peloids, hosted by peritidal sandstone and iron-carbonate facies (Hiatt, Pufahl, and Edwards, 2015). Comparably, the Doushantuo Formation of southern China also contains phosphorites associated with inner- and outer-shelf carbonates, though also with more quiescent basinal shale facies (Jiang et al., 2011; Xiao, Zhang, and Andrew H. Knoll, 1998). The Permian Phosphoria Sea deposits of the central United States represent a similar depositional environment, but phosphorite deposits there are comprised mainly of phosphatic peloids and other reworked grains rather than stromatolitic or in microbially-influenced laminae and hardgrounds (Hiatt and Budd, 2001). In all of these examples, despite some variation in diagenetic history and microfacies, phosphate mineralization and subsequent reworking seem to have occurred in settings that were distant or otherwise disconnected from upwelling zones, and experienced high current velocities. This would preclude upwelling of remineralized organic matter as a source of aqueous phosphate, as well as upwelling-related nutrient enrichment and primary production as a means of achieving supersaturation with respect to phosphate minerals. Rather, phosphogenesis in these shallow, marine settings is thought to have been driven by a combination of redox-stratified microbial activity and iron-redox cycling under oxic bottom waters. In such a model, phosphate is considered the limiting reactant for phosphate mineralization, and phosphate oversaturation is achieved by both abiotic and biotic mechanisms. Abiotic mechanisms include: winnowing and reworking of phosphatic hardgrounds by persistent energetic wave action, and the repeated adsorption and desorption of phosphate from oxidized and reduced iron minerals, respectively, below the sediment-oxic-bottom-water interface, as well as differences in flow-energy and sedimentation that might promote or prevent the accumulation of porewater phosphate. Biotic mechanisms include: the accumulation of phosphate by one group of microorganisms, and the microbially-mediated remineralization of organically bound and poly-phosphate as aqueous porewater phosphate. It is beyond the scope of this paper, and indeed the limitations of Precambrian taphonomy, to discuss the micro-textural evidence for and against all of these mechanisms in the Salitre and Sete Lagoas formations. The sedimentological data and depositional facies interpretations presented herein do, however, constrain the likelihood of those mechanisms of phosphogenesis dependent on location within the platform architecture and wave energy environment; and petrographic and spatially resolved compositional data may at least constrain the likelihood of phosphogenesis dependence on iron-redox cycling and microbially-mediated phosphate concentration and remineralization.

Caird et al., 2017 favored a depositional facies model wherein phosphatic stromatolite biostromes form in an intertidal zone environment and non-phosphatic stromatolite patch reefs occur in a shallow subtidal environment. In this model, persistent energetic tidal currents flush porewater phosphate out of the interstices of stromatolites, preventing the accumulation of phosphate necessary for the formation of authigenic carbonate fluorapatite cements. In contrast, stromatolites in the intertidal zone are characterized as forming in less permeable mud- and silt-scale sediments, and experiencing high sulfate concentrations related to evaporation in exposed tidal flats that might drive sulfur-based microbial ecologies related to phosphate accumulation (e.g., H. N. Schulz and H. D. Schulz, 2005). Our data, however, suggest significantly less distinction between the water depth and flow energy of phosphatic versus non-phosphatic stromatolite buildups within the Salitre Formation. In our study area, authigenic carbonate fluorapatite cements were common in the laminae of digitate stromatolites (Figs. 9, 12-13). Significantly, these are overlapped by and interfingered with high-energy facies associations (i.e., cross stratified grainstones, rudstones, and tabular intraclast conglomerate, as in Sections 3.2.1-2 and Figs. 3 and 9) rather than laminated muds as originally proposed. Our reinterpretation of putative tepee structures as symmetric wave ripples (Section 3.2.8, Fig. 7), and the lack of other indicators of exposure surfaces, support a subtidal rather than intertidal setting for the phosphatic stromatolite buildups. Furthermore, the close association of phosphatic and non-phosphatic microbially-influenced structures is well-preserved: phosphogenetic and non-phosphogenetic environments do not appear to have been separated by platform geometry or lateral facies transitions.

Therefore, we propose that the determinants of early phosphatic cement formation within the Salitre Formation were not water depth and flow-energy that controlled pore space advection and porewater phosphate loss. Rather, it seems that redox-stratified microbial communities persisted across a high-energy, shallow platform, and phosphate accumulation and mineralization within microbially-influenced deposits depended on highly local (centimeter-scale) variations in ecology and aqueous chemistry rather than platform geometry.

### **Local influences on the likelihood of phosphate mineralization**

Features of digitate versus columnar stromatolite morphology, such as size, prevalence of branching, and wall structure, may be related to the conditions that favor phosphogenesis in the Salitre Formation. Caird et al., 2017 alluded to this in their study: the idea that stromatolite laminae that continue across the top of a digit

and beyond the angle of repose, pinching out on the stromatolite flanks, might prevent the exchange of stromatolite porewaters (enriched in phosphate due to the degradation of phosphate-rich biomass within redox-stratified microbial mats or biofilms) with seawater or porewaters in grainy inter-stromatolite fill. Preliminary micro-scale petrography of phosphatic digitate stromatolites of the Salitre Formation challenge this model: Salitre stromatolites and microbial laminites containing carbonate fluorapatite cements do not always exhibit a barrier-like wall structure between stromatolite and adjacent grainstone (Figs. 12-14), whereas carbonate-cemented stromatolites sometimes do. This suggests that it is not the wall structure of individual stromatolite digits versus individual columns that directly causes the retention of porewater phosphate. Rather, it may be that the local sedimentary conditions that favor centimeter-diameter elongate digitate stromatolite development of small bioherms are also conducive to porewater phosphate accumulation and retention; while the conditions that favor larger, decimeter-scale stromatolites and larger bioherms are not. In Locality 5, described above and illustrated in Fig. 9, phosphatic digitate stromatolites compose the flanks and bottommost strata of observed meter-scale stromatolite buildups with mound- or bioherm-like shapes, whose component stromatolites grow less digitate and more disordered and mound-like toward the uppermost strata. The evolution of a stromatolite buildup from smaller, more distinct digits toward merged “cauliflower-like” structures may be the result of gradually diminishing sediment supply nearer the interior of the growing buildup. A larger sediment supply, which may lead to the bifurcation and divergence of individual digits (Tanja Bosak, Andrew H Knoll, and Alexander P Petroff, 2013; J. P. Grotzinger, 1989c; J. P. Grotzinger and A. H. Knoll, 1999; Pelechaty and J. P. Grotzinger, 1989), could also represent increased delivery of phosphate-adsorbing Fe- and Mn-(oxy)hydroxide sediments (Föllmi, 1996; Slomp et al., 1996), or oxygen-limitation of sulfur-oxidizing bacteria within the mats which may, in turn, stimulate polyphosphate metabolism and an increase of phosphate concentration in porewaters Brock and Schulz-Vogt, 2011; H. N. Schulz and H. D. Schulz, 2005. Both processes — retention of phosphate by adsorption to Fe- and Mn- (oxy)hydroxides, and contributions to porewater phosphate by the consortia of sulfide- oxidizing and sulfate-reducing microorganisms — are implicated in authigenic phosphate mineralization in modern and ancient phosphorites. Comparative micro-scale compositional and mineralogical analyses of phosphatic and non-phosphatic microbialites of the Salitre Formation are needed to test these mechanisms.

For instance, enrichment of iron in phosphatic digitate stromatolites relative to non-phosphatic stromatolites within the same buildup structure might support a hypothesis of iron-redox cycling as a key mechanism of porewater phosphate accumulation and retention, selected for by the sediment supply and flow velocity parameters that also enable digitate stromatolite formation. Spatially resolved compositional mapping of phosphatic and non-phosphatic facies of the Salitre Formation have so far not supported this mechanism. In this work and Shiraishi et al., 2019, iron is found to be negatively correlated with the occurrence of phosphorus-bearing minerals, and with possible positive correlation in some non-phosphatic, calcite-cemented stromatolites from within the same depositional facies. This is demonstrated in the comparison of Fe and P distributions in Figs. 14a and 14b. If the spatial extent of phosphate mineralization were controlled by the spatial extent of iron redox cycling, we would expect a positive correlation between Fe and P. Thus, it would seem that phosphogenesis in the Salitre formation cannot be explained by highly local variability of iron burial. The role of co-living sulfide-oxidizing (polyphosphate-accumulating) microorganisms and sulfate-reducing microorganisms may also be assessed by geochemical analysis of phosphatic versus non-phosphatic microbialite textures. Spatial correlation is expected between S abundance and microbial lamination due to the role of sulfate-reducing microorganisms in the anoxic strata of marine microbial mats, and indeed this is seen in elemental maps of digitate stromatolites of the Salitre Formation (Fig. 14a). However, it is the comparatively weaker correlation, even negative correlation, in non-phosphatic digitate stromatolites within the same formation and depositional facies (Fig. 14b) that suggests some difference between the biogeochemical cycling of S in phosphogenic and non-phosphogenic microfacies. The nature of this difference and its connection to the story of phosphogenesis in the Salitre Fm and correlative rocks cannot be elucidated by elemental and mineralogical compositions alone. Isotopic composition may. Greater depletion of  $^{34}\text{S}$  within phosphatic digitate stromatolites than in non-phosphatic stromatolites, relative to proxies for  $^{34}\text{S}$  content of contemporaneous seawater, might indicate that communities of sulfur-oxidizing microorganisms experienced conditions more favorable to polyphosphate metabolism under the sediment supply and flow velocity parameters conducive to digitate stromatolite formation. While isotopic analyses are beyond the scope of this study, we believe it is an essential next step in this case study of phosphogenesis at the Precambrian-Cambrian boundary.

## 2.7 Conclusions and future work

The Salitre and Sete Lagoas formations preserve remnants of an Ediacaran-age carbonate platform environment in the interior of the São Francisco Craton. Within the Salitre formation, we identify a range of lithofacies including: laminated, cross-stratified carbonate grainstone and rudstone, tabular intraclast conglomerate, planar-laminated, very-fine-grained limestone-dolostone, crinkly laminite, digitate stromatolite buildups and columnar stromatolite buildups (often elongate), and symmetric wave-rippled limestone (Figs. 3-7). The Sete Lagoas Formation, outcropping in the more southerly part of the craton, contains most of the same lithofacies. However, digitate stromatolite buildups are not observed within the Sete Lagoas Formation, and there are some localities with extensive aragonite crystal fan pseudomorphs associated with planar-laminated and wave-rippled limestone (Fig. 8). In both the Salitre and Sete Lagoas Formations, different lithofacies are observed to interfinger laterally over meter- and tens-of-meters-scales, with cross-stratified grainstone dominating much of the observed study area (Fig. 10). This supports a regional depositional facies model for both the Salitre and Sete Lagoas formations featuring a persistently submerged platform with high-energy sediment transport by waves, where local variations in sedimentation rate permitted establishment of microbial buildups (Fig. 2).

In the Salitre Formation, digitate stromatolite bioherms and biostromes contain extensive carbonate fluorapatite cements of early authigenic origin, forming at or just below the sediment-water interface (Figs. 4). These phosphatic cements are restricted to stromatolite laminae and are not present in grainy inter-stromatolite carbonate fill or in the cross-stratified grainstones, rudstones, and tabular intraclast conglomerates that interfinger with the stromatolite buildups (Figs. 4, 12-13). However, there are also non-phosphatic stromatolites within otherwise phosphate-bearing buildups, or forming nearby buildups that have no preferential phosphate enrichment (Fig. 9, 14). Because phosphatic and non-phosphatic stromatolites appear within the same depositional facies associations (i.e., high-energy, wave-swept subtidal), we propose a model of early phosphate mineralization that is not dependent on platform architecture or flow energy environment but rather on highly local, possibly microbial processes. Phosphatic cements of the Sete Lagoas Formation have been previously observed in association with aragonite crystal fan pseudomorphs but not stromatolites (Drummond et al., 2015; Okubo et al., 2018), suggesting a different mechanism for phosphogenesis in the more southern areas of the São Francisco Craton.

Analysis of micro-scale textures and mineralogical and elemental associations may help distinguish between different localized mechanisms of authigenic and early diagenetic phosphate mineralization in both the Salitre and Sete Lagoas formations. Spatially resolved elemental data from phosphatic and non phosphatic stromatolites of the Salitre Formation (Fig. 14, Supplementary Fig. 1a) reveal a negative correlation between P and Fe/Mn, suggesting that the role of Fe and Mn oxides in concentrating and retaining phosphate in sediment porewaters was probably not the determinant of early phosphate mineralization. However, positive correlation in the spatial distribution of P and S in phosphatic stromatolites, and a weaker to negative correlation in non-phosphatic stromatolites, may support models of phosphogenesis dependent on local differences in the biogeochemical cycling of S. Further comparative analyses of phosphatic and non-phosphatic textures at the micro-scale will be necessary to rigorously test the relationship between S and P mineralization, including isotopic and elemental data, on the São Francisco Craton and other phosphogenetic environments of the Ediacaran.

## 2.8 Acknowledgements

We the authors are incredibly grateful to Anelize Bahniuk Rumbelsperger, Leonardo Fadel Cury, Victor Dorneles, Almério Barros França, Angela Rodizes, Gabriel Ruviano, Larissa Santos, Lucas Valore, Kimberly Viera, and Hugo Yamassaki of the Laboratório de Análises de Minerais e Rochas (LAMIR) e Laboratório de Análise de Bacias (LABAP) da Universidade Federal do Paraná, as well as Filipe Nery Falcão of the Universidade Federal do Bahia, for their expertise, invaluable discussion, and assistance in the field. We also thank Gilsara Alves (Parque Nacional Cavernas do Peruaçu), Aly Brandenburg (Shell), Mauricio Calderón (Universidad Adres Bello), Bruce Levell (Oxford University), Juliana Okubo (Universidade Estadual Paulista), Daniel Martins de Oliveira (Petrobras), Alípio Pereira (Petrobras), Cícero da Paixão Pereira (Universidade Federal do Bahia), Chris Vasconcelos (Eidgenössische Technische Hochschule Zürich), and Lucas Warren (Universidade Estadual Paulista) for their vast collective knowledge, advice, and guidance, as well as Michele Santos, Ricardo Ramos Spreafico, and many others from the Companhia Baiana de Pesquisa Mineral (CBPM) for their expertise in the regional geology of Bahia, and for providing us access to Salitre Fm. drill cores.

In addition, we are wholly indebted to the farmers, miners, educators, and conservationists of the Chapada Diamantina and Cavernas do Peruaçu regions for their guidance and expertise.

We also wish to thank the reviewers, and to acknowledge that this work was supported by the National Science Foundation Graduate Research Fellowship Program (NSF GRFP), and the Simons Foundation.

Lastly, we humbly acknowledge the Xakriabá, the communities of and surrounding the historic Quilombo da Gruta dos Brejões, as well as other indigenous peoples whose names and identities may have been lost to colonialism and occupation, on whose land this work relies.

## References

- Alkmim, Fernando F., Stephen Marshak, et al. (2006). “Kinematic evolution of the Araçuaí-West Congo orogen in Brazil and Africa: Nutcracker tectonics during the Neoproterozoic assembly of Gondwana”. In: *Precambrian Research* 149.1-2, pp. 43–64. ISSN: 03019268. DOI: 10.1016/j.precamres.2006.06.007.
- Alkmim, Fernando F. and Marcelo A. Martins-Neto (2012). “Proterozoic first-order sedimentary sequences of the São Francisco craton, eastern Brazil”. In: *Marine and Petroleum Geology* 33.1, pp. 127–139. ISSN: 02648172. DOI: 10.1016/j.marpetgeo.2011.08.011. URL: <http://dx.doi.org/10.1016/j.marpetgeo.2011.08.011>.
- Allen, Philip A and James L Etienne (2008). “Sedimentary challenge to Snowball Earth”. In: *Nature Geoscience* 1, pp. 817–825.
- Allen, Philip A and Paul F Hoffman (2005a). “Extreme winds and waves in the aftermath of a Neoproterozoic glaciation”. In: *Nature* 433, pp. 123–127. URL: [papers2://publication/uuid/9A5FABD7-DD54-495C-A7DD-A0D08E88D239](https://doi.org/10.1038/nature04246).
- (2005b). “Paleoclimatology—Formation of Precambrian sediment ripples”. In: *Nature* 436, E1–E2.
- Allwood, Abigail C. et al. (2009). “Controls on development and diversity of Early Archean stromatolites”. In: *Proceedings of the National Academy of Sciences of the United States of America* 106.24, pp. 9548–9555. ISSN: 00278424. DOI: 10.1073/pnas.0903323106.
- Arning, E. T. et al. (2009). “Bacterial formation of phosphatic laminites off Peru”. In: *Geobiology* 7.3, pp. 295–307. ISSN: 14724669. DOI: 10.1111/j.1472-4669.2009.00197.x.
- Assereto, Ricardo L. A. M. and Christopher G. St Kendall (1977). “Nature, origin and classification of peritidal tepee structures and related breccias”. In: *Sedimentology* 24.2, pp. 153–210.
- Banerjee, D M, P C Basu, and N Srivastava (1980). “Petrology, Mineralogy, Geochemistry, and Origin of the Precambrian Aravallian Phosphorite Deposits of Udaipur and Jhabua, India”. In: *Economic Geology* 75.3, pp. 1181–1199.

- Banerjee, D. M. (1971). “Precambrian stromatolitic phosphorites of Udaipur, Rajasthan, India”. In: *Bulletin of the Geological Society of America* 82.8, pp. 2319–2330. ISSN: 19432674. DOI: 10.1130/0016-7606(1971)82[2319:PSPOUR]2.0.CO;2.
- Banerjee, DM, M Schidlowski, and JD Arneeth (1986). “Deposits of India : Isotopic Inferences From Carbonate”. In: *Precambrian Research* 33, pp. 239–253.
- Bathurst, Robin GC (1975). *Carbonate sediments and their diagenesis*. Second. Amsterdam: Elsevier.
- Bengtson, Stefan et al. (2017). “Three-dimensional preservation of cellular and subcellular structures suggests 1.6 billion-year-old crown-group red algae”. In: *PLoS Biology* 15.3, pp. 1–38. ISSN: 15457885. DOI: 10.1371/journal.pbio.2000735.
- Beukes, Nicolas J. and Donald R. Lowe (1989). “Environmental control on diverse stromatolite morphologies in the 3000 Myr Pongola Supergroup, South Africa”. In: *Sedimentology* 36.3, pp. 383–397. DOI: <https://doi.org/10.1111/j.1365-3091.1989.tb00615.x>.
- Bosak, T., V. Souza-Egipsy, and D. K. Newman (2004). “A laboratory model of abiotic peloid formation”. In: *Geobiology* 2.3, pp. 189–198. ISSN: 1472-4677. DOI: 10.1111/j.1472-4677.2004.00031.x.
- Bosak, Tanja, Andrew H Knoll, and Alexander P Petroff (2013). “The Meaning of Stromatolites”. In: *Annual Review of Earth and Planetary Sciences* 41, pp. 21–44. DOI: 10.1146/annurev-earth-042711-105327.
- Bottrell, S H and R Raiswell (2000). “Sulphur Isotopes and Microbial Sulfur Cycling”. In: *Microbial Sediments*. Ed. by Robert Riding and Stanley Awramik. Berlin: Springer-Verlag, pp. 96–104.
- Brasier, Martin and Richard Callow (2007). “Changes in the Patterns of Phosphatic Preservation across the Proterozoic-Cambrian Transition”. In: *Memoirs of the Association of Australasian Palaeontologists* 34, p. 377.
- Brock, Jörg and Heide N. Schulz-Vogt (2011). “Sulfide induces phosphate release from polyphosphate in cultures of a marine *Beggiatoa* strain”. In: *ISME Journal* 5.3, pp. 497–506. ISSN: 17517362. DOI: 10.1038/ismej.2010.135.
- Bustillo, Maria Ángeles (2010). “Silicification of continental carbonates”. In: *Carbonates in Continental Settings: processes, facies and applications* 62, pp. 153–174.
- Caird, R. A. et al. (2017). “Ediacaran stromatolites and intertidal phosphorite of the Salitre Formation, Brazil: Phosphogenesis during the Neoproterozoic Oxygenation Event”. In: *Sedimentary Geology* 350.January, pp. 55–71. ISSN: 00370738. DOI: 10.1016/j.sedgeo.2017.01.005. URL: <http://dx.doi.org/10.1016/j.sedgeo.2017.01.005>.

- Canfield, Don E., Simon W. Poulton, and Guy M. Narbonne (2007). “Late-Neoproterozoic deep-ocean oxygenation and the rise of animal life”. In: *Science* 315.5808, pp. 92–95. ISSN: 00368075. DOI: 10.1126/science.1135013.
- Castanier, Sabine, Gaële Levrel-Métayer, and Jean-Pierre Perthuisot (2000). “Bacterial Roles in the Precipitation of Carbonate Minerals”. In: *Microbial Sediments*. Ed. by Robert Riding and Stanley Awramik. Berlin: Springer-Verlag, pp. 32–39.
- Caxito, Fabrício de Andrade et al. (2012). “Marinoan glaciation in east central Brazil”. In: *Precambrian Research* 200-203, pp. 38–58. ISSN: 03019268. DOI: 10.1016/j.precamres.2012.01.005.
- Cecile, M. P. and F. H. A. Campbell (1978). “Regressive stromatolite reefs and associated facies, Middle Goulburn Group (Lower Proterozoic), in Kilohigok Basin, N.W.T.: An example of environmental control on stromatolite form”. In: *Bulletin of Canadian Petroleum Geology* 26.2, pp. 237–267.
- Chin, K. et al. (2003). “Remarkable Preservation of Undigested Muscle Tissue Within a Late Cretaceous Tyrannosaurid Coprolite from Alberta, Canada”. In: *Palaio* 18.3, pp. 286–294. ISSN: 0883-1351. DOI: 10.1669/0883-1351(2003)018<0286:rpoumt>2.0.co;2.
- Choudhuri, R. (1990). “Two decades of phosphorite investigations in India”. In: *Geological Society Special Publication* 52.52, pp. 305–311. ISSN: 03058719. DOI: 10.1144/GSL.SP.1990.052.01.22.
- Cook, P. J. (1992). “Phosphogenesis around the Proterozoic-Phanerozoic transition”. In: *Journal - Geological Society (London)* 149.4, pp. 615–620. ISSN: 0016-7649. DOI: 10.1144/gsjgs.149.4.0615.
- Cook, Peter J. and John H. Shergold (1984). “Phosphorus, phosphorites and skeletal evolution at the Precambrian - Cambrian boundary”. In: *Nature* 308.5956, pp. 231–236. ISSN: 00280836. DOI: 10.1038/308231a0.
- Cordani, Umberto G. and Kei Sato (1999). “Crustal evolution of the South American platform, based on Nd isotopic systematics on granitoid rocks”. In: *Episodes* 22.3, pp. 167–173. ISSN: 07053797. DOI: 10.18814/epiiugs/1999/v22i3/003.
- Creveling, Jessica R, Kristin D Bergmann, and John P Grotzinger (2016). “Cap carbonate platform facies model, Noonday Formation, SE California”. In: *GSA Bulletin* 128.7/8, pp. 1249–1269. DOI: 10.1130/B31442.1.
- Cruz, Simone C.P. and Fernando F. Alkmim (2006). “The tectonic interaction between the Paramirim Aulacogen and the Araçuaí Belt, São Francisco craton region, Eastern Brazil”. In: *Anais da Academia Brasileira de Ciências* 78.1, pp. 151–173. ISSN: 00027812.
- Dalton de Souza, João et al. (2003). *Mapa geológico do Estado da Bahia*. Tech. rep. CPRM - Serviço Geológico do Brasil, Governo do Estado da Bahia, Ministerio de Minas e Energia, Companhia Baiana de Pesquisa Mineral.

- Defforey, Delphine and Adina Paytan (2018). “Phosphorus cycling in marine sediments: Advances and challenges”. In: *Chemical Geology* 477, June 2017, pp. 1–11. ISSN: 00092541. DOI: 10.1016/j.chemgeo.2017.12.002.
- Delisle, Renee Alayne (2015). “Phosphatic Peritidal Limestone of the Neoproterozoic Salitre Formation, Brazil, and Precambrian Economic Phosphorite”. PhD thesis. Acadia University, p. 141. URL: <http://openarchive.acadiau.ca/utils/getdownloaditem/collection/Theses/id/1019/filename/1033.pdf/mapsto/pdf>.
- Diaz, Mara R. and Gregor P. Eberli (2019). “Decoding the mechanism of formation in marine ooids: A review”. In: *Earth-Science Reviews* 190, pp. 536–556. ISSN: 00128252. DOI: 10.1016/j.earscirev.2018.12.016. URL: <https://doi.org/10.1016/j.earscirev.2018.12.016>.
- Donnelly, T. H. et al. (1990). “Events leading to global phosphogenesis around the Proterozoic/Cambrian boundary”. In: *Geological Society Special Publication* 52.52, pp. 273–287. ISSN: 03058719. DOI: 10.1144/GSL.SP.1990.052.01.20.
- Dravis, Jeffrey J and Harold R Wanless (2008). “Caicos Platform models of quaternary carbonate deposition controlled by stronger easterly trade winds - applications to petroleum exploration”. In: *Developing Models and Analogs for Isolated Carbonate Platforms - Holocene and Pleistocene Carbonates of Caicos Platform, British West Indies*. SEPM (Society for Sedimentary Geology), pp. 21–27. ISBN: 9781565761346.
- Drummond, Justin B. R. et al. (2015). “Neoproterozoic peritidal phosphorite from the Sete Lagoas Formation (Brazil) and the Precambrian phosphorus cycle”. In: *Sedimentology* 62.7, pp. 1978–2008. DOI: 10.1111/sed.12214.
- Dunham, Robert J. (1962). “Classification of Carbonate Rocks According to Depositional Textures”. In: *M 1: Classification of Carbonate Rocks – A Symposium*. AAPG, pp. 108–121.
- Embry, Ashton F. and Edward Klovan (1971). “A late devonian reef tract on northeastern Banks Island, N.W.T.” In: *Bulletin of Canadian Petroleum Geology* 19.4, pp. 730–781.
- Fike, D. A. et al. (2006). “Oxidation of the Ediacaran ocean”. In: *Nature* 444.7120, pp. 744–747. ISSN: 14764687. DOI: 10.1038/nature05345.
- Filippelli, Gabriel M. (2011). “Phosphate rock formation and marine phosphorus geochemistry: The deep time perspective”. In: *Chemosphere* 84.6, pp. 759–766. ISSN: 00456535. DOI: 10.1016/j.chemosphere.2011.02.019.
- Filippelli, Gabriel M. and Margaret Lois Delaney (1996). “Phosphorus geochemistry of equatorial Pacific sediments”. In: *Geochimica et Cosmochimica Acta* 60.9, pp. 1479–1495. ISSN: 00167037. DOI: 10.1016/0016-7037(96)00042-7.
- Flügel, Erik (2010). *Microfacies of Carbonate Rocks: Analysis, Interpretation, and Application*. Second. Berlin Heidelberg: Springer-Verlag. ISBN: 9783642037955.

- Föllmi, KB (1996). “The phosphorus cycle, phosphogenesis phosphate-rich deposits”. In: *Earth-Science Reviews* 40, pp. 55–124.
- Fonseca, Marco Antônio et al. (2014). *Mapa Geológico do Estado de Minas Gerais*. Tech. rep. CPRM - Serviço Geológico do Brasil, Governo de Minas, Ministerio de Minas e Energia, Companhia de Desenvolvimento Econômico de Minas Gerais.
- Grotzinger, J. P. (1989a). “Construction of Early Proterozoic Reef Complex, Rocknest Platform, Northwest Territories”. In: *Reef: Canada and Adjacent Areas Memoir 13*. Ed. by H. H. J. Geldsetzer, N. P. James, and G. E. Tebbutt. Canadian Society of Petroleum Geologists, pp. 30–37.
- (1989b). “Facies and evolution of Precambrian carbonate depositional systems: emergence of the modern platform archetype”. In: *SEPM Special Publication: Controls on carbonate platform and basin development* 44, pp. 71–106. DOI: 10.2110/pec.89.44.0079.
- (1989c). “Introduction to Precambrian Reefs”. In: *Reef: Canada and Adjacent Areas Memoir 13*. Ed. by H. H. J. Geldsetzer, N. P. James, and G. E. Tebbutt. Canadian Society of Petroleum Geologists, pp. 9–12.
- Grotzinger, J. P. and A. H. Knoll (1999). “Stromatolites in Precambrian carbonates: Evolutionary mileposts or environmental dipsticks?” In: *Annual Review of Earth and Planetary Sciences* 27, pp. 313–358. ISSN: 00846597. DOI: 10.1146/annurev.earth.27.1.313.
- Grotzinger, J. P. and Z. Al-Rawahi (2014). “Depositional facies and platform architecture of microbialite-dominated carbonate reservoirs, ediacaran-cambrian ara group, sultanate of Oman”. In: *AAPG Bulletin* 98.8, pp. 1453–1494. ISSN: 01491423. DOI: 10.1306/02271412063.
- Guimarães, J. T. et al. (2011). “The Bebedouro Formation, Una Group, Bahia (Brazil)”. In: *Geological Society Memoir* 36.1, pp. 503–508. ISSN: 04354052. DOI: 10.1144/M36.47.
- Harouiya, Najatte et al. (2007). “The dissolution kinetics and apparent solubility of natural apatite in closed reactors at temperatures from 5 to 50 °C and pH from 1 to 6”. In: *Chemical Geology* 244.3-4, pp. 554–568. ISSN: 00092541. DOI: 10.1016/j.chemgeo.2007.07.011.
- Heilbron, Monica, Umberto Giuseppe Cordani, and Fernando F. Alkmim (2017). “São Francisco Craton, Eastern Brazil”. In: *Regional Geology Reviews* December, pp. 3–13. DOI: 10.1007/978-3-319-01715-0. URL: <http://link.springer.com/10.1007/978-3-319-01715-0>[https://doi.org/10.1007/978-3-319-01715-0\\_16](https://doi.org/10.1007/978-3-319-01715-0_16).
- Hesse, R. (1990). “Silica diagenesis: origin of inorganic and replacement cherts”. In: *Earth-Science Reviews* 26, pp. 253–276.

- Hiatt, Eric E. and David A. Budd (2001). “Sedimentary phosphate formation in warm shallow waters: New insights into the palaeoceanography of the Permian Phosphoria Sea from analysis of phosphate oxygen isotopes”. In: *Sedimentary Geology* 145.1-2, pp. 119–133. ISSN: 00370738. DOI: 10.1016/S0037-0738(01)00127-0.
- Hiatt, Eric E., Peir K. Pufahl, and Cole T. Edwards (2015). “Sedimentary phosphate and associated fossil bacteria in a Paleoproterozoic tidal flat in the 1.85Ga Michigamme Formation, Michigan, USA”. In: *Sedimentary Geology* 319, pp. 24–39. ISSN: 00370738. DOI: 10.1016/j.sedgeo.2015.01.006. URL: <http://dx.doi.org/10.1016/j.sedgeo.2015.01.006>.
- Hickman-Lewis, Keyron et al. (2019). “Mechanistic morphogenesis of organosedimentary structures growing under geochemically stressed conditions: Keystone to proving the biogenicity of some Archaean stromatolites?” In: *Geosciences (Switzerland)* 9.8. ISSN: 20763263. DOI: 10.3390/geosciences9080359.
- Hoffman, Paul (1969). “Proterozoic paleocurrents and depositional history of the East Arm fold belt, Great Slave Lake, Northwest Territories”. In: *Canadian Journal of Earth Sciences* 6.3, pp. 441–462. ISSN: 0008-4077. DOI: 10.1139/e69-042.
- Hurtgen, Matthew T, Michael A Arthur, and Galen P Halverson (2005). “Neoproterozoic sulfur isotopes, the evolution of microbial sulfur species, and the burial efficiency of sulfide as sedimentary pyrite”. In: *Geology* 33.1, pp. 41–44. DOI: 10.1130/G20923.1.
- Iglesias, Mario and Alexandre Uhlein (2009). “Estratigrafia do Grupo Bambuí e coberturas fanerozóicas no vale do rio São Francisco, norte de Minas Gerais”. In: *Revista Brasileira de Geociências* 39.2, pp. 256–266. DOI: 10.25249/0375-7536.2009392256266.
- Jiang, Ganqing et al. (2011). “Stratigraphy and paleogeography of the Ediacaran Doushantuo Formation (ca. 635-551Ma) in South China”. In: *Gondwana Research* 19.4, pp. 831–849. ISSN: 1342937X. DOI: 10.1016/j.gr.2011.01.006. URL: <http://dx.doi.org/10.1016/j.gr.2011.01.006>.
- Kendall, Brian S. et al. (2004). “Constraints on the timing of Marinoan “Snowball Earth” glaciation by 187Re-187Os dating of a Neoproterozoic, post-glacial black shale in Western Canada”. In: *Earth and Planetary Science Letters* 222.3-4, pp. 729–740. ISSN: 0012821X. DOI: 10.1016/j.epsl.2004.04.004.
- Knorre, Heike v and Wolfgang E Krumbein (2000). “Bacterial Calcification”. In: *Microbial Sediments*. Ed. by Robert Riding and Stanley Awramik. Berlin: Springer-Verlag, pp. 25–31.
- Kramer, James R (1964). “Sea Water: Saturation with Apatites and Carbonates”. In: *Science* 146.3644, pp. 637–638.

- Kuchenbecker, Matheus, Humberto Luis, and Daniel Galvão (2011). “Caracterização estrutural e considerações sobre a evolução tectônica da Formação Salitre na porção central da Bacia de Irecê , norte do Cráton do”. In: *Geonomos* 19.2, pp. 42–49.
- Kyle, J. Richard and Aroldo Misi (1997). “Origin of zn-pb-ag sulfide mineralization within upper proterozoic phosphate-rich carbonate strata, irecê basin, bahia, brazil”. In: *International Geology Review* 39.5, pp. 383–399. ISSN: 19382839. DOI: 10.1080/00206819709465279.
- Lamb, Michael P. et al. (2012). “Origin of giant wave ripples in snowball earth cap carbonate”. In: *Geology* 40.9, pp. 827–830. ISSN: 00917613. DOI: 10.1130/G33093.1.
- Lepland, Aivo et al. (2014). “Potential influence of sulphur bacteria on Palaeoproterozoic phosphogenesis”. In: *Nature Geoscience* 7.1, pp. 20–24. ISSN: 17520894. DOI: 10.1038/ngeo2005.
- Logan, Brian W (1961). “Cryptozoon and Associate Stromatolites from the Recent , Shark Bay , Western Australia”. In: *The Journal of Geology* 69.5, pp. 517–533.
- Lucia, F. J. (1995). “Rock-fabric/ptrophysical classification of carbonate pore space for reservoir characterization”. In: *American Association of Petroleum Geologists Bulletin* 79.9, pp. 1275–1300. ISSN: 01491423. DOI: 10.1306/7834d4a4-1721-11d7-8645000102c1865d.
- Martens, Christopher S. and Robert C. Harriss (1970). “Inhibition of apatite precipitation in the marine environment by magnesium ions”. In: *Geochimica et Cosmochimica Acta* 34.5, pp. 621–625. ISSN: 00167037. DOI: 10.1016/0016-7037(70)90020-7.
- Martins-Neto, M. A., A. C. Pedrosa-Soares, and S. A.A. Lima (2001). “Tectono-sedimentary evolution of sedimentary basins from Late Paleoproterozoic to Late Neoproterozoic in the São Francisco craton and Araçuaí fold belt, Eastern Brazil”. In: *Sedimentary Geology* 141-142, pp. 343–370. ISSN: 00370738. DOI: 10.1016/S0037-0738(01)00082-3.
- Merz-Preiß, Martina (2000). “Calcification in Cyanobacteria”. In: *Microbial Sediments*. Ed. by Robert Riding and Stanley Awramik. Berlin: Springer-Verlag, pp. 50–56.
- Misi, A. and J. R. Kyle (1994). “Upper Proterozoic carbonate stratigraphy, diagenesis, and stromatolitic phosphorite formation, Irece Basin, Bahia, Brazil”. In: *Journal of Sedimentary Research A: Sedimentary Petrology and Processes* 64 A.2, pp. 299–310.
- Misi, Aroldo, Alan J. Kaufman, et al. (2007). “Chemostratigraphic correlation of Neoproterozoic successions in South America”. In: *Chemical Geology* 237.1-2, pp. 143–167. ISSN: 00092541. DOI: 10.1016/j.chemgeo.2006.06.019.

- Misi, Aroldo and Ján Veizer (1998). “Neoproterozoic carbonate sequences of the Una Group, Irecê Basin, Brazil: Chemostratigraphy, age and correlations”. In: *Precambrian Research* 89.1-2, pp. 87–100. ISSN: 03019268.
- Möller, Nicola Kerstin and Knut Kvingan (1988). “The genesis of nodular limestones in the Ordovician and Silurian of the Oslo Region (Norway)”. In: *Sedimentology* 35.3, pp. 405–420. ISSN: 13653091. DOI: 10.1111/j.1365-3091.1988.tb00994.x.
- Mount, Jeffrey F and David Kidder (1993). “Combined flow origin of edgewise intra-clast conglomerates: Sellick Hill Formation (Lower Cambrian), South Australia”. In: *Sedimentology* 40, pp. 315–329.
- Muscente, A. D., Andrew D. Hawkins, and Shuhai Xiao (2015). “Fossil preservation through phosphatization and silicification in the Ediacaran Doushantuo Formation (South China): A comparative synthesis”. In: *Palaeogeography, Palaeoclimatology, Palaeoecology* 434, pp. 46–62. ISSN: 00310182. DOI: 10.1016/j.palaeo.2014.10.013. URL: <http://dx.doi.org/10.1016/j.palaeo.2014.10.013>.
- Narbonne, Guy M. (2005). “THE EDIACARA BIOTA: Neoproterozoic Origin of Animals and Their Ecosystems”. In: *Annual Review of Earth and Planetary Sciences* 33.1, pp. 421–442. ISSN: 0084-6597. DOI: 10.1146/annurev.earth.33.092203.122519.
- Narbonne, Guy M. and James G. Gehling (2003). “Life after snowball: The oldest complex Ediacaran fossils”. In: *Geology* 31.1, pp. 27–30. ISSN: 00917613. DOI: 10.1130/0091-7613(2003)031<0027:LASTOC>2.0.CO;2.
- Noffke, Nora, Andrew H. Knoll, and John P. Grotzinger (2002). “Sedimentary controls on the formation and preservation of microbial mats in siliciclastic deposits: A case study from the Upper Neoproterozoic Nama Group, Namibia”. In: *Palaios* 17.6, pp. 533–544. ISSN: 08831351. DOI: 10.1669/0883-1351(2002)017<0533:SCOTFA>2.0.CO;2.
- Okubo, J. et al. (2018). “Phosphogenesis, aragonite fan formation and seafloor environments following the Marinoan glaciation”. In: *Precambrian Research* 311.May 2017, pp. 24–36. ISSN: 03019268. DOI: 10.1016/j.precamres.2018.04.002. URL: <https://doi.org/10.1016/j.precamres.2018.04.002>.
- Papineau, Dominic (2010). “Global biogeochemical changes at both ends of the Proterozoic: Insights from phosphorites”. In: *Astrobiology* 10.2, pp. 165–181. ISSN: 15311074. DOI: 10.1089/ast.2009.0360.
- Paula-Santos, Gustavo Macedo et al. (2015). “New evidence of an Ediacaran age for the Bambuí Group in southern São Francisco craton (eastern Brazil) from zircon U-Pb data and isotope chemostratigraphy”. In: *Gondwana Research* 28.2, pp. 702–720. ISSN: 1342937X. DOI: 10.1016/j.gr.2014.07.012. URL: <http://dx.doi.org/10.1016/j.gr.2014.07.012>.

- Pedrosa-Soares, A. C. et al. (2008). “Similarities and differences between the Brazilian and African counterparts of the Neoproterozoic Araçuaí–West Congo orogen”. In: *Geological Society Special Publication* 294, pp. 153–172. ISSN: 03058719. DOI: 10.1144/SP294.9.
- Pelechaty, S. M. and J. P. Grotzinger (1989). “Stromatolite Bioherms of A 1.9 Ga Foreland Basin Carbonate Ramp, Beechey Formation, Kilohigok Basin, Northwest Territories”. In: *Reef: Canada and Adjacent Areas Memoir 13*. Ed. by H. H. J. Geldsetzer, N. P. James, and G. E. Tabbutt. Canadian Society of Petroleum Geologists, pp. 93–104.
- Petroff, Alexander P. et al. (2010). “Biophysical basis for the geometry of conical stromatolites”. In: *Proceedings of the National Academy of Sciences of the United States of America* 107.22, pp. 9956–9961. ISSN: 00278424. DOI: 10.1073/pnas.1001973107.
- Pflüger, Friedrich and Pieter G. Gresse (1996). “Microbial sand chips - A non-actualistic sedimentary structure”. In: *Sedimentary Geology* 102.3-4, pp. 263–274. ISSN: 00370738. DOI: 10.1016/0037-0738(95)00072-0.
- Planavsky, Noah and Kathleen Grey (2008). “Stromatolite branching in the Neoproterozoic of the Centralian Superbasin, Australia: An investigation into sedimentary and microbial control of stromatolite morphology”. In: *Geobiology* 6.1, pp. 33–45. ISSN: 14724677. DOI: 10.1111/j.1472-4669.2007.00116.x.
- Raaf, JFM de, JR Boersma, and A van Gelder (1977). “Wave-generated structures and sequences from a shallow marine succession, Lwer Carboniferous, County Cork, Ireland”. In: *Sedimentology* 25, pp. 451–483.
- Read, J. Fred (1985). “Carbonate Platform Facies Models.” In: *American Association of Petroleum Geologists Bulletin* 69.1, pp. 1–21. ISSN: 01491423. DOI: 10.1306/AD461B79-16F7-11D7-8645000102C1865D.
- Reineck, Hans-Erich and Indra Bir Singh (1980). “Current and Wave Ripples”. In: *Depositional Sedimentary Environments*. 2nd ed. Berlin: Springer-Verlag, pp. 22–52.
- Reis, Humberto L.S., Fernando F. Alkmim, et al. (2016). “The São Francisco Basin”. In: *The São Francisco Craton, Eastern Brazil: Tectonic Genealogy of a Miniature Continent*. Ed. by Monica Heilbron, Umberto G. Cordani, and Fernando F. Alkmim. 1st ed. August. Springer, pp. 117–143. ISBN: 9783319017150. DOI: 10.1007/978-3-319-01715-0.
- Reis, Humberto L.S., João F. Suss, et al. (2017). “Ediacaran forebulge grabens of the southern São Francisco basin, SE Brazil: Craton interior dynamics during West Gondwana assembly”. In: *Precambrian Research* 302. September, pp. 150–170. ISSN: 03019268. DOI: 10.1016/j.precamres.2017.09.023. URL: <http://dx.doi.org/10.1016/j.precamres.2017.09.023>.
- Rickard, David T (1975). “Kinetics and mechanism of pyrite formation at low temperatures”. In: *American Journal of Science* 275, pp. 636–652.

- Riding, Robert (2002). *Structure and composition of organic reefs and carbonate mud mounds: Concepts and categories*. Vol. 58. 1-2, pp. 163–231. ISBN: 4429208743. DOI: 10.1016/S0012-8252(01)00089-7.
- Riding, Robert E and Stanley M Awramik, eds. (2000). *Microbial Sediments*. Berlin: Springer-Verlag.
- Sallstedt, T. et al. (2018). “Evidence of oxygenic phototrophy in ancient phosphatic stromatolites from the Paleoproterozoic Vindhyan and Aravalli Supergroups, India”. In: *Geobiology* 16.2, pp. 139–159. ISSN: 14724669. DOI: 10.1111/gbi.12274.
- Sanchez, Evelyn Aparecida Mecenero (2014). “Microbialitos e microfósseis da Formação Sete Lagoas, Neoproterozoico, Brasil: implicações geomicrobiológicas em um contexto de mudanças climáticas e evolutivas”. PhD thesis. Universidade de São Paulo, p. 298.
- Sandberg, Philip (1985). “Aragonite cements and their occurrence in ancient limestones”. In: *Special Publications of SEPM: Carbonate Cements* SP36.
- Schulz, Heide N. and Horst D. Schulz (2005). “Large sulfur bacteria and the formation of phosphorite”. In: *Science* 307.5708, pp. 416–418. ISSN: 00368075. DOI: 10.1126/science.1103096.
- Semikhatov, Mikail A. and Maria E. Raaben (2000). “Proterozoic Stromatolite Taxonomy and Biostratigraphy”. In: *Microbial Sediments*. Ed. by Robert Riding and Stanley Awramik. Berlin Heidelberg: Springer.
- Seong-Joo, Lee, Kathleen M Browne, and Stjepko Golubic (2000). “On Stromatolite Lamination”. In: *Microbial Sediments*. Ed. by Robert Riding and Stanley Awramik. Berlin: Springer-Verlag, pp. 16–24.
- Sepkoski, J. J. (1982). “Flat-pebble conglomerates, storm deposits, and the Cambrian bottom fauna”. In: *Cyclic and event stratification*. Ed. by G. Einsele and A. Seilacher. Springer-Verlag. Chap. Part IIA: pp. 371–385.
- Sheldon, R. P. (1981). “Ancient marine phosphorites.” In: *Annual review of earth and planetary sciences*. Vol. 9, pp. 251–284. DOI: 10.1146/annurev.ea.09.050181.001343.
- Shiraishi, Fumito et al. (2019). “Potential photosynthetic impact on phosphate stromatolite formation after the Marinoan glaciation: Paleooceanographic implications”. In: *Sedimentary Geology* 380, pp. 65–82. ISSN: 00370738. DOI: 10.1016/j.sedgeo.2018.11.014. URL: <https://doi.org/10.1016/j.sedgeo.2018.11.014>.
- Simonson, Bruce M. and Karen E. Carney (1999). “Roll-up structures: Evidence of in situ microbial mats in late Archean deep shelf environments”. In: *Palaios* 14.1, pp. 13–24. ISSN: 08831351. DOI: 10.2307/3515358.

- Sisodia, M. S. and D. S. Chauhan (1990). “The influence of magnesium ions during the formation of stromatolitic phosphorites of Udaipur, Rajasthan, India”. In: *Geological Society Special Publication* 52.52, pp. 313–320. ISSN: 03058719. DOI: 10.1144/GSL.SP.1990.052.01.23.
- Slomp, Caroline P. et al. (1996). “A key role for iron-bound phosphorus in authigenic apatite formation in North Atlantic continental platform sediments”. In: *Journal of Marine Research* 54.6, pp. 1179–1205. ISSN: 00222402. DOI: 10.1357/0022240963213745.
- Soudry, David (2000). “Microbial Phosphate Sediment”. In: *Microbial Sediments*. Ed. by Stanley M Awramik and Robert E Riding. 1st ed. Berlin Heidelberg: Springer-Verlag, pp. 127–136. ISBN: 9783642082757.
- Southgate, P. N. (1980). “Cambrian stromatolitic phosphorites from the Georgina Basin, Australia”. In: *Nature* 285.5764, pp. 395–397. ISSN: 00280836. DOI: 10.1038/285395a0.
- Truche, Laurent et al. (2010). “Kinetics of pyrite to pyrrhotite reduction by hydrogen in calcite buffered solutions between 90 and 180°C: Implications for nuclear waste disposal”. In: *Geochimica et Cosmochimica Acta* 74.10, pp. 2894–2914. ISSN: 00167037. DOI: 10.1016/j.gca.2010.02.027. URL: <http://dx.doi.org/10.1016/j.gca.2010.02.027>.
- Uhlein, Gabriel J. et al. (2019). “Ediacaran paleoenvironmental changes recorded in the mixed carbonate-siliciclastic Bambuí Basin, Brazil”. In: *Palaeogeography, Palaeoclimatology, Palaeoecology* 517. December 2018, pp. 39–51. ISSN: 00310182. DOI: 10.1016/j.palaeo.2018.12.022. URL: <https://doi.org/10.1016/j.palaeo.2018.12.022>.
- Vieira, L. C. et al. (2015). “Aragonite Crystal Fans In Neoproterozoic Cap Carbonates: A Case Study From Brazil and Implications For the Post-Snowball Earth Coastal Environment”. In: *Journal of Sedimentary Research* 85.3, pp. 285–300. ISSN: 1527-1404. DOI: 10.2110/j.sr.2015.21.
- Vieira, Lucieth Cruz et al. (2007). “A Formação Sete Lagoas em sua área-tipo: fácies, estratigrafia e sistemas deposicionais”. In: *Revista Brasileira de Geociências* 37.4S, pp. 1–14. DOI: 10.25249/0375-7536.200737s4114.
- Visscher, Pletter T. et al. (1998). “Formation of lithified micritic laminae in modern marine stromatolites (Bahamas): The role of sulfur cycling”. In: *American Mineralogist* 83.11-12 PART 2, pp. 1482–1493. ISSN: 0003004X. DOI: 10.2138/am-1997-11-1236.
- Wacey, David et al. (2019). “1 Billion-Year-Old Cell Contents Preserved in Monazite and Xenotime”. In: *Scientific Reports* 9.1, pp. 1–8. ISSN: 20452322. DOI: 10.1038/s41598-019-45575-4.
- Warren, L. V. et al. (2014). “The puzzle assembled: Ediacaran guide fossil Cloudina reveals an old proto-Gondwana seaway”. In: *Geology* 42.5, pp. 391–394. ISSN: 19432682. DOI: 10.1130/G35304.1.

Xiao, Shuhai and Marc Laflamme (2009). “On the eve of animal radiation: phylogeny, ecology and evolution of the Ediacara biota”. In: *Trends in Ecology and Evolution* 24.1, pp. 31–40. ISSN: 01695347. DOI: 10.1016/j.tree.2008.07.015.

Xiao, Shuhai, Yun Zhang, and Andrew H. Knoll (1998). “Three-dimensional preservation of algae and animal embryos in a neoproterozoic phosphorite”. In: *Nature* 391.6667, pp. 553–558. ISSN: 00280836. DOI: 10.1038/35318.

## 2.9 Figures and tables

Table 2.1: See Appendix A for Table 2.1 and caption.

Table 2.2: See Appendix A for Table 2.2 and caption.

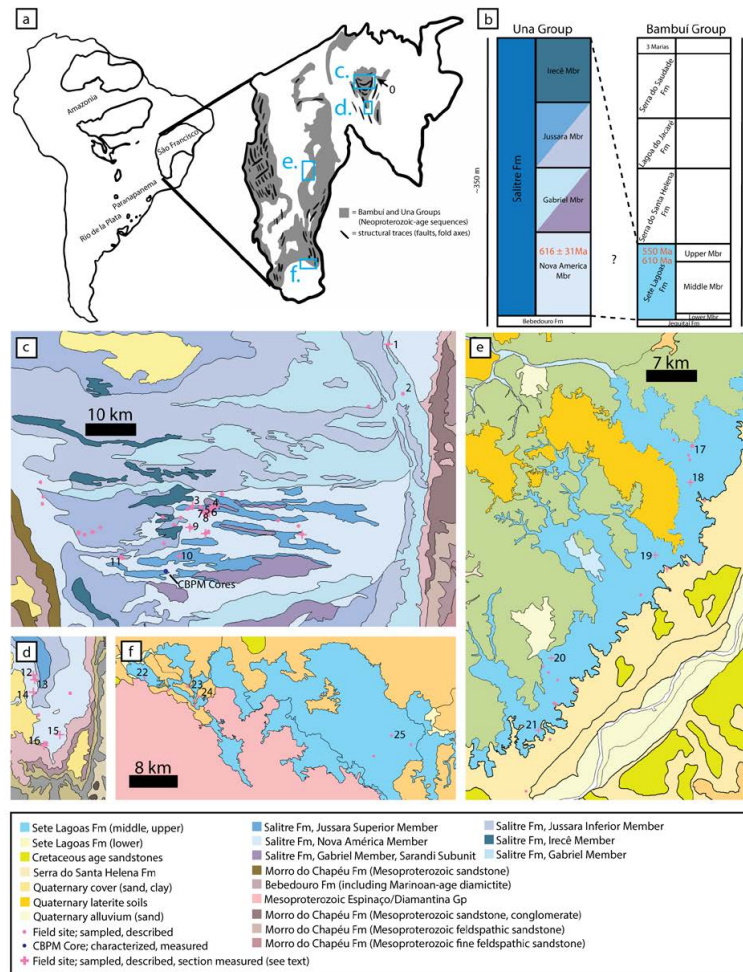


Figure 2.1: Geographic position and regional geologic context for Salitre and Sete Lagoas formations. (a) Location of São Francisco Craton and remnants of adjacent cratons on the South American continent (modified after Umberto G. Cordani and Sato, 1999), as well as distribution of Ediacaran and late Cryogenian lithostratigraphic units. Map of São Francisco Craton modified after Reis, Suss, et al., 2017 and Alkmim and Marcelo A. Martins-Neto, 2012. Blue rectangles represent the locations of the more magnified insets in (c-e). 0 corresponds to Localidade 0 (*Fazenda Arrecife*, Table 1). (b) Lithostratigraphic units relevant to this study and their putative stratigraphic correlation, with absolute age constraints in red. (c) Northern Irecê paleobasin. Field sites for this study are marked by pink circles and crosses, and those locations discussed in the text are numbered in black (Table 1). (d) Southern Irecê paleobasin (near Iraquara, MG, Brazil). Scale is the same as (c). (e) Januária area (near Cavernas do Peruçu National Park, MG, Brazil). (f) Sete Lagoas area. Maps are modified after those published by the Geologic Survey of Brazil or CPRM (Dalton de Souza et al., 2003; Fonseca et al., 2014).

Depositional Facies Model:  
High-Energy, Wave-Swept, Subtidal Zone Carbonate Platform

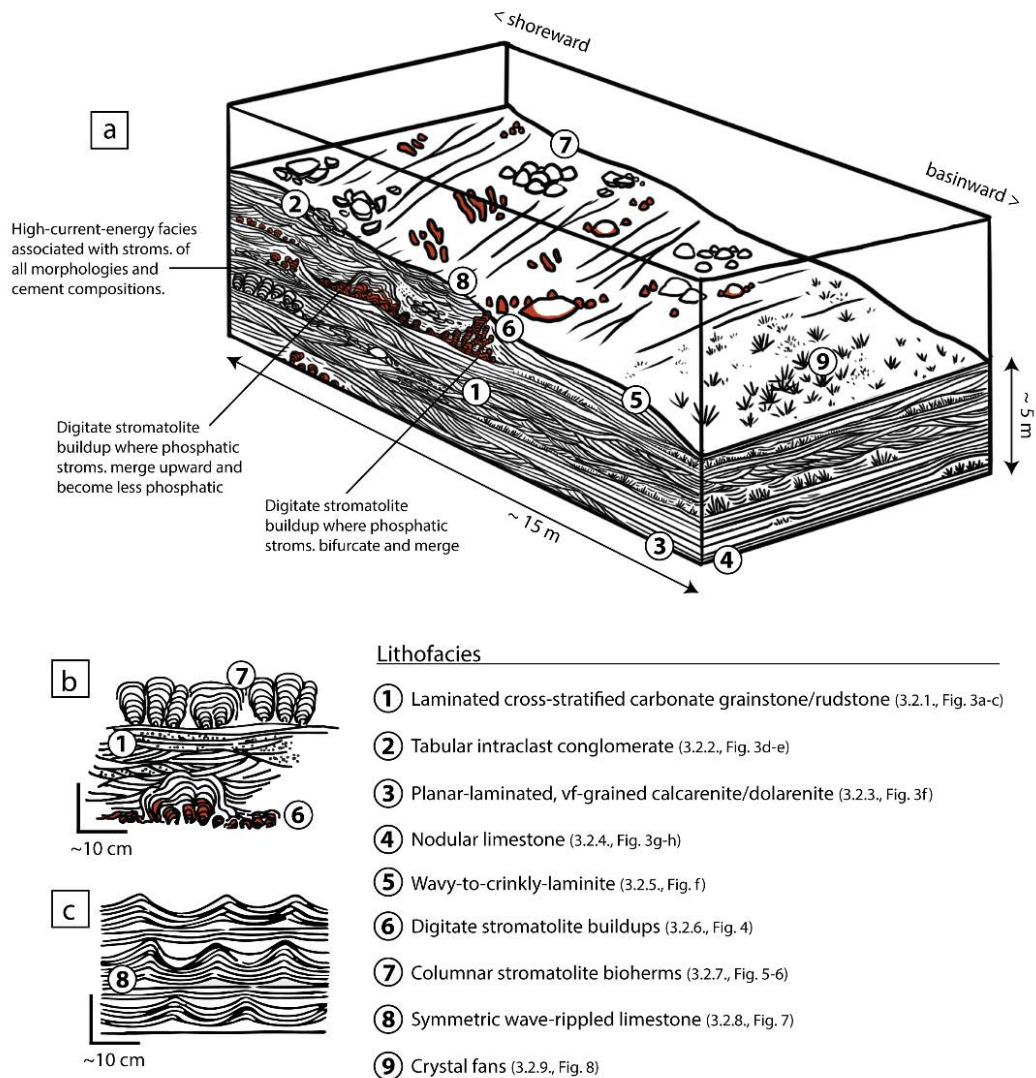


Figure 2.2: Depositional facies model illustration, featuring 9 distinct lithofacies and their spatial relationships. (a) Illustration of depositional settings for 9 identified lithofacies. Red color denotes authigenic or early diagenetic CFA cements. (b) Illustration of phosphatic (CFA-cemented) and non-phosphatic (carbonate-cemented) textures, as they occur in study area: associated with laminated cross-stratified carbonate grainstone/rudstone. (c) Illustration of symmetric wave-rippled limestone lithofacies.

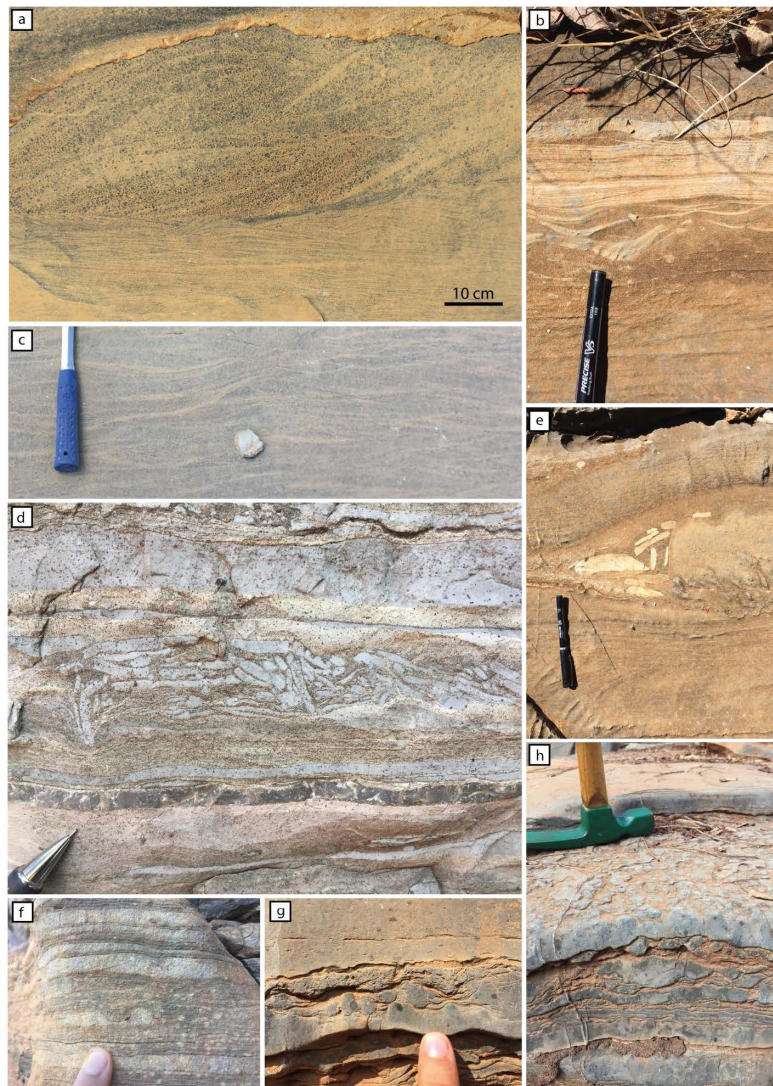


Figure 2.3: Lithofacies of the Salitre and Sete Lagoas formations. (a-c) Lithofacies 1, laminated cross-stratified carbonate grainstone/rudstone. (d-e) Lithofacies 2, tabular intraclast conglomerate. (f) Lithofacies 3, planar laminated very fine-grained limestone/dolostone, interbedded with examples of Lithofacies 4, nodular limestone, and Lithofacies 5, crinkly laminite. (g-h) Lithofacies 4, nodular limestone, interbedded with Lithofacies 5, crinkly laminite. | (a) Laminated, cross-stratified carbonate grainstone, preserving possible asymmetric wave ripples, climbing ripples, and troughs. Section broadly coarsens upward, with the coarsest intervals being replete with ooids and aggregate grains (e.g., grapestones). Salitre Fm, Locality 4 (Fig. 1c), Io 4. (b) Finer-grained lenses within laminated, cross-stratified grainstones. Salitre Fm, Locality 11 (Fig. 1c), Vila Morro Grande. (c) Irregular trough cross-stratification. Salitre Formation, Locality 4 (Fig. 1c), Io 4. (Caption continues on next page.)

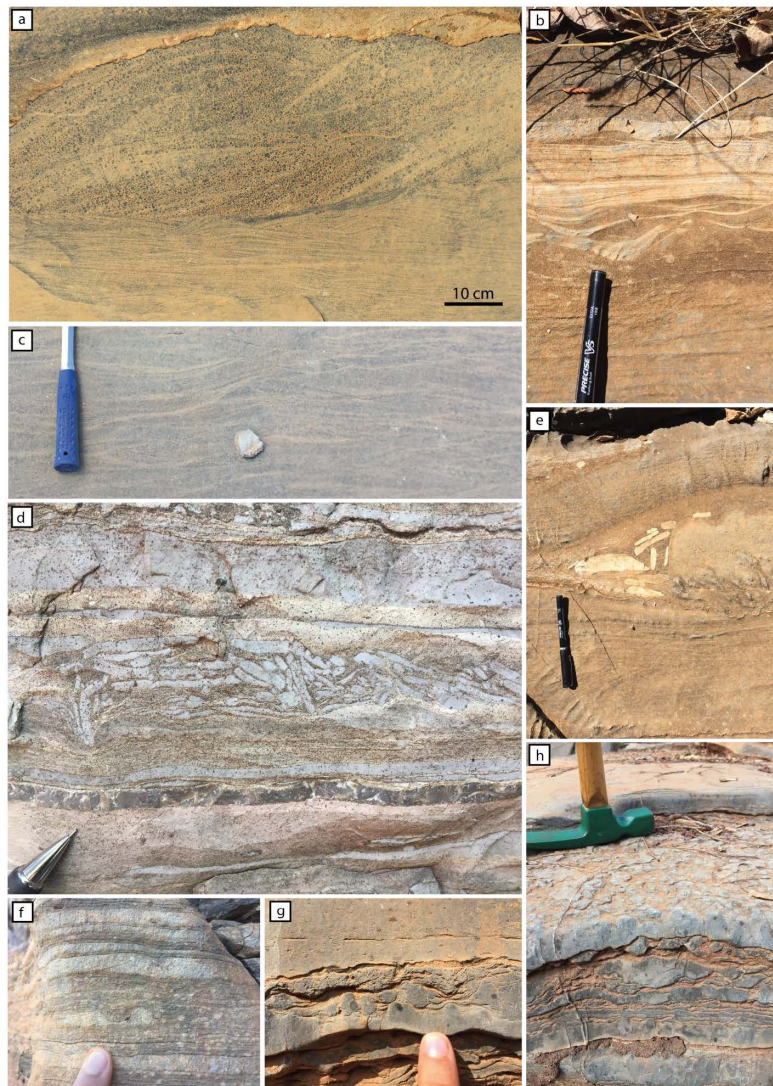


Figure 2.4: Continued from previous page... (d) Tabular intraclast conglomerate below and among cross-stratified grainstone. Salitre Fm, Locality 15 (Fig. 1d), Cabbage Patch. (e) Intraclast conglomerate among cross-stratified, oolitic dolostone, where pebble- and cobble-scale intraclasts abut a boulder. Salitre Fm, Locality 11 (Fig. 1c), Vila Morro Grande. (f) Crinkly and undulating beds of laminated limestone. Centimeter-scale mounds near middle of image appear to be nodular hardgrounds draped by fine laminated sediment. Salitre Fm, Locality 14 (Fig. 1d), Coxinha Antiga. (g) Nodular limestone, where cohesive mounds are draped by fine sediment. Salitre Fm, Locality 19 (Fig. 1e), Levinópolis. (h) Nodular limestone over fine, planar laminated limestone, with bedding plane visible. Sete Lagoas Fm, Locality 19 (Fig. 1e), Levinópolis. Note: finger is 1.5 centimeter wide, pen is 1 centimeter wide and 11 centimeter long, hammer handles are 4-5 centimeter wide. Otherwise, scale is indicated in the frame.

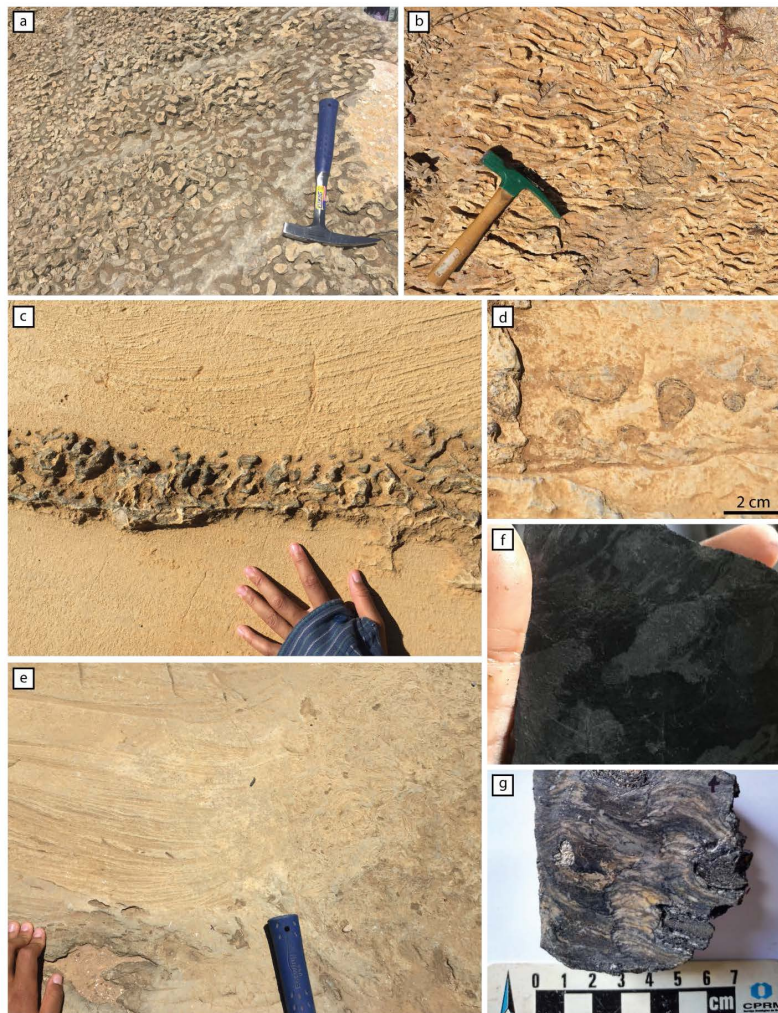


Figure 2.5: Digitate stromatolite-bearing lithofacies of the Salitre Formation (Lithofacies 6). (a) Bedding-plane view of phosphatic digitate stromatolite biostrome, showing merging and dividing growth habit. This biostrome is between 1 and 2 meters thick with a lateral extent of perhaps 10 meters. Locality 3 (Fig. 1c), Fazenda Nova Canãa. (b) Bedding-plane view of phosphatic digitate stromatolite biostrome of similar dimension to (a), showing elongation of stromatolites. Locality 9 (Fig. 1c), Lonely Road. (c) Digitate stromatolite biostrome in Locality 7 (Fig. 1c), Cerberus. This biostrome was perhaps 20 meters in lateral extent with vertical thickness that varied between 1 and 20 centimeters. Stromatolites are predominately composed of CFA, though there is sometimes some late, patchy silicification, while contemporaneous and vertically bounding cross-stratified grainstones are dolomite. (Caption continues on next page.)

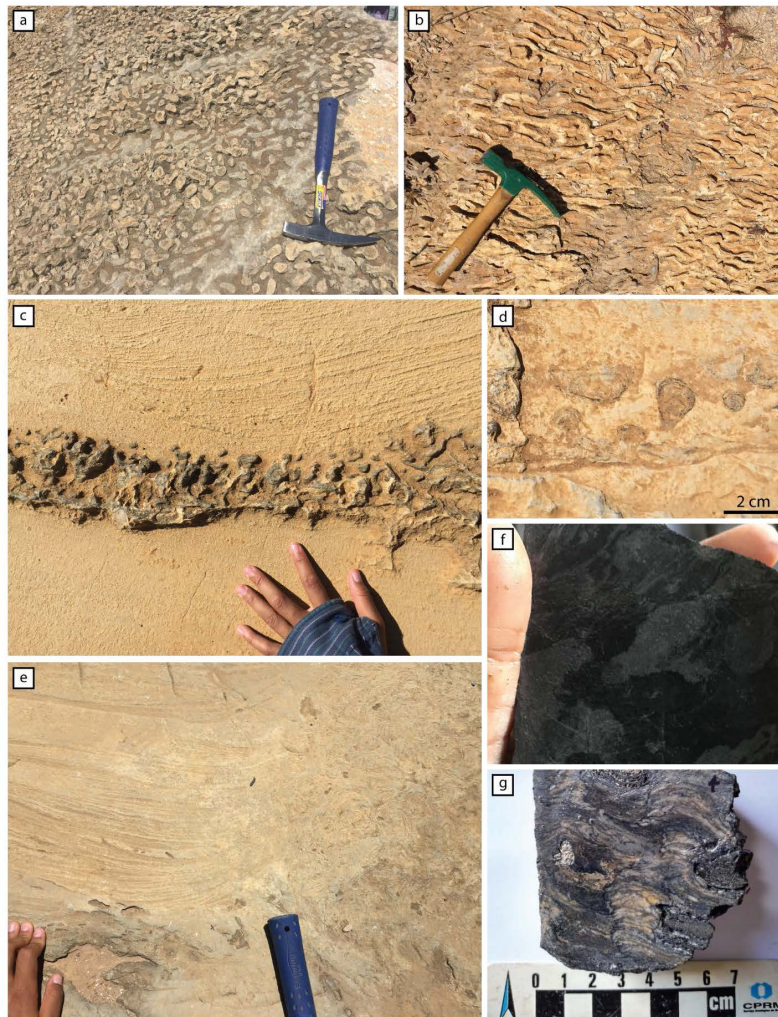


Figure 2.6: Continued from previous page. (d) Incipient digitate stromatolites from the same interval photographed in (c). (e) Stromatolite mound at Locality 5 (Fig. 1c), Aristeia, where phosphatic digitate stromatolites merge over several decimeters of growth to form laminated, but internally disordered and irregular, mounds. Also pictured is cross-stratified grainstone onlapping the stromatolitic mound. (f) Cut face of a hand sample from a depth of 33.3 meters in CBPM Core 010 (Fig. 1c). Darkest gray/black regions are finely laminated digitate stromatolites in oblique cross section, and intraclasts thereof. Lightest gray regions are the very fine matrix of recrystallized and micritized, but originally well-rounded, well-sorted, calcite grains against which the stromatolites grew. (g) Cut face of a hand sample from a depth of 8.6 meters in CBPM Core 011 (Fig. 1c). Mottled dark grey and light gray regions are finely laminated limestone, while pale orange and tan regions are mostly CFA. Note: finger is 1.5 centimeters wide, pen is 1 centimeter wide and 11 centimeter long, hammer handles are 4-5 centimeter wide. Otherwise, scale is indicated in the frame.



Figure 2.7: Domal and columnar stromatolite bioherm (Lithofacies 7) and associated grainstone facies (Lithofacies 1) in the Salitre and Sete Lagoas formations. (a) Photograph of a columnar stromatolite bioherm. The bioherm appears to have had at least half a meter of synoptic relief on the seafloor during its growth, with a maximum diameter approaching 6 meters. Stromatolites near the center of the bioherm appear more stratiform, while they are more distinctly columnar and elongate near the margins. Locality 0 (Fig. 1a), Fazenda Arrecife. (b) Plan view of two adjacent stromatolite bioherms at Locality 0 (Fig. 1a). In this locality, bioherms have elliptical footprints with 0.8-3.6 m semi-minor axes and 1.3-6.3 m semi-major axes (based on a survey of 25 such bioherms over an area of  $1e4m^2$ ). Bioherms universally appear to have 10-30 centimeter-thick laminated “carapaces” or envelopes of roughly even width around their entire perimeter. Stromatolites within bioherms are closely, polygonally packed, with stromatolites near these envelopes being the most elongate. Channels between bioherms are filled variously with tabular intraclast conglomerate, medium-to-coarse grainstones with abundant cross-stratification. Bioherm carapaces are picked out in white. Measuring tape in frame shows 0.7 m. (Caption continues on next page.)



Figure 2.8: Continued from previous page. (c) Red arrows indicate thin layers of very coarse lime grainstone, partially silicified, within finer laminated sediments on the margins of one of the stromatolite bioherm. Locality 0 (Fig. 1c), Fazenda Arrecife. The grainstones pictured here contain primary phosphatic intraclasts, with roughly 5% of all intraclasts/reworked grains being phosphatic (CFA) and 95% being calcitic. (d) Calcitic digitate stromatolites merged into a disordered/irregular stromatolite mass (bottom third of image), gradually merging to form a domal stromatolite with 7-10 centimeter of synoptic relief. (Boundaries between irregular/disordered mass and large, domal stromatolite are picked out in white.) The darkest region (top third of image) is comprised of medium-to-coarse, oolitic lime grainstone, featuring abundant 5-40 centimeter cross-sets describing assymmetric wave ripples and some possible swaley cross-stratification. São Francisco Riverbank Locality (Table 1). Card is 9 centimeters tall and 4.5 centimeter wide. Hammer handles are 4-5 centimeter wide. Otherwise, scale is indicated in the frame.

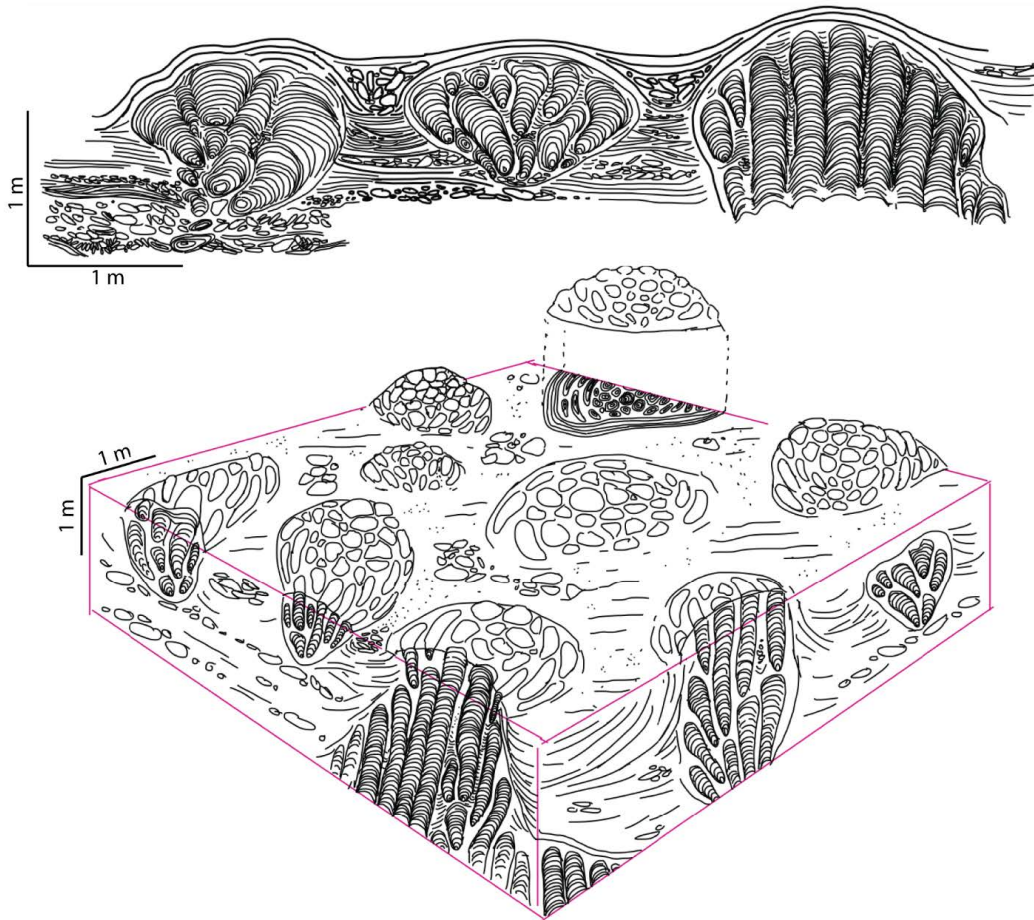


Figure 2.9: Illustrations of columnar stromatolite bioherms and associated intra-clast conglomerate and cross-stratified lime grainstone, depicted in plan view and bedding-perpendicular cross sections. Upper illustration represents sketches from an outcrop in Locality 0 (Fig. 1a, Table 1), Fazenda Arrecife. Lower illustration is a schematic representation of the facies (based on a survey of 25 bioherms over an area of  $1e4m^2$ ).

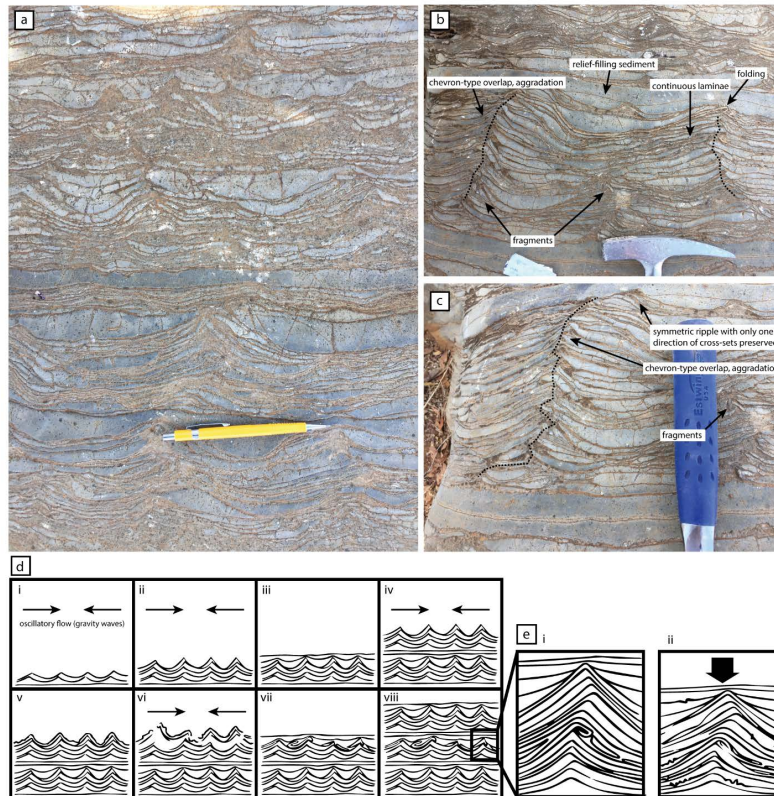


Figure 2.10: Annotated field photographs and depositional model for symmetric wave-rippled limestone (Lithofacies 8). (a) Wave-rippled limestone. Salitre Formation, Locality 6, Fazenda Catavento. Pencil is 13 centimeter length, <1 centimeter width. (b) Wave-rippled limestone in same location as (a). Dotted lines indicate location of ripple crests for a 20-centimeter-scale interval of vertical section. (c) Wave-rippled limestone in same location as (a-b). Hammer handle is 5 centimeter wide and 15 centimeters long. (d) Depositional model for wave-rippled limestone lithofacies: (i) Oscillatory flow in high-energy, shallow platform environment organizes sediment into symmetric ripples. (ii) Variations in carbonate sediment supply and flow energy result in chevron-style overlapping of laminae, with ripple crest location migrating back and forth. Ripple crests may be stabilized by early cementation. (iii) Period of lower-energy flow and high sediment supply fills ripple troughs, dampens relief. (Continues on next page.)

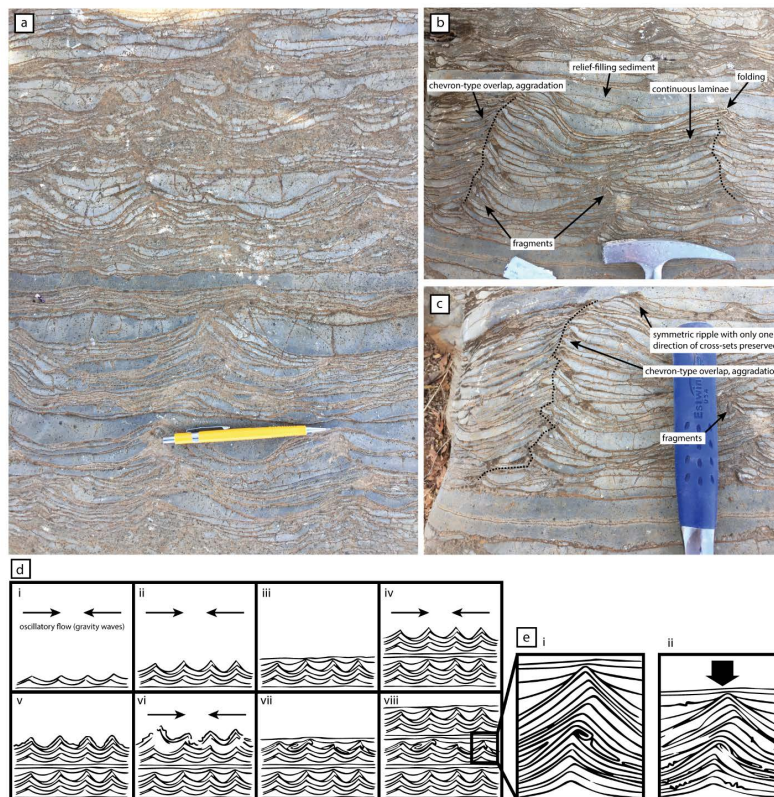


Figure 2.11: Continued from previous page. (iv) Another generation of symmetric ripple formation. (v) Period of lower-energy flow and low sediment supply allows colonization of seafloor locally by microbial mats or biofilms. These biofilms stabilize the morphology of the ripple crests and may contribute locally to partial cementation of uppermost laminae. (vi) Resumption of higher-energy oscillatory flow disrupts and fragments laminae that are partially cemented or otherwise stabilized by mats. (vii) Period of lower-energy flow allows fragments to settle, being redeposited over cemented, stabilized ripple structures. Sediment fills troughs and dampens relief of ripple structures. (viii) Cycle repeats. (e) Inset from (d)(viii), demonstrating the effect of compaction (force indicated by black arrow) and later pressure solution on the appearance of ripples' internal structure: suturing of laminae boundaries, loss of definition of individual laminae, variation in laminae thickness, and stylolites.

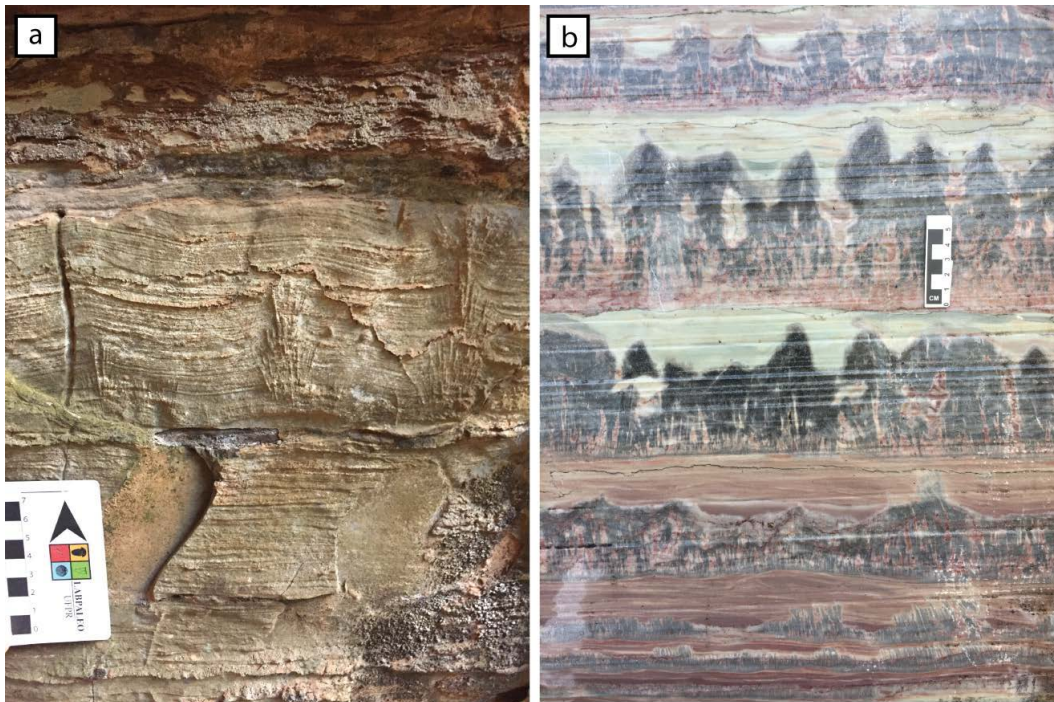


Figure 2.12: Calcite pseudomorphs after aragonite crystal fans (Lithofacies 9) among planar-laminated and asymmetric ripple cross-stratified mudstone to very fine grainstone (Lithofacies 1 and 3). (a) Semi-isolated fans at Locality 17, Gruto do Janelão. (b) Laterally extensive (10s of meters) beds of crystal fans at Locality 22, Riacho do Campo.

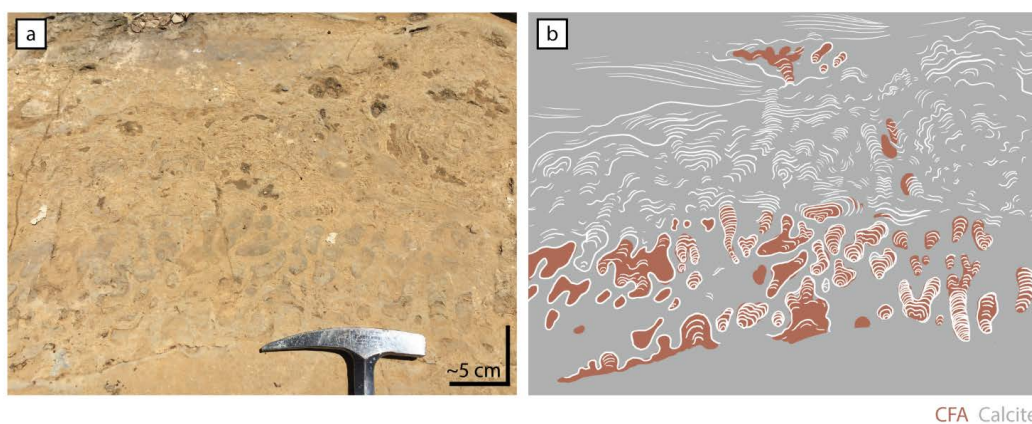


Figure 2.13: Stromatolite bioherm comprised of both phosphatic digitate stromatolites and merged, irregular calcitic stromatolites. Locality 5 (Fig. 1c, Table 1), Aristeia. (a) Outcrop photo. (b) Annotation of (a), where laminae are traced in white. Carbonate fluorapatite (CFA) cements are shaded in red. Calcite cements are shaded in gray. Grains are calcitic peloids and ooids. More isolated digitate stromatolites branch and merge upsection, transitioning into bioherm with centimeters to decimeters of synoptic relief. Cross-stratified oolitic grainstone (Lithofacies 1) forms the initiation surface of the bioherm, onlapping it upsection.



Feature	Depositional	At Seafloor	Early Authigenic, Shallow Burial	Later Diagenetic, Deep Burial	Deepest Burial	Latest Diagenetic
Carbonate sedimentation > ooids/grapestones > peloids	██████████ ██████████					
Trapping and binding by biofilms, mats	██████████					
Aragonite crystal fans <sup>1</sup>		██████████				
Calcite, aragonite, and CFA <sup>2</sup> cements		██████████	██████████			
Reworking textures	██████████					
Fe(II) sulfides (pyrite, pyrrhotite)		██████████	██████████		██████████	
Calcite micrite		██████████	██████████	██████████		
Recrystallization textures; anhedral interlocking calcite mosaic			██████████	██████████		
Zoned euhedral dolomite			██████████	██████████		
Fe(III)-(oxy)hydroxides, oxides			██████████	██████████		██████████
Compaction, pressure solution features			██████████	██████████	██████████	
Replacive dolomite (granular, anhedral to subhedral spar)			██████████	██████████	██████████	
Replacive silica			██████████	██████████		
Horsetail stylolites, Fe(III)-oxide associated				██████████	██████████	
Replacive fluorite					██████████	
Tectonic fractures					██████████	██████████
Sparry fracture fill (calcite, quartz)						██████████
Displacive and replacive MVT deposits; sphalerite, galena, stratiform pyrite etc.					██████████	██████████

Figure 2.15: Generalized timing of mineral phases and fabrics observed in the Salitre and Sete Lagoas formations. Time proceeds from left to right: earliest textures related to the depositional environments are farthest left, and features of latest diagenesis are farthest right. <sup>1</sup>Feature observed only in the Sete Lagoas Formation. <sup>2</sup>Feature observed only in the Salitre Formation. Pale gray features are considered “later diagenetic,” and therefore not directly relevant to the processes of authigenic and early diagenetic phosphogenesis.

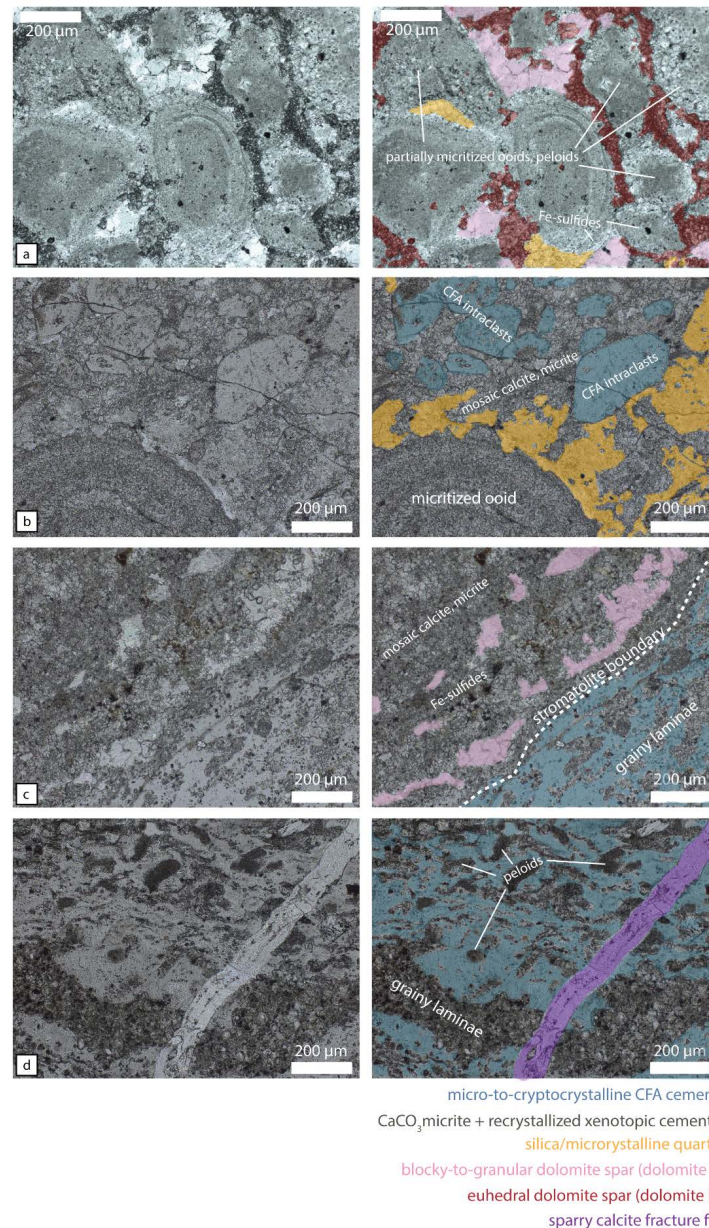


Figure 2.16: Thin section photomicrographs, taken in plane-polarized light, capturing representative microtextures within grainstone/rudstone and digitate stromatolite facies of the Salitre Formation. Images at right are annotated versions of images at left. Colors, as indicated in the key, represent different diagenetic phases: blue = micro-to-cryptocrystalline CFA, colorless/gray =  $\text{CaCO}_3$  micrite and recrystallized xenotopic cements, orange = replacive silica/microcrystalline quartz cements pink = blocky-to-granular dolomite spar filling early porosity (Dolomite I), red = euhedral to subhedral dolomite spar nucleating at primary grain boundaries (Dolomite II), and purple = fracture-filling calcite spar. (Continues on next page.)

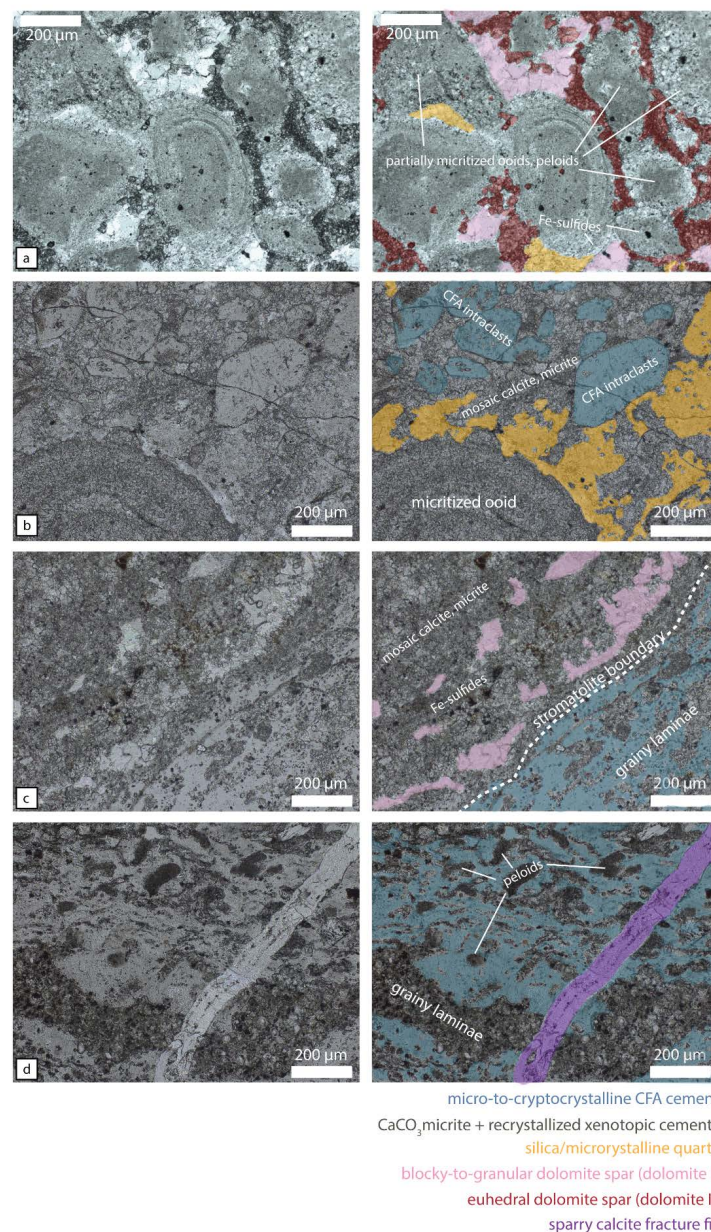


Figure 2.17: Continued from previous page... (a) Ooids and peloids from grainstone facies, Locality 4 (Fig. 1c, Table 1). (b) Grainy inter-stromatolite fill from Locality 0 (Table 1), with CFA intraclasts, ooids, and peloids. (c) Left-hand flank of a phosphatic digitate stromatolite from Locality 5 (Fig. 1c, Table 1). (d) Laminae of a phosphatic digitate stromatolite from CBPM Core 011 (Fig. 1c), cross-cut by a fracture filled with calcite spar.

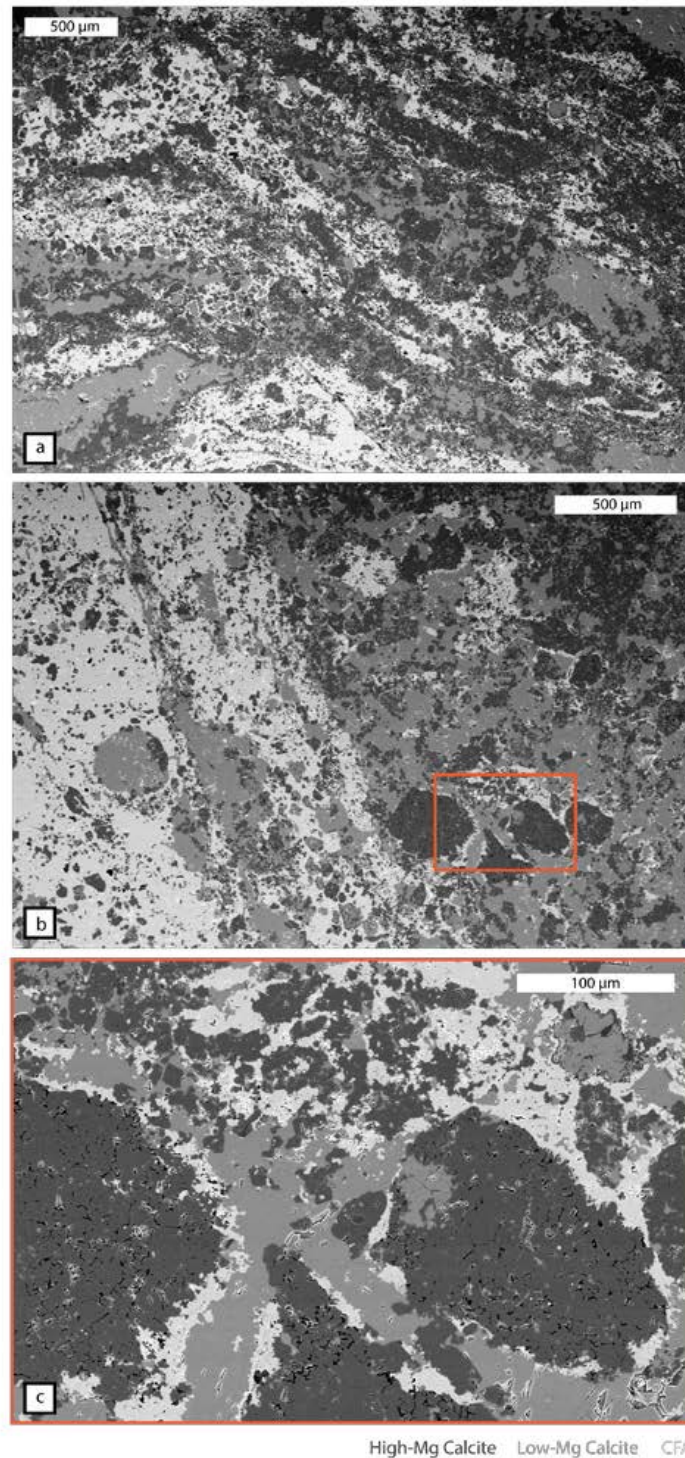


Figure 2.18: Back-scattered electron (BSE) images of a phosphatic digitate stromatolite from Locality 5 (Fig. 1c, Table 1), where white/lightest gray indicates CFA, medium gray indicates low-Mg calcite, and dark gray indicates high-Mg calcite. (a) A view of the CFA- and calcite-cemented laminae near core of stromatolite. (b) Margin of the same stromatolite as (a), where the contact between stromatolite and associated crinkly laminite is defined by the transition from CFA cement to calcite cement. (c) Higher-magnification view of the area indicated by the orange box in (b), emphasizing the rim of isopachous CFA cement around rounded calcite grains near the stromatolite margin.

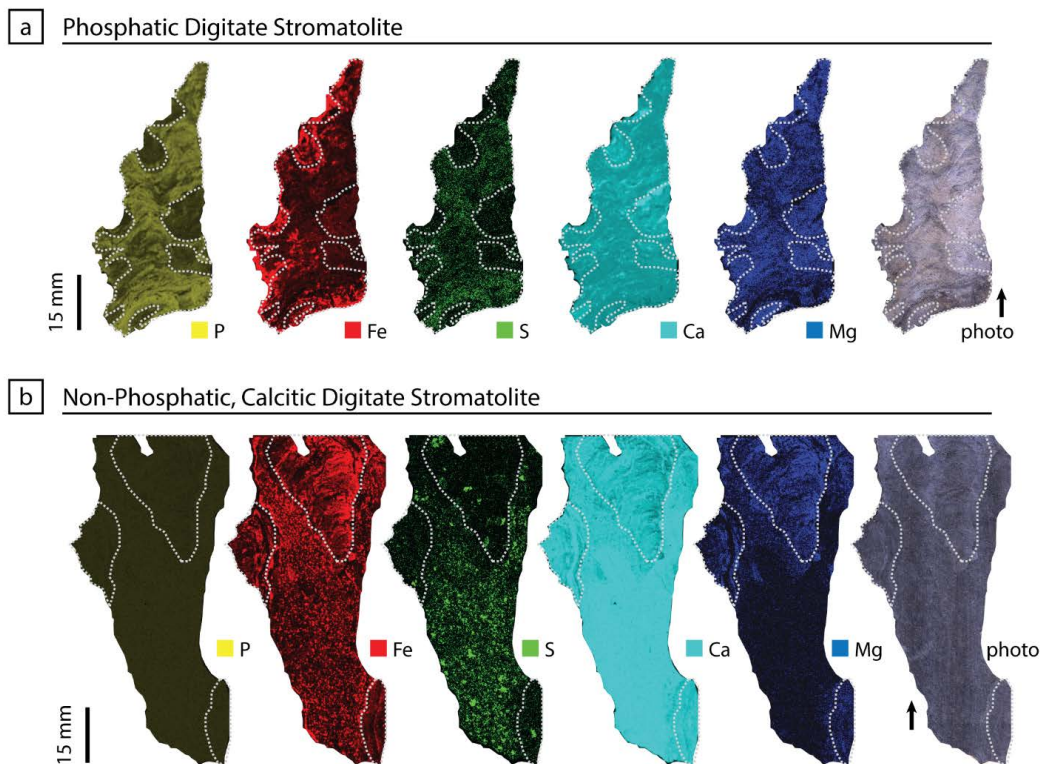


Figure 2.19: XRF images of cut, unpolished slabs of phosphatic and non-phosphatic digitate stromatolites of the Salitre Fm, where specified colors indicate fluorescence intensity of P, Fe, S, Ca, and Mg (from left to right). Far right images are reflected white light photographs. Dotted lines demarcate boundary between stromatolites and grainy interstromatolite fill. Arrows indicate stratigraphic up. (a) Branching and merging digitate stromatolites from Locality 5 (Fig. 1c, Table 1). (b) Digitate stromatolites from CBPM Core 011 (Fig. 1c).

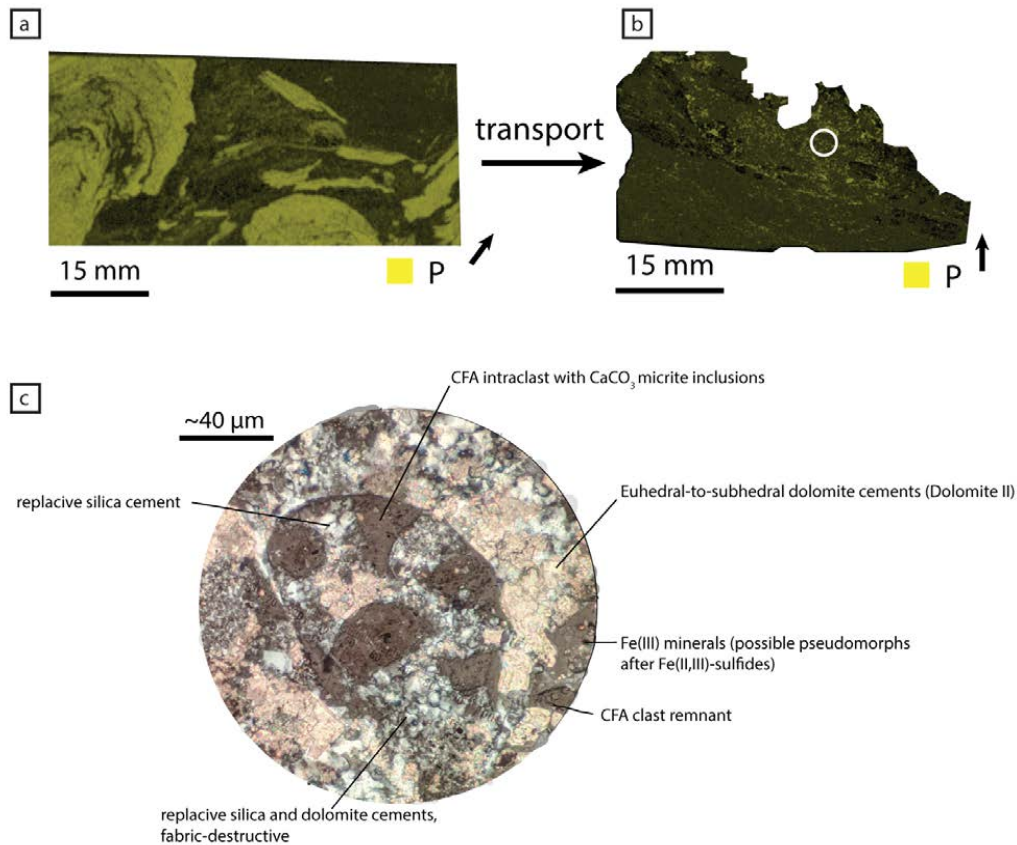


Figure 2.20: Early-to-mid-stage diagenesis of phosphatic textures. Small arrows indicate stratigraphic up. (a) XRF image of cut, unpolished slab from CBPM Core 011 (Fig. 1c), featuring phosphatic digitate stromatolites and phosphatic intraclasts derived from said stromatolites near margin of stromatolitic buildup (Lithofacies 6). Color yellow indicates fluorescence intensity of P. (b) XRF image of cut, unpolished slab from Locality 0 (Fig. 1a, Table 1), featuring phosphatic intraclasts within carbonate grainstone facies near margins of columnar and digitate stromatolite buildups. Such intraclasts are interpreted as more distally and/or energetically transported derivatives of intraclasts like those pictured in (a). (c) Annotated thin section photomicrograph from within the white circled area in (b), featuring an altered phosphatic intraclast. This is a representative example of the extent of fabric-destructive diagenesis of phosphatic facies observed within the Salitre Fm.

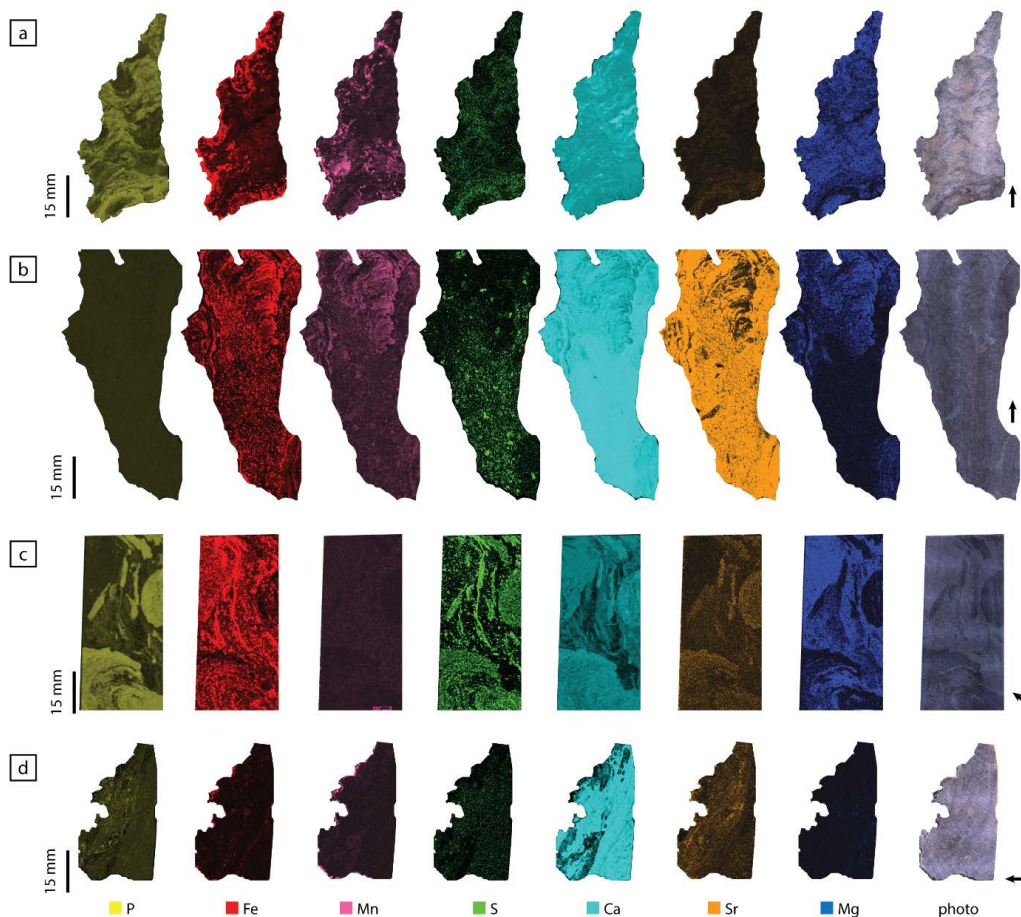


Figure 2.21: X-ray fluorescence (XRF) images of cut, unpolished slabs of phosphatic and non-phosphatic textures of the Salitre Fm, where specified colors indicate fluorescence intensity of the indicated elements. Far right images are reflected white light photographs. Dotted lines demarcate boundaries between stromatolites and grainy, interstromatolite fill. Arrows indicate stratigraphic up. (a) Branching and merging digitate stromatolites from Locality 5 (Fig. 1c, Table 1). (b) Digitate stromatolites from CBPM Core 011 (Fig. 1c). (c) Phosphatic digitate stromatolites and phosphatic intraclasts derived from said stromatolites near margin of stromatolitic buildup (Lithofacies 6). Billet from CBPM Core 011 (Fig. 1c). (d) Calcitic, dolomitic, and phosphatic intraclasts within carbonate grainstone facies near margins of columnar and digitate stromatolite buildups. Locality 0 (Fig. 1a, Table 1).

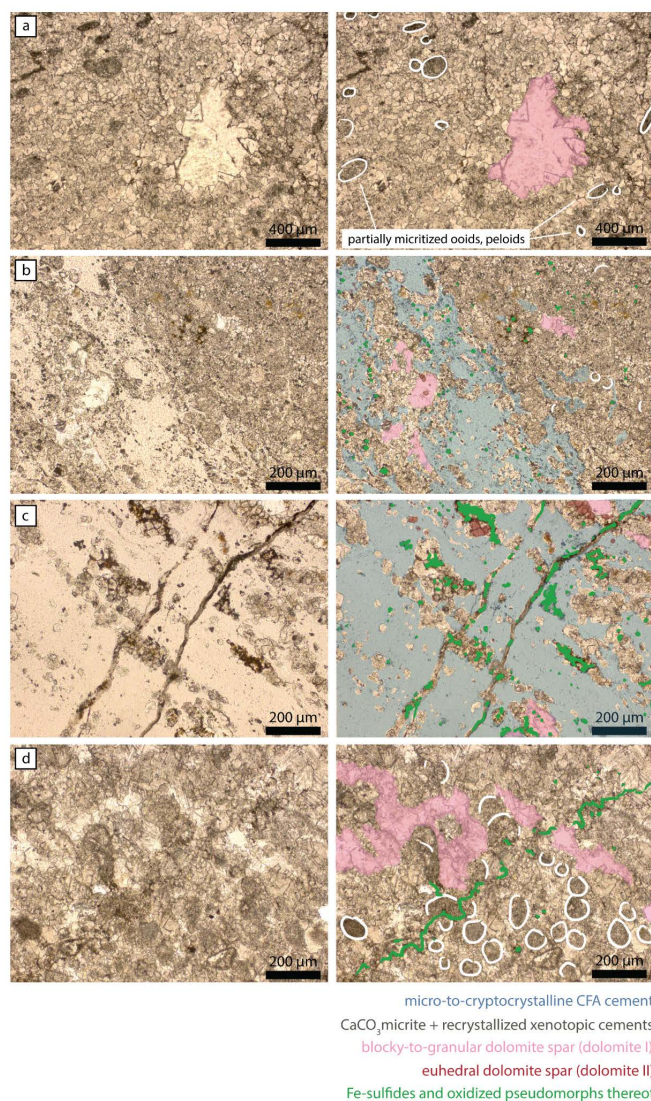


Figure 2.22: Thin section photomicrographs, taken in plane-polarized light, capturing representative microtextures within grainstone/rudstone and digitate stromatolite facies of the Salitre Formation. Images at right are annotated versions of images at left. White outlines highlight primary grain boundaries. Colors, as indicated in the key, represent different diagenetic phases: pink = blocky-to-granular dolomite spar, green = Fe-sulfides and oxidized pseudomorphs thereof, blue = CFA, and colorless/tan = CaCO<sub>3</sub> micrite and recrystallized xenotopic cements. (a) Grainy inter-stromatolite fill from Locality 5 (Fig. 1c, Table 1), with blocky dolomite spar filling early porosity. (b) Right-hand flank of a phosphatic digitate stromatolite from Locality 5 (Fig. 1c, Table 1). (c) Later fractures filled with calcite spar and associated with Fe-sulfides, cross-cutting phosphatic digitate stromatolite laminae, Locality 5 (Fig. 1c, Table 1). (d) Recrystallized ooid grainstone from Locality 4 (Fig. 1c, Table 1), featuring Fe-associated stylolite.

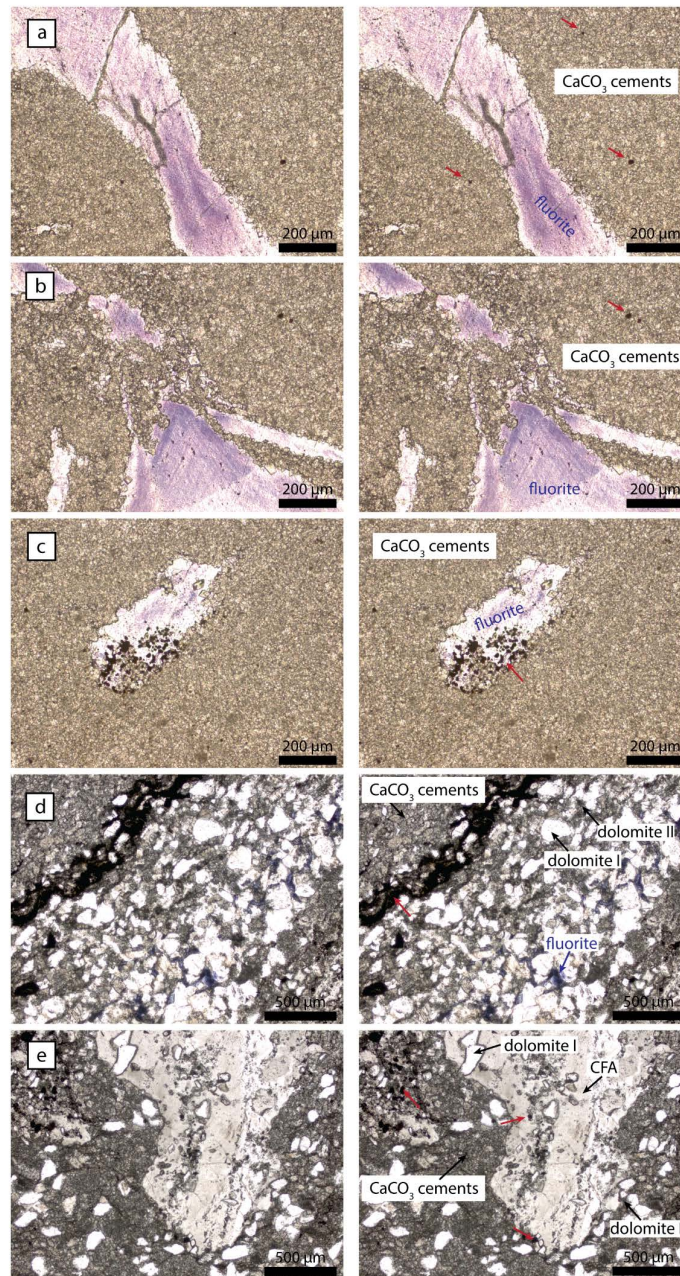


Figure 2.23: Thin section photomicrographs, taken in plane-polarized light, capturing representative examples of microtextures that exhibit features of late-stage hydrothermal diagenesis within grainstone/rudstone and digitate stromatolite facies of the Salitre Formation. Images at right are annotated versions of images at left. Red arrows indicate examples of Fe-sulfides and oxidized pseudomorphs thereof. (a-c) Replacive fluorite among recrystallized and partially dolomitized sparry cements, showing spatial relationships to Fe-sulfide minerals. Sample from Core 011 (Fig. 1c). (Continues on next page.)

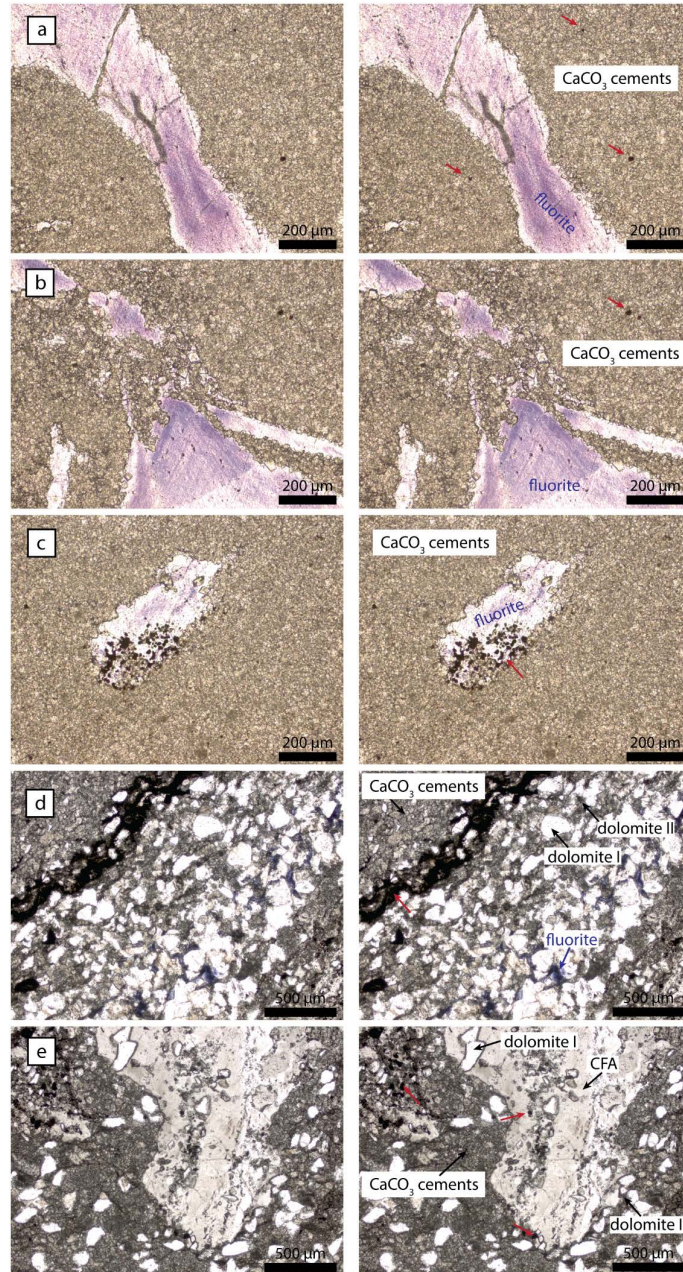


Figure 2.24: Continued from previous page. (d) Blocky dolomite spar (Dolomite I) filling early porosity within inter-stromatolite grainstone, with margins of individual crystals recrystallized to murky, more finely crystalline dolomite spar (Dolomite II). Dolomite II associated with fluorite cement, and Fe-sulfide-bearing veins. Sample from CBPM Core 010 (Fig. 1c). (e) Same microfacies shown in D from CBPM Core 010 (Fig. 1c), but showing internally laminated CFA-cemented intraclast derived from digitate stromatolite afloat in recrystallized  $CaCO_3$  cements.

*Chapter 3*

PARAGENESIS OF AN EDIACARAN  
CARBONATE-PLATFORM PHOSPHORITE: CONSTRAINTS  
FROM OPTICAL PETROGRAPHY AND TEXTURE-SPECIFIC  
CLUMPED ISOTOPE PALEOTHERMOMETRY

Cecilia B. Sanders, John C. Eiler, and John P. Grotzinger<sup>1</sup>

*... May there not come that even bolder adventurer – the first geolinguist, who, ignoring the delicate, transient lyrics of the lichen, will read beneath it the still less communicative, still more passive, wholly atemporal, cold, volcanic poetry of the rocks: each one a word spoken, how long ago, by the Earth itself, in the immense solitude, the immenser community, of space.*

— Ursula K. Leguin, *The Author of the Acacia Seeds*

### 3.1 Abstract

The Salitre Formation is comprised of several hundred meters of primarily carbonate rocks, representing sedimentation in an intracratonic foreland basin during the Ediacaran Period (c.600-550 Ma). The lowermost member of the Salitre Formation contains sedimentary phosphorite deposits, in which the dominant phosphate-bearing phase is cryptocrystalline carbonate-rich fluorapatite (CFA) cement. These CFA cements occur exclusively associated with digitate stromatolite buildups, decimeters to meters in vertical and lateral scale, which interfinger with cross-stratified grainstone. Notably, there are also non-phosphatic stromatolite buildups in close proximity to the phosphatic, in the same depositional facies. This implies that the mechanisms that control the distribution of phosphate cement development versus carbonate cement development are not driven by the location of depositional facies within the architecture of the Salitre paleobasin. Other models which could explain the distribution and style of phosphate mineralization there include: (1) differential diagenesis involving diagenetic fluids which infiltrate one lithofacies more pervasively than another to effect the replacement of primary cement mineralogies according to microtextural differences, and (2) differences in primary

---

<sup>1</sup>Division of Geological and Planetary Sciences, California Institute of Technology, Pasadena, CA 91125, USA

porewater chemistries over minute spatial scales which result in the formation of different primary cement phases. In this study, we present paired petrographic thin sections and novel measurements of  $\Delta_{47}$ ,  $\delta^{13}C_{mineral}$ , and  $\delta^{18}O_{mineral}$ . We provide a paragenetic framework for phosphatic and non-phosphatic lithofacies of the Salitre Formation which constrains the thermal and chemical alteration history of CFA, calcite, and dolomite cements. Structural carbonate in the CFA and calcite cements co-occurring in partially phosphatic digitate stromatolite buildups and adjacent carbonate grainstone generally yield similar  $\delta^{13}C_{mineral}$  values (0-5‰VPDB),  $\delta^{18}O_{mineral}$  values (-5-0‰VPDB), as well as similar  $\Delta_{47}$  temperatures (90-115°C) and calculated  $\delta^{18}O_{water}$  (10-19‰VSMOW), supporting a scenario in which CFA and calcite formed and then both recrystallized in equilibrium with the same diagenetic fluids under low water-rock ratio conditions at depth. Dolomite cements yielded similar  $\delta^{18}O_{mineral}$  values to CFA and calcite, and similar to slightly higher temperatures (85-150°C) – supporting a scenario in which dolomite cements were recrystallized in equilibrium with a different, and isotopically lighter, generation of fluids. Given the general absence of pervasive, fabric-destructive replacement is scarce, these geochemical data do not support later stage, differential diagenesis as a mechanism for controlling the distribution of phosphatic versus non-phosphatic cements. Rather, primary differences in porewater biogeochemistry seem the likeliest explanation. This is important, as it implies that the ecology of the Edicaran seafloor controlled the style and quality of mineralization observed today, and that the presence of CFA cements in these rocks represents a unique taphonomic window for select microbial communities.

### 3.2 Introduction

The formation of phosphate-enriched sedimentary deposits via authigenic or early diagenetic processes ("phosphogenesis") represents a unique taphonomic window for microbial and multicellular life, with phosphate minerals capable of preserving subcellular structures in great detail despite episodic dissolution and recrystallization over hundreds of millions of years Muscente, Hawkins, and Xiao, 2015; Xiao, Zhang, and Knoll, 1998. The particular biogeochemical and sedimentological conditions necessary to facilitate phosphogenesis are therefore of great interest to paleobiology and paleoecological reconstruction, as is the diagenetic fate of sedimentary phosphate deposits.

Phosphogenesis in the modern world is spatially restricted to environmental niches in the coastal upwelling zones of West Africa Goldhammer et al., 2010; H. N.

Schulz and H. D. Schulz, 2005; Küster-Heins et al., 2010; Compton and Bergh, 2016, Western Australia Heggie et al., 1990, Western South and Central America Arning et al., 2009; Scholz et al., 2011; Jahnke et al., 1983, and the Arabian Plate Schenau, Slomp, and De Lange, 2000. Historically, however, there have been at least ten major episodes of globally widespread phosphogenesis throughout geologic time, producing sedimentary phosphate deposits in a wide range of depositional settings Föllmi, 1996; Cook and McElhinny, 1979. One of the most extensive phosphogenetic episodes in history occurred at the Ediacaran-Cambrian boundary, a time of major climatological and ecological upheaval associated with the global rise of atmospheric oxygen Donald E. Canfield and Teske, 1996; Don E. Canfield, Poulton, and Narbonne, 2007; Fike et al., 2006 and the emergence of complex, multicellular life Xiao and Laflamme, 2009. But while oxygenation and postglacial overturn of the oceans likely increased the availability of dissolved phosphate in the water column on a global scale Laakso et al., 2020, regional and local controls on sedimentation rate and porewater chemistry are likely to have determined the actual spatial distribution and timing of phosphogenesis, and thus phosphate mineralization around organic structures.

Major Ediacaran and Lower Cambrian sedimentary phosphate deposits outcrop today in China Jiang et al., 2011; Cui et al., 2015; Schwid et al., 2020; Xiao, Zhang, and Knoll, 1998, Mongolia Anderson et al., 2017; Pruss et al., 2019; Ilyin and Ratnikova, 1981; Ilyin, Zaitsev, and Bjamba, 1986; Ilyin, 2004; Anttila, Macdonald, and Bold, 2021; Osokin and Tyzhinov, 1998, Kazakhstan Sergeev, Schopf, and Kudryavtsev, 2020, Australia Southgate, 1980, Algeria Bertrand-Sarfati et al., 1997, India Sallstedt et al., 2018; D. M. Banerjee, 1971; D M Banerjee, Basu, and Srivastava, 1980; Choudhuri, 1990, and Brazil Drummond et al., 2015; Okubo et al., 2018; Caird et al., 2017; A. Misi and J. R. Kyle, 1994; J. Richard Kyle and Aroldo Misi, 1997; Shiraishi et al., 2019; Sanders and Grotzinger, 2021, with numerous other minor deposits worldwide. In each locality, a detailed sedimentological and stratigraphic framework have been key to establishing the depositional setting in which the phosphorites formed. Furthermore, geochemical proxies for paleoredox conditions, including REE abundance Shields and Stille, 2001; Redivo, Mizusaki, and Santana, 2019; Chen et al., 2003 and sulfur isotopes Leśniak et al., 2003; Wotte et al., 2012, have allowed researchers to constrain the porewater chemistries that may have enabled phosphogenesis. Each phosphatic sedimentary assemblage provides an opportunity to better understand the range of processes that controlled phosphogenesis in a range of depositional environments – the better to understand the ways

in which phosphorites, and whatever biota they preserve, represent global versus local processes. They also provide opportunities to study how the tectonosedimentary evolution of the phosphate-bearing regions affects the preservation potential of primary textures via phosphate mineralization and related processes.

To this end, we present the results of a case study in the formation and diagenesis of phosphatic fabrics from Ediacaran phosphorites: the phosphate-bearing strata of Eastern Brazil, namely the Salitre Formation of Bahia state. A depositional facies model of the Salitre Formation, supported by sedimentological and stratigraphic data, as well as insights into the paragenetic sequence of mineral phases from optical petrography and micron-scale X-ray fluorescence mapping has been established Sanders and Grotzinger, 2021. These findings provide geologic context for this study's texture-specific measurements of  $\delta^{18}O$ ,  $\delta^{13}C$ , and  $\Delta_{47}$  of carbonate in authigenic and early diagenetic calcite, dolomite, and carbonate-rich fluorapatite (francolite, or CFA) cements. The studied cements are associated with the phosphate-bearing stromatolitic and grainstone-rudstone lithofacies. We use these data to constrain the thermal and chemical evolution of the phosphate-bearing units, and their potential for preservation of primary biogeochemical signatures.

### **3.3 Geologic and stratigraphic framework**

The São Francisco Craton forms much of Eastern Brazil, bordered by the Parapanema Block, and the Río de la Plata and Amazonian cratons Heilbron, Umberto Giuseppe Cordani, and Alkmim, 2017; M. A. Martins-Neto, Pedrosa-Soares, and Lima, 2001; Reis, Alkmim, et al., 2016. Cryogenian and Ediacaran-age rocks outcrop in its interior and along its rim, and are referred to in different regions as the Una and Bambuí groups (Fig.3.1). These rocks represent sedimentation within a Neoproterozoic intracratonic foreland basin system Alkmim and Marcelo A. Martins-Neto, 2012; Aroldo Misi, Kaufman, et al., 2007; Aroldo Misi and Veizer, 1998 developed during collision of the São Francisco and the West Congo cratons; it is contemporaneous with the Brasília and West African orogenies, the closure of the Macaúbas seaway to the southeast, and the inversion of the Paleoproterozoic-age rift deposits of the Paramirim and Pirapora corridors Alkmim, Marshak, et al., 2006; Reis, Suss, et al., 2017; Reis, Alkmim, et al., 2016. In early Cambrian time, the collision of the São Francisco Craton and the Amazonian Craton to the northwest, associated with the Rio Preto mountain belt, created a pattern of interfering fold-thrust belts that deformed the sedimentary successions of the craton interior Cruz and Alkmim, 2006; M. A. Martins-Neto, Pedrosa-Soares, and Lima, 2001. This complex tectonic

history has resulted in the current configuration of the Una and Bambuí groups: riding atop a shallowly dipping detachment fault above Archean and Paleoproterozoic basement and earlier Proterozoic metasedimentary rocks, visibly deformed by thrust faults and associated folding nearer the cratonic margins and the interior of the Irecê paleobasin Reis, Alkmim, et al., 2016.

The Una Group (Northern São Francisco Craton) and Bambuí Group (Southern São Francisco Craton) both contain phosphatic intervals which are roughly correlative with respect to lithostratigraphy and age, each occurring tens to several hundred meters above basal glaciogenic diamictite units Alkmim and Marcelo A. Martins-Neto, 2012; Caxito et al., 2012; Drummond et al., 2015; Guimarães et al., 2011; Iglesias and Uhlein, 2009; J. Richard Kyle and Aroldo Misi, 1997; Aroldo Misi, Kaufman, et al., 2007; Paula-Santos et al., 2015; Aroldo Misi and Veizer, 1998; Sanders and Grotzinger, 2021. The Salitre Formation is the phosphatic interval of the Una Group and has a thickness of 300 to 400 meters, typically divided into four members of roughly equal thicknesses: Nova America, Gabriel, Jussara, and Irecê Aroldo Misi, Kaufman, et al., 2007; A. Misi and J. R. Kyle, 1994; Aroldo Misi and Veizer, 1998. The upper three members (Gabriel, Jussara, and Irecê) are comprised of cross-stratified and wavy laminated carbonate grainstone with laterally discontinuous tabular intraclast conglomerate beds and lenses. The Nova America Member also is composed of cross-stratified grainstone and intraclast conglomerate beds, with abundant intraclast conglomerates and oolitic intervals Caird et al., 2017; A. Misi and J. R. Kyle, 1994; Aroldo Misi and Veizer, 1998; Sanders and Grotzinger, 2021. CFA cements appear in the digitate stromatolite facies of the Nova America member, which interfinger on meter and 10s-of-meters scales with the cross-stratified grainstone facies. Cryptocrystalline CFA appears specifically as an early cement in digitate stromatolites and very occasionally as well-rounded intraclasts in medium to very coarse cross-stratified carbonate grainstone adjacent to the stromatolites Caird et al., 2017; A. Misi and J. R. Kyle, 1994; Sanders and Grotzinger, 2021. The Salitre Formation has an age of  $616 \pm 31$  Ma based on U-Pb dating of these CFA cements Shiraishi et al., 2019.

### **Depositional facies model**

Previous workers have reported sedimentological and stratigraphic data from the phosphorite-bearing Nova America member of the Salitre Formation (Irecê Paleobasin area), which support a depositional facies model of a persistently submerged, wave-swept carbonate platform environment – subtidal zone, above fair-weather

wave-base Sanders and Grotzinger, 2021; Caird et al., 2017; Shiraishi et al., 2019; A. Misi and J. R. Kyle, 1994. In this environment, shoals comprised of carbonate sediments – peloids, ooids, and grapestones – migrated around and over meter- and tens-of-meter diameter tabular and herm-like stromatolitic buildups. Lithofacies within the Nova America have been most recently categorized in Sanders and Grotzinger (2021) as: (1) laminated, cross-stratified carbonate grainstone and rudstone, tabular intraclast conglomerate, (3) planar-laminated, very fine-grained limestone-dolostone, (4) crinkly laminite, (5) digitate stromatolite buildups, (6) columnar stromatolite buildups, and (7) symmetric wave-rippled limestone – this last being a reinterpretation of textures described in earlier literature Caird et al., 2017; A. Misi and J. R. Kyle, 1994 as intertidal zone tepee structures Sanders and Grotzinger, 2021.

### **3.4 Sedimentary context and origin of phosphate mineralization in the Salitre Fm.**

In the Salitre Formation, phosphate mineralization is expressed mainly as micro-to-cryptocrystalline carbonate fluorapatite (CFA) cements in the interfingering stromatolitic and cross-stratified grainstone facies, spatially restricted to 1-5 centimeter diameter digitate stromatolites with synoptic relief  $\leq 1$  cm. These cements bind laminae composed of calcite peloids and ooids and amorphous organic material. Universally, the boundary between CFA-cemented stromatolites and carbonate-cemented grainy inter-stromatolite fill is sharp, with the exception of thin (10s of micrometers) partial rims around peloids and ooids that are immediately adjacent to the phosphatic stromatolites. However, while phosphatic CFA cements are restricted to stromatolitic textures, not all stromatolitic textures contain CFA cements. Indeed some bioherms and buildups have CFA-cemented incipient stromatolites that merge to form more disordered, internally laminated mounds and domes which become progressively less phosphatic from core to outer laminae (e.g., Fig.3.1c). Still other stromatolitic buildups – primarily those comprised of decimeter-scale columnar stromatolites – and crinkly, microbially-influenced laminae contain only carbonate cements.

Any models of phosphate mineralization and diagenesis in these facies must explain the spatial restriction of phosphatic cements to digitate stromatolite buildups, to the exclusion of other stromatolite buildups and microbially-influenced sedimentary laminae within the same, wave-swept, carbonate-precipitating depositional setting. Such models fall into two categories:

- **Differential diagenesis** → Phosphatic cements precipitate from a different generation of fluids than carbonate cements. Precipitation of phosphatic cements is spatially restricted to digitate stromatolites due to differences in porespace volume and connectivity at a given stage of burial, or other primary physical and chemical characteristics that might distinguish between microbialite types.
- **Differences in primary porewater chemistry of phosphatic stromatolites and non-phosphatic stromatolites** → Porewaters within digitate stromatolites had higher saturation with respect to CFA and/or fewer kinetic barriers to CFA precipitation than porewaters within columnar stromatolites, crinkly laminae, and grainy inter-stromatolite fill.

These models may be tested by constructing a paragenetic sequence for CFA-cemented and non-CFA-cemented sediments from within the stromatolitic and cross-stratified grainstone facies of the Salitre Formation. A paragenetic framework was presented in Sanders and Grotzinger (2021), elaborating upon those of Caird et al. (2017) and Shiraishi et al. (2019), and is reiterated below Sanders and Grotzinger, 2021; Caird et al., 2017; Shiraishi et al., 2019. This framework establishes the sequence of mineralization, supporting a model in which microcrystalline CFA and carbonate cements are likely the earliest-formed mineral phases preserved in the rocks. However, petrographic imaging alone does not reveal whether the cements were precipitated from sediment porewaters shortly after deposition or during burial diagenesis; nor can it establish whether they represent fabric-retentive diagenetic replacement of original cements. The measurement of  $\Delta_{47}$ ,  $\delta^{18}O_{mineral}$ , and  $\delta^{13}C_{mineral}$  in the structural carbonate of CFA and carbonate cement phases may constrain the likelihood of extensive fluid diagenesis or resetting of primary geochemistry at depth and high temperatures (i.e., hydrothermal processes). To help reconstruct the diagenetic history of these rocks, we present new  $\Delta_{47}$ ,  $\delta^{18}O_{mineral}$ , and  $\delta^{13}C_{mineral}$  measurements of CFA and carbonate cements within the sedimentary context and paragenetic frameworks established by previous studies.

### **Paragenetic framework**

The paragenesis of those intervals of the Salitre Formation in which carbonate and CFA cements both occur, in stromatolitic and non-stromatolitic laminae,

can be divided into four stages: primary depositional, early diagenetic, mid-stage diagenetic, and latest diagenetic. See Fig.3.4.

*Primary Components:* Primary depositional components include carbonate ooids with micritic nuclei, rounded micritic grains (peloids), and organic material (Fig.3.4b-i). These components represent the accumulation of carbonate ooids and peloids at the seafloor, sometimes interlaminated with microbial biomass. Seawater in this setting must have been saturated with respect to carbonate minerals, hence the formation of ooids and peloids at and above the seafloor. However, as grains and microbial cells accumulated, seawater would have been trapped in the interstitial space and experienced restricted communication with the water column, resulting in marine sediment porewaters. Microbial processes occurring within porewaters, such as aerobic and anaerobic respiration of biomass via seawater oxygen, sulfate, nitrate, iron, etc., would have acted under closed- or restricted-system conditions, with diffusive and advective transport between the porewaters, seawater above the sediment-water interface, and deeper porewaters controlling the abundance of bioavailable oxidants and reductants. Diffusive and advective transport of biochemical substrates is a function of burial depth in the sediments, as well as pore volume and connectivity. As sediment and biomass continued to accumulate, porespace would have been buried deeper and become increasingly disconnected from seawater chemistry – leading to changing saturation states. Textural evidence for these processes is preserved as cements, the first "early diagenetic" phases.

*Early Diagenetic:* CFA and carbonate cements fill the interstitial space between grains and organic material in stromatolitic and adjacent grainstone facies occasionally pocked with Fe-sulfide crystals such as pyrite and pyrrhotite (minor components, ubiquitous across facies). (Fig.3.4b-ii, and Fig.3.5). These cements may have nucleated on porewalls/grains, biomass, or in suspension, occluding porespace. Micro-to-cryptocrystalline carbonate ("micrite") is known to form at the seafloor and in the water column, but may also result from thin-film dissolution/reprecipitation ("recrystallization") of primary carbonate crystals, resulting in partial or total destruction of the internal laminae of ooids, and the creation of diffuse, ragged boundaries between grain and cement matrix. Such textures are all present in the Salitre Formation rocks. Also present are early pressure solution features such as sutured grain boundaries and minor stylolites (Fig.3.4b.iii-v). The replace-

ment of acicular carbonate crystals (likely aragonite) by calcite is shown by the fabric-retentive, anhedral calcite mosaics that co-occur with micrite.

Micritization and early calcite recrystallization/reordering are textures typically associated with seawater advection through shallowly buried, partially lithified rock – such that small aragonite and calcite crystals encounter reduced saturation states and partially dissolve Flügel, 2010. Microbial respiration of organic matter via various oxidants – depending on distance from and rate of exchange with seawater – would have co-occurred with early cementation, possibly affecting the saturation state and precipitation kinetics of porewaters with respect to carbonate and CFA minerals via changes to alkalinity, abundance of chemical inhibitors, and availability of nucleation sites. Amorphous organic material incorporated into cements is visible in stromatolitic and non-stromatolitic microfacies of the Salitre Formation, and may be interpreted as evidence of the co-occurrence of cementation with remineralization of biomass in porewaters.

Microbial cells or their structures may be preserved during early cementation when (a) cements nucleate on and surround the cell – disconnecting it from processes of chemical degradation that occur in porefluids and during later diagenesis, or (b) when the cell structure itself is mineralized in such a way that the structure remains distinct from the matrix with respect to mineralogy, crystal size, or the abundance of inclusions. In our study, such preservation was observed only rarely, which could be the result of fabric-destructive recrystallization of primary cements, or the occurrence of early cementation during or after remineralization of biomass below the sediment-water interface. These two cases cannot be distinguished in petrographic thin sections.

*Mid-Stage Diagenetic:* Mid-stage diagenetic phases include (1) 100s-of-micrometer-scale patches of coarsely crystalline anhedral mosaic dolomite cement apparently replacing or co-precipitating with micrite and calcite mosaic cements, (2) fabric-retentive and fabric-destructive partial silica (chert) replacement of carbonate grains and carbonate and CFA cements, and (3) fabric-destructive rims of zoned, euhedral dolomite rhombs templated on primary grain boundaries. There are also (4) prominent pressure solution horizons or stylolites that cross-cut grain boundaries and calcite and CFA cements, e.g. Fig. 3.5d. Replacive chert is commonly observed in both phosphatic and non-phosphatic stromatolites, crinkly laminae, and grain-

stone. Replacive dolomite cement and euhedral rhombs occur mostly among calcite-cemented laminae and grainstone. (These features are illustrated in Fig.3.4b.vi-viii,c.viii).

These phases and features are interpreted as evidence of multiple generations of diagenetic fluids passing through already lithified strata. Fabric-retentive patchy anhedral mosaic dolomite cements are typically associated with burial diagenesis at shallow depths, where Mg-rich seawater may circulate through rock at depths of tens to hundreds of meters, effecting recrystallization of calcite to dolomite (Flügel, 2010; Bathurst, 1975). Mixture of seawater with meteoric waters is known to produce dolomitization as meteoric freshwater facilitates dissolution of earlier carbonate phases, with seawater providing a source of magnesium resulting in dolomite precipitation. Meanwhile, chertification, when not associated with supratidal facies, is typically interpreted as the effect of deep burial brines rather than evaporative brines circulating through rock (Bustillo, 2010; Flügel, 2010; Hesse, 1990). Large, zoned, fabric-destructive euhedral dolomite crystals forming rims around primary grain boundaries and cross-cutting earlier recrystallized cements are typically associated with deeper burial brines as well. Altogether, these mid-stage diagenetic phases seem to represent dissolution and reprecipitation by a sequence of diagenetic fluids originating from mixtures of freshwater, seawater, and deep possibly hydrothermal brines circulating through porous carbonate and phosphorite of the Salitre Formation during burial at depth scales of a few hundred meters to 1-2 kilometers.

*Late Diagenetic:* Latest diagenetic phases include: fabric-destructive, blocky, euhedral dolomite spar; vein-filling blocky calcite spar; and euhedral Fe-sulfide and Fe-oxide crystals associated with vein spar. Rarely, there are translucent purple microcrystalline fluorite spars replacing primary fabrics. (Fig.3.4b-ix,c-ix). These phases are interpreted as the result of deep burial fluids – possibly hydrothermal in origin – which remobilize phosphate, carbonate, and various cations from elsewhere in the sedimentary strata and pass through rock via connected porespace and tectonic fractures, dissolving and re-precipitating minerals as they go (Caird et al., 2017; J. Richard Kyle and Aroldo Misi, 1997; Sanders and Grotzinger, 2021). The geochemical measurements presented here, meant to constrain the origin and diagenesis of the earliest cements, avoid these pockets and veins of sparry calcite and dolomite and metal enrichment.

### 3.5 $\Delta_{47}$ , $\delta^{18}O$ , and $\delta^{13}C$ values of carbonate in calcite, dolomite, and CFA

Primary depositional and early diagenetic phases were sampled by mm-scale drilling of thin section offcut billets or slabs corresponding to examined thin sections, such that only well-characterized fabrics were sampled and the mixture of primary, early, and later diagenetic phases could be minimized. Targeted phases occurred within the "Primary Depositional" and "Early Diagenetic" fabrics described above: micritic and anhedral interlocking mosaic calcite cements, dolomite cements, and micro-to-cryptocrystalline CFA cements. These fabrics occurred within the stromatolitic, crinkly laminae, and oolitic grainstone lithofacies — the primary components of the phosphorite-bearing strata of the Salitre Formation. (See Methods for description of sampling protocol and preparation of powders for acid digestion, gas capture, mass spectrometry, data treatment and processing.) For ease of analysis, samples are here organized in groups of 1–7, with each group containing powders collected centimeters to meters from one another at the same level within the same measured stratigraphic sections. See Fig. 3.1–3.2, in which sample mineralogies, locations, lithofacies associations, and groupings are shown in context of stratigraphic columns. Groups of samples from the same stratigraphic sections may be expected to have had similar formation and burial histories with respect to depositional setting and temperature evolution, and are color-coded according to their stratigraphic section in Figs. 3.1, 3.2, and 3.3. Samples of the same mineral phase (calcite, dolomite, or CFA) are shape-coded, with circles indicating calcite, triangles indicating dolomite, and squares indicating CFA.

*Aristeia* is one of two stratigraphic sections for which more than one mineral phase was sampled within the same section at similar stratigraphic levels and co-occurring lithofacies. These subsets of the data represent a rare opportunity to directly compare the diagenesis of co-occurring cement phases as recorded by carbon and oxygen isotope geochemistry. From *Aristeia*, two samples of anhedral interlocking mosaic and micritic calcite were collected, alongside two interlocking mosaic dolomite cement samples, and three cryptocrystalline CFA cement samples. All of these occurred within the same closely (meter and centimeter-scale) interfingering digitate stromatolite, crinkly laminite, and cross-stratified grainstone – representing the same primary depositional facies. These calcite samples yielded  $\Delta_{47}$  temperatures of

$92.09 \pm 8.174733^\circ\text{C}$ , and  $110.549 \pm 13.60045^\circ\text{C}$ . (Note: these values are the averages  $\pm$  propagated standard errors of a population of 8 mass spectrometric measurements/acquisitions of the same calcite-derived  $\text{CO}_2$ , corrected for fractionation effects introduced during sample processing — see Methods). The  $\delta^{18}\text{O}$  of these two calcite samples from which the analyzed  $\text{CO}_2$  was derived were  $-2.35 \pm 0.0023\text{‰}$ (VPDB) and  $-2.03659 \pm 0.001244\text{‰}$ (VPDB). The  $\delta^{18}\text{O}$  of the water/fluids with which the measured calcite samples last equilibrated was calculated using the measured  $\delta^{18}\text{O}_{\text{mineral}}$  for calcite and their temperatures of last equilibration, derived based on measured  $\Delta_{47}$ , and an empirical formula relating equilibrium isotope fractionation between water and calcite (Kim and O’Neil, 1997):  $11.028 \pm 1.104846\text{‰}$ (VSMOW) and  $13.80 \pm 1.67\text{‰}$ (VSMOW).  $\delta^{13}\text{C}$  values of structural carbonate in the measured calcite samples were  $1.74 \pm 0.0010\text{‰}$ (VPDB) and  $1.90 \pm 0.00068\text{‰}$ (VPDB). Because the two calcite samples yield values that are within one standard error of one another, it seems highly probable that our measurement interrogated samples of the same paragenetic phase successfully.

Dolomite samples from *Aristeia* yielded considerably higher  $\Delta_{47}$  temperatures than directly comparable calcite samples, but were consistent to within one standard error of each other:  $143.64 \pm 14.06^\circ\text{C}$ ,  $147.8138 \pm 12.25045^\circ\text{C}$ . The  $\delta^{18}\text{O}$  of these two dolomite samples were both roughly 1 per mille lighter than the calcite:  $-3.01415 \pm 0.00095\text{‰}$ (VPDB) and  $-3.51 \pm 0.0043\text{‰}$ (VPDB). The  $\delta^{18}\text{O}$  of the water/fluids with which the measured dolomite samples last equilibrated were:  $5.94 \pm 1.46\text{‰}$ (VSMOW) and  $5.795813 \pm 1.246418\text{‰}$ (VSMOW) Horita, 2014.  $\delta^{13}\text{C}$  values of structural carbonate in the measured dolomite samples were  $1.911786 \pm 0.001185\text{‰}$ (VPDB) and  $5.059 \pm .001401\text{‰}$ (VPDB).

The three CFA samples from *Aristeia* yielded values more similar to the co-occurring calcite cement samples than the dolomite samples, and were consistent with one another to within one standard error:  $\text{Temperatures}_{\Delta_{47},\text{CFA}} = 116.96 \pm 4.16^\circ\text{C}$ ,  $119.84 \pm 5.44^\circ\text{C}$ ,  $113.54 \pm 12.00^\circ\text{C}$ ;  $\delta^{18}\text{O}_{\text{mineral}}$  for CFA =  $-3.13 \pm 0.001896\text{‰}$ (VPDB),  $-3.31 \pm 0.0038\text{‰}$ (VPDB),  $-1.80 \pm 0.001756\text{‰}$ (VPDB); and calculated  $\delta^{18}\text{O}_{\text{water}} = 13.47 \pm 0.50\text{‰}$ (VSMOW),  $13.63 \pm 0.64\text{‰}$ (VSMOW),  $14.42 \pm 1.45\text{‰}$ (VSMOW).  $\delta^{13}\text{C}$  values of structural carbonate in the measured CFA samples were  $0.47 \pm 0.00097\text{‰}$ (VPDB),  $-0.17 \pm 0.00069\text{‰}$ (VPDB), and  $1.37 \pm 0.0012\text{‰}$ (VPDB).

Taken together, these data may be used to test hypotheses for the paragenesis

of the co-occurring calcite and CFA cements in the microbialite and ooid grainstone facies of *Aristeia*.

The dolomite cements from *Aristeia* record  $\Delta_{47}$  temperatures roughly 30-40°C higher than those recorded in co-occurring CFA and calcite cements. It is possible that all of the measured cement phases experienced these higher temperatures, but that only the dolomite faithfully recorded this temperature due to its greater blocking temperature. (Blocking temperatures are the temperatures below which changes in clumped isotopic composition due to solid-state reordering occur extremely slowly or negligibly, provided heating/cooling is gradual. For dolomite, blocking temperatures are between 200–250°C (Dennis and Schrag, 2010; Ferry et al., 2010), for calcite – 100–200°C (Stolper and Eiler, 2015; Henkes, Passey, Grossman, et al., 2014; Lloyd, Eiler, and Nabelek, 2017), and for CFA – 100 °C (R. a. Eagle et al., 2011; Stolper and Eiler, 2015; Stolper and Eiler, 2016).) However, the dolomite also records roughly the same  $\delta^{18}O_{mineral}$  as calcite and CFA and slightly heavier  $\delta^{13}C_{mineral}$ . If all of the rock experienced the same temperature of 140-150°C and recrystallized entirely or partially in equilibrium with fluid of the same  $\delta^{18}O$  composition, one would expect the  $\delta^{18}O_{mineral}$  for dolomite to be several per mille heavier than the  $\delta^{18}O_{calcite,CFA}$ . (The equilibrium oxygen isotope fractionation between dolomite and calcite precipitated from the same fluid is observed in experimental studies and theoretical models to be roughly 3‰ (Vasconcelos et al., 2005). If measured dolomite and calcite phases equilibrated with the same waters, then one would expect similar  $\Delta_{47}$  temperatures for both minerals, but a roughly 3‰ difference between  $\delta^{18}O_{mineral}$  for calcite and  $\delta^{18}O_{mineral}$  for dolomite.) If the dolomite equilibrated with fluids that were isotopically lighter by several per mille than those that equilibrated with the CFA and calcite (but at the same temperature), one would expect the dolomite to record roughly the same  $\delta^{18}O_{mineral}$  as the CFA and calcite. If both the temperature was higher and the  $\delta^{18}O_{water}$  was several per mille lighter for the dolomitizing fluids, one would expect the dolomite cement to be isotopically lighter than the CFA and calcite. Our data (similar  $\delta^{18}O_{mineral}$ ,  $\Delta_{47}$  temperatures at blocking temperature for CFA/calcite but below blocking temperature for dolomite) are consistent with a scenario where dolomite may have been formed/altered by a different generation of diagenetic fluids than the CFA and calcite cements — a generation that was isotopically lighter but at a similar or slightly higher temperature.

The other stratigraphic section for which more than one mineral phase was sampled within the same microfacies was *CBPM Core 10*. The sampled fabrics from *CBPM Core 10* were, as in *Aristeia*, part of a digitate stromatolite buildup interfingering with oolitic, cross-stratified grainstones. In this case, most early carbonate cements were preserved as recrystallized dolomite — anhedral, interlocking cements around micritic grains in the interstromatolite fill. Stromatolitic laminae were cemented with micro-to-cryptocrystalline CFA — which appeared to share the same position in the sequence of cross-cutting paragenetic phases as the dolomite cement.

A single dolomite cement sample was collected from *CBPM Core 10*, yielding a  $\Delta_{47}$  temperature of  $115.15 \pm 12.09^\circ\text{C}$ . This sample had a  $\delta^{18}\text{O}_{\text{mineral}}$  of  $-4.38 \pm 0.0023\text{‰}$ (VPDB). The calculated  $\delta^{18}\text{O}_{\text{water}}$  was  $1.70 \pm 1.445818\text{‰}$ (VSMOW). Measured  $\delta^{13}\text{C}$  for the dolomite was  $5.645 \pm 0.001395\text{‰}$ (VPDB). Meanwhile, two CFA cement samples from the same core and microfacies yielded  $\Delta_{47}$  temperatures of  $143.89 \pm 33.13723^\circ\text{C}$  and  $96.1525 \pm 8.12^\circ\text{C}$ .  $\delta^{18}\text{O}_{\text{mineral}}$  for CFA values were  $3.93 \pm 0.0044\text{‰}$ (VPDB) and  $4.314385 \pm 0.0053\text{‰}$ (VPDB).  $\delta^{18}\text{O}_{\text{water}}$  values calculated for these CFA samples were  $14.37 \pm 3.44\text{‰}$ (VSMOW) and  $8.99 \pm 1.073\text{‰}$ (VSMOW). Measured  $\delta^{13}\text{C}$  values for the CFA samples were  $3.93 \pm 0.0044\text{‰}$ (VPDB) and  $4.31 \pm 0.0053\text{‰}$ (VPDB). As for the *Aristeia* samples, CFA samples recorded temperatures above the known blocking temperature for that mineral R. a. Eagle et al., 2011; Stolper and Eiler, 2015; Stolper and Eiler, 2016, while dolomite records a temperature well below its blocking temperature (Dennis and Schrag, 2010; Ferry et al., 2010).  $\delta^{18}\text{O}_{\text{mineral}}$  values are close (within 1 per mille) between co-occurring CFA and dolomite. Calculated  $\delta^{18}\text{O}_{\text{water}}$  for dolomite is also significantly lighter than that for CFA. These data, like those for *Aristeia*, are consistent with a scenario wherein dolomite equilibrated with a generation of fluids that may have been isotopically lighter by several per mille with respect to oxygen and at similar or higher temperatures than the fluids with which the CFA last equilibrated. However, the heterogeneity of the isotopic composition of the measured CFA should be noted, and may imply a more complicated thermochemical history across the entire section.

For the remaining five localities, it was not possible to measure earliest CFA and carbonate cement phases within the same microfacies in the same well-characterized hand samples. Therefore, measurements of  $\Delta_{47}$ ,  $\delta^{18}\text{O}$ , and  $\delta^{13}\text{C}$  from different localities likely do not describe formation and recrystallization

from exactly the same succession of diagenetic fluids. However, it is still possible to compare among them given that (a) all samples are taken from the same lithofacies and at similar stratigraphic levels within the broader Salitre formation, and (b) all samples were from similar microtextural associations, having similar cross-cutting relationships identifiable in petrographic thin section.

Two dolomite cement samples from the *Cerberus* locality yielded  $\Delta_{47}$  temperatures of  $98.96 \pm 10.90^\circ\text{C}$  and  $84.94 \pm 10.39^\circ\text{C}$  – well below the blocking temperature range for dolomite.  $\delta^{18}\text{O}_{\text{mineral}}$  for dolomite values were  $-2.08 \pm 0.0012\text{‰}$ (VPDB) and  $-2.05 \pm 0.0014\text{‰}$ (VPDB). Their  $\delta^{13}\text{C}_{\text{dolomite}}$  values were  $1.18 \pm 0.000865\text{‰}$ (VPDB) and  $1.17 \pm 0.0012\text{‰}$ (VPDB). These values are consistent with other dolomite samples from the *Aristeia* and *CBPM Core 10*, with respect to  $\delta^{18}\text{O}_{\text{mineral}}$  for dolomite,  $\Delta_{47}$  temperature, and calculated  $\delta^{18}\text{O}_{\text{water}}$ .

5 calcite samples from wavy/crinkly laminite and cross-stratified grainstone facies in the *Minotaur* locality yielded a wide range of  $\Delta_{47}$  temperatures between about 90 and  $130^\circ\text{C}$ , all close to or just above the blocking temperatures known for calcite. (See Tables 4.1–3.2 for exact values and standard errors). Their  $\delta^{18}\text{O}_{\text{mineral}}$  for calcite values ranged from around -3 to  $1\text{‰}$ (VPDB), their  $\delta^{13}\text{C}_{\text{calcite}}$  from 0-5 $\text{‰}$ (VPDB), and their calculated  $\delta^{18}\text{O}_{\text{water}}$  from 10-20 $\text{‰}$ (VSMOW). These values are consistent with the calcite samples measured from the *Aristeia* locality.

Two samples of calcite cement and micritic grains from the cross-stratified grainstone facies in the *Io* locality have similar  $\Delta_{47}$  temperatures to the bulk of the data ( $107.98 \pm 8.00^\circ\text{C}$  and  $116.19 \pm 10.98571^\circ\text{C}$ ) and similar if slightly depleted  $\delta^{18}\text{O}_{\text{mineral}}$  for calcite ( $-6.70 \pm 0.00099\text{‰}$ (VPDB) and  $-6.71891 \pm 0.0013\text{‰}$ (VPDB)). Consequently their calculated  $\delta^{18}\text{O}_{\text{water}}$  values ( $8.66 \pm 1.35\text{‰}$ (VSMOW) and  $9.68 \pm 1.31\text{‰}$ (VSMOW)) are also consistent with those of the calcite samples in *Minotaur* and *Aristeia*. However, the *Io*  $\delta^{13}\text{C}_{\text{calcite}}$  values are conspicuously heavier than other samples', around  $10\text{‰}$ (VPDB) rather than the 0-5 $\text{‰}$ (VPDB) range observed across other phases and localities.

A single CFA sample from a digitate stromatolite interval in *CBPM Core 5* yielded a  $\Delta_{47}$  temperature of  $126.05 \pm 6.21^\circ\text{C}$ , a  $\delta^{18}\text{O}_{\text{mineral}}$  for CFA value of  $-4.93 \pm 0.0022\text{‰}$ (VPDB),  $\delta^{13}\text{C}_{\text{CFA}}$  value of  $3.11 \pm 0.001145\text{‰}$ (VPDB), and

calculated  $\delta^{18}O_{water}$  of  $12.70 \pm 0.70\text{‰}$ (VSMOW). These values are consistent with CFA samples from the *Aristeia* and *CBPM Core 10* localities.

A single CFA sample from a digitate stromatolite interval in *CBPM Core 11* stands apart from the rest of the CFA data, with a  $\Delta_{47}$  temperature of  $51.99 \pm 7.506015^\circ\text{C}$  – a temperature below the blocking temperature of CFA and therefore likely to reflect the actual temperature at which the cements were last open to recrystallization/ion exchange with fluids. The  $\delta^{18}O_{mineral}$  value for this *CBPM Core 11* sample is  $-6.36 \pm 0.0035\text{‰}$ (VPDB), in agreement with other CFA samples from other localities to within a couple per mille; but its  $\delta^{13}C_{CFA}$  value is much lighter than all of the other measured phases:  $-4.01 \pm 0.0026\text{‰}$ (VPDB). Its calculated  $\delta^{18}O_{water}$  of  $0.61 \pm 1.28\text{‰}$ (VSMOW) is also relatively light.

In summary, the dolomite, calcite, and CFA samples from *Minotaur*, *Cerberus*, *CBPM Core 5*, and *Io* yield similar  $\Delta_{47}$  temperatures to the equivalent phases measured in samples from *Aristeia* and *CBPM Core 10* in that the dolomite samples record temperatures 50-100°C below the blocking temperature of dolomite, while calcite and CFA are consistently within 10-20°C of their blocking temperatures. However, the range of temperatures recorded among all of the dolomite samples, all of the calcite samples, and all of the CFA samples, across all of these localities, is large and overlapping. Dolomite cements from *CBPM Core 10* record a lower  $\Delta_{47}$  temperature than equivalent dolomite cements in *Aristeia*, in closer agreement with the  $\Delta_{47}$  temperatures of CFA and calcite from *Aristeia*, *Minotaur*, *Cerberus*, and *CBPM Core 5*. There is no discernible pattern of one phase recording consistently hotter or cooler temperatures than another beyond error. The only statistical outlier with respect to temperature occurs with the CFA sample from *CBPM Core 11*, whose low temperature combined with depleted  $\delta^{13}C_{CFA}$  and  $\delta^{18}O_{mineral}$  for CFA suggest interactions with diagenetic fluids distinct from those that equilibrated with all of the other measured phases.

Thus, with the exception of the CFA sample from *CBPM Core 11*,  $\delta^{18}O_{mineral}$  values and  $\Delta_{47}$  apparent temperatures for dolomite, calcite, and CFA considered together are consistent with a scenario in which co-occurring calcite and CFA cements equilibrated with fluids of similar carbon and oxygen isotope composition, and likely at similar temperatures — above the blocking temperatures of those minerals. Dolomites, which record comparable  $\delta^{18}O_{mineral}$

values to CFA and calcite, and relatively depleted  $\delta^{13}C_{mineral}$  values, likely equilibrated with a different generation of fluids from the CFA and calcite. These dolomitizing fluids likely had more depleted  $\delta^{18}O_{water}$  values, and at similar or slightly hotter temperatures, compared to the fluids that equilibrated with the co-occurring CFA and calcite cements.

In the next section, we discuss how these results constrain models of formation and diagenesis of phosphatic versus non-phosphatic textures throughout the Salitre Formation.

### 3.6 Discussion and conclusions

Building on conclusions from thin section petrography and elemental mapping from previous works (Sanders and Grotzinger, 2021; Caird et al., 2017; Shiraishi et al., 2019), this study applies further microimaging — combined with fabric-selective measurements of  $\Delta_{47}$ ,  $\delta^{18}O$ , and  $\delta^{13}C$  of structural carbonate in CFA, calcite, and dolomite cements — to the phosphorite-bearing member of the Salitre Formation. These data permit the testing of hypotheses for the origin and spatial distribution of phosphatic and non-phosphatic cements: whether a consequence of differential diagenesis temporally removed from the original stromatolite-forming environment, or an indicator of authigenic and earliest diagenetic processes that might shed light on the phosphogenetic paleoenvironment and paleoecology.

The phosphorite-bearing member of the Salitre Formation is comprised mostly of stromatolite buildups, cross-stratified oolitic grainstone, and crinkly laminite lithofacies, which interfinger on meter- and tens-of-meter scales. Phosphate enrichment in the form of CFA cement is restricted to digitate stromatolite facies. However, the digitate stromatolite facies are not universally or uniformly phosphatic. Digitate stromatolites, columnar stromatolites, and more disordered stromatolitic buildups and laminites cemented by calcite and dolomite are common and often occur within meters to centimeters of phosphatic stromatolites, suggesting highly local controls on the distribution of phosphate mineralization.

Cross cutting relationships between mineral phases at centimeter to micrometer scales constrain the relative timing of different stages of deposition, mineralization, and remineralization. "Primary Depositional" phases include carbonate allochems (ooids, peloids, and aggregates thereof), and amorphous

organic material. "Early Diagenetic" phases include both CFA and carbonate cements — overlapping in the relative timeline of mineralization, as well as Fe-sulfides, and carbonate micrite. Mid-stage diagenetic phases include more coarsely crystalline dolomite cements and patchy silicification. Latest diagenetic phases include fabric-destructive coarsely crystalline, euhedral dolomite spars, vein-filling calcite spars, and Fe minerals spatially associated with fractures and stylolites.

Photomicrographs of closely associated phosphatic and non-phosphatic textures — i.e., at the margins of phosphatic and non-phosphatic digitate stromatolites — reveal carbonate and CFA cements to be either synformational, or otherwise fabric-retentive replacements of what once were synformational cements.

$\Delta_{47}$ ,  $\delta^{18}O$ , and  $\delta^{13}C$  measurements of structural carbonate in CFA, calcite, and dolomite cements constrain the likeliest sequence of diagenetic fluids and thermal change that resulted in the observed distribution of cements:

#### **Differential diagenesis: deep-circulating fluids**

Deep-circulating fluids are fluids whose chemical and isotopic composition reflect ion exchange with minerals that form the walls of pore space at depth, meters to tens of meters below the Earth's surface or seafloor. When these fluids convect/advect through a shallower package of rock/sediment, in a shallower thermochemical regime than the package they were last equilibrated with, these fluids may be considered hydrothermal, and may alter the shallower package of rock in a way that evolves away from the rock's primary geochemistry and, provided water-rock ratios are high, toward the geochemistry of the deeper thermochemical regime. Generally, such fluids are expected to be enriched relative to seawater with respect to  $^{13}C$ , due to isotope exchange with  $^{12}C$ -depleted carbonate rocks many tens of meters below the sediment-water interface (Swart and Oehlert, 2018; Swart, 2015). Their  $\delta^{18}O$  values may be depleted due to less sequestration of  $^{18}O$  in carbonate minerals at high temperatures, or enriched due to isotope exchange with  $^{18}O$ -enriched rocks (Swart, 2015). Often, they are enriched with respect to a range of metals, as well as inorganic phosphate remobilized during the passage of fluids through rocks rich in decayed organic matter. One possible model for the enrichment of specific mineral fabrics of the Salitre Formation with respect to phosphate minerals involves deep-circulating fluids passing through the strata

of the Salitre Formation. In such a model, subtle differences in pore space and grain size between different stromatolite morphologies and grainstone facies could have allowed the deep-sourced fluids to interact more pervasively with some textures than others, resulting in texture-specific enrichment of P and the replacement of primary cements — likely carbonate — with CFA. In such a scenario, one would expect CFA cements to yield  $\Delta_{47}$  temperatures equal to or higher than associated carbonate cements, as well as higher  $\delta^{13}\text{C}$  values and higher (or at least, systematically different)  $\delta^{18}\text{O}_{\text{mineral}}$  values. One would also expect calculated  $\delta^{18}\text{O}_{\text{water}}$  to differ between CFA and carbonate cements. Most of the CFA, calcite, and dolomite cements that were measured yielded similar  $\Delta_{47}$  temperatures, similarly neutral to slightly positive  $\delta^{13}\text{C}$ , and positive calculated  $\delta^{18}\text{O}_{\text{water}}$ . There is no significant distinction between the measured CFA and calcite cements with respect to temperature or  $^{13}\text{C}$  enrichment, nor with respect to  $\delta^{18}\text{O}_{\text{mineral}}$ . However,  $\delta^{18}\text{O}_{\text{mineral}}$  for dolomite was also similar to CFA and calcite, which due to the different equilibrium isotope effects between calcite-and-water and dolomite-and-water, would require the dolomitizing fluids to have lighter  $\delta^{18}\text{O}_{\text{water}}$  by several per mille and/or interact with the dolomite crystals at higher temperatures than the calcite/CFA-recrystallizing fluids. These relationships are inconsistent with a scenario in which phosphate mineralization was facilitated by microfacies-selective permeation by deep-sourced fluids – the measured  $\delta^{18}\text{O}_{\text{mineral}}$ ,  $\Delta_{47}$  temperatures, and calculated  $\delta^{18}\text{O}_{\text{water}}$  for CFA and calcite are effectively the same, not different. Deep-sourced fluids may, however, have been instrumental to the formation of dolomite cements – since dolomite seems to record  $\delta^{18}\text{O}_{\text{mineral}}$  similar to that of calcite and CFA, along with higher temperatures, and more depleted  $\delta^{18}\text{O}_{\text{water}}$ .

### **Differential diagenesis: meteoric fluids**

Meteoric fluids — freshwater that has percolated down through organic-rich soils of the vadose zone to interact with rock — are expected to have chemical and isotopic compositions that reflect their surface origin. If meteoric fluids enriched with respect to organically-derived phosphorus were responsible for the observed distribution of CFA versus carbonate cements in the Salitre phosphorite, one might expect the CFA and carbonate phases to differ geochemically and isotopically in the following ways. Meteoric fluids are typically depleted with respect to  $^{18}\text{O}$ , due to the effect of Rayleigh Distillation

on rainwater isotopic composition, and typically have negative  $\delta^{13}\text{C}$  due to isotope exchange with  $^{13}\text{C}$ -depleted organic matter near the Earth's surface (Allan and Matthews, 2009; Swart and Oehlert, 2018). If either the CFA or the carbonate cements measured had been influenced by meteoric fluids, either the CFA or the carbonate cements would record depleted  $\delta^{18}\text{O}_{\text{mineral}}$  values, depleted  $\delta^{13}\text{C}_{\text{mineral}}$  values, and lower  $\Delta_{47}$  temperatures than the other measured phase. Most of our samples of CFA cement from the Salitre Formation do not exhibit depleted  $\delta^{13}\text{C}$  or  $\delta^{18}\text{O}$  values, with the notable exception of Sample *XI810*. Sample *XI810*, consisting of CFA cement within a digitate stromatolite in *CBPM Core 11*, yielded a  $\Delta_{47}$  temperature around  $52 \pm 7.5^\circ\text{C}$  – considerably lower than all other measured phases – as well as depleted values for  $^{13}\text{C}$  ( $-4\text{‰ VPDB}$ ) and calculated  $^{18}\text{O}_{\text{water}}$  ( $0.6\text{‰ VSMOW}$ ). The isotopic composition of Sample *XI810* is therefore consistent with a scenario of equilibrium exchange between rock and meteoric fluids. The majority of our measurements, however, are not. Indeed, most of our samples (CFA, calcite, and dolomite alike), record  $\delta^{13}\text{C}$  values that are fairly enriched relative to seawater, and yield enriched calculated  $\delta^{18}\text{O}_{\text{water}}$  values. Furthermore, meteoric fluids are expected to yield correlated  $\delta^{18}\text{O}_{\text{mineral}}$  and  $\delta^{13}\text{C}_{\text{mineral}}$  values, due to both carbon and oxygen isotopic compositions of meteoric fluids becoming simultaneously more enriched with depth below the surface. Such a correlation is not observable in our data (Fig. 3.3c). Thus, meteoric diagenesis as a mechanism of phosphogenesis is not supported.

### **Interaction with marine porefluids**

Marine porefluids are expected to form with carbon and oxygen isotopic compositions similar to that of their source seawater. As burial increasingly restricts diffusive and advective transport between porespace and bottom waters, and temperatures rise according to the local geothermal gradient, these compositions are expected to evolve under the influence of microbial activity, temperature dependence of equilibrium isotope exchange, and the transition from open to increasingly closed-system dynamics (Swart, 2015; Bathurst, 1975). Respiration/remineralization of organic matter by heterotrophic microorganisms should lower the  $\delta^{13}\text{C}$  of porefluids, which then may exchange at increasingly high temperatures with the minerals which comprise the pore walls. Exchange of oxygen isotopes between fluid and mineral should become less mass-selective at higher temperatures. This, combined with the relatively

low water-rock ratio expected at depth, should lead to  $^{18}\text{O}$ -enrichment of the porefluids. Thus, sediments buried and exchanging ions with marine porewaters at increasing depth might be expected to form carbonate and CFA cements according to the organic matter abundance and composition of the porewaters, with  $^{18}\text{O}$ -enrichment relative to starting seawater and evolving toward the composition of the bulk rock.

With the exception of two calcite cement samples from the *Io* locality and the altered CFA cement sample from *CBPM Core 11*, most of our measurements of  $\delta^{13}\text{C}$  of structural carbonate in CFA, calcite, and dolomite cements were between 0-5‰ VPDB, all equal or slightly positive relative to values expected for marine carbonates during Ediacaran time (Halverson et al., 2010). Most of our measurements of  $\delta^{18}\text{O}$  of structural carbonate in CFA, calcite, and dolomite cements were between roughly -5 and 2‰ VPDB. These and their  $\Delta_{47}$  temperatures allow the calculation of  $\delta^{18}\text{O}_{\text{water}}$  values between roughly 5 and 20 ‰ VSMOW, with dolomites having generally lighter  $\delta^{18}\text{O}_{\text{water}}$  than spatially related calcite and CFA. These values are consistent with precipitation or recrystallization of cements with porefluids up to 2-5 kilometers deep in low water-rock settings (e.g. Brand, Assonov, and Coplen, 2010; Veillard et al., 2019; Goldberg et al., 2021).

Overall,  $\delta^{18}\text{O}$  and  $\delta^{13}\text{C}$  values of CFA, calcite, and dolomite are consistent with a scenario wherein CFA and calcite precipitated from or recrystallized via diagenetic fluids of roughly the same isotopic composition and at roughly the same temperature, while dolomite was open to exchange with a different, likely isotopically lighter generation of diagenetic fluids at similar or higher temperatures. The range of carbon and oxygen isotope compositions measured in CFA and calcite cements is also more consistent with ion exchange between CFA/calcite and marine-derived porefluids buffered to the composition of the bulk rock, rather than meteoric or deep-sourced hydrothermal fluids in large quantities.

### **Determinants of phosphate versus carbonate mineralization**

If CFA and calcite cements alike precipitated/recrystallized in equilibrium with pore fluids of similar isotopic composition, with limited to no modification by deep-sourced hydrothermal fluids or surface-sourced meteoric fluids, then one must invoke differences in the chemical composition of the formational porefluids to explain the distribution of co-occurring CFA and

carbonate cements. The spatial restriction of CFA cements to digitate stromatolites might suggest that differences in abundance of organic material in early porewaters controlled differences in saturation state with respect to CFA or calcite/dolomite. However, there are numerous examples of non-phosphatic stromatolites and other microbially-influenced sedimentary structures, some immediately adjacent to phosphatic structures on the scale of centimeters to meters. The presence of decaying microbial mats would have influenced porewater chemistry during early burial in both CFA-forming and carbonate mineral-forming environments, and so alone cannot explain the observed patterns of phosphogenesis. What else can?

Variation in the abundance of chemical inhibitors to carbonate or CFA cement nucleation and growth (such as metal ions) and variation in the abundance of inorganic phosphate derived from organic materials could vary on small spatial scales and be texturally associated with microbially-influenced sedimentary structures. For example, it is well-documented that different mat-forming and colonial microorganisms have different capacities for the production of extracellular polymeric substances under environmental stresses (Steele, Franklin, and Underwood, 2014; Silva et al., 2020; Decho and Gutierrez, 2017). These polymeric substances may adsorb cations and reduce kinetic inhibitions for the complexing and accumulation of silica, contributing to the preservation of microbial cells in chert (Moore, Pajusalu, et al., 2020; Moore, Gong, et al., 2021). It is also documented that phosphate-accumulating sulfur bacteria are more abundant in modern marine environments where phosphatic allochems and hardgrounds form than in non-phosphogenetic environments (Arning et al., 2009; Leland et al., 2014; H. N. Schulz and H. D. Schulz, 2005). Considering these observations of modern natural and laboratory taphonomic mechanisms, it is conceivable that in ancient marine environments different portions of microbial mats endured different levels of stress due to minor variations in sedimentation rates or the availability of oxygen in porewaters, and responded with metabolic strategies that may have enhanced or discouraged CFA mineralization. The mechanisms by which microorganisms may have produced such a preference – by their impact on porewater cation abundance or utilization of polyphosphate catabolism, or something else entirely – could be complex, and different from one phosphorite to another.

The geochemical and textural data presented in this study support a scenario in which phosphatic CFA cements of the Salitre Formation formed relatively

early, at or just below the seafloor and then went on to experience shallow burial and limited opportunities for diagenetic resetting of their intrinsic geochemistry. This implies that trace metals, rare earth element signatures, and metabolically-specific sulfur isotope signatures of early CFA and carbonate cements could be implemented as proxies for the reconstruction of the primary paleoenvironmental and paleoecological conditions that enabled phosphogenesis on the Ediacaran São Francisco Craton. Such measurements could further constrain the differences between the formation conditions of phosphatic compared to non-phosphatic textures.

### **3.7 Methods**

#### **Sample selection and preparation**

##### **Sample collection**

Samples from phosphatic and non-phosphatic members of the Salitre Formation were collected primarily from outcrop and drill cores of the Irecê paleobasin, capturing hundreds of meters of strata containing cross-stratified grainstone and rudstone-to-intraclast-conglomerate facies and stromatolitic facies (Fig. 3.1). Samples were correlated to stratigraphic sections, described by Sanders and Grotzinger, 2021, and several drill cores, included here (Fig. 3.2). Samples' stratigraphic height (or depth) within the measured sections and cores are shown in Figs. 3.1 and 3.2.

##### **Analysis of thin sections and slabs, selection of phases for stable isotope geochemistry**

Hand samples were cut and processed to produce thin sections and corresponding, unpolished billets or slabs ("offcuts"). These were examined via optical petrography, and with the Caltech Geological and Planetary Sciences Division Analytical Facility's scanning electron microscope (ZEISS 1550VP Field Emission SEM/EDS, using 15 kV accelerating voltage, 13 mm working distance), and micro-XRF spectrometer (Bruker 217 M4 Tornado, using 50 KeV X-ray tube voltage). Bulk mineralogy was constrained through X-ray diffraction using a PANalytical X'Pert Pro diffractometer with a Cu  $K\alpha$  source. These data — stratigraphic context, petrographic images, maps of elemental composition, and bulk mineralogy — were used to identify the most primary preserved mineral phases within phosphate bearing facies, in regions

of samples devoid of late-forming spar-filled fractures, stylolites, and other interfering textures. Powders of earliest CFA, calcite, and dolomite cements were sampled by mm-scale drilling of target fabrics.

### **Purification of CFA samples**

Mixed CFA-carbonate powder samples were placed in microcentrifuge tubes with 3%  $H_2O_2$ , shaken, then allowed to sit overnight (approximately 16 hours) to remove organic material outside of the mineral lattice. Powders were resuspended by shaking, then centrifuged for 5 minutes at 13,200 rpm. Supernate was removed and discarded. We then resuspended samples in Milli-Q filtered and deionized water, centrifuged, and discarded supernate. This Milli-Q rinse was performed a total of three times before samples were resuspended in 0.1 M acetic acid then continuously agitated for approximately 36 hours. Afterward, samples were rinsed three times with Milli-Q water again, centrifuging and discarding supernate between each rinse, then dried in an oven at 65°C for 14 hours. 7–10 mg aliquots of each rinsed, dried powder were weighed into open silver foil cups in advance of stable isotope measurements. This protocol for the preparation of CFA for stable isotope measurement is modified from that used in previous studies of carbonate and CFA geochemistry (Stolper and Eiler, 2016; R. a. Eagle et al., 2011).

### **Separation of calcite and dolomite mixtures by stepped acid digestion**

Powders composed of mixtures of calcite and dolomite were subjected to stepped phosphoric acid digestion, with the resulting  $CO_2$  gas collected in sealed pyrex tubes for analysis. Our method is adapted primarily from that of Max Lloyd, and previous workers (Guo et al., 2009; Lloyd, Eiler, and Nabelek, 2017; Al-Aasm, B. E. Taylor, and South, 1990). 15-750 mg of sample or carbonate standard powders were weighed into one side of a two-sided reaction vessel, depending on relative abundance of calcite and dolomite in the samples as determined by XRD, such that a complete reaction would produce roughly 0.1 mmol  $CO_2$ . 103% phosphoric acid was added to the other side of the vessel. The vessel was then sealed, and pumped down on a vacuum line which continuously purged the headspace of the reaction vessel while the acid was degassed by heating with a heat gun. Reaction vessels were equilibrated in a water bath at 25°C for a minimum 3 hours before being

pumped down again. To collect  $CO_2$  gas evolved from the reaction of calcite with concentrated phosphoric acid, acid was tipped into the side of the reaction vessel containing the powder. Gas was directed through the vacuum line using a system of valves. Calcite reactions proceeded at room temperature on the vacuum line, while  $CO_2$  was purified by traveling twice between a series of u-bend cold traps, chilled respectively with liquid nitrogen and ethanol slush, and finally collected in a pyrex tube. The tube was sealed with a oxygen-natural gas cutting torch at one end while the sample gas was frozen via liquid nitrogen cooling into the other end to prevent loss of sample or standard material and re-equilibration at higher temperatures. Each reaction vessel was then sealed off and removed from the vacuum line, and the acid reaction allowed to continue for approximately 24 hours in a  $50^\circ C$  water bath before repeating the vacuum line collection procedure. The gas evolved during this higher temperature digestion, after the purging of gas evolved from the room temperature reaction, was derived only from the dolomite fraction of the original powder. Thus, from a powdered mixture of calcite and dolomite, separate fractions of  $CO_2$  were collected. Note: only one reaction vessel was attached to the vacuum line at a time.

**Stable isotope measurements:  $\Delta_{47}$ ,  $\delta^{18}O$ , and  $\delta^{13}C$  of carbonate in calcite, dolomite, and francolite**

**Gas-source isotope ratio mass spectrometry**

Powders of pure calcite, dolomite, and cleaned CFA were digested sequentially in a common bath of 103% phosphoric acid under vacuum, and the resulting gases directed by automated valves through a packed GC column and into the analytical pipeline of the MAT 253 isotope ratio mass spectrometer located in Caltech's Division of Geological and Planetary Sciences. Gas extracted via stepped acid digestion and collected in sealed pyrex tubes, as described above, was directed through the GC column and Mat 253 analytical path by automated valves as well, following injection into the pathway by cracking or breaking the tubes open in an ancillary vacuum chamber.

Thus,  $CO_2$  gas derived from sample and standard gases and powders entered the analytical pathway of the MAT 253 after purification through a GC column and dehydration via a series of transfers between liquid nitrogen and dry ice cold traps. The purified  $CO_2$  from the sample or standard was then passed

through a gas ion source. Resulting ion beams corresponding to  $\frac{m}{z}$  of 44, 45, 46, 47, and 48 (ionized isotopologues of  $CO_2$ ) were analyzed by magnetic sector mass spectrometry on a Thermo Scientific MAT 253 equipped with Faraday cup detectors read through amplifiers with resistances ranging from  $3 \times 10^8 - 3 \times 10^{12} \Omega$ . Automated valves switched the gas source rapidly between the  $CO_2$  derived from each sample or standard and a reservoir of laboratory reference  $CO_2$  with well-characterized abundances of isotopologues and isotopic composition. Each measurement of sample/standard gas was comprised of 7-8 acquisitions each bracketed by acquisitions for the reference gas, such that current produced by the subset of ions striking the Faraday cups was registered continuously over a total 1344 seconds. Ion intensity ratios between  $\frac{m}{z} = 44$  and  $\frac{m}{z} = 45, 46, 47, \text{ and } 48$  (e.g., 45/44) were derived from the relationship between measured voltage  $V = I$  (current)  $\times R$  (resistance) at each Faraday cup detector.

In addition to  $CO_2$  derived from acid digestion of calcite, dolomite, and CFA samples and calcite and dolomite standards, we also repeatedly measured aliquots of  $CO_2$  gas equilibrated at 25°C and 1000°C, referred to in prior literature as equilibrated gas (EG) and heated gas (HG), respectively. These EG and HG measurements were used to project the data into an absolute reference frame, in a procedure previously described by Eiler and E. Schauble, 2004, Huntington et al., 2009, and Dennis, Affek, et al., 2011, and summarized below.

### **Isotopic data processing**

Raw data — calculated ratios of isotopologue abundances in sample, standard, EG, or HG relative to the reference gas — were projected into an absolute reference frame, examined for several metrics of data quality, and corrected for fractionation effects introduced by the analytical pipeline:

First, we used our measurements of  $CO_2$  gas equilibrated at known temperatures (EG and HG) to project all measurements into an absolute reference frame so that they would be comparable to similar measurements made at other institutions with different mass spectrometers and sample treatments. The relationship between  $\Delta_{47}$  and  $\delta_{47}$  describes the nonlinear and instrument-specific relationship between actual and measured isotopologue abundances. A plot of these values for EGs and HGs measured within the same analytical

session as samples and carbonate standards (over the course of several days to weeks) produces a linear trend which defines a reference frame for those measurements. A least-squares fit of the population of HG or EG data in  $\delta_{47}$  vs.  $\Delta_{47}$  space has an intercept equal to the difference in  $\Delta_{47}$  of the equilibrated gas and the reference gas when their bulk isotopic composition with respect to carbon and oxygen is the same — denoted in the literature as  $\Delta_{47-[EGvsWG]0}$  (Dennis, Affek, et al., 2011). This empirical  $\Delta_{47-[EGvsWG]0}$  can be plotted against theoretical values based on models of the temperature dependence of relative isotopologue abundance (Wang, E. A. Schauble, and Eiler, 2004) to plot an empirical transfer function, mapping measured  $\Delta_{47}$  to a calibration based on theoretically expected values. The empirical transfer function may change through time, but has been demonstrated to be relatively stable over the course of several weeks to one month (Dennis, Affek, et al., 2011). In the course of our measurements, it was necessary to derive two different empirical transfer functions, to project data collected from two different analytical sessions into the absolute reference frame. (Note: 2 measurements of heated gases that were beyond one and a half standard deviations of the average  $\Delta_{47}$  and  $\delta_{47}$  values for the whole population of heated gases were excluded. 11 heated gas and 9 equilibrated gas measurements remained from which to derive the empirical transfer functions.)

In a like process,  $\Delta_{48}$  values, which describe the abundance of the rare isotopologue  $^{18}\text{O}^{12}\text{C}^{18}\text{O}$ , were also projected into the absolute reference frame defined by EG and HG measurements.  $\Delta_{48,sample}$  differing significantly from  $\Delta_{48,EG/HG}$  — that of equilibrated and heated gases measured within several weeks of a given sample — are indicative of contamination by substances other than  $\text{CO}_2$ , pressure imbalance between analytical and reference ionized gas sources, or other sources of inaccuracy. There were 4 powdered samples (all CFA in composition) and 1 offline-extracted gas sample (calcite) which were excluded from the dataset presented here on the basis of  $\Delta_{48}$  values that differed from the near-stochastic values of the HG and EG measurements by more than 1‰, across all analytical sessions.

Comparison of measurements of samples and standards to the shot noise limit was used as an additional screen for data quality. The shot noise limit is the limit of a measurement's precision given the total number of ions that reach the Faraday cup detectors, assuming each ion generating a voltage at the detector represents a discrete event, and that the ion beam represents a

population of such discrete events (a Poisson distribution). This limit, for all of the measurements not already excluded from analysis on the basis of  $\Delta_{48}$  anomalies, was approximately 0.01‰. Acquisitions for which the standard error of  $\Delta_{47}$  exceeded the shot noise limit of 0.01‰ by a factor of two or more were considered to have unacceptable, uncharacterizable sources of error, and were excluded from analysis. Overall, other than the 4 measurements already excluded on the basis of their  $\Delta_{48}$  anomalies, only one additional sample was excluded from analysis for having a  $\Delta_{47}$  standard error greater than 2x its shot noise limit of 0.00957‰.

Next, the remaining samples and standards  $\Delta_{47}$  measurements (projected into the absolute reference frame) were corrected for the difference in the oxygen isotope fractionation between carbonate-containing minerals and the  $CO_2$  gas liberated during their incomplete reaction with concentrated phosphoric acid. The fractionation effect of the calcite-phosphoric acid reaction results in a +0.092‰ difference between  $\Delta_{47}$  values of the calcite-derived  $CO_2$  gas produced at 25°C and that produced at 90°C. This effect was measured by previous workers for calcite (Guo et al., 2009; Henkes, Passey, Wanamaker, et al., 2013), and has since been utilized for similar data processing procedures for calcite and CFA alike (R. A. Eagle et al., 2010; Stolper and Eiler, 2015; Stolper and Eiler, 2016). The difference in  $\Delta_{47}$  values of the calcite-derived  $CO_2$  gas produced at 25°C and that produced at 50°C is +0.07‰ (Murray, Arienzo, and Swart, 2016; Müller et al., 2017). All  $\Delta_{47}$  values reported in Table 3.2 assume an acid reaction temperature of 90°C in order that the the  $\Delta_{47}$ -temperature relation derived by Bonifacie et al., 2017, which assumes acid digestion at 90°C, could be applied to all. This means that the two dolomite samples measured offline at 50°C have had a correction of -0.022 applied to their measured  $\Delta_{47}$  values — the difference expected between the  $\Delta_{47}$  values of the carbonate-derived  $CO_2$  gas produced at 70°C and that produced at 90°C.

Finally, as a check of accuracy, the  $\Delta_{47}$  values of calcite and dolomite standards measured alongside the samples, after projection into an absolute reference frame and correction for acid reaction temperature, were compared to their accepted  $\Delta_{47}$  values. Alternating with our 21 measurements of unknown samples, we made 16 measurements of high-temperature calcite standard Carrara Limestone (nominally,  $\Delta_{47} = 0.405$ ‰), 10 measurements of low-temperature calcite standard Travertine TV-04 (nominally,  $\Delta_{47} = 0.665$ ‰),

and 2 measurements of ETH-1, a second high-temperature calcite standard (nominally,  $\Delta_{47} = 0.32\text{‰}$ ). Standard measurements for which the difference between measured and accepted  $\Delta_{47}$  was greater than 2x the shot noise limit were flagged, and samples measurements bracketed by such standards would have been excluded. However, there were no samples excluded from analysis by this metric that had not already been excluded on the basis of their  $\Delta_{48}$  anomalies and/or their  $\Delta_{47}$  standard errors.

### Calculating $\Delta_{47}$ temperatures and $\delta^{18}O$ of formational fluids

$\Delta_{47}$  values, projected into an absolute reference frame (ARF), were used to calculate an apparent temperature. This value ideally represents the temperature at which a given mineral phase was last closed to exchange of carbon and oxygen isotopes in structural carbonate with carbon and oxygen isotopes in fluids. We used a  $\Delta_{47}$ -temperature relationship established empirically through the measurement of a range of carbonate standards of known isotopic composition and thermal history by Bonifacie et al.:  $\sqrt{\frac{42200}{(\Delta_{47,ARF} \pm \sigma_{\Delta_{47}}) - 0.1262}} - 273.15 = T(^{\circ}C)$ , Bonifacie et al., 2017.  $\Delta_{47,ARF}$  here refers to  $\Delta_{47}$  measurements projected into an absolute reference frame established — as above-described — by measurement of heated and low-temperature gases alongside samples and standards. The Bonifacie et al. (2017) relationship is calibrated assuming powdered carbonate samples are reacted with concentrated phosphoric acid at  $90^{\circ}C$  to liberate  $CO_2$  for analysis, and so  $\Delta_{47}$  values for samples reacted at lower temperatures were corrected for the difference in fractionation effects of acid digestion at different temperatures (see previous section).

$\delta^{18}O$  values of carbonate in calcite, dolomite, and CFA are also subject to the kinetic fractionation effect of the phosphoric acid digestion reaction. The  $\delta^{18}O$  of the structural carbonate in dolomite is enriched by  $9.27\text{‰}$ , relative to the  $\delta^{18}O$  of the  $CO_2$  gas liberated by reaction with 103% phosphoric acid at  $90^{\circ}C$ . At  $50^{\circ}C$ , dolomite is enriched by  $10.60\text{‰}$ , relative to the  $\delta^{18}O$  of the  $CO_2$  gas liberated by acid digestion. These values are interpolated from previous workers' acid digestion experiments (Rosenbaum and Sheppard, 1986; Lloyd, Ryb, and Eiler, 2018). The  $\delta^{18}O$  of the structural carbonate in calcite is enriched by  $8.10\text{‰}$ , relative to the  $\delta^{18}O$  of the  $CO_2$  gas liberated by reaction with 103% phosphoric acid at  $90^{\circ}C$ ; a similar enrichment is thought to exist

for CFA, though this has not been directly measured (Kim, Mucci, and Bruce E. Taylor, 2007; Stolper and Eiler, 2016). The  $\delta^{18}O_{mineral}$  values reported in Table 4.1 and Fig. 3.3 are the measured  $\delta^{18}O_{gas}$  minus the appropriate acid digestion correction for the given mineral and acid reaction temperature.

Using  $\Delta_{47}$  temperatures and  $\delta^{18}O$  of carbonate in calcite, dolomite, and CFA, we then calculated the  $\delta^{18}O$  of the fluids that were last capable of isotopic exchange with the minerals' structural carbonate. For this calculation, we used the equilibrium fractionation relationship derived by Kim and O'Neil, 1997 for calcite and CFA samples:  $\delta^{18}O_{mineral,VPDB} - \frac{18030}{T_{\Delta 47}(K)} + 32.4 = \delta^{18}O_{water,VPDB}$  (Kim and O'Neil, 1997). We used the relationship derived by Horita (2014) for dolomite samples:  $\delta^{18}O_{mineral,VPDB} - \frac{3140000}{T_{\Delta 47}(K)^2} - 3.14 = \delta^{18}O_{water,VPDB}$  Horita, 2014.  $\delta^{18}O_{water,VPDB}$  values were converted to  $\delta^{18}O_{water,VSMOW}$  via:  $1.03092 \times \delta^{18}O_{water,VPDB} = \delta^{18}O_{water,VSMOW}$  (Kim, Coplen, and Horita, 2015).

### 3.8 Acknowledgements

We extend a heartfelt thanks to our collaborators in Brazil for their expertise, field assistance, patience, and comments: Anelize Bahniuk Rumbelsperger, Leonardo Fadel Cury, Victor Dorneles, Almério Barros França, Angela Rodizes, Gabriel Ruviano, Larissa Santos, Lucas Valore, Kimberly Viera, and Hugo Yamassaki of the Laboratório de Análises de Minerais e Rochas (LAMIR) e Laboratório de Análise de Bacias (LABAP) da Universidade Federal do Paraná, as well as Filipe Nery Falcão. We also thank Michele Santos, Ricardo Ramos Spreafico, and many others from the Companhia Baiana de Pesquisa Mineral (CBPM) for their expertise in the regional geology of Bahia, and for providing us access to Salitre Fm. drill cores.

Many thanks as well to Nami Kitchen, Nivedita (Nithya) Thiagarajan, Uri Ryb, and Max Lloyd for their graciously given expertise in the stable isotope techniques employed in this study.

We would also like to acknowledge the many farmers, miners, educators, and conservationists of the Chapada Diamantina and Cavernas do Peruaçu regions for their generosity, kindness, and insightful guidance.

We acknowledge the Xakriabá, the communities of and surrounding the historic Quilombo da Gruta dos Brejões, as well as other indigenous peoples whose names and identities may have been lost to colonialism and occupa-

tion, whose land is the subject of this work. We endeavor to find meaningful ways to memorialize, preserve, and communicate their stories, and learn to contextualize our small works in the history of their stewardship, exploration, and purposing of the land that is now Brazil.

We also wish to thank the reviewers, and to acknowledge that this work was supported by the National Science Foundation Graduate Research Fellowship Program (NSF GRFP), and the Simons Foundation Collaboration on the Origins of Life.

## References

- Al-Aasm, Ihsan S., B. E. Taylor, and B. South (1990). “Stable isotope analysis of multiple carbonate samples using selective acid extraction”. In: *Chemical Geology: Isotope Geoscience Section* 80.2, pp. 119–125. ISSN: 01689622. DOI: 10.1016/0168-9622(90)90020-D.
- Alkmim, Fernando F., Stephen Marshak, et al. (2006). “Kinematic evolution of the Araçuaí-West Congo orogen in Brazil and Africa: Nutcracker tectonics during the Neoproterozoic assembly of Gondwana”. In: *Precambrian Research* 149.1-2, pp. 43–64. ISSN: 03019268. DOI: 10.1016/j.precamres.2006.06.007.
- Alkmim, Fernando F. and Marcelo A. Martins-Neto (2012). “Proterozoic first-order sedimentary sequences of the São Francisco craton, eastern Brazil”. In: *Marine and Petroleum Geology* 33.1, pp. 127–139. ISSN: 02648172. DOI: 10.1016/j.marpetgeo.2011.08.011. URL: <http://dx.doi.org/10.1016/j.marpetgeo.2011.08.011>.
- Allan, J. R. and R. K. Matthews (2009). “Isotope Signatures Associated with Early Meteoric Diagenesis”. In: *Carbonate Diagenesis*, pp. 197–217. DOI: 10.1002/9781444304510.ch16.
- Anderson, Ross P. et al. (2017). “Doushantuo-type microfossils from latest Ediacaran phosphorites of northern Mongolia”. In: *Geology* 45.12, pp. 1079–1082. ISSN: 19432682. DOI: 10.1130/G39576.1.
- Anttila, Eliel, Francis Macdonald, and Uyanga Bold (2021). “Stratigraphy of the Khuvsgul Group, Mongolia”. In: *Mongolian Geoscientist* 26.52, pp. 2–15.
- Arning, E. T. et al. (2009). “Bacterial formation of phosphatic laminites off Peru”. In: *Geobiology* 7.3, pp. 295–307. ISSN: 14724669. DOI: 10.1111/j.1472-4669.2009.00197.x.
- Banerjee, D M, P C Basu, and N Srivastava (1980). “Petrology, Mineralogy, Geochemistry, and Origin of the Precambrian Aravallian Phosphorite De-

- posits of Udaipur and Jhabua, India”. In: *Economic Geology* 75.3, pp. 1181–1199.
- Banerjee, D. M. (1971). “Precambrian stromatolitic phosphorites of Udaipur, Rajasthan, India”. In: *Bulletin of the Geological Society of America* 82.8, pp. 2319–2330. ISSN: 19432674. DOI: 10.1130/0016-7606(1971)82[2319:PSPOUR]2.0.CO;2.
- Bathurst, Robin GC (1975). *Carbonate sediments and their diagenesis*. Second. Amsterdam: Elsevier.
- Bertrand-Sarfati, Janine et al. (1997). “Lower Cambrian apatitic stromatolites and phospharenites related to the glacio-eustatic cratonic rebound (Sahara, Algeria)”. In: *Journal of Sedimentary Research* 67.5, pp. 957–974. ISSN: 1359-0286. DOI: 10.1016/j.cossms.2010.07.001. URL: <http://dx.doi.org/10.1016/j.cossms.2010.07.001>.
- Bonifacie, Magali et al. (2017). “Calibration of the dolomite clumped isotope thermometer from 25 to 350 °C, and implications for a universal calibration for all (Ca, Mg, Fe)CO<sub>3</sub> carbonates”. In: *Geochimica et Cosmochimica Acta* 200, pp. 255–279. ISSN: 00167037. DOI: 10.1016/j.gca.2016.11.028. URL: <http://dx.doi.org/10.1016/j.gca.2016.11.028>.
- Brand, Willi A., Sergey S. Assonov, and Tyler B. Coplen (2010). “Correction for the 17O interference in  $\delta(13C)$  measurements when analyzing CO<sub>2</sub> with stable isotope mass spectrometry (IUPAC Technical Report)”. In: *Pure and Applied Chemistry* 82.8, pp. 1719–1733. ISSN: 00334545. DOI: 10.1351/PAC-REP-09-01-05.
- Bustillo, Maria Ángeles (2010). “Silicification of continental carbonates”. In: *Carbonates in Continental Settings: processes, facies and applications* 62, pp. 153–174.
- Caird, R. A. et al. (2017). “Ediacaran stromatolites and intertidal phosphorite of the Salitre Formation, Brazil: Phosphogenesis during the Neoproterozoic Oxygenation Event”. In: *Sedimentary Geology* 350. January, pp. 55–71. ISSN: 00370738. DOI: 10.1016/j.sedgeo.2017.01.005. URL: <http://dx.doi.org/10.1016/j.sedgeo.2017.01.005>.
- Canfield, Don E., Simon W. Poulton, and Guy M. Narbonne (2007). “Late-Neoproterozoic deep-ocean oxygenation and the rise of animal life”. In: *Science* 315.5808, pp. 92–95. ISSN: 00368075. DOI: 10.1126/science.1135013.
- Canfield, Donald E. and Andreas Teske (1996). “Late proterozoic rise in atmospheric oxygen concentration inferred from phylogenetic and sulphur-isotope studies”. In: *Nature* 382.6587, pp. 127–132. ISSN: 00280836. DOI: 10.1038/382127a0.

- Caxito, Fabrício de Andrade et al. (2012). “Marinoan glaciation in east central Brazil”. In: *Precambrian Research* 200-203, pp. 38–58. ISSN: 03019268. DOI: 10.1016/j.precamres.2012.01.005.
- Chen, Duo Fu et al. (2003). “Possible REE constraints on the depositional and diagenetic environment of Doushantuo Formation phosphorites containing the earliest metazoan fauna”. In: *Chemical Geology* 201.1-2, pp. 103–118. ISSN: 00092541. DOI: 10.1016/S0009-2541(03)00235-3.
- Choudhuri, R. (1990). “Two decades of phosphorite investigations in India”. In: *Geological Society Special Publication* 52.52, pp. 305–311. ISSN: 03058719. DOI: 10.1144/GSL.SP.1990.052.01.22.
- Compton, John S. and Eugene W. Bergh (2016). “Phosphorite deposits on the Namibian shelf”. In: *Marine Geology* 380, pp. 290–314. ISSN: 00253227. DOI: 10.1016/j.margeo.2016.04.006. URL: <http://dx.doi.org/10.1016/j.margeo.2016.04.006>.
- Cook, Peter J. and Michael W. McElhinny (1979). “A reevaluation of the spatial and temporal distribution of sedimentary phosphate deposits in the light of plate tectonics”. In: *Economic Geology* 74, pp. 315–330.
- Cordani, Umberto G. and Kei Sato (1999). “Crustal evolution of the South American platform, based on Nd isotopic systematics on granitoid rocks”. In: *Episodes* 22.3, pp. 167–173. ISSN: 07053797. DOI: 10.18814/epiugs/1999/v22i3/003.
- Cruz, Simone C.P. and Fernando F. Alkmim (2006). “The tectonic interaction between the Paramirim Aulacogen and the Araçuaí Belt, São Francisco craton region, Eastern Brazil”. In: *Anais da Academia Brasileira de Ciências* 78.1, pp. 151–173. ISSN: 00027812.
- Cui, Huan et al. (2015). “Redox architecture of an Ediacaran ocean margin: Integrated chemostratigraphic correlation of the Doushantuo Formation, South China”. In: *Chemical Geology* 405, pp. 48–62. ISSN: 00092541. DOI: 10.1016/j.chemgeo.2015.04.009. URL: <http://dx.doi.org/10.1016/j.chemgeo.2015.04.009>.
- Dalton de Souza, João et al. (2003). *Mapa geológico do Estado da Bahia*. Tech. rep. CPRM - Serviço Geológico do Brasil, Governo do Estado da Bahia, Ministério de Minas e Energia, Companhia Baiana de Pesquisa Mineral.
- Decho, Alan W. and Tony Gutierrez (2017). “Microbial extracellular polymeric substances (EPSs) in ocean systems”. In: *Frontiers in Microbiology* 8.922.
- Dennis, Kate J., Hagit P. Affek, et al. (2011). “Defining an absolute reference frame for ‘clumped’ isotope studies of CO<sub>2</sub>”. In: *Geochimica et Cosmochimica Acta* 75.22, pp. 7117–7131. ISSN: 00167037. DOI: 10.1016/

j.gca.2011.09.025. URL: <http://dx.doi.org/10.1016/j.gca.2011.09.025>.

- Dennis, Kate J. and Daniel P. Schrag (2010). “Clumped isotope thermometry of carbonatites as an indicator of diagenetic alteration”. In: *Geochimica et Cosmochimica Acta* 74.14, pp. 4110–4122. ISSN: 00167037. DOI: 10.1016/j.gca.2010.04.005. URL: <http://dx.doi.org/10.1016/j.gca.2010.04.005>.
- Drummond, Justin B. R. et al. (2015). “Neoproterozoic peritidal phosphorite from the Sete Lagoas Formation (Brazil) and the Precambrian phosphorus cycle”. In: *Sedimentology* 62.7, pp. 1978–2008. DOI: 10.1111/sed.12214.
- Eagle, Robert a et al. (2011). “Dinosaur body temperatures determined from isotopic ordering in fossil biominerals”. In: *Science* 333, pp. 443–445.
- Eagle, Robert A. et al. (2010). “Body temperatures of modern and extinct vertebrates from  $^{13}\text{C}$ - $^{18}\text{O}$  bond abundances in bioapatite”. In: *Proceedings of the National Academy of Sciences of the United States of America* 107.23, pp. 10377–10382. ISSN: 00278424. DOI: 10.1073/pnas.0911115107.
- Eiler, John M. and Edwin Schauble (2004). “ $^{18}\text{O}$  $^{13}\text{C}$  $^{16}\text{O}$  in Earth’s atmosphere”. In: *Geochimica et Cosmochimica Acta* 68.23, pp. 4767–4777. ISSN: 00167037. DOI: 10.1016/j.gca.2004.05.035.
- Ferry, John M. et al. (2010). “Assessment of grain-scale homogeneity and equilibration of carbon and oxygen isotope compositions of minerals in carbonate-bearing metamorphic rocks by ion microprobe”. In: *Geochimica et Cosmochimica Acta* 74.22, pp. 6517–6540. ISSN: 00167037. DOI: 10.1016/j.gca.2010.08.039. URL: <http://dx.doi.org/10.1016/j.gca.2010.08.039>.
- Fike, D. A. et al. (2006). “Oxidation of the Ediacaran ocean”. In: *Nature* 444.7120, pp. 744–747. ISSN: 14764687. DOI: 10.1038/nature05345.
- Flügel, Erik (2010). *Microfacies of Carbonate Rocks: Analysis, Interpretation, and Application*. Second. Berlin Heidelberg: Springer-Verlag. ISBN: 9783642037955.
- Föllmi, KB (1996). “The phosphorus cycle, phosphogenesis phosphate-rich deposits”. In: *Earth-Science Reviews* 40, pp. 55–124.
- Fonseca, Marco Antônio et al. (2014). *Mapa Geológico do Estado de Minas Gerais*. Tech. rep. CPRM - Serviço Geológico do Brasil, Governo de Minas, Ministerio de Minas e Energia, Companhia de Desenvolvimento Econômico de Minas Gerais.
- Goldberg, Samuel L. et al. (2021). “A high-resolution record of early Paleozoic climate”. In: *Proceedings of the National Academy of Sciences of the United States of America* 118.6. ISSN: 10916490. DOI: 10.1073/pnas.2013083118.

- Goldhammer, Tobias et al. (2010). “Microbial sequestration of phosphorus in anoxic upwelling sediments”. In: *Nature Geoscience* 3.8, pp. 557–561. ISSN: 17520894. DOI: 10.1038/ngeo913.
- Guimarães, J. T. et al. (2011). “The Bebedouro Formation, Una Group, Bahia (Brazil)”. In: *Geological Society Memoir* 36.1, pp. 503–508. ISSN: 04354052. DOI: 10.1144/M36.47.
- Guo, Weifu et al. (2009). “Isotopic fractionations associated with phosphoric acid digestion of carbonate minerals: Insights from first-principles theoretical modeling and clumped isotope measurements”. In: *Geochimica et Cosmochimica Acta* 73.24, pp. 7203–7225. ISSN: 00167037. DOI: 10.1016/j.gca.2009.05.071. URL: <http://dx.doi.org/10.1016/j.gca.2009.05.071>.
- Halverson, Galen P. et al. (2010). “Neoproterozoic chemostratigraphy”. In: *Precambrian Research* 182.4, pp. 337–350. ISSN: 03019268. DOI: 10.1016/j.precamres.2010.04.007. URL: <http://dx.doi.org/10.1016/j.precamres.2010.04.007>.
- Heggie, D. T. et al. (1990). “Organic carbon cycling and modern phosphorite formation on the East Australian continental margin: An overview”. In: *Geological Society Special Publication* 52.52, pp. 87–117. ISSN: 03058719. DOI: 10.1144/GSL.SP.1990.052.01.07.
- Heilbron, Monica, Umberto Giuseppe Cordani, and Fernando F. Alkmim (2017). “São Francisco Craton, Eastern Brazil”. In: *Regional Geology Reviews* December, pp. 3–13. DOI: 10.1007/978-3-319-01715-0. URL: <http://link.springer.com/10.1007/978-3-319-01715-0>  
[https://doi.org/10.1007/978-3-319-01715-0\\_16](https://doi.org/10.1007/978-3-319-01715-0_16).
- Henkes, Gregory A., Benjamin H. Passey, Ethan L. Grossman, et al. (2014). “Temperature limits for preservation of primary calcite clumped isotope paleotemperatures”. In: *Geochimica et Cosmochimica Acta* 139, pp. 362–382. ISSN: 00167037. DOI: 10.1016/j.gca.2014.04.040.
- Henkes, Gregory A., Benjamin H. Passey, Alan D. Wanamaker, et al. (2013). “Carbonate clumped isotope compositions of modern marine mollusk and brachiopod shells”. In: *Geochimica et Cosmochimica Acta* 106, pp. 307–325. ISSN: 00167037. DOI: 10.1016/j.gca.2012.12.020. URL: <http://dx.doi.org/10.1016/j.gca.2012.12.020>.
- Hesse, R. (1990). “Silica diagenesis: origin of inorganic and replacement cherts”. In: *Earth-Science Reviews* 26, pp. 253–276.
- Horita, Juske (2014). “Oxygen and carbon isotope fractionation in the system dolomite-water-CO<sub>2</sub> to elevated temperatures”. In: *Geochimica et Cosmochimica Acta* 129, pp. 111–124. ISSN: 00167037. DOI: 10.1016/j.gca.2013.12.027.

- Huntington, K. W. et al. (2009). "Methods and limitations of 'clumped' CO<sub>2</sub> isotope ( $\Delta 47$ ) analysis by gas-source isotope ratiomass spectrometry". In: *Journal of Mass Spectrometry* 44.9, pp. 1318–1329. ISSN: 10765174. DOI: 10.1002/jms.1614.
- Iglesias, Mario and Alexandre Uhlein (2009). "Estratigrafia do Grupo Bambuí e coberturas fanerozóicas no vale do rio São Francisco, norte de Minas Gerais". In: *Revista Brasileira de Geociências* 39.2, pp. 256–266. DOI: 10.25249/0375-7536.2009392256266.
- Ilyin, A. V. (2004). "The Khubsugul phosphate-bearing basin: New data and concepts". In: *Lithology and Mineral Resources* 39.5, pp. 454–467. ISSN: 00244902. DOI: 10.1023/B:LIMI.0000040735.76025.80.
- Ilyin, A. V. and G. I. Ratnikova (1981). "Primary, bedded, structureless phosphorite of the Khubsugul Basin, Mongolia." In: *Journal of Sedimentary Petrology* 51.4, pp. 1215–1222. ISSN: 00224472. DOI: 10.1306/212f7e69-2b24-11d7-8648000102c1865d.
- Ilyin, A. V., N. S. Zaitsev, and Z. Bjamba (1986). *Proterozoic and Cambrian phosphorites - deposits: Khubsugul, Mongolian People's Republic*.
- Jahnke, Richard A. et al. (1983). "The present day formation of apatite in Mexican continental margin sediments". In: *Geochimica et Cosmochimica Acta* 47.2, pp. 259–266. ISSN: 00167037. DOI: 10.1016/0016-7037(83)90138-2.
- Jiang, Ganqing et al. (2011). "Stratigraphy and paleogeography of the Ediacaran Doushantuo Formation (ca. 635-551Ma) in South China". In: *Gondwana Research* 19.4, pp. 831–849. ISSN: 1342937X. DOI: 10.1016/j.gr.2011.01.006. URL: <http://dx.doi.org/10.1016/j.gr.2011.01.006>.
- Kim, Sang Tae, Tyler B. Coplen, and Juske Horita (2015). "Normalization of stable isotope data for carbonate minerals: Implementation of IUPAC guidelines". In: *Geochimica et Cosmochimica Acta* 158, pp. 276–289. ISSN: 00167037. DOI: 10.1016/j.gca.2015.02.011. URL: <http://dx.doi.org/10.1016/j.gca.2015.02.011>.
- Kim, Sang Tae, Alfonso Mucci, and Bruce E. Taylor (2007). "Phosphoric acid fractionation factors for calcite and aragonite between 25 and 75 °C: Revisited". In: *Chemical Geology* 246.3-4, pp. 135–146. ISSN: 00092541. DOI: 10.1016/j.chemgeo.2007.08.005.
- Kim, Sang Tae and James R. O'Neil (1997). "Equilibrium and nonequilibrium oxygen isotope effects in synthetic carbonates". In: *Geochimica et Cosmochimica Acta* 61.16, pp. 3461–3475. ISSN: 00167037. DOI: 10.1016/S0016-7037(97)00169-5.

- Küster-Heins, Kathrin et al. (2010). “Phosphorus cycling in marine sediments from the continental margin off Namibia”. In: *Marine Geology* 274.1-4, pp. 95–106. ISSN: 00253227. DOI: 10.1016/j.margeo.2010.03.008. URL: <http://dx.doi.org/10.1016/j.margeo.2010.03.008>.
- Kyle, J. Richard and Aroldo Misi (1997). “Origin of zn-pb-ag sulfide mineralization within upper proterozoic phosphate-rich carbonate strata, irecê basin, bahia, brazil”. In: *International Geology Review* 39.5, pp. 383–399. ISSN: 19382839. DOI: 10.1080/00206819709465279.
- Laakso, Thomas A. et al. (2020). “Ediacaran reorganization of the marine phosphorus cycle”. In: *Proceedings of the National Academy of Sciences of the United States of America* 117.22. ISSN: 10916490. DOI: 10.1073/pnas.1916738117.
- Lepland, Aivo et al. (2014). “Potential influence of sulphur bacteria on Palaeoproterozoic phosphogenesis”. In: *Nature Geoscience* 7.1, pp. 20–24. ISSN: 17520894. DOI: 10.1038/ngeo2005.
- Leśniak, P. M. et al. (2003). “Extreme sulfur isotopic fractionation between sulfate of carbonate fluorapatite and authigenic pyrite in the Neocomian sequence at Wawał, Central Poland”. In: *Chemical Geology* 200.3-4, pp. 325–337. ISSN: 00092541. DOI: 10.1016/S0009-2541(03)00198-0.
- Lloyd, Max K., John M. Eiler, and Peter I. Nabelek (2017). “Clumped isotope thermometry of calcite and dolomite in a contact metamorphic environment”. In: *Geochimica et Cosmochimica Acta* 197, pp. 323–344. ISSN: 00167037. DOI: 10.1016/j.gca.2016.10.037. URL: <http://dx.doi.org/10.1016/j.gca.2016.10.037>.
- Lloyd, Max K., Uri Ryb, and John M. Eiler (2018). “Experimental calibration of clumped isotope reordering in dolomite”. In: *Geochimica et Cosmochimica Acta* 242, pp. 1–20. ISSN: 00167037. DOI: 10.1016/j.gca.2018.08.036. URL: <https://doi.org/10.1016/j.gca.2018.08.036>.
- Martins-Neto, M. A., A. C. Pedrosa-Soares, and S. A.A. Lima (2001). “Tectono-sedimentary evolution of sedimentary basins from Late Paleoproterozoic to Late Neoproterozoic in the São Francisco craton and Araçuaí fold belt, Eastern Brazil”. In: *Sedimentary Geology* 141-142, pp. 343–370. ISSN: 00370738. DOI: 10.1016/S0037-0738(01)00082-3.
- Misi, A. and J. R. Kyle (1994). “Upper Proterozoic carbonate stratigraphy, diagenesis, and stromatolitic phosphorite formation, Irece Basin, Bahia, Brazil”. In: *Journal of Sedimentary Research A: Sedimentary Petrology and Processes* 64 A.2, pp. 299–310.
- Misi, Aroldo, Alan J. Kaufman, et al. (2007). “Chemostratigraphic correlation of Neoproterozoic successions in South America”. In: *Chemical Geology* 237.1-2, pp. 143–167. ISSN: 00092541. DOI: 10.1016/j.chemgeo.2006.06.019.

- Misi, Aroldo and Ján Veizer (1998). “Neoproterozoic carbonate sequences of the Una Group, Irecê Basin, Brazil: Chemostratigraphy, age and correlations”. In: *Precambrian Research* 89.1-2, pp. 87–100. ISSN: 03019268.
- Moore, Kelsey R., Jian Gong, et al. (2021). “A new model for silicification of cyanobacteria in Proterozoic tidal flats”. In: *Geobiology* 19.5, pp. 438–449. ISSN: 14724669. DOI: 10.1111/gbi.12447.
- Moore, Kelsey R., Mihkel Pajusalu, et al. (2020). “Biologically mediated silicification of marine cyanobacteria and implications for the Proterozoic fossil record”. In: *Geology* 48.9, pp. 862–866. ISSN: 19432682. DOI: 10.1130/G47394.1.
- Müller, Inigo A. et al. (2017). “Clumped isotope fractionation during phosphoric acid digestion of carbonates at 70 °C”. In: *Chemical Geology* 449, pp. 1–14. ISSN: 00092541. DOI: 10.1016/j.chemgeo.2016.11.030.
- Murray, Sean T., Monica M. Arienzo, and Peter K. Swart (2016). “Determining the  $\Delta 47$  acid fractionation in dolomites”. In: *Geochimica et Cosmochimica Acta* 174, pp. 42–53. ISSN: 00167037. DOI: 10.1016/j.gca.2015.10.029. URL: <http://dx.doi.org/10.1016/j.gca.2015.10.029>.
- Muscente, A. D., Andrew D. Hawkins, and Shuhai Xiao (2015). “Fossil preservation through phosphatization and silicification in the Ediacaran Doushan-tuo Formation (South China): A comparative synthesis”. In: *Palaeogeography, Palaeoclimatology, Palaeoecology* 434, pp. 46–62. ISSN: 00310182. DOI: 10.1016/j.palaeo.2014.10.013. URL: <http://dx.doi.org/10.1016/j.palaeo.2014.10.013>.
- Okubo, J. et al. (2018). “Phosphogenesis, aragonite fan formation and seafloor environments following the Marinoan glaciation”. In: *Precambrian Research* 311.May 2017, pp. 24–36. ISSN: 03019268. DOI: 10.1016/j.precamres.2018.04.002. URL: <https://doi.org/10.1016/j.precamres.2018.04.002>.
- Osokin, P.V. and A.V. Tyzhinov (1998). *Precambrian tilloids in the Okhubsugul phosphorite-bearing basin (Eastern Sayan, Northern Mongolia)*.
- Paula-Santos, Gustavo Macedo et al. (2015). “New evidence of an Ediacaran age for the Bambuí Group in southern São Francisco craton (eastern Brazil) from zircon U-Pb data and isotope chemostratigraphy”. In: *Gondwana Research* 28.2, pp. 702–720. ISSN: 1342937X. DOI: 10.1016/j.gr.2014.07.012. URL: <http://dx.doi.org/10.1016/j.gr.2014.07.012>.
- Pruss, Sara B. et al. (2019). “Phosphatized early Cambrian archaeocyaths and small shelly fossils (SSFs) of southwestern Mongolia”. In: *Palaeogeography, Palaeoclimatology, Palaeoecology* 513, pp. 166–177. ISSN: 00310182. DOI: 10.1016/j.palaeo.2017.07.002. URL: <https://doi.org/10.1016/j.palaeo.2017.07.002>.

- Redivo, Henrique V., Ana M.P. Mizusaki, and Ana V.A. Santana (2019). “REE patterns and trustworthiness of stable carbon isotopes of Salitre Formation, Irecê Basin (Neoproterozoic), São Francisco Craton”. In: *Journal of South American Earth Sciences* 90.November 2018, pp. 255–264. ISSN: 08959811. DOI: 10.1016/j.jsames.2018.11.030. URL: <https://doi.org/10.1016/j.jsames.2018.11.030>.
- Reis, Humberto L.S., Fernando F. Alkmim, et al. (2016). “The São Francisco Basin”. In: *The São Francisco Craton, Eastern Brazil: Tectonic Genealogy of a Miniature Continent*. Ed. by Monica Heilbron, Umberto G. Cordani, and Fernando F. Alkmim. 1st ed. August. Springer, pp. 117–143. ISBN: 9783319017150. DOI: 10.1007/978-3-319-01715-0.
- Reis, Humberto L.S., João F. Suss, et al. (2017). “Ediacaran forebulge grabens of the southern São Francisco basin, SE Brazil: Craton interior dynamics during West Gondwana assembly”. In: *Precambrian Research* 302.September, pp. 150–170. ISSN: 03019268. DOI: 10.1016/j.precamres.2017.09.023. URL: <http://dx.doi.org/10.1016/j.precamres.2017.09.023>.
- Rosenbaum, J. and S. M.F. Sheppard (1986). “An isotopic study of siderites, dolomites and ankerites at high temperatures”. In: *Geochimica et Cosmochimica Acta* 50.6, pp. 1147–1150. ISSN: 00167037. DOI: 10.1016/0016-7037(86)90396-0.
- Sallstedt, T. et al. (2018). “Evidence of oxygenic phototrophy in ancient phosphatic stromatolites from the Paleoproterozoic Vindhyan and Aravalli Supergroups, India”. In: *Geobiology* 16.2, pp. 139–159. ISSN: 14724669. DOI: 10.1111/gbi.12274.
- Sanders, Cecilia and John Grotzinger (2021). “Sedimentological and stratigraphic constraints on depositional environment for Ediacaran carbonate rocks of the São Francisco Craton: Implications for phosphogenesis and paleoecology”. In: *Precambrian Research* 363.June, p. 106328. ISSN: 03019268. DOI: 10.1016/j.precamres.2021.106328. URL: <https://doi.org/10.1016/j.precamres.2021.106328>.
- Schenau, S. J., C. P. Slomp, and G. J. De Lange (2000). “Phosphogenesis and active phosphorite formation in sediments from the Arabian Sea oxygen minimum zone”. In: *Marine Geology* 169.1-2, pp. 1–20. ISSN: 00253227. DOI: 10.1016/S0025-3227(00)00083-9.
- Scholz, Florian et al. (2011). “Early diagenesis of redox-sensitive trace metals in the Peru upwelling area - response to ENSO-related oxygen fluctuations in the water column”. In: *Geochimica et Cosmochimica Acta* 75.22, pp. 7257–7276. ISSN: 00167037. DOI: 10.1016/j.gca.2011.08.007. URL: <http://dx.doi.org/10.1016/j.gca.2011.08.007>.

- Schulz, Heide N. and Horst D. Schulz (2005). “Large sulfur bacteria and the formation of phosphorite”. In: *Science* 307.5708, pp. 416–418. ISSN: 00368075. DOI: 10.1126/science.1103096.
- Schwid, Maxwell F. et al. (2020). “Iron phosphate in the Ediacaran Doushantuo Formation of South China: A previously undocumented marine phosphate sink”. In: *Palaeogeography, Palaeoclimatology, Palaeoecology* 560. August, p. 109993. ISSN: 00310182. DOI: 10.1016/j.palaeo.2020.109993. URL: <https://doi.org/10.1016/j.palaeo.2020.109993>.
- Sergeev, Vladimir N., J. William Schopf, and Anatoliy B. Kudryavtsev (2020). “Global microfossil changes through the Precambrian-Cambrian phosphogenic event: The Shabakta Formation of the phosphorite-bearing Maly Karatau Range, South Kazakhstan”. In: *Precambrian Research* 349. December 2018, p. 105386. ISSN: 03019268. DOI: 10.1016/j.precamres.2019.105386. URL: <https://doi.org/10.1016/j.precamres.2019.105386>.
- Shields, Graham and Peter Stille (2001). “Diagenetic constraints on the use of cerium anomalies as palaeoseawater redox proxies: an isotopic and REE study of Cambrian phosphorites”. In: *Chemical Geology* 175, pp. 29–48.
- Shiraishi, Fumito et al. (2019). “Potential photosynthetic impact on phosphate stromatolite formation after the Marinoan glaciation: Paleooceanographic implications”. In: *Sedimentary Geology* 380, pp. 65–82. ISSN: 00370738. DOI: 10.1016/j.sedgeo.2018.11.014. URL: <https://doi.org/10.1016/j.sedgeo.2018.11.014>.
- Silva, Mariana B. et al. (2020). “Influence of culture conditions on the production of extracellular polymeric substances (EPS) by *Arthrospira platensis*”. In: *Bioresources and Bioprocessing* 7.
- Southgate, P.N. (1980). “Cambrian stromatolitic phosphorites from the Georgina Basin, Australia”. In: *Nature* 285.5764, pp. 395–397. ISSN: 00280836. DOI: 10.1038/285395a0.
- Steele, Deborah J., Daniel J. Franklin, and Graham J.C. Underwood (2014). “Protection of cells from salinity stress by extracellular polymeric substances in diatom biofilms”. In: *The Journal of Bioadhesion and Biofilm Research* 30.8.
- Stolper, Daniel A. and John M. Eiler (2015). “The kinetics of solid-state isotope-exchange reactions for clumped isotopes: A study of inorganic calcites and apatites from natural and experimental samples”. In: *American Journal of Science* 315.5, pp. 363–411. ISSN: 00029599. DOI: 10.2475/05.2015.01.
- (2016). “Constraints on the formation and diagenesis of phosphorites using carbonate clumped isotopes”. In: *Geochimica et Cosmochimica Acta* 181,

pp. 238–259. ISSN: 00167037. DOI: 10.1016/j.gca.2016.02.030. URL: <http://dx.doi.org/10.1016/j.gca.2016.02.030>.

Swart, Peter K. (2015). “The geochemistry of carbonate diagenesis: The past, present and future”. In: *Sedimentology* 62.5, pp. 1233–1304. ISSN: 13653091. DOI: 10.1111/sed.12205.

Swart, Peter K. and Amanda M. Oehlert (2018). “Revised interpretations of stable C and O patterns in carbonate rocks resulting from meteoric diagenesis”. In: *Sedimentary Geology* 364, pp. 14–23. ISSN: 00370738. DOI: 10.1016/j.sedgeo.2017.12.005. URL: <https://doi.org/10.1016/j.sedgeo.2017.12.005>.

Vasconcelos, C. et al. (2005). “Calibration of the  $\delta^{18}\text{O}$  paleothermometer for dolomite precipitated in microbial cultures and natural environments”. In: *Geology* 33.4, pp. 317–320.

Veillard, Claire M.A. et al. (2019). “Rock-buffered recrystallization of Marion Plateau dolomites at low temperature evidenced by clumped isotope thermometry and X-ray diffraction analysis”. In: *Geochimica et Cosmochimica Acta* 252, pp. 190–212. ISSN: 00167037. DOI: 10.1016/j.gca.2019.02.012.

Wang, Zhengrong, Edwin A. Schauble, and John M. Eiler (2004). “Equilibrium thermodynamics of multiply substituted isotopologues of molecular gases”. In: *Geochimica et Cosmochimica Acta* 68.23, pp. 4779–4797. ISSN: 00167037. DOI: 10.1016/j.gca.2004.05.039.

Wotte, Thomas et al. (2012). “Paired  $\delta^{34}\text{S}$  data from carbonate-associated sulfate and chromium-reducible sulfur across the traditional Lower-Middle Cambrian boundary of W-Gondwana”. In: *Geochimica et Cosmochimica Acta* 85, pp. 228–253. ISSN: 00167037. DOI: 10.1016/j.gca.2012.02.013.

Xiao, Shuhai and Marc Laflamme (2009). “On the eve of animal radiation: phylogeny, ecology and evolution of the Ediacara biota”. In: *Trends in Ecology and Evolution* 24.1, pp. 31–40. ISSN: 01695347. DOI: 10.1016/j.tree.2008.07.015.

Xiao, Shuhai, Yun Zhang, and Andrew H. Knoll (1998). “Three-dimensional preservation of algae and animal embryos in a neoproterozoic phosphorite”. In: *Nature* 391.6667, pp. 553–558. ISSN: 00280836. DOI: 10.1038/35318.

### 3.9 Figures and tables

Table 3.1: Isotopic data.

Sample ID*	Mineralogy	Collection Method <sup>◊</sup>	$\delta^{18}O_{\text{mineral}}(\text{VPDB})^{\square}$	1 S.E. <sup>ˆ</sup>	$\delta^{13}C_{\text{mineral}}(\text{VPDB})^{\square}$	1 S.E. <sup>ˆ</sup>
Aris 3.6 16 a	Calcite	Online at 90°C	-2.35	0.0023	1.74	0.0010
Aris 3.6 16 b	Calcite	Online at 90°C	-2.04	0.0012	1.90	0.0007
Aris16Reef	Dolomite	Online at 90°C	-3.01	0.0010	1.91	0.0012
Aris1B 31.8 60.8	CFA	Online at 90°C	-3.13	0.0019	0.47	0.0010
Aris2 10.8	Dolomite	Online at 90°C	-3.51	0.0043	5.06	0.0014
Aris 31.8 60	CFA	Online at 90°C	-3.31	0.0038	-0.17	0.0007
Aris 31.8 8.5	CFA	Online at 90°C	-1.80	0.0018	1.37	0.0012
Cer23f a	Dolomite	Offline at 50°C	-2.08	0.0012	1.18	0.0009
Cer23f b	Dolomite	Offline at 50°C	-2.05	0.0014	1.16	0.0013
I04c a	Calcite	Online at 90°C	-6.70	0.0010	10.67	0.0007
I04c b	Calcite	Online at 90°C	-6.72	0.0013	10.65	0.0013
Min 16.8 b	Calcite	Online at 90°C	-2.34	0.0012	0.86	0.0005
Min 4.5 a	Calcite	Online at 90°C	0.87	0.0064	4.38	0.0023
Min 4.5 c	Calcite	Online at 90°C	-1.67	0.0027	4.85	0.0014
Min 41.6 a	Calcite	Online at 90°C	-3.32	0.0011	4.18	0.0010
Min 41.6 b	Calcite	Online at 90°C	-3.62	0.0015	4.06	0.0013
V2460	CFA	Online at 90°C	-4.93	0.0022	3.11	0.0011
X3330 a	CFA	Online at 90°C	-5.24	0.0151	3.93	0.0044
X3330 b	Dolomite	Online at 90°C	-4.38	0.0023	5.64	0.0014
X3340	CFA	Online at 90°C	-4.87	0.0109	4.31	0.0053
XI810	CFA	Online at 90°C	-6.36	0.0035	-4.01	0.0026

\* Sample ID includes abbreviation for stratigraphic column and locality, as well as numbers indicating stratigraphic height and lateral distance (both in meters) from a datum for the given column. Powders collected from the same hand samples (within centimeters of each other) are indicated with lowercase letters a-c. Compare to Fig. 3.1-3.2: Aris = Aristeia, Io4 = Io, Min = Minotaur, V = CBPM Core 5, X = CBPM Core 10, XI = CBPM Core 11.

◊ Online digestions were performed in a common phosphoric acid bath at 90°C under vacuum, with liberated  $CO_2$  and  $H_2O$  entering the GC column and dehydrating cold traps before advancing down the analytical pipeline of the MAT 253 MS. Offline digestions were performed in reaction vessels under vacuum, with liberated  $CO_2$  and  $H_2O$  being passed over dehydrating cold traps on a separate vacuum line before being frozen down into pyrex tubes; which are introduced to the MAT 253 analytical pipeline manually. Offline digestions were performed by immersing reaction vessel under vacuum in 50°C water bath. See Methods for more information.

□ ‰, with respect to Vienna Pee Dee Bellemnitte (VPDB).

ˆ 1 S.E. = 1 standard error, describing a set of 7-8 acquisitions.

Table 3.2: Isotopic data, continued.

Sample ID*	Mineralogy	$\Delta_{47}$ <sup>•</sup>	1 S.E. <sup>‡</sup>	$\Delta_{47}$ Temperature (°C) <sup>†</sup>	1 S.E. <sup>‡</sup>	$\delta^{18}O_{water}(VSMOW)$ <sup>‡</sup>	1 S.E. <sup>‡</sup>
Aris 3.6 16 a	Calcite	0.44	0.0142	92.09	8.17	11.03	1.10
Aris 3.6 16 b	Calcite	0.41	0.0203	110.55	13.60	13.80	1.67
Aris16Reef	Dolomite	0.37	0.0164	143.64	14.06	5.94	1.46
Aris1B 31.8 60.8	CFA	0.40	0.0059	116.96	4.16	13.47	0.49
Aris2 10.8	Dolomite	0.36	0.0139	147.81	12.25	5.80	1.25
Aris 31.8 60	CFA	0.40	0.0076	119.84	5.44	13.63	0.64
Aris 31.8 8.5	CFA	0.41	0.0175	113.54	12.00	14.42	1.45
Cer23f a	Dolomite	0.43	0.0179	98.96	10.90	2.16	1.42
Cer23f b	Dolomite	0.46	0.0191	84.94	10.39	0.32	1.46
I04c a	Calcite	0.42	0.0166	107.98	10.86	8.66	1.35
I04c b	Calcite	0.40	0.0157	116.19	10.99	9.68	1.31
Min 16.8 b	Calcite	0.42	0.0123	107.25	8.00	13.06	1.00
Min 4.5 a	Calcite	0.39	0.0168	125.55	12.62	18.62	1.43
Min 4.5 c	Calcite	0.43	0.0144	97.75	8.71	12.51	1.14
Min 41.6 a	Calcite	0.43	0.0169	99.10	10.30	10.99	1.34
Min 41.6 b	Calcite	0.44	0.0116	93.77	6.81	9.95	0.91
V2460	CFA	0.39	0.0082	126.05	6.21	12.70	0.70
X3330 a	CFA	0.37	0.0386	143.89	33.14	14.37	3.44
X3330 b	Dolomite	0.41	0.0174	115.15	12.09	1.70	1.45
X3340	CFA	0.44	0.0136	96.15	8.12	8.99	1.07
XI810	CFA	0.53	0.0184	51.99	7.51	0.61	1.28

<sup>•</sup>  $\Delta_{47}$  (‰) is here shown projected into the absolute reference frame Dennis, Affek, et al., 2011; Stolper and Eiler, 2016 and assuming an acid digestion temperature of 90°C, such that no acid-fractionation correction is applied for samples reacted at 90°C, and a correction of -0.07‰ is applied for samples reacted at 50° Bonifacie et al., 2017; Murray, Arienzo, and Swart, 2016; Müller et al., 2017. See Methods.

<sup>†</sup> Temperature (°C) calculated via empirical relationships between  $\Delta_{47}$  and temperature for carbonate minerals Stolper and Eiler, 2016; Dennis, Affek, et al., 2011. See Methods.

<sup>‡</sup> Calculated  $\delta^{18}O_{water}$  (‰, relative to Vienna Pee Dee Bellemnite or VPDB), based on equilibrium isotope fractionation between water and calcite or CFA Kim and O’Neil, 1997, and water and dolomite Horita, 2014.  $\delta^{18}O_{water}$  (‰, relative to Vienna Standard Mean Ocean Water or VSMOW), shown here, is converted from  $\delta^{18}O_{water}$  (‰, VPDB), as is the standard convention for expressing  $\delta^{18}O$  of fluids. Kim, Coplen, and Horita, 2015.

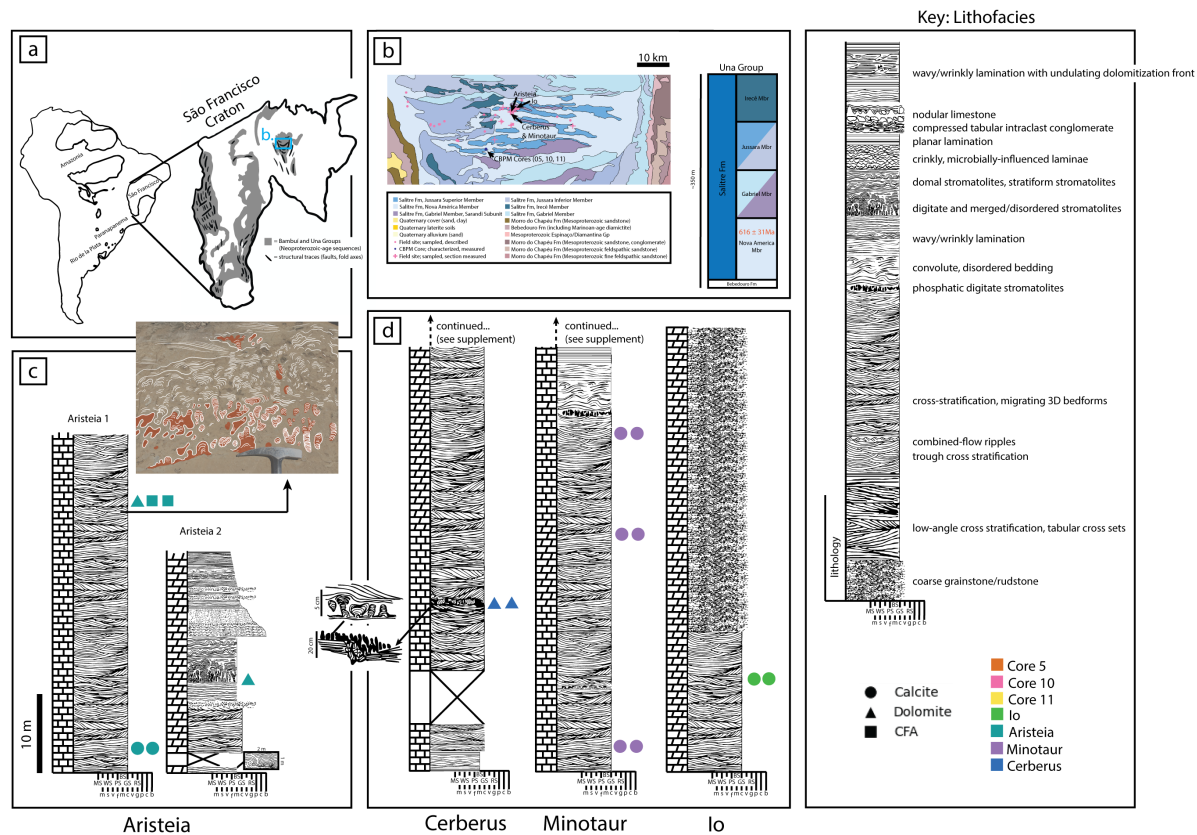


Figure 3.1: Geographical and stratigraphic context of presented geochemical measurements. (a) Map depicting the location of the São Francisco craton relative to nearby cratonic remnants (modified after Sanders and Grotzinger, 2021; Umberto G. Cordani and Sato, 1999; Reis, Suss, et al., 2017; Alkmim and Marcelo A. Martins-Neto, 2012). (b) Geologic map of region indicated in (a), and stratigraphy of the Una Group. (Dalton de Souza et al., 2003; Fonseca et al., 2014). (c) Simplified stratigraphic columns from the Aristeia locality (indicated in (b), see also TABLE), with inset previously published in Sanders and Grotzinger (2021) depicting digitate stromatolite buildup in which CFA cements – colored red – are prevalent at the base/core of the buildup, and are less common in the more merged/disordered laminated textures. (d) Simplified stratigraphic columns from the Cerberus, Minotaur, and Io localities (indicated in (b)). Shapes adjacent to the columns indicate the location in each stratigraphic column from which geochemical samples and their corresponding thin sections and slabs were collected.

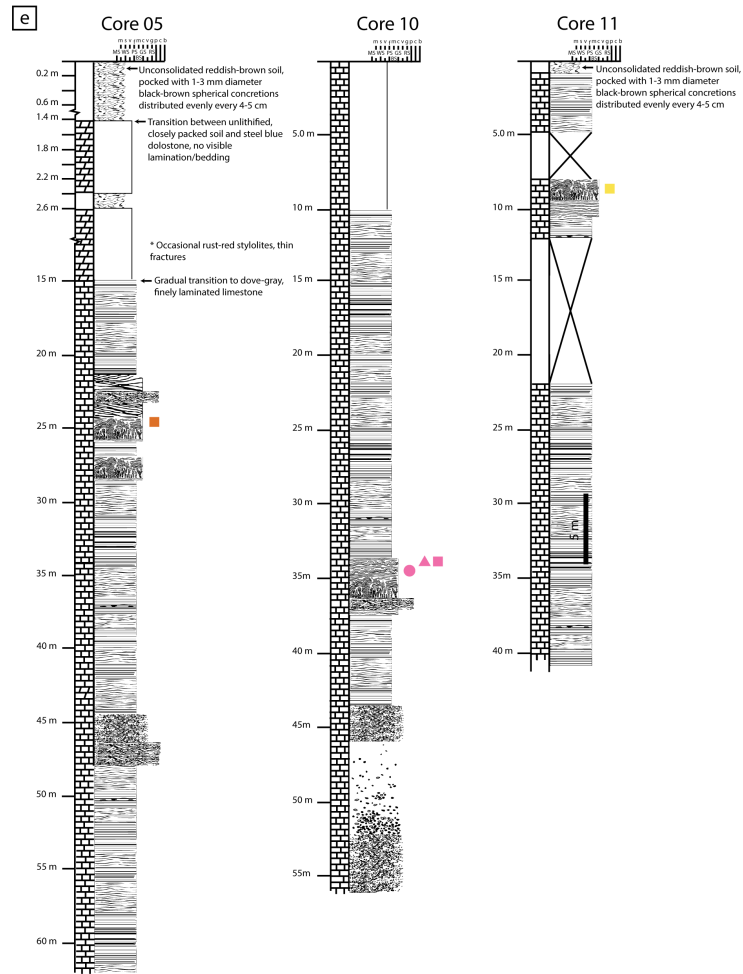


Figure 3.2: Sedimentological characterization of CBPM drill cores. Colored shapes adjacent to the columns indicate the location in each stratigraphic column from which geochemical samples and their corresponding thin sections and slabs were collected, according to the same key as Fig. 3.1. Location of drill cores in Fig. 3.1b.

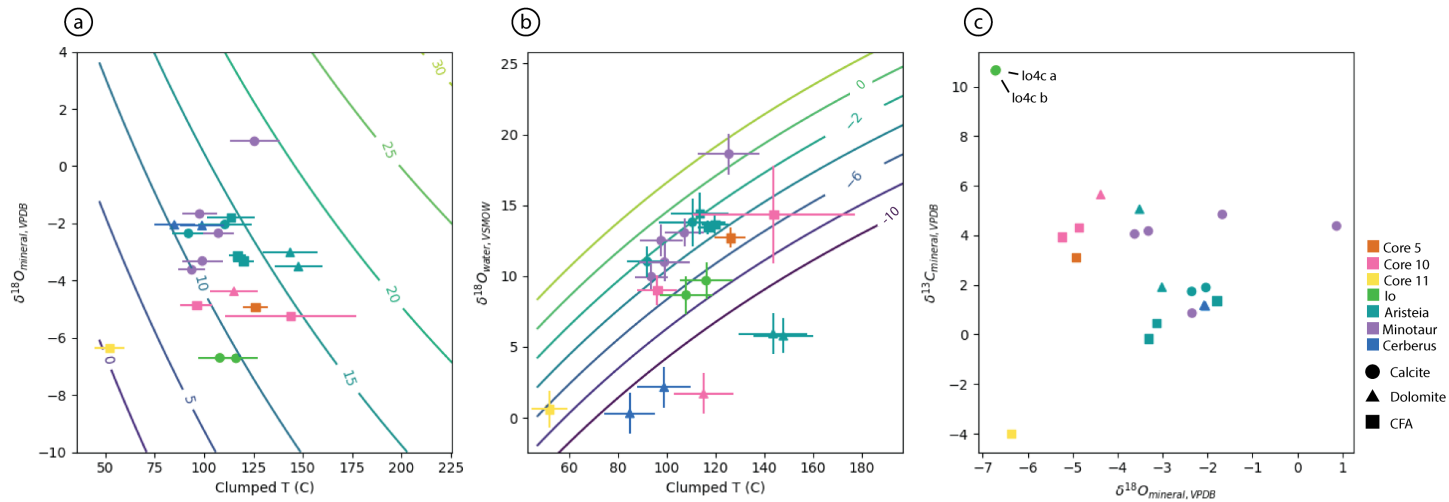


Figure 3.3: Measured  $\Delta_{47}$ ,  $\delta^{13}C_{\text{mineral}}$ ,  $\delta^{18}O_{\text{mineral}}$ , and calculated  $\delta^{18}O_{\text{water}}$  data for sample powders extracted by micro-scale drilling of earliest cement fabrics in syndepositional phosphatic and non-phosphatic facies. Error bars represent  $\pm 1$  S.E. (standard error). (a)  $\Delta_{47}$ -derived temperature vs.  $\delta^{18}O_{\text{mineral}}$ . Contours indicate  $\delta^{18}O_{\text{water}}$  based on equilibrium fractionation models. (b)  $\Delta_{47}$ -derived temperature vs. calculated  $\delta^{18}O_{\text{water}}$ . Contours indicate  $\delta^{18}O_{\text{mineral}}$  based on equilibrium fractionation models. (c)  $\delta^{18}O$  vs.  $\delta^{13}C$ . Labels indicate where multiple measurements overlap. In (a-c), circles indicate measurement of calcite sample, triangles dolomite, and squares CFA. Like colors indicate samples collected from the same locality and/or stratigraphic context. See Figs.3.1-3.2 for sample locations and facies associations.

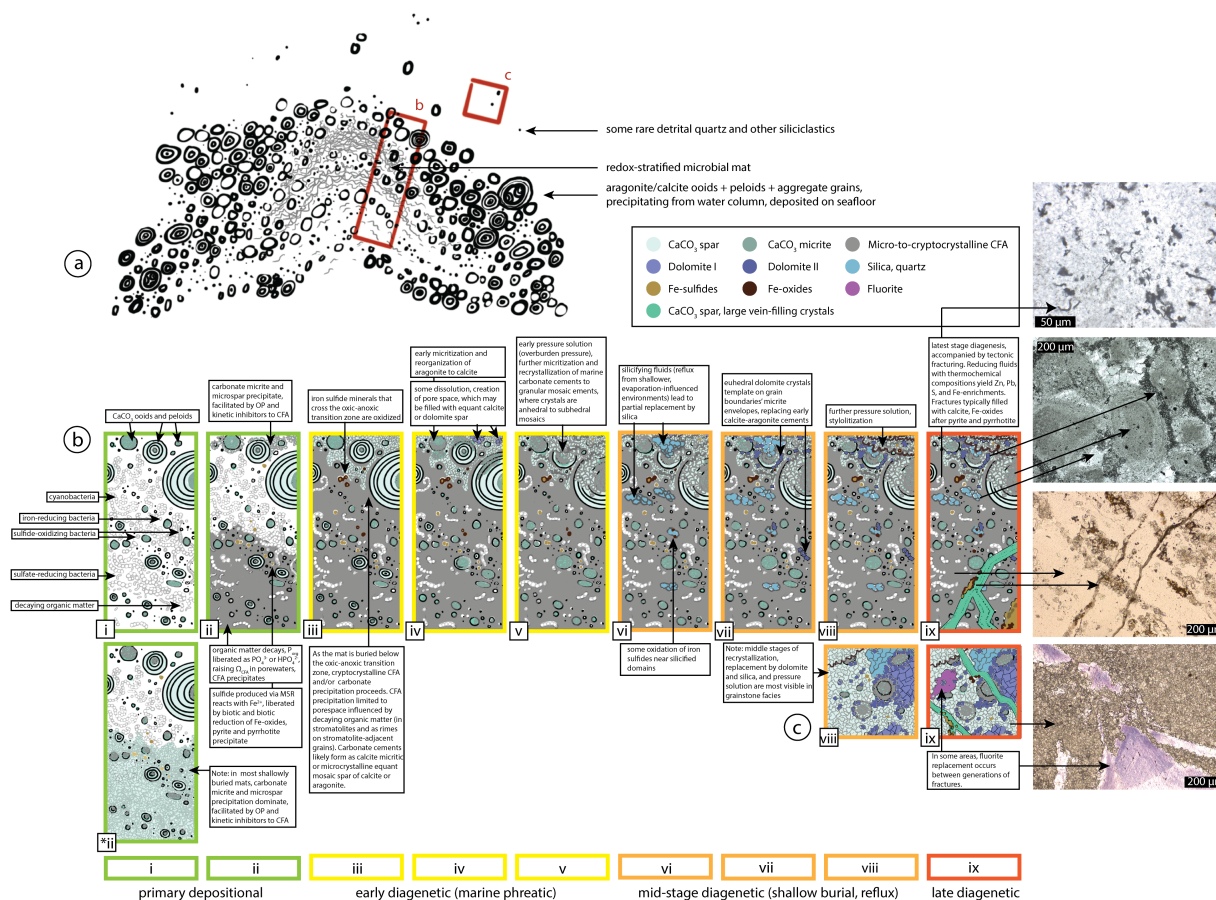


Figure 3.4: Annotated illustration of the formation and diagenesis of a digitate stromatolite and adjacent carbonate grainstone, representative of the phosphatic members of the Salitre Formation. Illustration is schematic and combines in several slides true features observed in dozens of petrographic thin sections and slabs. (a) Illustration of a stromatolite in active formation amidst carbonate ooid and peloid sedimentation. (b-c) Insets indicated in (a), depicting the stages of diagenesis as interpreted from petrographic imagery and geochemical data in this and previous work (Sanders and Grotzinger, 2021). At far left, thin section photomicrographs (plane polarized light) of the illustrated features. See text.

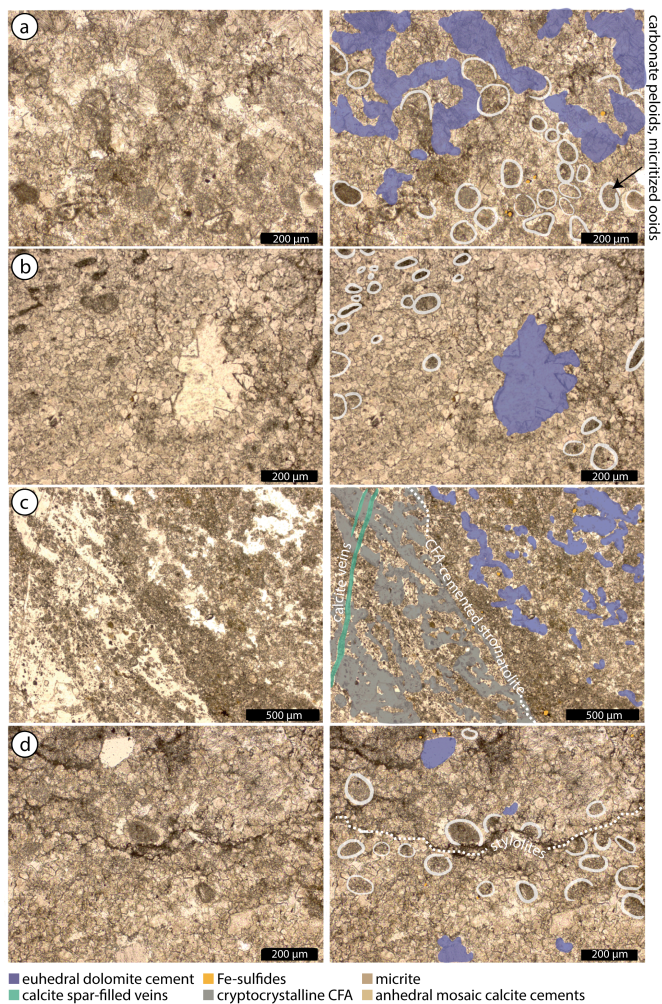


Figure 3.5: Additional photomicrographs of the major mineral phases identified within the digitate stromatolite and grainstone facies of the Salitre Formation. At left, transmitted plane-polarized light photomicrographs, at right annotated versions of the same. (a) Carbonate peloids and ooids within the grainstone/rudstone lithofacies, with varying levels of fabric-retentive to partially fabric-destructive micritization. Cements are a combination of anhedronal mosaic calcite spar and micrite and more euhedral dolomite spar — which, as illustrated in Fig. 3.4, is likely the result of recrystallization of primary calcite or aragonite cements in equilibrium with a different generation of diagenetic fluids. (b) Carbonate peloids and ooids, in a photomicrograph showing the spatial relationships between the different cement mineralogies. (c) Right-hand flank of a digitate stromatolite, showing the sharp distinction between cryptocrystalline CFA cement in the laminated interior of the stromatolite and calcite micrite and calcite/dolomite spar cements in the grainstone immediately adjacent to the stromatolite. A vein containing lateritic blocky calcite spar is also visible. (d) Example of a later-stage stylolite, cross-cutting recrystallized carbonate ooids and peloids. In all panels, Fe-sulfides (pyrite, and oxidized pseudomorphs thereafter) are a minor, sparsely distributed phase.

*Chapter 4***SULFUR GEOCHEMISTRY OF THE SALITRE FORMATION  
PHOSPHORITES: IMPLICATIONS FOR THE ROLE OF SULFUR  
CYCLING IN PHOSPHOGENESIS ON AN EDIACARAN  
CARBONATE PLATFORM**

Cecilia B. Sanders, Theodore M. Present, Selva Marroquín, and John P.  
Grotzinger<sup>1</sup>

*One of the extraordinary things about life is the sort of places it's prepared to put up with living. Anywhere it can get some kind of grip, whether it's the intoxicating seas of Santraginus V, where the fish never seem to care whatever the heck kind of direction they swim in, the fire storms of Frastra, where, they say, life begins at 40,000 degrees, or just burrowing around in the lower intestine of a rat for the sheer unadulterated hell of it, life will always find a way of hanging on in somewhere.*

— Douglas Adams, *Mostly Harmless*

**4.1 Abstract**

The distribution and activity of polyphosphate-accumulating sulfide oxidizing bacteria within marine sediments control the spatial distribution of sedimentary phosphorite formation in the modern ocean. In modern phosphogenetic settings, the concerted effect of microbial sulfide oxidation and microbial sulfate reduction in sediment pore waters is preserved in the sulfur isotope composition of trace sulfate in authigenic and early-stage diagenetic carbonate cements and phosphatic cements, as well as that of authigenic pyrite. If such variations in microbial sulfur metabolism controlled the spatial distribution of early phosphate mineralization in the geologic past, then one would expect to find differences between the sulfur isotope composition of cement-forming minerals in phosphatic and non-phosphatic facies of ancient sedimentary phosphate deposits. Here, we present paired measurements of the sulfur isotope composition of structural sulfate and structural sulfide in pore cements from co-occurring phosphatic and non-phosphatic facies of the Ediacaran

---

<sup>1</sup>Division of Geological and Planetary Sciences, California Institute of Technology, Pasadena, CA 91125, USA

Salitre Formation (Northeastern Brazil). The difference between  $\delta^{34}\text{S}$  of trace structural sulfate in carbonate cements (CAS) or phosphate cements (PAS) and  $\delta^{34}\text{S}$  of structural sulfide in pyrite or chromium-reducible sulfur (CRS), defined as  $\Delta^{34}\text{S}$ , provides a constraint on sulfur cycling within the pore waters from which the cements precipitated. In carbonate-cemented textures of the Salitre Formation,  $\Delta^{34}\text{S} = 12$  to  $31\text{‰}$ . In phosphate-cemented textures, however, PAS and pyrite crystals had more similar sulfur isotope compositions:  $\Delta^{34}\text{S} = -5$ - $12\text{‰}$ . These values support the hypothesis that microbial sulfide oxidation was more prevalent in pore waters where phosphate mineralization occurred compared to pore waters where carbonate mineralization occurred – suggesting that microbial sulfide oxidation may have enabled the formation of sedimentary phosphorite on an Ediacaran carbonate platform just as in modern phosphogenetic sites.

## 4.2 Introduction and background

There is broad consensus among biogeochemical researchers that phosphate-rich sedimentary deposits – phosphorites – are important to our understanding of past environments. Phosphorus is a vital nutrient, an essential component of biomass, and its concentration and accumulation in sediments at specific temporal horizons and in specific depositional environments has major consequences for global biogeochemical cycling throughout Earth history (Anschutz et al., 1998; Donald E. Canfield and Teske, 1996; Cook, 1992; Defforey and Paytan, 2018; Filippelli, 2011; Föllmi, 1996; Laakso et al., 2020; Papineau, 2010; Paytan and Mclaughlin, 2007; G. Shields et al., 2004; Sundby et al., 1992). Phosphate minerals such as hydroxapatite and carbonate-rich fluorapatite have, by virtue of their crystal structure and dissolution-recrystallization kinetics, the capacity to fossilize and preserve biological structures in exquisite detail, providing insight into the evolution of life (1998; Bengtson et al., 2017; Creveling, Andrew H Knoll, and David T Johnston, 2014; Demidenko et al., 2003; Pruss et al., 2019; Sallstedt et al., 2018; Xiao and Andrew H. Knoll, 1999).

The spatial and temporal distributions of phosphorite provide insight into spatial and temporal variations in climate, ecology, and marine chemistry. Our understanding of the mechanisms by which environment and ecology effected phosphogenesis in the geologic past is yet imperfect; but in actively-forming modern phosphorites, it is possible to observe the mechanisms that control phosphate accumulation and mineralization in situ and through laboratory culture experiments. Modern phosphogenesis thus provides a model for phosphogenesis in the past which may be tested

by examining ancient phosphorite deposits for geochemical and textural evidence of processes analogous to those in modern phosphogenetic environments.

There is a wealth of data that support a critical role for sulfur-metabolizing microorganisms in the formation of sedimentary phosphate deposits (phosphorite) at the modern seafloor. Sulfide-oxidizing microorganisms – specifically, polyphosphate-accumulating sulfide oxidizing bacteria including *Thiomargarita*, *Beggiatoa*, and *Thioplaca* – have been found in close association with phosphatic sediments of the Namibian shelf (H. N. Schulz and H. D. Schulz, 2005) and the Pacific margin of Costa Rica (J. V. Bailey et al., 2013). Phosphatic laminites from the Peruvian shelf are enriched with respect to organic molecules characteristic of sulfate-reducing bacteria and sulfide-oxidizing bacteria relative to non-phosphatic crusts in the same locality, and contain structural sulfate with  $\delta^{34}\text{S}$  values which are lighter than that of ambient sea water to a degree consistent with fractionation via microbial sulfide oxidation (Arning et al., 2009). Laboratory cultures of model communities of polyphosphate-accumulating sulfide-oxidizing bacteria are observed to lyse their polyphosphate-accumulating vacuoles and release of aqueous phosphate ions to surrounding media in response to anoxia and increased sulfide abundance (Brock and Schulz-Vogt, 2011; Crosby and Jake V. Bailey, 2012; H. N. Schulz and H. D. Schulz, 2005). Furthermore,  $^{33}\text{P}$ -radiotracer experiments have demonstrated the conversion of intracellular phosphate to extracellular apatite by living communities of giant sulfide bacteria cultured from Namibian shelf sediments – a process that did not occur in kill controls in which non-living cells failed to template apatite growth (Goldhammer et al., 2010).

All of these data support the prevailing model: that marine phosphogenesis occurs where communities of sulfate-reducing and sulfide-oxidizing bacteria effect elevated porewater phosphate concentrations and actively lower kinetic barriers to apatite mineral nucleation and growth under anoxic conditions. However, ancient sedimentary phosphorites occur in a wider range of depositional environments than modern sedimentary phosphorites (reviewed by Sheldon, 1981; Föllmi, 1996; Southgate, 2005). They also exhibit a wider range of mineral growth textures, and formed from pore waters and bottom waters derived from different ocean chemistries. Is it possible that the same microbially-mediated processes that facilitate modern phosphogenesis also were active in ancient phosphogenetic environments? If so, the isotopic composition of oxidized and reduced sulfur phases in pore cements of ancient sedimentary phosphorites might reflect the isotopic fractionation of oxidized

and reduced sulfur pools by microbial metabolic activity during the formation of those phases.

Trace structural sulfate in carbonate minerals and phosphate minerals which precipitated from pore fluids represents aqueous sulfate in those porefluids during mineral nucleation and growth (Richardson et al., 2019). The isotopic composition of that porewater sulfate reflects the net effects of isotopic fractionation by sulfate-consuming reactions (microbial sulfate reduction, microbial sulfur disproportionation) and sulfate-producing reactions (microbial sulfide oxidation, microbial sulfur disproportionation) acting upon a pool of sulfate derived from seawater (D. E. Canfield, 2019; Fike et al., 2008; G. A. Shields et al., 1999; Wotte et al., 2012). Likewise, the isotopic composition of sulfur in pyrite (FeS) should reflect the net effects of sulfide-generating reactions (microbial sulfate reduction, microbial sulfur disproportionation) and sulfide-consuming reactions (microbial sulfide oxidation, microbial sulfur disproportionation) prevalent in porefluids near the redoxcline where aqueous  $Fe^{2+}$  is available to scavenge  $H_2S$  and form pyrite.

The interplay of all the possible influences of different microbial sulfur metabolisms may result in a wide range of  $\delta^{34}S_{SO_4} - \delta^{34}S_S = \Delta^{34}S$  in cements precipitating from pore fluids, from which it may be impossible to reconstruct the precise network of biochemical pathways in primary sediment pore waters. It may, however, be possible to constrain the range of likely pathways which existed in phosphate mineralizing facies, and compare them to the pathways which existed in non-phosphate mineralizing facies in the same geological place and time. If phosphogenesis was enabled by the metabolic activities of a given community of sulfur-metabolizing microorganisms, then – all other environmental parameters being the same – one would expect the isotopic signature  $\delta^{34}S$  of their metabolisms to be present in phosphatic pore cements and absent from non-phosphatic pore cements.

To this end, we measured  $\delta^{34}S$  of structural sulfate and sulfide in mineral phases associated with both phosphatic and non-phosphatic textures of an ancient phosphorite: the Ediacaran Salitre Formation of Northeastern Brazil. The measured phases include carbonate cements (calcite and dolomite) in cross-stratified grainstone and crinkly laminated mudstone and phosphate, and phosphate cements (carbonate-rich fluorapatite or CFA) in digitate stromatolite buildups which interfinger with the grainstone and laminated mudstone facies. The geochemistry of these cements, precipitated from sediment pore waters on an Ediacaran carbonate platform, should reflect the geochemistry of those sediment pore waters and the processes that enabled

either carbonate or phosphate mineralization – or else diagenetic modification. We interpret these new  $\delta^{34}S$  data in their paragenetic context to determine whether they are consistent with biological sulfur cycling as observed in modern phosphogenetic environments.

### 4.3 Geologic context

Geologic samples analyzed in this study were collected at various localities across the Irecê and Salitre paleobasins, sub-basins within a foreland basin system that existed in the interior of the São Francisco Craton during the Neoproterozoic Era (Kuchenbecker, Luis, and Galvão, 2011; M. A. Martins-Neto, Pedrosa-Soares, and Lima, 2001; Reis, Alkmim, et al., 2016). Two major sedimentary rock units describe these sub-basin deposits, called the Una Group: (1) the Bebedouro Formation – <200 m in thickness, containing glaciogenic diamictites associated with the Marinoan glaciation (Caxito et al., 2012; Guimarães et al., 2011), and (2) the Salitre Formation – roughly 300-400 m in thickness, comprised of 4 members of roughly equal thickness which contain carbonate platform deposits with increasingly high siliciclastic input (A. Misi and Kyle, 1994; Aroldo Misi, Kaufman, et al., 2007; Aroldo Misi and Veizer, 1998). The phosphorite-bearing member of the Salitre Formation is its oldest, the Nova America member, comprised of massively bedded limestone and dolostone, featuring cross-stratified grainstone/rudstone, intraclast conglomerate, crinkly and planar laminated mudstones, and stromatolite buildup lithofacies (Sanders and Grotzinger, 2021). The phosphorite deposits of the Nova America member occur within a subset of the stromatolite buildups in which the stromatolites have a branching, digitate morphology and are comprised of laminated organic matter and carbonate peloids and ooids cemented by carbonate fluorapatite (CFA). Inter-stromatolite fill is comprised of carbonate peloids and ooids cemented by carbonate minerals only. Digitate stromatolite buildups interfinger on meter- and tens-of-meter scales with cross-stratified grainstone and occasionally planar- and crinkly-laminated mudstone. Non-phosphatic stromatolites have a similar spatial distribution, and may even occur within the same buildups as phosphatic stromatolites.

Previous studies have described the paragenesis of the Salitre Formation's phosphorite deposits in detail, based on optical petrography, elemental mapping, and carbon and oxygen isotopic compositions and clumped-isotope constrained paleotemperatures (Caird et al., 2017; Sanders, J. Eiler, and Grotzinger, 2022). These studies concluded that the spatial distribution of textural associations of phosphatic

CFA cements was consistent with phosphate enrichment by authigenic or very early diagenetic processes, rather than pervasive diagenesis by deep circulating fluids. Though the Salitre phosphorites are 647-585 million years old and have experienced kilometers of burial and uplift, geochemical and textural data both suggest that later-stage diagenesis occurred under low water-rock ratio conditions and that diagenetic resetting of the isotopic composition of structural sulfur in cement fabrics was likely limited (Sanders and Grotzinger, 2021).

For this study, we selected a range of hand samples from within the phosphorite interval of the Salitre Formation's Nova America member. Samples were taken from measured outcrops in the Irece and Salitre paleobasin regions (Figure 1), and represent both phosphatic and non-phosphatic cement-forming environments within the same stratigraphic interval. Phosphatic textures include CFA-cemented laminae within digitate stromatolites. Non-phosphatic textures include carbonate-cemented grainy inter-stromatolite fill associated with phosphate-rich digitate stromatolite buildups, as well as carbonate-cemented grainstone immediately adjacent to stromatolite buildups, and carbonate-cemented mudstones. Representative images and annotated illustrations of these textures are presented in Figure 2.

#### **4.4 Methods**

This study required the integration of many different techniques for the extraction, purification, and isotopic analysis of sulfur in specific co-occurring mineral phases/reservoirs in natural geologic samples, summarized in Figure 3. Mineral phases analyzed included the micro- to cryptocrystalline carbonate fluorapatite (CFA) cement matrix of phosphatic digitate stromatolites, the micritic and interlocking anhedral mosaic calcite and dolomite cement matrix of non-phosphatic stromatolites and inter-stromatolite grainstone, and minor pyrite intergrown with and cross-cutting the carbonate and CFA cements.

#### **Selection of samples**

Mineral fabrics suitable for such texturally-specific sulfur isotope analysis were selected via optical petrography, Raman microscopy, and paired scanning electron microscopy and energy dispersive spectrometry (SEM/EDS) of petrographic thin sections and their corresponding offcuts/billets, previously prepared for the characterization of the Salitre Formation's formation and paragenesis. These elemental and mineralogical analyses were performed in Caltech's Division of Geological and Planetary Sciences Analytical Facility, using an optical petrographic microscope,

Renishaw InVia Confocal Raman Microscope with 514 nm primary laser, and Zeiss 1550VP Field Emission SEM using 15-20 KeV electron beam. Compositional maps, annotated thin section photomicrographs, etc. are presented in the results of previous studies (**sanders2021a**). Thus, we identified and collected images and compositional maps of microcrystalline CFA and carbonate mineral cement fabrics which were devoid of late stage diagenetic features (such as fractures and associated sparry cements) on sub-millimeter spatial scales (Sanders, J. Eiler, and Grotzinger, 2022; Sanders and Grotzinger, 2021). Table 1 summarizes the mineralogy and microtextural associations (“microfacies”) of all samples selected for this study.

We used the characterization of sample thin sections to select corresponding fabrics in their offcuts for texture-specific, mm-scale drilling to collect powders (10s-of- $\mu\text{m}$  scale grains). Some fabrics which were homogeneous over a spatial scale of 1 cm were reduced to gravels/granules using a rock hammer, then reduced to powders using an agate ball mill. Drilled and milled sample fabrics which yielded more than several mg of powder (of which there was at least 1 from each locality) had their bulk mineralogy verified via X-Ray powder diffraction using Caltech’s Crystallography Facility’s Panalytical X’Pert Pro instrument. Calcite, dolomite, and CFA were the only minerals present in the sample powders above the instrumental limit of detection. The presence of trace pyrite crystals associated with the targeted CFA and carbonate cements was ascertained from the spectroscopy and reflected light microscopy of thin sections.

Powder extracted from fabrics which consisted of carbonate cement with minor pyrite was allocated for extraction of trace carbonate-associated sulfate (CAS) and extraction of pyrite sulfur as chromium-reducible sulfur (CRS). Powder extracted from fabrics which consisted of CFA cement with minor pyrite was allocated for extraction of phosphate-associated sulfate (PAS) and extraction of pyrite sulfur as CRS. Pyrite from those powder samples for which CRS extraction yielded less than 4  $\mu\text{g}$  S were instead analyzed via Secondary Ion Mass Spectrometry, in situ with respect to the mineral fabric. See below for all extraction and purification protocols, and sulfur isotope mass spectrometry.

### **Extraction of carbonate-associated sulfate (CAS)**

Structural sulfate in the carbonate mineral lattice is a trace component of the rock, with low concentrations on the order of hundreds to thousands of ppm for most abiogenic carbonates (Staudt and Schoonen, 1995). Because the abundance of the

target analyte is so low, extraction and purification protocols, adapted from previous studies of trace sulfate in carbonate undertaken in the same laboratory facilities (Paris, Sessions, et al., 2013; Paris, Fehrenbacher, et al., 2014; Present, Paris, et al., 2015; Present, Gutierrez, et al., 2019), were performed under cleanroom conditions meant to minimize contamination of samples from background sulfate.

10% NaCl Rinse to remove easily soluble sulfate: 12 sample powders comprised of near-pure carbonate minerals (i.e., calcite and dolomite), as well as a consistency standard derived from modern coral, were weighed into microcentrifuge tubes with 10% NaCl solution, and sonicated for >8 hours. Samples and standard were then centrifuged at 13,200 rpm for five minutes, and NaCl supernate removed and discarded via micropipette. Samples and standard were then rinsed 3 times with deionized and filtered Milli-Q water (each rinse consisting agitation/resuspension of the powders in Milli-Q water, followed by centrifuging, and removal of supernate). Powders were resuspended in Milli-Q water and transferred to acid-clean microcentrifuge tubes, and dried at 65°C for >8 hours. This protocol is adapted from that of Present et al. (2015; Present, Gutierrez, et al., 2019)

Acid Digestion of carbonate minerals: 0.5 N HCl was added to each vial of dried sample powders and 2 additional empty vials (“blanks”). Samples were allowed to react for 4.25 hours at ambient lab temperatures (25°C), being periodically agitated/resuspended every 30 minutes. Then, samples and blanks were centrifuged for 5 minutes at 13,200 rpm, and their supernate transferred to acid-clean PTFE Savillex vials. Acid-insoluble residues were dried at 65°C for >8 hours and stored. At this time, an additional seawater standard was also added to a PTFE vial. The acid-soluble fractions of 1 coral standard, 1 seawater standard, and all samples, as well as the 2 complete procedural blanks, were then allowed to dry inside a laminar flow chamber at 95°C for >8 hours. This protocol is adapted from that of Present et al. (Present, Gutierrez, et al., 2019; Present, Paris, et al., 2015).

Separation of sulfate via ion exchange chromatography: Dried samples, standards, and blanks were resuspended in 3.3 mN HCl, then transferred via micropipette to sterile Poly-Prep chromatography columns. Each column was pre-prepared with a slurry of BioRad AG-1-X8 strong anion resin, 10% HCl, and Milli-Q water. The resin was “rinsed” twice by the addition and elution of 3.3 N HCl, followed by Milli-Q water, then 1.6 N  $HNO_3$ , then once by 3.3 N HCl, and finally conditioned with 0.165 N HCl and Milli-Q water. The resuspended samples, standards, and blanks were each added to their own resin-filled columns and allowed to elute for 35

minutes. Columns were then rinsed 3 times with Milli-Q water (i.e., water added to column and allowed to elute 3x). This eluent, which ideally contained all cations in the acid-soluble fraction of the samples and standards except sulfate, was discarded. Each column was then rinsed 3 times with 0.5 N  $HNO_3$ , to remove sulfate bound to active sites in the resin. This acidic eluent ideally contained only pure sulfate, and was captured in PTFE Savillex vials for drying inside a laminar flow chamber at 95°C for >8 hours. This protocol is adapted from those devised and refined by Paris et al. (Paris, Fehrenbacher, et al., 2014; Paris, Sessions, et al., 2013).

Measurement of sulfate abundance via ion chromatography: Each vial of purified sulfate was diluted with Milli-Q water to bring each to an approximate target sulfate concentration of 0-70  $\mu M$ . A small aliquot (250  $\mu L$ ) of each diluted sample, standard, and blank solution was aliquoted for compositional analysis via ion chromatography using a Dionex ICS-2000 in the Caltech Environmental Analysis Center, using the same method described by Johnson et al. (Johnson et al., 2021). Samples which did not yield clean sulfate peaks (i.e., contained ions other than sulfate), and/or had sulfate concentrations below the limit of detection were excluded from further analysis. 4 samples were thus excluded on the basis of either insufficient or unquantifiable sulfate content. Preparation for ICP-MS: The remaining 8 samples, as well as the coral standard and seawater standard, and the 2 procedural blanks, were then dried for >8 hours at 95°C in a laminar flow hood. Dried samples and standards were then resuspended in a sufficient volume of 5%  $HNO_3$  and amended with 500  $\mu M Na^+$  solution, to bring each vial's  $[SO_4^{2-}]$  to 10  $\mu M$ , and  $[Na^+]$  to 20  $\mu M$  to match the matrix of the in-house MC-ICP-MS bracketing standard (Paris, Sessions, et al., 2013). Procedural blanks were brought up in sufficient sodium solution in 5%  $HNO_3$  to have  $[Na^+] = 20 \mu M$ . Samples, standards, and blanks were then transferred to 1.5 mL volume autosampler vials for MC-ICP-MS.

### **Extraction of phosphate-associated sulfate (PAS)**

Structural sulfate in carbonate fluorapatite (CFA), called phosphate-associated sulfate or PAS, is more abundant than structural sulfate in carbonate minerals, likely due to the similarity in size of sulfate and monophosphate anions, both of which are larger than the carbonate anion. The more accommodating crystal structure of carbonate fluorapatite allows structural sulfate concentration in phosphorites to be 1-3 orders of magnitude greater than that of carbonate rocks, obviating the need for trace sulfate extraction protocols. Texture-specific drilling at millimeter scales generated sufficient mass of carbonate fluorapatite powders that “bulk” PAS extrac-

tion methods (Eagle et al., 2010; Stolper and J. M. Eiler, 2016) could be employed outside of a cleanroom environment.

Removal of easily soluble sulfate, organics: Because the CFA samples are all associated with organic-rich laminae in association with stromatolites, a split of powdered CFA samples were first submerged in 3%  $H_2O_2$  and agitated periodically for >8 hours, to oxidize any organic matter to water and oxygen. Because  $H_2O_2$  may also oxidize sulfide minerals, resulting in leaching of trace pyrite, another split of each powdered sample was treated with 1 M NaCl rinse, also for >8 hours. Both the  $H_2O_2$  and the NaCl-washed samples were then centrifuged at 13,200 rpm for five minutes, and supernate removed via micropipette. Samples were then rinsed 3 times with deionized and filtered Milli-Q water (each rinse consisting agitation/resuspension of the powders in Milli-Q water, followed by centrifuging, and removal of supernate).

Carbonate mineral leaching: Carbonate minerals (calcite and dolomite) were removed from the powders by acetic acid leaching. Washed powders were suspended in 0.1 M acetic acid and agitated continuously for 36 hours at ambient lab temperatures (  $25^\circ\text{C}$ ). Afterward, powders were resuspended using a mini-vortexer, centrifuged for 5 minutes at 13,200 rpm, and the supernate discarded. Again, samples rinsed 3 times with deionized and filtered Milli-Q water (each rinse consisting agitation/resuspension of the powders in Milli-Q water, followed by centrifuging, and removal of supernate). Leached and rinsed samples were then dried at  $65^\circ\text{C}$  for >8 hours.

Acid digestion of carbonate fluorapatite: Dried CFA powders, cleaned of easily soluble sulfate, organic material, and carbonate minerals, were placed in 2 N HCl and allowed to react at  $25^\circ\text{C}$  for >8 hours. The acidic leachate ( $\text{pH} = 2$ ) was then filtered through  $0.05 \mu\text{m}$  nitrocellulose filter paper and allowed to react at ambient lab temperatures (  $25^\circ\text{C}$ ) with 5%  $BaCl_2$  for >8 hours. Acid-insoluble residues (collected on filter paper) were stored and dried at  $60^\circ\text{C}$  for >8 hours before being scraped by aluminum spatula into microcentrifuge tubes for extraction of chromium-reducible sulfur.

### **Extraction of chromium-reducible sulfur (CRS)**

Modified reduced sulfur extraction protocol: Acid insoluble residues, collected after the acid digestion by 2 N HCl of carbonate and CFA sample powders as described above, were rinsed three times with Milli-Q water, collected on  $0.05 \mu\text{m}$

nitrocellulose filter paper, dried, and weighed. For each sample, between 5 and 500 mg of dried acid-insoluble residue was added to an acid-washed, triple-necked glass reaction vessel, along with a small ( $< 1$  mL) volume of EtOH to prevent static cling of dry sample to reaction vessel wall. Reaction vessels were placed in a heating nest and warmed. To each reaction vessel, we attached (1) a valve-controlled connection to a continuous flow of  $N_2$  gas, (2) a cannula allowing for the introduction of liquid reagents, and (3) a cold water condenser attached to a gas-escape tube which was submerged in a “sulfide trap” solution of 10%  $NH_4OH$  and 3% Zn-acetate. Through cannula (2), we gradually introduced the following reagents to each reaction vessel: 10 mL of 12 N HCl and 20 mL of a chromium reduction solution (2 M  $Cr(III)Cl_3 \cdot 6H_2O$  in 0.5 N HCl solution, passed through a column packed with Zn pellets – amalgamated from powder via reaction with mercuric nitrate – under vacuum). Chromium-reducible sulfur was released from the dissolving powders as gaseous  $H-2S$ , separated from water vapor during passage through the cold-water condenser on reaction vessel neck (3) and bubbled through the trap solution of  $NH_4OH$  and Zn-acetate. In this basic trap solution,  $H_2S$  is converted to  $HS^-$  and  $S_2$ , which react with zinc ions in solution to yield ZnS. A small aliquot of ZnS in trap solution from each sample was extracted and measured via colorimetric assay to ascertain sulfide abundance. The remaining ZnS in trap solution was treated with  $AgNO_3$  solution to fix sulfide as solid  $Ag_2S$  for combustion to  $SO_2$  and measurement via EA-IRMS.

**Colorimetric Assay for Sulfide Abundance:** Abundance of sulfide in solution is commonly measured through a modified version of the Cline Assay (Cline, 1969), wherein solutions where sulfide species have been fixed as ZnS are reacted with Cline Reagent, a mixture of N,N-dimethyl-p-phenylenediamine sulfate and hydrated ferric chloride dissolved in 50% HCl. The colored complex formed between ZnS and diamine and  $Fe^{3+}$  has a maximum absorbance at  $\lambda = 670 \mu m$ , and the intensity of this absorbance scales directly with ZnS abundance in the treated solution. Aliquots of trap solution for each sample were serially diluted with Milli-Q water alongside a range of standards of known ZnS concentration in 96-well acrylic plates. These were each treated with the Cline Reagent, allowed to react for 2 hours, and their absorbance at  $\lambda = 670 \mu m$ , measured using a plate-reading spectrophotometer. The absorbances of a range of standards of known ZnS concentration were used to calibrate the relationship between absorbance and  $[ZnS]$ , which was then applied to the samples of unknown concentration.

## MC-ICP-MS

Collection of isotopic data: The  $\delta^{34}S$  values of structural sulfate extracted from carbonate mineral samples (CAS) were measured via Thermo Fisher Scientific Neptune Plus multicollector inductively-coupled plasma-source mass spectrometry (MC-ICP-MS) with a Cetac Aridus II desolvating spray chamber following methods of Paris et al. (Paris, Sessions, et al., 2013). Autosampler vials containing 8 carbonate samples' extracted trace sulfate as sodium sulfate in  $HNO_3$  solution were measured alongside vials containing trace sulfate from 1 seawater standard, 1 coral standard, and 2 procedural blanks – each vial's contents being measured twice. Each measurement was bracketed by the measurement of a laboratory reference sodium sulfate solution of known isotopic composition.

Reduction of isotopic data: Each set of 50 acquisition cycles for each intermediate replicate of samples, standards, and procedural blanks were monitored for any time-dependent trends in intensity (i.e., correlations between measured mass ratio  $^{34}R/^{32}R$  and acquisition number). Drift in the instrument's ionization efficiency and detector response to ion flux over time is expected, and may be quantified and corrected for using bracketing laboratory standard solution. But significant drift on timescales smaller than the acquisition time of a single sample are indicative of instrumental effects that cannot be well-quantified, and measurements whose accuracy and precision cannot be well-constrained. 1 replicate measurement of sample Aris\_10.8 was excluded from further analysis by this metric, as well as 1 replicate measurement of Min\_26.4.

Procedural blanks provided a constraint for the isotopic composition and abundance of background sulfate. Sulfate abundance in the 2 procedural blanks (4 total measurements) was: 1.37 nmol and 0.40 nmol total, with  $\delta^{34}S$  of  $13.58 \pm 0.08\text{‰}$ (VCDT) and  $4.06 \pm 0.23\text{‰}$ (VCDT), respectively. Isotope mass ratios for all samples and standards were corrected for this background sulfate. Depending on the sulfate mass in each sample, this correction affected  $\delta^{34}S$  values by +0.004 to 1.1‰, values which were smaller than the standard error of the population of 50 acquisition cycles which described the precision of each measurement.

Measurement of the seawater standard and the coral standard provided a metric of accuracy for corrected  $\delta^{34}S$  values of unknown samples. Corrected for background sulfate measured via procedural blanks, measured  $\delta^{34}S$  of the coral standard was  $22.68 \pm 0.18\text{‰}$ (VCDT). For the seawater standard, blank-corrected  $\delta^{34}S$  was  $21.05 \pm 0.19\text{‰}$ (VCDT). These values are within one standard error of the accepted

$\delta^{34}\text{S}$  values for these standard materials (Paris, Sessions, et al., 2013).

Relative intensity (RI) of the signal from each sample measurement compared to the signal from bracketing laboratory reference measurements was monitored throughout. RI values near 1.0 indicate that the amount of sulfate in the sample is close to the amount of sulfate in the laboratory standard, and therefore should have similar mass bias. RI values between 0.9 and 1.1 reflect samples whose mass bias due to mismatching of the sample matrix with that of the in-house bracketing standard is less than analytical precision (Paris, Sessions, et al., 2013). 3 samples with RI values outside of this range were excluded from further analysis; poor matrix-matching resulted in inaccurate  $\delta^{34}\text{S}$  data, and potentially incomplete sulfate purification by anion exchange chromatography which was not detected by ion chromatography. These 3 samples were all from the same locality and collected from within the same stratigraphic section, and indeed all 3 yielded significant amounts of acid-insoluble residue during the sample preparation and cleaning process – suggesting that samples may have had high abundance of unquantified contaminants.

$\Delta^{33}\text{S}$  represents the difference between measured  $\delta^{33}\text{S}$  of a sample, standard, or reference material, and the  $\delta^{33}\text{S}$  expected based on mass-dependent fractionation of  $^{32}\text{S}$ ,  $^{33}\text{S}$ , and  $^{34}\text{S}$ . As no mass-independent fraction of  $^{33}\text{S}$  is expected in these Neoproterozoic samples,  $\Delta^{33}\text{S}$  values outside of error from 0‰ were considered a metric of plasma interferences and contamination of signal by ions other than sulfur. Thus, measurements of samples with  $\Delta^{33}\text{S}$  outside the range -1.5 to 1.5‰ were excluded from further analysis. 2 samples would have been excluded by this metric, but had already been culled from the dataset on the basis of unacceptably large relative intensities consistent with ineffective sulfate purification by anion exchange chromatography. Ultimately, 5 of the original 12 samples yielded  $\delta^{34}\text{S}$  of CAS for which precision and accuracy were considered reliable.

### **EA-IRMS**

Collection of isotopic data: The  $\delta^{34}\text{S}$  values of structural sulfate extracted from CFA-cemented samples (PAS) and of chromium-reducible sulfide (CRS) were measured via a combined Thermo Elemental Analyzer and Thermo Delta Plus XL isotope ratio mass spectrometer (EA-IRMS). Samples of PAS fixed as dried  $\text{BaSO}_4$  powders and samples of CRS fixed as  $\text{Ag}_2\text{S}$  powders, as well as  $\text{Ag}_2\text{S}$  standards with a range of known isotopic composition, were weighed into tin foil capsules, each containing between 4 and 5  $\mu\text{g}$  sulfur, which were sealed and compressed to remove air.

These were loaded into the elemental analyzer, undergoing combustion with  $O_2$  gas, such that sulfur in  $BaSO_4$  and  $Ag_2S$  was converted to  $SO_2$ .  $SO_2$  gas was passed through a network of solid and gaseous reagents which ensured its redox state, then a chromatographic column and water trap to remove non- $SO_2$  contaminants which may have volatilized during the combustion process, then into the ion source and analytical path of the isotope ratio mass spectrometer. A series of automated valves alternated the stream of the  $SO_2$  gas from combusted samples and standards with aliquots from a reservoir of laboratory reference  $SO_2$  gas of known isotopic composition. Each measurement consisted of multiple cycles of reference gas and analyte gas via magnetic sector isotope ratio mass spectrometry, wherein Faraday cups attached to amplifiers measured the flux of ions of  $m/z = 64$  and  $66$ , allowing for the calculation of the mass ratio  $^{34}R/^{32}R$  and thereby  $\delta^{34}S$  of PAS, CRS, and sulfur isotope standards.

Reduction of isotopic data: All measurements of samples and standards were corrected for instrumental drift with respect to ionization efficiency, detector response, and other sources of non-linearity between isotopic composition of a gas and measured composition, by monitoring  $^{34}R/^{32}R$  of laboratory standard  $SO_2$  gas over the course analysis.

Measurements of sets of 10 samples of unknown isotopic composition were bracketed by 2 sets of measurements of at least 6 standards of known isotopic composition (i.e., paired replicates of 3 different standard materials). Least-squares linear regression was performed to describe the linear relationship between standards' measured  $\delta^{34}S$  and their known/accepted  $\delta^{34}S$  values. Each sample's measured  $\delta^{34}S$  value was converted into the reference frame established by the bracketing standards by applying the linear relationship between measured-and-accepted values from the preceding set of standards as well as the linear relationship from the succeeding set of standards, and taking the average of the two converted values.

### **7f-GEO-SIMS**

Collection of isotopic data: Samples for which the yield of chromium reducible sulfur (CRS) extraction was less than the analytical limit of EA-IRMS (  $4 \mu g$  S), but in which intergrowth of pyrite with CFA cements was still observable via petrographic thin section, were identified as targets for analysis using the Caltech Microanalysis Center's Cameca IMS 7f-GEO Secondary Ion Mass Spectrometer (SIMS). Individual pyrite crystals or aggregates of crystals with diameters  $\geq 20 \mu m$

were identified using reflected light microscopy.

Petrographic thin sections containing target pyrite crystals, 30  $\mu\text{m}$  thick, were sputter-coated with gold, negatively charged via electron gun, then bombarded with a pulsed primary ion beam of  $\text{Cs}^+$  cations which – at the voltages employed, had a beam width of roughly 20  $\mu\text{m}$ . The energetic primary  $\text{Cs}^+$  ions generated by the 7f-GEO SIMS ion source displace and liberate a cascade of secondary ions from a small analytical volume within the target crystals. These secondary ions enter a magnetic sector mass spectrometer via a series of ion optics. Faraday cup detectors equipped with amplifiers measured flux of secondary ions of  $m/z = 32, 33,$  and 34 (sulfur) as well as 16 (oxygen). These ion fluxes were used to calculate  $^{34}\text{R}/^{32}\text{R}$  and thus  $\delta^{34}\text{S}$  of the structural sulfur of the interrogated pyrite crystals.

Reduction of isotopic data: Each measurement consisted of 29-30 acquisitions of secondary ion flux from the same pyrite crystal. Measurements of target pyrite crystals of unknown composition were bracketed by repeated measurements of an in-house pyrite standard. Replicate standard measurements were used to quantify the relationship between signal/instrument response and actual sulfur isotopic composition of the sample, capturing any fractionation between the analyte and the population of secondary ions generated. The standard error of  $\delta^{34}\text{S}$  values measured for the bracketing standards was propagated with standard error of the population of 29-30 acquisitions for each measurement of a pyrite crystal of unknown composition, to quantify the measurements' precision (0.6-0.7‰).

#### 4.5 Results

In this study, we present  $\delta^{34}\text{S}$  values of (1) structural sulfate in the mineral lattice of dolomite and calcite cements, or carbonate-associated sulfate (CAS), (2) structural sulfate in the mineral lattice of carbonate fluorapatite cements, or phosphate-associated sulfate (PAS), and (3) sulfide in the mineral lattice of pyrite crystals ( $\text{FeS}_2$ ). CAS is a trace chemical component of carbonate rock, having concentrations of ppt to ppm in most natural samples, and ideally represents a subsample of the aqueous sulfate in the fluids from which the carbonate rock precipitated. PAS is more abundant than CAS per unit mass of the host mineral, with concentrations of order 10-100 ppm. The sulfate incorporated into the structure of these cement-forming minerals ideally are an isotopically representative subset of the aqueous  $\text{SO}_4^{2-}$  in the fluids from which the cements precipitated. Likewise, sulfide in pyrite represents the aqueous  $\text{H}_2\text{S}$  and  $\text{S}^{2-}$  in the parent solution from which the pyrite grew. Thus, paired

measurements of  $\delta^{34}S$  of CAS/PAS and  $\delta^{34}S$  of pyrite in rocks that were deposited and cemented at the same time and place provide a snapshot of the difference in isotopic composition of oxidized and reduced sulfur species in the same porefluid. We interrogate two distinct textural classifications: (a) carbonate-cemented, and (b) phosphate-cemented. The carbonate cemented class includes laminated and/or cross-stratified carbonate grainstones, mudstones, and boundstones (stromatolite buildups), comprised of carbonate grains in carbonate cements. The phosphate-cemented class includes stromatolitic laminae in boundstone/mudstone, comprised of carbonate micrite and grains in cryptocrystalline carbonate fluorapatite cement. Abundance of CAS and pyrite and paired  $\delta^{34}S$  measurements of CAS and pyrite in “a” should – theoretically – provide a constraint on sulfur cycling in the pore waters in which carbonate mineralization was favored. Abundance of PAS and pyrite and paired  $\delta^{34}S$  measurements of PAS and pyrite in “b” should provide a constraint on sulfur cycling in phosphate-mineralizing pore waters. These data are described below, and summarized in Table 1.

#### **Abundance and $\delta^{34}S$ of CAS and Fe-Sulfides in Carbonate-Cemented Textures**

The weight percent of sulfate in the carbonate-cemented samples analyzed here was calculated from the molar concentration of  $SO_4^{2-}$  in the purified, acid-soluble fraction of each powdered and cleaned sample of mm-scale drill tailings (as measured by ion chromatography) relative to the original mass of the powder sample – see Methods. Samples which had sulfate concentrations above the detection limit of the ion chromatograph, sufficient to aerosolize and convert to an ionized beam for ICP-MS, had concentrations of 7-42 ppm. Carbonate samples at the lower end of this range included Cer\_23e ([CAS] = 7.3 ppm) and Aris2\_10.8 ([CAS] = 12 ppm), which are taken from cross-stratified oolitic grainstone facies characterized in the Cerberus and Aristeia localities, respectively. In the case of Cer\_23e, the sampled grainstone was immediately adjacent to (i.e., within a few lateral centimeters of) CFA-cemented digitate stromatolites, and represent carbonate sedimentation at the same time interval and depositional setting as the cementation of the stromatolites. Carbonate samples at the higher end of the observed range of CAS abundances included FuroX\_3330 and FuroX\_3340 (which sample the carbonate grainstone immediately adjacent to CFA-cemented digitate and disordered stromatolite facies in CBPM Core 10, with [CAS] of 30 ppm and 31 ppm, respectively), and FuroV\_3400 (which sampled very fine planar-to-crinkly-laminated carbonate mudstone in CBPM Core 5, with [CAS] of 42 ppm).

The  $\delta^{34}S$  value of CAS ( $\delta^{34}S_{CAS}$ ) in the 5 above-described samples represents sulfur isotope composition of an admixture of the structural sulfate in micritic and interlocking anhedral mosaic cements of calcite and/or dolomite, with minor contributions from the micritized peloids and ooids suspended in those cements. Procedures to remove easily soluble sulfate phases outside of the carbonate mineral lattice, and from oxidized sulfide minerals, should minimize the contributions of these phases to the measured samples. Carbonate grainstone facies immediately adjacent to CFA-cemented stromatolite facies yielded  $\delta^{34}S_{CAS}$  of  $33.64 \pm 0.88\text{‰(VCDT)}$  (Cer\_23e),  $19.79 \pm 0.45\text{‰(VCDT)}$  (FuroX\_3330), and  $26.59 \pm 0.23\text{‰(VCDT)}$  (FuroX\_3340), where errors represent  $\pm 1$  standard error around the mean of a population of 50 acquisition cycles for a given sample. Carbonate grainstone facies not associated with stromatolites yielded  $\delta^{34}S_{CAS}$  of  $37.91 \pm 0.73\text{‰(VCDT)}$  (Aris2\_10.8). Carbonate mudstone facies not associated with stromatolites yielded  $\delta^{34}S_{CAS}$  of  $29.41 \pm 0.32\text{‰(VCDT)}$  (FuroV\_3400).

Pyrite which cross-cut or are intergrown with micritic and interlocking anhedral mosaic carbonate cements represent an extremely minor component in the carbonate-cemented rocks of the Salitre Formation. Structural sulfur in this pyrite was extracted as CRS. Cline Assay of CRS fixed as ZnS provided a minimum constraint on the abundance of CRS in the measured samples Aris\_31.8\_80 and Min\_44.2: <10 ppm S in each. Note: concentrations are calculated via the measured concentration of CRS in an aliquot of the rinsed, dried, acid-insoluble residue after washing and HCl-leaching of carbonate samples (described in Methods), and represent the sulfide extracted from the mineral pyrite ( $FeS_2$ ), but not from other sulfide pools such as pyrrhotite (FeS) or organically-bound sulfide. The  $\delta^{34}S$  values of CRS ( $\delta^{34}S_{CRS}$ ) in our three carbonate-cemented samples which had abundances above the threshold of our analyses (See Methods), represent the sulfur isotope composition of the reduced  $H_2S$  or  $S^{2-}$  which was captured by reaction with reduced iron ( $Fe^{2+}$ ) during and subsequent to cementation/lithification. Our sampling method, which avoided veins and close spatial associations with late-stage diagenetic phases, should have minimized the contribution to CRS from sulfide associated with diagenetic fluids after deep burial, such that the measurements may be considered a proxy for sulfide scavenged by trace  $Fe^{2+}$  in anoxic to suboxic sediment pore waters (early diagenesis). Pyrite S extracted as CRS, associated with carbonate-cemented stromatolite laminae, yielded  $\delta^{34}S_{CRS}$  of  $6.92 \pm 1.06\text{‰(VCDT)}$  (average and standard error of 2 replicates of Aris\_31.8\_80). Pyrite S extracted as CRS, associated with carbonate-cemented cross-stratified grainstone, yielded  $\delta^{34}S_{CRS}$  of  $6.95 \pm 1.29\text{‰(VCDT)}$  (average and

standard error of 2 replicates of Min\_44.2).

### **Abundance and $\delta^{34}\text{S}$ of PAS and Fe-Sulfides in Phosphate-Cemented Textures**

The abundance of structural sulfate in carbonate fluorapatite cement samples (PAS) could only be given a minimum constraint, based on the mass yield of  $\text{BaSO}_4$  from  $\text{BaCl}_2$  reaction with decarbonated, acid-soluble filtrates derived from purified powders of carbonate fluorapatite – see Methods. 500 mg of cleaned and purified CFA powder yielded 5 mg of  $\text{BaSO}_4$  (0.192 mg  $-\text{SO}_4$ ), implying PAS concentration in the measured samples of at least 384 ppm.

The  $\delta^{34}\text{S}$  value of structural sulfate in carbonate fluorapatite cements ( $\delta^{34}\text{S}_{\text{PAS}}$ ) represents sulfur isotope composition of the aqueous sulfate in the pore waters from which the cements precipitated. There were only a few samples suitable for this analysis (i.e., extracted from well-characterized fabrics and having sufficiently high PAS concentrations to allow for bulk rather than trace sulfate extraction methods). These included: Aris1A\_31.8\_60.8, Aris1B\_31.8\_60.8, and FuroX\_3340, from digitate stromatolite buildups in the Aristeia locality and CBPM Core 10. A set of 3 replicate measurements of the sulfur isotope composition for PAS in Aris1A\_31.8\_60.8 yielded values of  $\delta^{34}\text{S}_{\text{PAS}} = 30.94 \pm 0.71\text{‰}$ (VCDT). 3 replicate measurements for PAS in Aris1B\_31.8\_60.8 yielded  $\delta^{34}\text{S}_{\text{PAS}} = 30.94 \pm 0.39\text{‰}$ (VCDT). 3 replicate measurements for PAS in FuroX\_3340 yielded  $\delta^{34}\text{S}_{\text{PAS}} = 33.42 \pm 0.16\text{‰}$ (VCDT). (Note: confidence intervals are given as the standard error.)

Sulfide minerals that were intergrown with or appeared to cross-cut cryptocrystalline carbonate fluorapatite cements were in low abundance, and their structural sulfide could not be extracted as CRS from the small quantities of powder that result from mm-scale drilling of specific textures. Individual pyrite crystals and aggregates of crystals within the relevant textures and larger than the  $\text{Cs}^+$  beam of the 7f-GEO-SIMS at a given current (here,  $\geq 20 \mu\text{m}$ ) were thus selected for SIMS analysis, but total abundance and bulk isotopic composition of phosphate-associated pyrite was not measured.

The  $\delta^{34}\text{S}$  value of pyrite associated with carbonate fluorapatite-cemented textures ( $\delta^{34}\text{S}_{\text{pyr}}$ ), as in the carbonate-cemented facies, represent the sulfur isotope composition of the reduced  $\text{H}_2\text{S}$  or  $\text{S}^{2-}$  which was captured by reaction with reduced iron ( $\text{Fe}^{2+}$ ) during and subsequent to cement precipitation from sediment pore waters. The mineral pyrite ( $\text{FeS}_2$ ) may form by the reaction of  $\text{Fe}^{2+}$  and sulfide ions in solution, but so can other phases such as marcasite (also  $\text{FeS}_2$ ), or

troilite/pyrrhotite (FeS). Pyrite is one of the more stable iron sulfide phases in the temperature and pressure regimes of the crust's upper few kilometers, and so may represent the primary phase in which sulfide was mineralized or recrystallized pseudomorphs after less stable or less oxidized iron sulfide minerals. Measuring the isotopic composition of iron sulfide minerals via SIMS allows for the analysis of individual and aggregate crystals of iron sulfide phases whose mineralogies have been independently confirmed by other methods to be pyrite, and which are not spatially associated with later-stage diagenetic features. However, we did analyze some iron sulfide crystal aggregates which may have integrated the secondary ions generated by sputtering of not only pyrite, but other closely associated minor iron-sulfide phases, namely marcasite and pyrrhotite (Figure 4). Such secondary ions would not have been generated according to the same physics as the interaction of the primary ion beam with the pyrite standard, and so the  $\delta^{34}S$  measured on less-than-pure-pyrite SIMS targets (henceforth,  $\delta^{34}S_{pyr,mix}$  would likely be inaccurate (Kita et al., 2011; Kozdon et al., 2010; Riciputi, Paterson, and Ripperdan, 1998).  $\delta^{34}S_{pyr}$  of confirmed pyrite crystals  $\geq 20 \mu\text{m}$  in diameter and associated with carbonate-fluorapatite-cemented textures were successfully measured via SIMS in only one well-characterized sample: FuroX\_3330, a sample from phosphatic digitate stromatolite facies within CBPM Core 10.  $\delta^{34}S_{pyr}$  values in this sample were:  $23.77 \pm 0.64\text{‰(VCDT)}$ ,  $18.24 \pm 0.60\text{‰(VCDT)}$ ,  $21.79 \pm 0.60\text{‰(VCDT)}$ ,  $23.97 \pm 0.60\text{‰(VCDT)}$ ,  $33.14 \pm 0.58\text{‰(VCDT)}$ ,  $23.71 \pm 0.60\text{‰(VCDT)}$ , and  $38.47 \pm 0.60\text{‰(VCDT)}$ , where errors are the standard error of a set of 50 measurements of a continuously generated secondary ion beam, corrected for instrumental response according to parallel measurements of a pyrite standard of known composition (see Methods). This wide range of values (18-38‰(VCDT)) were retrieved for pure pyrite crystals in the same sample, and from at the same position in the paragenetic sequence of that sample – reflecting either a wide range in porewater sulfide compositions at the time of their formation (due to micro-scale variations in aqueous chemistry in pores under conditions of limited pore connectivity, and/or a wide range in the timing of each crystal's formation with respect to sulfur cycling in the porespace.

A population of possible admixtures of pyrite with other iron-sulfide minerals including pyrrhotite and marcasite was measured as well, yielding  $\delta^{34}S_{pyr,mix}$  of  $-1.56 \pm 0.76\text{‰(VCDT)}$ ,  $-0.38 \pm 0.61\text{‰(VCDT)}$ ,  $-4.24 \pm 0.63\text{‰(VCDT)}$ ,  $-8.25 \pm 0.71\text{‰(VCDT)}$ , and  $-7.88 \pm 0.73\text{‰(VCDT)}$ . These values may reflect reduced-iron capture of isotopically lighter sulfide introduced to the sedimentary rock by a different generation of porefluids, but the difference in matrix effects on secondary ion beam production

between pure pyrite and possible mixtures of pyrite and other iron-sulfide phases cannot here be constrained, and so these measured values should be excluded from analysis.

#### 4.6 Discussion and conclusions

##### **Interpretation of $\delta^{34}S$ in phosphatic- and non-phosphatic cemented textures**

As earlier stated, the isotopic composition of sulfur incorporated into early-forming pore cements as structural sulfate and as minor pyrite represent the net effect of many different sulfur reactions occurring in porefluids. The importance of these reactions (i.e., the proportion of the porefluid sulfur on which they act), and the kinetic fractionation effects with which they are associated, are many and varied. Furthermore, mineralization of CFA and carbonate cements with trace sulfate, and mineralization of sulfide as pyrite, may have occurred at any point in the progress of sulfate- and sulfide-involved reactions – such that the  $\delta^{34}S$  of sulfate in co-occurring cements, or of sulfide in intergrown pyrite crystals, may represent porewater sulfate and sulfide in different moments of isotopic disequilibrium. It may not be possible to deconvolve all of the reactions affecting sulfur isotopic composition of sulfate and sulfide based on the “snapshots” provided by the  $\delta^{34}S$  of sulfur in structural sulfate and sulfide in co-occurring mineral phases. However, it may be possible to constrain the likelihood that certain reactions were prevalent in porefluids at the time of cementation, and which may have enabled or inhibited precipitation of phosphate minerals. Significant differences in the quantity  $\Delta^{34}S = \delta^{34}S_{SO_4} - \delta^{34}S_{sulfide}$  between CFA and carbonate-cemented textures may provide a clue to differences in microbial metabolic activity which determined the spatial distribution of sedimentary phosphorite. If starting seawater sulfate concentrations are low – as may be the case in some Edicaran basins (Galen P. Halverson and Matthew T. Hurtgen, 2007; Laakso et al., 2020; Loyd et al., 2012; Ries et al., 2009) – or there is limited communication between porefluids and the wider ocean, isotopic fractionation might be small between sulfide derived from microbial sulfate reduction and fixed as pyrite and the starting sulfate pool due to kinetic fractionation effects in a closed system. Sulfate incorporated into the pore-filling cements, however, rather than in the interiors of grains precipitated from the water column, is likely more representative of the residual porewater sulfate during early diagenetic microbial sulfate reduction. Therefore, one may expect  $\Delta^{34}S$  between cement-associated sulfate and pyrite sulfide on the order of 15-30‰ or even more, when microbial sulfate reduction is prevalent in pore waters (Boudreau and Westrich, 1984; Bradley et al.,

2016; Brunner and Bernasconi, 2005; Donald E. Canfield, Farquhar, and Zerkle, 2010; Gomes and David T. Johnston, 2017; Habicht and Donald E. Canfield, 2001; Harrison and Thode, 1958). Sulfur disproportionating microorganisms are also capable of producing large fractionations between sulfate and sulfide pools. The light isotopologue of  $SO_4^{2-}$  is preferentially taken up by these microorganisms, and then preferentially reduced to  $SO_3^{2-}$  (sulfite),  $S_2O_3^{2-}$  (thiosulfate), and  $S_0$  and other intermediate sulfur species. Light isotopologues of these intermediates are then preferentially reduced to sulfide. The sulfide pool produced by reduction of sulfur intermediates is thus more  $^{34}S$  depleted relative to the starting sulfate pool than if only direct microbial sulfate reduction had taken place, which may result in  $\Delta^{34}S$  of 40-70‰ (Farquhar et al., 2003; Habicht and Donald E. Canfield, 2001; Ohn et al., 1998; Matthew T Hurtgen, Arthur, and Galen P Halverson, 2005; David T. Johnston et al., 2005; Leśniak et al., 2003).

If microbial sulfide oxidation to sulfate is prevalent in sediment porefluids, there may be a significant contribution to the porewater sulfate pool of  $^{34}S$ -depleted sulfate – since the  $H_2S$  utilized by sulfide-oxidizing microorganisms is the direct metabolic product of microbial sulfate reduction, which can produce large sulfate-sulfide fractionations. This could result in similar  $\delta^{34}S$  values for structural sulfate and sulfide, i.e.  $\Delta^{34}S \approx 0$ ‰ (Arning et al., 2009; Dale et al., 2009; Gomes and David T. Johnston, 2017). In addition, the kinetic fractionation effects of microbial sulfide oxidation may result in several-per-mille  $^{34}S$ -enrichment of the sulfide pool ( $\Delta^{34}S = -5$ - $0$ ‰), depending on the biochemical pathways utilized and whether ancient sulfide-oxidizing microorganisms utilized  $O_2$  and  $NO_3^-$  like their counterparts in modern phosphogenic environments (Kaplan and Rafter, 1958; Poser et al., 2014). Interestingly, it is also possible for some sulfide-oxidizing microorganisms to disproportionate the  $S_0$  intermediate, resulting in highly  $^{34}S$ -enriched sulfate – producing  $\delta^{34}S$  comparable to microbial sulfate reduction (Pellerin et al., 2019).

### **Sulfur cycling recorded by carbonate-cemented textures of the Salitre Fm.**

Non-phosphatic textures of the Salitre Formation include calcite- and dolomite-cemented grainstone and mudstone between stromatolites and adjacent to stromatolite buildups, as well as calcite- and dolomite-cemented stromatolitic boundstone. Structural sulfate in sampled calcite and dolomite cements associated with oolitic grainstone and laminated mudstone yielded a wide range of  $\delta^{34}S$  values, between roughly 19 and 38‰ (VCDT) – see Table 1. Structural sulfide in pyrite, measured as CRS, which was associated with carbonate-cemented laminated mudstone and

carbonate-cemented digitate stromatolites yielded  $\delta^{34}S$  values around 7‰(VCDT). We were unable to confidently measure CRS and CAS in carbonate-cemented textures drilled from the exact same hand samples due to too-low or poorly constrained CAS concentrations in some samples, and too-low CRS extraction yields in others. Nevertheless, because our sampling protocols were texturally specific the same paragenetic phases within the same textures, the difference  $\Delta^{34}S$  between  $\delta^{34}S_{SO_4}$  and  $\delta^{34}S_S$  may still provide a constraint on sulfur isotope systematics in carbonate-precipitating porefluids of the Salitre Formation.  $\Delta^{34}S$  in these carbonate-cemented textures had a range of about 12 to 31‰. This range of values is consistent with the range of kinetic isotope effects associated with microbial sulfate reduction; i.e., microbial sulfate reduction alone can explain  $\delta^{34}S$  of sulfate and sulfide in pore fluids at the time carbonate cements were forming. Sulfur disproportionation and sulfide oxidation may have also occurred in pore fluids at the same time, or even before the sampled sediments were buried below the chemocline and cements precipitated, but the fractionation effects of these metabolisms may not have been as prevalent at the “moment” captured by the crystallizing carbonate minerals and pyrite.

#### **Sulfur cycling in CFA cement-forming sediments of the Salitre Fm.**

Phosphatic textures of the Salitre Formation are defined by the predominance of cryptocrystalline CFA cement, including the laminae of phosphatic digitate stromatolites. Structural sulfate in CFA cement samples yielded  $\delta^{34}S$  of 30-34‰— see Table 1. Structural sulfide in pyrite associated with CFA-cemented textures was too low in abundance to yield a measurable mass of CRS, and so individual pyrite crystals and aggregates of pyrite crystals were measured via SIMS from a single sample: FuroX\_3330. These pyrites yielded  $\delta^{34}S$  between about 18 and 39‰. As with the carbonate-cemented facies, it was not possible to directly measure the sulfur isotope composition of pyrite PAS within the same hand samples. However,  $\delta^{34}S$  between associated PAS and pyrite within comparable textures is still informative.  $\delta^{34}S$  in CFA-cemented facies is small: between -5 and 12‰. This small fractionation, and possible reverse fractionation, is clearly different from that observed in the carbonate-cemented facies. Rather, it is more consistent with a scenario in which sulfide oxidation was also prevalent in pore fluids – such that some significant fraction of the  $^{34}S$ -depleted sulfide produced via microbial sulfate reduction was converted to sulfate and the remaining sulfide pool correspondingly  $^{34}S$ -enriched.

Alternatively, it is possible that the measured CFA cement-associated was not representative of biogenic sulfide in sediment pore waters and instead resulted from

thermochemical reduction of sulfate during late-stage diagenesis at temperatures  $>110^{\circ}\text{C}$  (Cui et al., 2018), temperatures well within the range experienced by the measured rocks (Sanders, J. Eiler, and Grotzinger, 2022). However, carbonate-cemented textures in these samples experienced the same thermal history as the CFA-cemented samples – being within centimeters to meters of one another at the same or similar stratigraphic levels, in the same localities – and we found no  $^{34}\text{S}$ -enriched CRS measurements among samples from the carbonate-cemented textures. Thus, we find that a biogenic origin for the sulfide incorporated into the pyrite crystals measured is likely, and that  $\delta^{34}\text{S}$  in CFA-cemented facies indeed reflects a porewater chemistry impacted by metabolisms other than microbial sulfate reduction – likely microbial sulfide oxidation.

Sample FuroX\_3340 was the sole sample in which it was possible to measure both PAS and CAS. CFA-cemented stromatolite laminae and carbonate-cemented inter-stromatolite fill from this sample yielded  $\delta_{PAS}^{34}$  of  $33.42 \pm 0.28\text{‰}$  and  $\delta_{CAS}^{34}$  of  $26.59 \pm 0.23\text{‰}$ , respectively. These values are similar enough – considering the variability among  $\delta^{34}\text{S}$  in the same mineral phases within the same samples – that we consider neither CAS nor PAS to be substantially  $^{34}\text{S}$ -enriched relative to the other. Phosphatic crusts in which  $\delta^{34}\text{S}_{PAS} < \delta^{34}\text{S}_{seawaterSO4}$  have been interpreted as evidence of microbial sulfide oxidation in modern phosphogenetic environments (Arning et al., 2009). However, it seems unlikely that  $\delta^{34}\text{S}_{CAS}$  as measured in this study (i.e., within pore cements) is truly representative of  $\delta^{34}\text{S}_{seawaterSO4}$ . Rather, it seems likely that  $\delta^{34}\text{S}_{CAS}$  and  $\delta^{34}\text{S}_{PAS}$  in co-occurring CFA and carbonate cements within the same hand sample represent porewater sulfate during cementation.

In the Sete Lagoas Formation, the corollary of the Salitre Formation representing sedimentation in a more southern sub-basin of the Sao Francisco Craton's Ediacaran sea (Drummond et al., 2015; J. Okubo et al., 2018; Sanders and Grotzinger, 2021), bulk CAS and CRS measurements from carbonate rock unaffiliated with phosphatic cements or intraclasts both yielded high  $\delta^{34}\text{S}$  values, around 30-50‰VCDT (Juliana Okubo et al., 2022). These values were found to be consistent with models in which low-abundance seawater sulfate in restricted pore waters undergoes isotopic distillation. While this may have applied broadly to the more northern Salitre Formation as well, the textures-specific measurements of CAS, PAS, CRS, and pyrite crystals presented here allow us to distinguish sulfur isotope systematics in phosphogenetic microenvironments from those in non-phosphogenetic microenvironments. This distinction could illuminate how the ecology of marine sediments determined the

spatial distribution of phosphogenesis.

### **Sulfur cycling and phosphogenesis in the Salitre Fm.**

Carbonate-cemented textures and CFA-cemented textures of the Salitre Formation preserve different  $\delta^{34}S$ . In carbonate-cemented textures, CAS was generally  $^{34}S$ -enriched with respect to pyrite extracted as CRS:  $\delta^{34}S = 12$  to  $31\%$ , where the range reflects the variability among CAS measurements and among CRS measurements. In CFA-cemented textures – i.e., phosphatic textures – PAS and pyrite crystals had similar sulfur isotope compositions:  $\delta^{34}S = -5$ - $12\%$ . This suggests that there was a significant difference in sulfur-cycling dynamics between carbonate-precipitating and phosphate-precipitating textures. Furthermore, it suggests that while microbial sulfate reduction alone can explain the observed  $\delta^{34}S$  in carbonate-cemented textures, it may be necessary to invoke microbial sulfide oxidation and microbial sulfate reduction within the same pore waters to explain the  $\delta^{34}S$  of CFA-cemented textures. In modern phosphogenetic environments, microbial sulfide oxidation appears to be instrumental in enabling early phosphate mineralization in marine sediments. Biomarkers associated with polyphosphate-accumulating sulfide oxidizers are more abundant in phosphogenetic sediments than co-occurring non-phosphogenetic sediments (Arning et al., 2009). Actively growing phosphatic crusts incorporate body fossils of both sulfate-reducing and sulfide-oxidizing microorganisms (Arning et al., 2009; J. V. Bailey et al., 2013; Goldhammer et al., 2010; H. N. Schulz and H. D. Schulz, 2005). Cultures of sulfide-oxidizing organisms from modern phosphogenetic environments can be induced to raise aqueous phosphate concentrations sharply under conditions of high sulfide concentration (Brock and Schulz-Vogt, 2011; H. N. Schulz and H. D. Schulz, 2005).

There is evidence of sulfide oxidizing metabolisms at work in ancient phosphogenetic settings. Microbial fossils with morphologies and size distributions comparable to modern polyphosphate-accumulating microorganisms have been identified in the Ediacaran phosphatic stromatolites of Central and Northern India (Bengtson et al., 2017; Sallstedt et al., 2018). The Doushantuo Formation of Southern China also contains microbial fossils which resemble modern sulfide-oxidizing microorganisms (J. V. Bailey et al., 2013; Jake V. Bailey et al., 2007), as does the Miocene Monterey Formation in the Western United States (J. V. Bailey et al., 2013). Lipid biomarkers associated with sulfide oxidizing bacteria have been identified in the phosphorite deposits of the Mishash/Ghareb Formation in Israel (Alsenz et al., 2015). However, there are few comparative studies of ancient phosphorites

that demonstrate paleoenvironmental and paleoecological differences between phosphogenetic and non-phosphogenetic facies, and which demonstrate the presence of sulfide-oxidizing microorganisms in the former and absence in the latter. This study presents isotopic data which support the hypothesis that differences in sulfur-metabolizing microbial communities begat differences in the prevalence of early phosphate mineralization.

#### **4.7 Future work**

The Salitre Formation is one of a dozen major phosphorite deposits formed near the Precambrian-Cambrian boundary which have been identified all over the world. It is among the best-characterized, with respect to its sedimentology, stratigraphy, mineral fabrics, and diagenetic history, making it an excellent case for a texture-specific comparative geochemical study. However, it is not among the best-preserved, and the collection of paired  $\delta^{34}\text{S}$  measurements of structural sulfate and sulfide was difficult to achieve within the same hand samples and stratigraphic sections. Other Ediacaran and Lower Cambrian phosphorites, which may exhibit different styles of phosphate mineralization and different levels of organic matter preservation, should be subjected to similar paired sulfate-sulfide studies and textural analyses in the future. Together, they may provide a more rigorous and comprehensive test of the role of sulfide oxidation in ancient phosphogenesis than the Salitre Formation alone.

#### **4.8 Acknowledgements**

The authors extend their gratitude to Wu Fenfang, Guan Yunbin, Grecia “Grace” Ames, and Antoine Cremiere of Caltech’s Division of Geological and Planetary Sciences, for the gift of their expertise, and their patience, as we learned new techniques on new analytical instruments.

We also express our gratitude for the friendship and collaboration with the students, professors, and researchers of the Laboratório de Análises de Minerais e Rochas (LAMIR) e Laboratório de Análises de Bacias (LABAP) da Universidade Federal do Paraná, as well as our collaborators from the Universidade Federal do Bahia, without whom we could not have collected our samples and immersed ourselves in the geology and culture of the studied region. We are also wholly indebted to the farmers, miners, educators, and conservationists of the Chapada Diamantina and Cavernas do Peruaçu regions for their guidance and expertise.

We also wish to thank the reviewers, and to acknowledge that this work was supported by the National Science Foundation Graduate Research Fellowship Program (NSF

GRFP), and the Simons Foundation. We thank the Simons Collaboration on the Origins of Life (SCOL) for funding and support.

Lastly, we humbly acknowledge the Xakriab'a, the communities of and surrounding the historic Quilombo da Gruta dos Brejoes, as well as other indigenous peoples whose names and identities may have been lost to colonialism and occupation, on whose land this work relies.

## References

- Alkmim, Fernando F. and Marcelo A. Martins-Neto (2012). “Proterozoic first-order sedimentary sequences of the São Francisco craton, eastern Brazil”. In: *Marine and Petroleum Geology* 33.1, pp. 127–139. ISSN: 02648172. DOI: 10.1016/j.marpetgeo.2011.08.011. URL: <http://dx.doi.org/10.1016/j.marpetgeo.2011.08.011>.
- Alsenz, Heiko et al. (2015). “Geochemical evidence for the link between sulfate reduction, sulfide oxidation and phosphate accumulation in a late cretaceous upwelling system”. In: *Geochemical Transactions* 16.1, pp. 1–13. ISSN: 14674866. DOI: 10.1186/s12932-015-0017-1. URL: ???.
- Anschutz, Pierre et al. (1998). “Burial efficiency of phosphorus and the geochemistry of iron in continental margin sediments”. In: *Limnology and Oceanography* 43.1, pp. 53–64. ISSN: 00243590. DOI: 10.4319/lo.1998.43.1.0053.
- Arning, E. T. et al. (2009). “Bacterial formation of phosphatic laminites off Peru”. In: *Geobiology* 7.3, pp. 295–307. ISSN: 14724669. DOI: 10.1111/j.1472-4669.2009.00197.x.
- Bailey, J. V. et al. (2013). “Filamentous sulfur bacteria preserved in modern and ancient phosphatic sediments: Implications for the role of oxygen and bacteria in phosphogenesis”. In: *Geobiology* 11.5, pp. 397–405. ISSN: 14724677. DOI: 10.1111/gbi.12046.
- Bailey, Jake V. et al. (2007). “Evidence of giant sulphur bacteria in Neoproterozoic phosphorites”. In: *Nature* 445.7124, pp. 198–201. ISSN: 14764687. DOI: 10.1038/nature05457.
- Bengtson, Stefan et al. (2017). “Three-dimensional preservation of cellular and subcellular structures suggests 1.6 billion-year-old crown-group red algae”. In: *PLoS Biology* 15.3, pp. 1–38. ISSN: 15457885. DOI: 10.1371/journal.pbio.2000735.
- Boudreau, Bernard P. and Joseph T. Westrich (1984). “The dependence of bacterial sulfate reduction on sulfate concentration in marine sediments”. In: *Geochimica et Cosmochimica Acta* 48.12, pp. 2503–2516. ISSN: 00167037. DOI: 10.1016/0016-7037(84)90301-6.

- Bradley, A. S. et al. (2016). “Patterns of sulfur isotope fractionation during microbial sulfate reduction”. In: *Geobiology* 14.1, pp. 91–101. ISSN: 14724669. DOI: 10.1111/gbi.12149.
- Brock, Jörg and Heide N. Schulz-Vogt (2011). “Sulfide induces phosphate release from polyphosphate in cultures of a marine *Beggiatoa* strain”. In: *ISME Journal* 5.3, pp. 497–506. ISSN: 17517362. DOI: 10.1038/ismej.2010.135.
- Brunner, Benjamin and Stefano M. Bernasconi (2005). “A revised isotope fractionation model for dissimilatory sulfate reduction in sulfate reducing bacteria”. In: *Geochimica et Cosmochimica Acta* 69.20, pp. 4759–4771. ISSN: 00167037. DOI: 10.1016/j.gca.2005.04.015.
- Caird, R. A. et al. (2017). “Ediacaran stromatolites and intertidal phosphorite of the Salitre Formation, Brazil: Phosphogenesis during the Neoproterozoic Oxygenation Event”. In: *Sedimentary Geology* 350.January, pp. 55–71. ISSN: 00370738. DOI: 10.1016/j.sedgeo.2017.01.005. URL: <http://dx.doi.org/10.1016/j.sedgeo.2017.01.005>.
- Canfield, D. E. (2019). “Biogeochemistry of sulfur isotopes”. In: *Stable Isotope Geochemistry* 43, pp. 607–636. DOI: 10.1515/9781501508745-015.
- Canfield, Donald E., James Farquhar, and Aubrey L. Zerkle (2010). “High isotope fractionations during sulfate reduction in a low-sulfate euxinic ocean analog”. In: *Geology* 38.5, pp. 415–418. ISSN: 00917613. DOI: 10.1130/G30723.1.
- Canfield, Donald E. and Andreas Teske (1996). “Late proterozoic rise in atmospheric oxygen concentration inferred from phylogenetic and sulphur-isotope studies”. In: *Nature* 382.6587, pp. 127–132. ISSN: 00280836. DOI: 10.1038/382127a0.
- Caxito, Fabrício de Andrade et al. (2012). “Marinoan glaciation in east central Brazil”. In: *Precambrian Research* 200-203, pp. 38–58. ISSN: 03019268. DOI: 10.1016/j.precamres.2012.01.005.
- Cline, Joel D. (1969). “Spectrophotometric determination of hydrogen sulfide in natural waters”. In: *Association for the Sciences of Limnology and Oceanography* 14.3, pp. 454–458.
- Cook, P. J. (1992). “Phosphogenesis around the Proterozoic-Phanerozoic transition”. In: *Journal - Geological Society (London)* 149.4, pp. 615–620. ISSN: 0016-7649. DOI: 10.1144/gsjgs.149.4.0615.
- Cordani, Umberto G. and Kei Sato (1999). “Crustal evolution of the South American platform, based on Nd isotopic systematics on granitoid rocks”. In: *Episodes* 22.3, pp. 167–173. ISSN: 07053797. DOI: 10.18814/epiiugs/1999/v22i3/003.
- Creveling, Jessica R, Andrew H Knoll, and David T Johnston (2014). “Taphonomy of Cambrian phosphatic small shelly fossils”. In: *Palaios* 29, pp. 295–308.
- Crosby, Chris H. and Jake V. Bailey (2012). “The role of microbes in the formation of modern and ancient phosphatic mineral deposits”. In: *Frontiers in Microbiology* 3.JUL, pp. 1–7. ISSN: 1664302X. DOI: 10.3389/fmicb.2012.00241.

- Cui, Huan et al. (2018). “Questioning the biogenicity of Neoproterozoic super-heavy pyrite by SIMS”. In: *American Mineralogist* 103.9, pp. 1362–1400. ISSN: 19453027. DOI: 10.2138/am-2018-6489.
- Dale, Andrew W. et al. (2009). “An integrated sulfur isotope model for Namibian shelf sediments”. In: *Geochimica et Cosmochimica Acta* 73.7, pp. 1924–1944. ISSN: 00167037. DOI: 10.1016/j.gca.2008.12.015.
- Dalton de Souza, João et al. (2003). *Mapa geológico do Estado da Bahia*. Tech. rep. CPRM - Serviço Geológico do Brasil, Governo do Estado da Bahia, Ministerio de Minas e Energia, Companhia Baiana de Pesquisa Mineral.
- Defforey, Delphine and Adina Paytan (2018). “Phosphorus cycling in marine sediments: Advances and challenges”. In: *Chemical Geology* 477. June 2017, pp. 1–11. ISSN: 00092541. DOI: 10.1016/j.chemgeo.2017.12.002.
- Demidenko, Yu E. et al. (2003). “Age of phosphorites from the Khubsugul basin (Mongolia)”. In: *Doklady Earth Sciences* 389.3, pp. 317–321. ISSN: 1028334X.
- Drummond, Justin B. R. et al. (2015). “Neoproterozoic peritidal phosphorite from the Sete Lagoas Formation (Brazil) and the Precambrian phosphorus cycle”. In: *Sedimentology* 62.7, pp. 1978–2008. DOI: 10.1111/sed.12214.
- Eagle, Robert A. et al. (2010). “Body temperatures of modern and extinct vertebrates from 13C-18O bond abundances in bioapatite”. In: *Proceedings of the National Academy of Sciences of the United States of America* 107.23, pp. 10377–10382. ISSN: 00278424. DOI: 10.1073/pnas.0911115107.
- Farquhar, James et al. (2003). “Multiple sulphur isotopic interpretations of biosynthetic pathways: implications for biological signatures in the sulphur isotope record”. In: *Geobiology* 1.1, pp. 27–36. ISSN: 1472-4677. DOI: 10.1046/j.1472-4669.2003.00007.x.
- Fike, David Andrew et al. (2008). “Micron-scale mapping of sulfur cycling across the oxycline of a cyanobacterial mat : a paired nanoSIMS and CARD-FISH approach”. In: *ISME Journal* 2, pp. 749–759. DOI: 10.1038/ismej.2008.39.
- Filippelli, Gabriel M. (2011). “Phosphate rock formation and marine phosphorus geochemistry: The deep time perspective”. In: *Chemosphere* 84.6, pp. 759–766. ISSN: 00456535. DOI: 10.1016/j.chemosphere.2011.02.019.
- Föllmi, KB (1996). “The phosphorus cycle, phosphogenesis phosphate-rich deposits”. In: *Earth-Science Reviews* 40, pp. 55–124.
- Fonseca, Marco Antônio et al. (2014). *Mapa Geológico do Estado de Minas Gerais*. Tech. rep. CPRM - Serviço Geológico do Brasil, Governo de Minas, Ministerio de Minas e Energia, Companhia de Desenvolvimento Econômico de Minas Gerais.
- Goldhammer, Tobias et al. (2010). “Microbial sequestration of phosphorus in anoxic upwelling sediments”. In: *Nature Geoscience* 3.8, pp. 557–561. ISSN: 17520894. DOI: 10.1038/ngeo913.

- Gomes, Maya L. and David T. Johnston (2017). “Oxygen and sulfur isotopes in sulfate in modern euxinic systems with implications for evaluating the extent of euxinia in ancient oceans”. In: *Geochimica et Cosmochimica Acta* 205, pp. 331–359. ISSN: 00167037. DOI: 10.1016/j.gca.2017.02.020. URL: <http://dx.doi.org/10.1016/j.gca.2017.02.020>.
- Guimarães, J. T. et al. (2011). “The Bebedouro Formation, Una Group, Bahia (Brazil)”. In: *Geological Society Memoir* 36.1, pp. 503–508. ISSN: 04354052. DOI: 10.1144/M36.47.
- Habicht, Kirsten S. and Donald E. Canfield (2001). “Isotope fractionation by sulfate-reducing natural populations and the isotopic composition of sulfide in marine sediments”. In: *Geology* 29.6, pp. 555–558. ISSN: 00917613. DOI: 10.1130/0091-7613(2001)029<0555:IFBSRN>2.0.CO;2.
- Halverson, Galen P. and Matthew T. Hurtgen (2007). “Ediacaran growth of the marine sulfate reservoir”. In: *Earth and Planetary Science Letters* 263.1-2, pp. 32–44. ISSN: 0012821X. DOI: 10.1016/j.epsl.2007.08.022.
- Harrison, A. G. and H. G. Thode (1958). “Mechanism of the bacterial reduction of sulphate from isotope fractionation studies”. In: *Transactions of the Faraday Society* 54, pp. 84–92. ISSN: 00147672. DOI: 10.1039/tf9585400084.
- Hurtgen, Matthew T, Michael A Arthur, and Galen P Halverson (2005). “Neoproterozoic sulfur isotopes , the evolution of microbial sulfur species , and the burial efficiency of sulfide as sedimentary pyrite”. In: *Geology* 33.1, pp. 41–44. DOI: 10.1130/G20923.1.
- Johnson, Daniel L. et al. (2021). “Carbonate associated sulfate (CAS)  $\delta^{34}\text{S}$  heterogeneity across the End-Permian Mass Extinction in South China”. In: *Earth and Planetary Science Letters* 574, p. 117172. ISSN: 0012821X. DOI: 10.1016/j.epsl.2021.117172. URL: <https://doi.org/10.1016/j.epsl.2021.117172>.
- Johnston, David T. et al. (2005). “Multiple sulfur isotope fractionations in biological systems: A case study with sulfate reducers and sulfur disproportionators”. In: *American Journal of Science* 305.6-8 SPEC. ISS. Pp. 645–660. ISSN: 00029599. DOI: 10.2475/ajs.305.6-8.645.
- Kaplan, I.R. and T.A. Rafter (1958). “Fractionation of stable isotopes of sulfur by thiobacilli”. In: *Science* 127, pp. 517–518.
- Kita, N. T. et al. (2011). “High-precision SIMS oxygen, sulfur and iron stable isotope analyses of geological materials: Accuracy, surface topography and crystal orientation”. In: *Surface and Interface Analysis* 43.1-2, pp. 427–431. ISSN: 01422421. DOI: 10.1002/sia.3424.
- Kozdon, Reinhard et al. (2010). “In situ sulfur isotope analysis of sulfide minerals by SIMS: Precision and accuracy, with application to thermometry of

- 3.5Ga Pilbara cherts”. In: *Chemical Geology* 275.3-4, pp. 243–253. ISSN: 00092541. DOI: 10.1016/j.chemgeo.2010.05.015. URL: <http://dx.doi.org/10.1016/j.chemgeo.2010.05.015>.
- Kuchenbecker, Matheus, Humberto Luis, and Daniel Galvão (2011). “Caracterização estrutural e considerações sobre a evolução tectônica da Formação Salitre na porção central da Bacia de Irecê , norte do Cráton do”. In: *Geonomos* 19.2, pp. 42–49.
- Laakso, Thomas A. et al. (2020). “Ediacaran reorganization of the marine phosphorus cycle”. In: *Proceedings of the National Academy of Sciences of the United States of America* 117.22. ISSN: 10916490. DOI: 10.1073/pnas.1916738117.
- Leśniak, P. M. et al. (2003). “Extreme sulfur isotopic fractionation between sulfate of carbonate fluorapatite and authigenic pyrite in the Neocomian sequence at Wawalł, Central Poland”. In: *Chemical Geology* 200.3-4, pp. 325–337. ISSN: 00092541. DOI: 10.1016/S0009-2541(03)00198-0.
- Loyd, Sean J. et al. (2012). “Sustained low marine sulfate concentrations from the Neoproterozoic to the Cambrian: Insights from carbonates of northwestern Mexico and eastern California”. In: *Earth and Planetary Science Letters* 339-340, pp. 79–94. ISSN: 0012821X. DOI: 10.1016/j.epsl.2012.05.032. URL: <http://dx.doi.org/10.1016/j.epsl.2012.05.032>.
- Martins-Neto, M. A., A. C. Pedrosa-Soares, and S. A.A. Lima (2001). “Tectono-sedimentary evolution of sedimentary basins from Late Paleoproterozoic to Late Neoproterozoic in the São Francisco craton and Araçuaí fold belt, Eastern Brazil”. In: *Sedimentary Geology* 141-142, pp. 343–370. ISSN: 00370738. DOI: 10.1016/S0037-0738(01)00082-3.
- Misi, A. and J. R. Kyle (1994). “Upper Proterozoic carbonate stratigraphy, diagenesis, and stromatolitic phosphorite formation, Irece Basin, Bahia, Brazil”. In: *Journal of Sedimentary Research A: Sedimentary Petrology and Processes* 64 A.2, pp. 299–310.
- Misi, Aroldo, Alan J. Kaufman, et al. (2007). “Chemostratigraphic correlation of Neoproterozoic successions in South America”. In: *Chemical Geology* 237.1-2, pp. 143–167. ISSN: 00092541. DOI: 10.1016/j.chemgeo.2006.06.019.
- Misi, Aroldo and Ján Veizer (1998). “Neoproterozoic carbonate sequences of the Una Group, Irecê Basin, Brazil: Chemostratigraphy, age and correlations”. In: *Precambrian Research* 89.1-2, pp. 87–100. ISSN: 03019268.
- Ohn, M Atthew J K et al. (1998). “Sulfur isotope variability in biogenic pyrite : Reflections of heterogeneous bacterial colonization ?” In: 83, pp. 1454–1468.
- Okubo, J. et al. (2018). “Phosphogenesis, aragonite fan formation and seafloor environments following the Marinoan glaciation”. In: *Precambrian Research* 311.May 2017, pp. 24–36. ISSN: 03019268. DOI: 10.1016/j.precamres.2018.04.002. URL: <https://doi.org/10.1016/j.precamres.2018.04.002>.

- Okubo, Juliana et al. (2022). “The sulfur isotopic consequence of seawater sulfate distillation preserved in the Neoproterozoic Sete Lagoas post-glacial carbonate, eastern Brazil”. In: *Journal of the Geological Society*, pp. 2021–091. ISSN: 0016-7649. DOI: 10.1144/jgs2021-091. URL: <https://doi.org/10.1144/jgs2021-091>.
- Papineau, Dominic (2010). “Global biogeochemical changes at both ends of the Proterozoic: Insights from phosphorites”. In: *Astrobiology* 10.2, pp. 165–181. ISSN: 15311074. DOI: 10.1089/ast.2009.0360.
- Paris, Guillaume, Ennifer S. Fehrenbacher, et al. (2014). “Experimental determination of carbonate-associated sulfate  $\delta^{34}\text{S}$  in planktonic foraminifera shells”. In: *Geochemistry, Geophysics, Geosystems* 15, pp. 1452–1461. DOI: 10.1002/2014GC005295. Received.
- Paris, Guillaume, Alex L. Sessions, et al. (2013). “MC-ICP-MS measurement of  $\delta^{34}\text{S}$  and  $\Delta^{33}\text{S}$  in small amounts of dissolved sulfate”. In: *Chemical Geology* 345, pp. 50–61. ISSN: 00092541. DOI: 10.1016/j.chemgeo.2013.02.022. URL: <http://dx.doi.org/10.1016/j.chemgeo.2013.02.022>.
- Paytan, Adina and Karen Mclaughlin (2007). “The Oceanic Phosphorus Cycle”. In: *Chemistry Reviews* 107, pp. 263–576. DOI: 10.1021/cr0503613.
- Pellerin, André et al. (2019). “Large sulfur isotope fractionation by bacterial sulfide oxidation”. In: *Science Advances* 5.7, pp. 1–7. ISSN: 23752548. DOI: 10.1126/sciadv.aaw1480.
- Poser, Alexander et al. (2014). “Stable sulfur and oxygen isotope fractionation of anoxic sulfide oxidation by two different enzymatic pathways”. In: *Environmental Science and Technology* 48.16, pp. 9094–9102. ISSN: 15205851. DOI: 10.1021/es404808r.
- Present, Theodore M., Melissa Gutierrez, et al. (2019). “Diagenetic controls on the isotopic composition of carbonate-associated sulphate in the Permian Capitan Reef Complex, West Texas”. In: *Sedimentology* 66.7, pp. 2605–2626. ISSN: 13653091. DOI: 10.1111/sed.12615.
- Present, Theodore M., Guillaume Paris, et al. (2015). “Large Carbonate Associated Sulfate isotopic variability between brachiopods, micrite, and other sedimentary components in Late Ordovician strata”. In: *Earth and Planetary Science Letters* 432, pp. 187–198. ISSN: 0012821X. DOI: 10.1016/j.epsl.2015.10.005. URL: <http://dx.doi.org/10.1016/j.epsl.2015.10.005>.
- Pruss, Sara B. et al. (2019). “Phosphatized early Cambrian archaeocyaths and small shelly fossils (SSFs) of southwestern Mongolia”. In: *Palaeogeography, Palaeoclimatology, Palaeoecology* 513, pp. 166–177. ISSN: 00310182. DOI: 10.1016/j.palaeo.2017.07.002. URL: <https://doi.org/10.1016/j.palaeo.2017.07.002>.

- Reis, Humberto L.S., Fernando F. Alkmim, et al. (2016). “The São Francisco Basin”. In: *The São Francisco Craton, Eastern Brazil: Tectonic Genealogy of a Miniature Continent*. Ed. by Monica Heilbron, Umberto G. Cordani, and Fernando F. Alkmim. 1st ed. August. Springer, pp. 117–143. ISBN: 9783319017150. DOI: 10.1007/978-3-319-01715-0.
- Reis, Humberto L.S., João F. Suss, et al. (2017). “Ediacaran forebulge grabens of the southern São Francisco basin, SE Brazil: Craton interior dynamics during West Gondwana assembly”. In: *Precambrian Research* 302.September, pp. 150–170. ISSN: 03019268. DOI: 10.1016/j.precamres.2017.09.023. URL: <http://dx.doi.org/10.1016/j.precamres.2017.09.023>.
- Richardson, Jocelyn A. et al. (2019). “Depositional and diagenetic constraints on the abundance and spatial variability of carbonate-associated sulfate”. In: *Chemical Geology* 523.May, pp. 59–72. ISSN: 00092541. DOI: 10.1016/j.chemgeo.2019.05.036.
- Riciputi, Lee R., Bruce A. Paterson, and Robert L. Ripperdan (1998). “Measurement of light stable isotope ratios by SIMS: Matrix effects for oxygen, carbon, and sulfur isotopes in minerals”. In: *International Journal of Mass Spectrometry* 178.1-2, pp. 81–112. ISSN: 13873806. DOI: 10.1016/s1387-3806(98)14088-5.
- Ries, Justin B. et al. (2009). “Superheavy pyrite ( $\delta^{34}\text{S}_{\text{pyr}} > \delta^{34}\text{S}_{\text{SCAS}}$ ) in the terminal Proterozoic Nama Group, southern Namibia: A consequence of low seawater sulfate at the dawn of animal life”. In: *Geology* 37.8, pp. 743–746. ISSN: 00917613. DOI: 10.1130/G25775A.1.
- Sallstedt, T. et al. (2018). “Evidence of oxygenic phototrophy in ancient phosphatic stromatolites from the Paleoproterozoic Vindhyan and Aravalli Supergroups, India”. In: *Geobiology* 16.2, pp. 139–159. ISSN: 14724669. DOI: 10.1111/gbi.12274.
- Sanders, Cecilia, John Eiler, and John Grotzinger (2022). “Chapter 2: Paragenesis of an Ediacaran carbonate-platform phosphorite, Constraints from optical petrography and texture-specific clumped isotope paleothermometry”. PhD thesis. Caltech.
- Sanders, Cecilia and John Grotzinger (2021). “Sedimentological and stratigraphic constraints on depositional environment for Ediacaran carbonate rocks of the São Francisco Craton: Implications for phosphogenesis and paleoecology”. In: *Precambrian Research* 363.June, p. 106328. ISSN: 03019268. DOI: 10.1016/j.precamres.2021.106328. URL: <https://doi.org/10.1016/j.precamres.2021.106328>.
- Schulz, Heide N. and Horst D. Schulz (2005). “Large sulfur bacteria and the formation of phosphorite”. In: *Science* 307.5708, pp. 416–418. ISSN: 00368075. DOI: 10.1126/science.1103096.

- Sheldon, R. P. (1981). "Ancient marine phosphorites." In: *Annual review of earth and planetary sciences*. Vol. 9, pp. 251–284. DOI: 10.1146/annurev.ea.09.050181.001343.
- Shields, Graham et al. (2004). "Sulphur isotopic evolution of Neoproterozoic-Cambrian seawater: New francolite-bound sulphate  $\delta^{34}\text{S}$  data and a critical appraisal of the existing record". In: *Chemical Geology* 204.1-2, pp. 163–182. ISSN: 00092541. DOI: 10.1016/j.chemgeo.2003.12.001.
- Shields, Graham A. et al. (1999). "Sulphur isotope compositions of sedimentary phosphorites from the basal Cambrian of China: Implications for Neoproterozoic-Cambrian biogeochemical cycling". In: *Journal of the Geological Society* 156.5, pp. 943–955. ISSN: 00167649. DOI: 10.1144/gsjgs.156.5.0943.
- Southgate, P. N. (2005). "Proterozoic and Cambrian phosphorites – specialist studies: Middle Cambrian phosphatic hardgrounds, phoscrete profiles and stromatolites and their implications for phosphogenesis". In: *Phosphate Deposits of the World: Vol. 1*. Ed. by P.J. Cook and J.H. Shergold. Cambridge University Press, pp. 327–351.
- Staudt, Wilfried J. and Martin A. A. Schoonen (1995). "Geochemical Transformations of Sedimentary Sulfur: Sulfate Incorporation into Sedimentary Carbonates". In: *ACS Symposium Series*. Vol. 612. Chap. 18, pp. 332–345. DOI: 10.1021/bk-1995-0612.ch018.
- Stolper, Daniel A. and John M. Eiler (2016). "Constraints on the formation and diagenesis of phosphorites using carbonate clumped isotopes". In: *Geochimica et Cosmochimica Acta* 181, pp. 238–259. ISSN: 00167037. DOI: 10.1016/j.gca.2016.02.030. URL: <http://dx.doi.org/10.1016/j.gca.2016.02.030>.
- Sundby, Bjørn et al. (1992). "The phosphorus cycle in coastal marine sediments". In: *Limnology and Oceanography* 37.6, pp. 1129–1145.
- Wotte, Thomas et al. (2012). "Paired  $\delta^{34}\text{S}$  data from carbonate-associated sulfate and chromium-reducible sulfur across the traditional Lower-Middle Cambrian boundary of W-Gondwana". In: *Geochimica et Cosmochimica Acta* 85, pp. 228–253. ISSN: 00167037. DOI: 10.1016/j.gca.2012.02.013.
- Xiao, Shuhai and Andrew H. Knoll (1999). "Fossil preservation in the Neoproterozoic Doushantuo phosphorite Lagerstätte, South China". In: *Lethaia* 32.3, pp. 219–238. ISSN: 00241164. DOI: 10.1111/j.1502-3931.1999.tb00541.x.

## 4.9 Figures and tables

Table 4.1: Measured  $\delta^{34}S$  of CAS, PAS, CRS, and pyrite in phosphatic and non-phosphatic microfacies of the Salitre Formation.

Sample ID*	Locality/Section <sup>◊</sup>	Microfacies <sup>†</sup>	Target Phase <sup>‡</sup>	$\delta^{34}S$ ‰(VCDT) <sup>‡</sup>
Aris2_10.8	Aristeia 2	A	CAS (dolomite)	37.91±0.73
Cer_23e	Cerberus	B	CAS (dolomite)	33.64±0.88
FuroV_3400	CBPM Core 5	D	CAS (calcite)	29.41±0.31
FuroX_3330	CBPM Core 10	C	CAS (dolomite/calcite)	19.79±0.45
FuroX_3340	CBPM Core 11	C	CAS (dolomite/calcite)	26.59±0.23
Aris1A_31.8_60.8_1	Aristeia 1	F	PAS (CFA)	30.94±0.71
Aris1B_31.8_60.8_1	Aristeia 1	F	PAS (CFA)	30.94±0.39
FuroX_3340_1	Aristeia 1	F	PAS (CFA)	33.42±0.16
Aris_31.8_80	Aristeia 1	E	CRS (pyrite)	6.92±1.06
Min_44.2	Minotaur	D	CRS (pyrite)	6.95±1.29
FuroX_3330_1	CBPM Core 10	F	pyrite	23.77±0.64
FuroX_3330_2	CBPM Core 10	F	pyrite	18.24±0.60
FuroX_3330_3	CBPM Core 10	F	pyrite	21.78±0.60
FuroX_3330_4	CBPM Core 10	F	pyrite	23.97±0.60
FuroX_3330_5	CBPM Core 10	F	pyrite	33.14±0.58
FuroX_3330_6	CBPM Core 10	F	pyrite	23.71±0.60
FuroX_3330_7	CBPM Core 10	F	pyrite	38.47±0.60
FuroX_3330_8	CBPM Core 10	F	pyrite	-1.56±0.76
FuroX_3330_9	CBPM Core 10	F	pyrite/marcasite/pyrrhotite	-0.38±0.61
FuroX_3330_10	CBPM Core 10	F	pyrite/marcasite/pyrrhotite	-4.24±0.63
FuroX_3330_11	CBPM Core 10	F	pyrite/marcasite/pyrrhotite	-8.25±0.71
FuroX_3330_12	CBPM Core 10	F	pyrite/marcasite/pyrrhotite	-7.88±0.73

\* Sample ID includes abbreviation for stratigraphic column and locality, as well as numbers indicating stratigraphic height and lateral distance in a measured section (both in meters) from a datum for the given column, or depth in a drill core (in cm) from the top of the core. Powders collected from the same hand samples (within centimeters of each other) are indicated with lowercase letters a-c.

<sup>◊</sup> Locality/Section names, stratigraphic columns, and geographic location are provided in Figure 4.2.

<sup>†</sup> Microfacies A = carbonate-cemented grainstone, B = carbonate-cemented grainstone adjacent to phosphatic digitate stromatolite buildup, C = carbonate-cemented grainy inter-stromatolite fill, D = carbonate-cemented laminated mudstone, E = carbonate-cemented stromatolite laminae, and F = CFA-cemented stromatolite laminae.

<sup>‡</sup> CAS = trace structural sulfate in the lattice of the indicated carbonate mineral(s), collected via protocols for trace sulfate extraction and purification, and measured via ICP-MS. PAS = trace structural sulfate in the lattice of the indicated phosphate mineral, collected via protocols for bulk phosphate-associated sulfate extraction, and measured via EA-IRMS. CRS = chromium-reducible sulfur, extracted and fixed as  $Ag_2S$  from acid-insoluble residues, representative of sulfur in the lattice of pyrite measured via EA-IRMS. "Pyrite" and "pyrite/marcasite/pyrrhotite" refer to SIMS measurement of structural sulfur in individual crystals or aggregates of crystals.

<sup>‡</sup> ‰ = *per mille*, with respect to Vienna Canyon Diablo Troilite (VCDT).

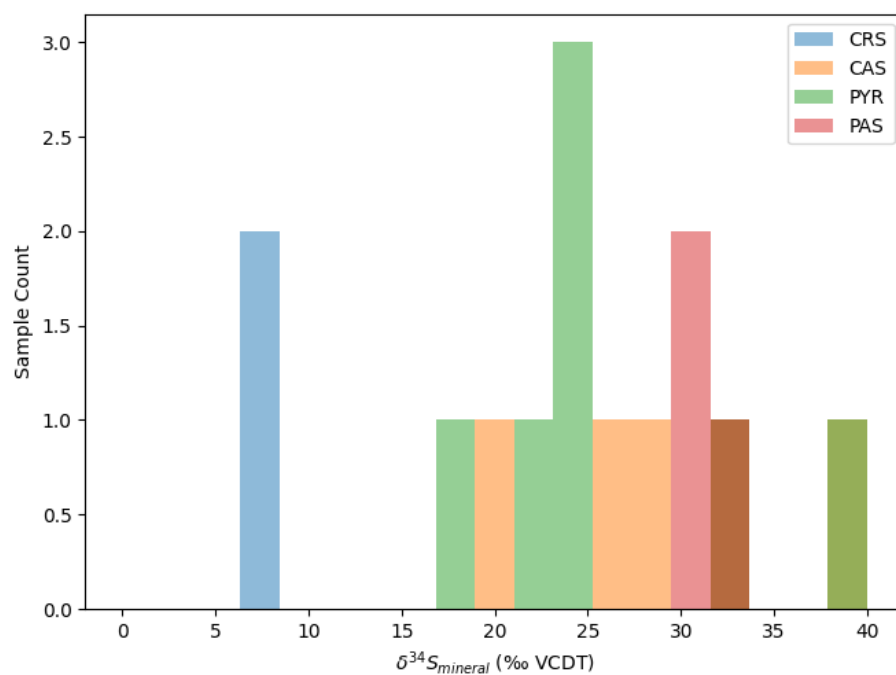


Figure 4.1: Histogram of  $\delta^{34}S_{\text{mineral}}$  values. CAS and PYR represent  $\delta^{34}S_{\text{calcite/dolomite}}$  measured via ICP-MS and  $\delta^{34}S_{\text{pyrite}}$  measured via SIMS, respectively. PAS represents  $\delta^{34}S_{\text{PAS}}$  measured via EA-IRMS. CRS represents  $\delta^{34}S_{\text{pyrite,CRS}}$  measured via EA-IRMS.



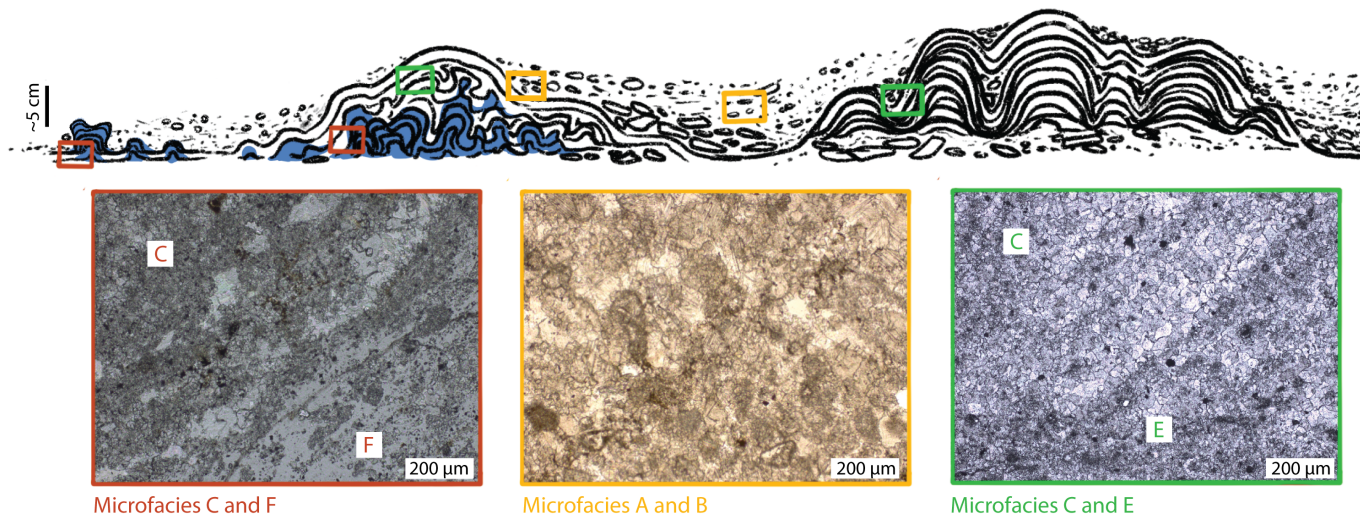


Figure 4.3: Illustration of distinct microtextural associations ("microfacies") examined in this study, and example thin section photomicrographs thereof. Microfacies A = carbonate-cemented grainstone, B = carbonate-cemented grainstone adjacent to phosphatic digitate stromatolite buildup, C = carbonate-cemented grainy inter-stromatolite fill, D = carbonate-cemented laminated mudstone, E = carbonate-cemented stromatolite laminae, and F = CFA-cemented stromatolite laminae. Blue shading indicates spatial distribution of phosphatic cements (i.e., Microfacies F). Colored boxes indicate textural associations of each microfacies at the outcrop/hand sample scale and example thin section photomicrographs of mineral fabrics therein. Red boxes = C and F, yellow boxes = A and B, and green boxes = C and E. D is not pictured, due to its similarity to A and B (yellow boxes).

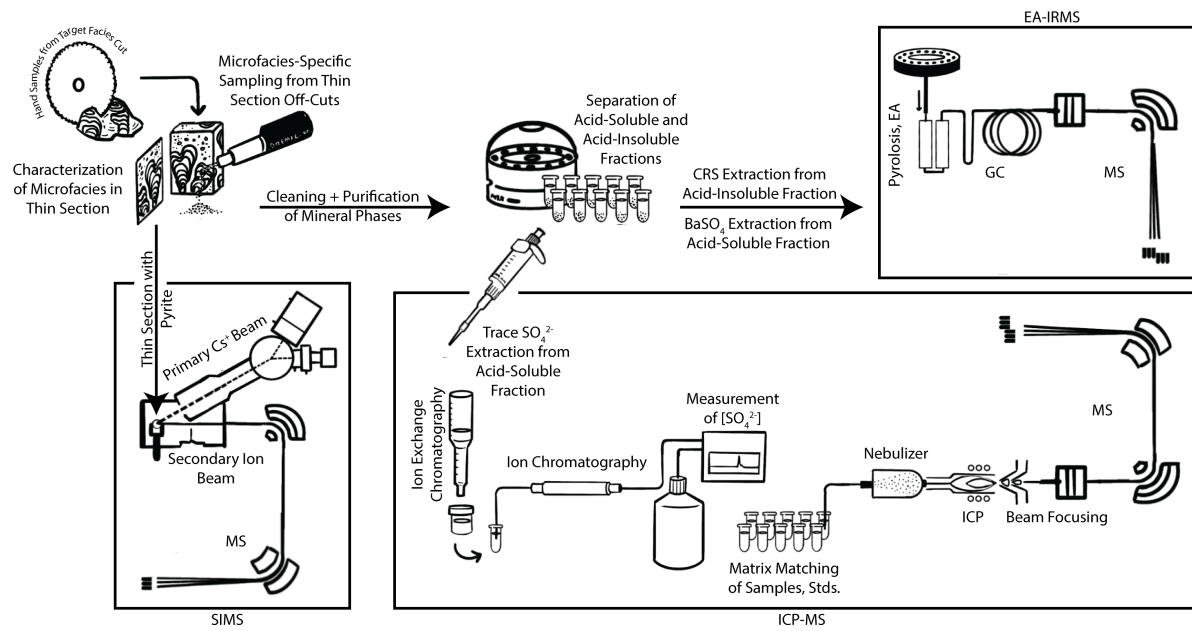


Figure 4.4: Summary of sample preparation and methods.

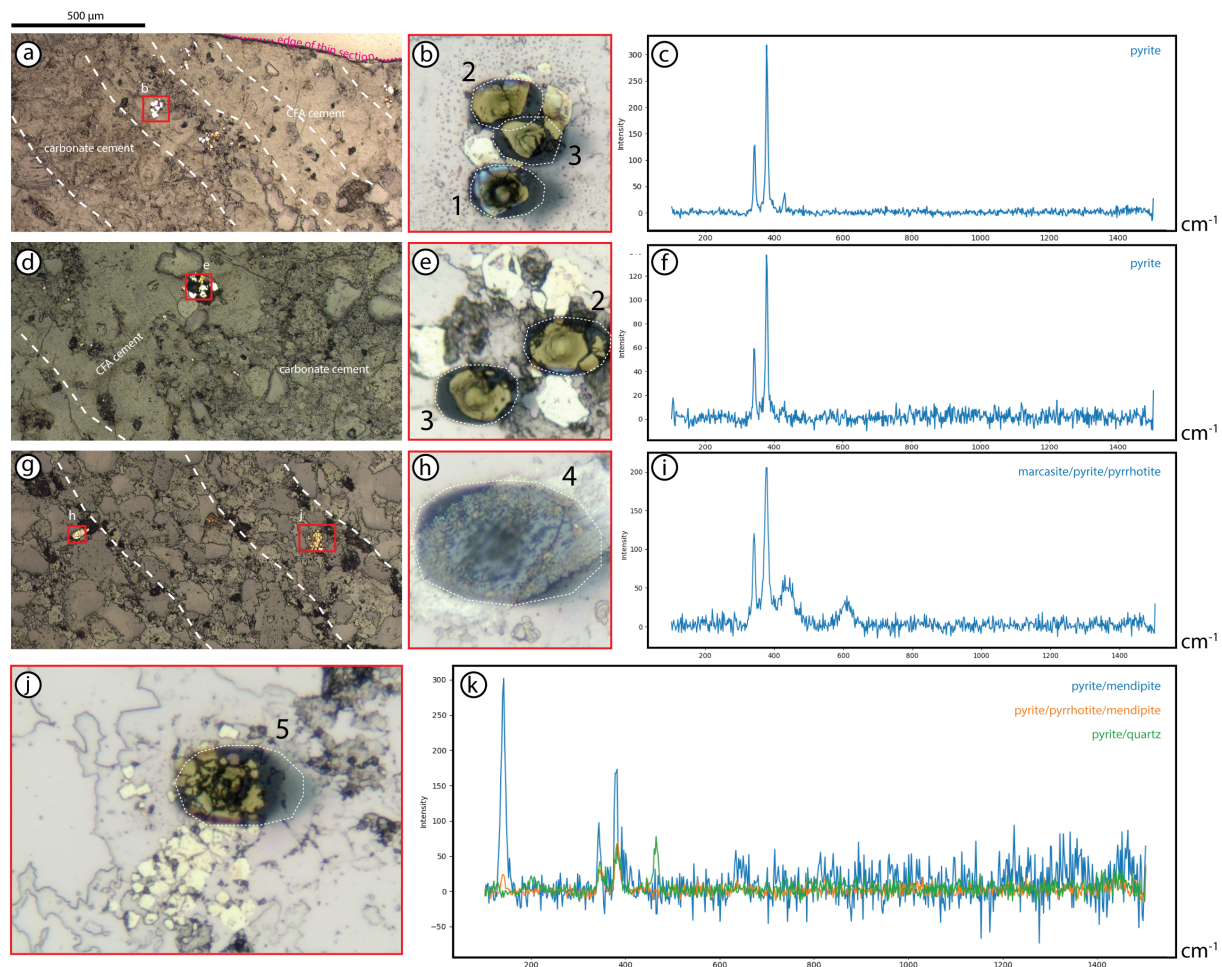


Figure 4.5: Reflected light photomicrographs and Raman spectra of a representative subset of individual and aggregate Fe-sulfide crystals in thin section, whose  $\delta^{34}\text{S}$  compositions were measured via SIMS. (a,d, and g) Annotated photomicrographs of target crystals in their microfacies context. (b,e,h, and j) Magnified insets of crystals and crystal aggregates. Dotted white lines demarcate the area sputtered by the primary ion beam, and numbers indicate the order in which measurements were made in each pictured area. (c,f,i, and k) Raman spectra collected from crystals within the sputtered areas, and the mineralogies with which they are associated.

*Appendix A*

## OVERLARGE TABLES FROM CHAPTER 2

**Appendix Table 2.1.** Notable study locations and brief descriptions, from North to South. Locality numbers are provided for Fig. 2.1.

Locality Number (Fig. 1)	Locality Name	Abbreviation	Formation/Member	Latitude	Longitude	Description
1	Gruta dos Brejoes 1	GdB	Salitre/Nova America	-11.017	-41.438	Beds (120/15) of laminated blue-gray limestone. Frequently cross-stratified and containing abundant tabular intraclast conglomerate.
	Lajes do Batata 1	CapW	Salitre/Nova America	-11.048674	-40.78735	Near the eastern boundary of the Salitre paleobasin, roadside outcrop of dusky-rose and maroon-weathering, finely laminated, carbonate mudstone. Horizontal dip. This is the western half of the outcrop, where thin, intercalated siliciclastic muds were most visible.
	Lajes do Batata 2	CapE	Salitre/Nova America	-11.048825	-40.787265	Near the eastern boundary of the Salitre paleobasin, roadside outcrop of dusky-rose and maroon-weathering, finely laminated, carbonate mudstone. Horizontal dip. This is the eastern half of the outcrop, where there were abundant vugs lined with blocky calcite spar.
0	Fazenda Arrecife	FA	Salitre/Nova America	-11.102437	-41.029183	Extensive columnar stromatolite bioherm "field," where dozens to several hundred of meter- and ten-meter-scale elliptical bioherms are exposed. Ellipses contain hundreds of decimeter-diameter, several centimeter-synoptic-relief columnar stromatolites. Stromatolites are closely packed and elongate near bioherm margins. Bioherms often have laminated "carapace" of fine- to medium-grained lime grainstone. Inter-stromatolite and inter-bioherm channels are filled with coarse, oolitic calcite sediment. Pebble-to-boulder-scale intraclast conglomerates are common.
2	Fazenda Raimundo	FR	Salitre/Gabriel	-11.109	-41.411	Finely laminated, thinly bedded, blue-gray limestone. Heavily folded (toothpaste).
	Scorched Earth	SE	Salitre/Nova America	-11.3	-42.078	Pale blue-gray, finely laminated limestone. Some low-angle cross-stratification, some ripple cross-stratification. Slightly deformed, with decimeter-scale offsets and meter-scale folding. Some superficial silicification.
3	Fazenda Nova Canãa	FNC	Salitre/Nova America	-11.316237	-41.801176	Heavily folded and faulted outcrop of finely laminated dove-gray dolostone, with frequent tabular reefs of phosphatic digitate stromatolites. Inter-stromatolite fill often weathered out, producing a honeycomb

						appearance in the stromatolite reefs.
4	Io4 Beginning	Io4	Salitre/Nova America	-11.318898	-41.765257	Just north of BA-052 near Irecê, Bahia, an outcrop of near-vertically-dipping blue-gray limestone and dolostone. Finely laminated, extravagantly cross-stratified, with oscillatory flow, current, and combined-flow ripples, well-defined troughs, and evidence of frequently migrating flow direction and energy. Often grains and medium-to-granule-scale, well-rounded micritized ooids and aggregate grains.
5	Aristeia 2	Aris	Salitre/Nova America	-11.32915	-41.773911	Just east of Aris I start, this large outcrop contains finely laminated, often cross-stratified limestone and dolostone, intraclast conglomerate, and some stromatolite mounds.
6	Fazenda Catavento	FC	Salitre/Nova America	-11.329404	-41.770422	Extensive outcrop of near-vertically-dipping beds of repeated intervals of compressed wave-agitated thin intraclasts and fine sediment drapes, previously interpreted as tee-pees.
7	Cerberus	Cer	Salitre/Nova America	-11.329496	-41.778997	Western part of a large (nearly square km) outcrop, with beds dipping 60-90 degrees toward the North. Parts of the outcrop are obscured by karstic weathering textures, but most is plainly dove-gray to blue-gray limestone and dolostone, preserving oscillatory and combined-flow ripples, variable current ripples, and digitate stromatolite patch reefs. Some lately silicified nodules and thin (centimeter-scale) strata. Unconformably overlying the Salitre formation outcrop, there are some sparse fossiliferous packstone deposits with abundant gastropod and possible brachiopod shell fragments, as well as corals -- possibly as young as Cenozoic.
	Aristeia 1	Aris	Salitre/Nova America	-11.329857	-41.777114	Just south of BA-052 near Irecê, Bahia, an outcrop of near-vertically-dipping blue-gray limestone and dolostone. Finely laminated, frequently cross-stratified, and replete with flat-bottomed, domed tabular intraclast conglomerate beds. Contains extensive phosphatic digitate stromatolite patch reefs and carbonate stromatolite mounds.
8	Minotaur	Mino	Salitre/Nova America	-11.329978	-41.779408	Eastern part of a large (nearly square km) outcrop, with beds dipping 60-90 degrees toward the North. Parts of the outcrop are obscured by karstic weathering textures, but most is

						plainly dove-gray to blue-gray limestone and dolostone, preserving oscillatory and combined-flow ripples, variable current ripples, and digitate stromatolite patch reefs. Some lately silicified nodules and thin (centimeter-scale) strata.
9	Lonely Road	LR	Salitre/Nova America	-11.35683	-41.806009	Large outcrop south of BA-052 containing several-meter-thick digitate strom reefs interbedded with finely laminated, tan-weathering, vf-grained dolostone (low-angle and ripple cross stratification common) ... Blue/pink/purple-weathering limestone near top of section. Lots of meter- to 10-meter-scale folding and deformation, though continuous section is discernible over ~10 m scale.
	Capricorn	Ca	Salitre/Jussara	-11.366	-41.988	Laminated blue-gray limestone with centimeter-scale beds of intraclast conglomerate within mostly low-angle-cross-stratified massive beds. Bedding orientation 100/85.
	Gemini	Ge	Salitre/Jussara	-11.368	-42.013	Laminated blue-gray limestone with centimeter-scale beds of intraclast conglomerate within mostly low-angle-cross-stratified massive beds. Bedding orientation 270/80.
	Minotaur cont. 1	Mino1	Salitre/Nova America	-11.368143	-41.777701	Continuation of eastern part of a large (nearly square km) outcrop, with beds dipping 60-90 degrees toward the North. Parts of the outcrop are obscured by karstic weathering textures, but most is plainly dove-gray to blue-gray limestone and dolostone, preserving oscillatory and combined-flow ripples, variable current ripples, and digitate stromatolite patch reefs. Some lately silicified nodules and thin (centimeter-scale) strata.
	Philotetes	Phil	Salitre/Nova America	-11.370337	-41.5975	Outcrop of almost vertically dipping finely laminated blue-gray dolostone, with abundant low-angle cross stratification. Heavily structurally deformed, with abundant centimeter- and meter-scale hairpin folds and large, 20-30-meters-across recumbent folds.
10	Lapão1	Lapão	Salitre/Jussara	-11.409974	-41.825402	Steeply south-dipping roadcut exposure of mixed carbonate and siliclastic muds or marls, heavily altered/weathered. Some digitate stromatolites preserved in lately formed chert.
11	Vila Morro Grande	VMG	Salitre/Gabriel	-11.413	-41.936	Medium blue-gray limestone. 1-5-meter-scale cross sets, with grain sizes varying from fine/indistinct to very coarse intraclasts. Heavily folded, difficult to determine

						continuous section of more than 10 meters. Bedding orientation 280/85.
12	Gilvan's Backyard	Gilvan	Salitre/Gabriel	-12.318668	-41.610175	Near-horizontally-bedded, laminated blue-gray limestone with abundant tabular intraclast conglomerate.
13	Lapa Doce	LD	Salitre/Nova America	-12.32742	-41.607597	Near-horizontally-bedded, laminated blue-gray limestone with abundant tabular intraclast conglomerate.
14	Coxinha Antiga	CA	Salitre/Nova America	-12.35	-41.61	Finely laminated gray and tan planar laminated and nodular limestone. Cliff wall exposure, near-horizontal bedding.
15	Cabbage Patch	CP	Salitre/Nova America	-12.43	-41.56	Beds of laminated dark blue-gray limestone, oriented 350/20 (right-hand notation), exposed in a cliff wall. Extensive ripple cross-stratification, tabular intraclast conglomerate.
16	Rio Preto Quarry	RPQ	Salitre/Nova America	-12.45	-41.59	Finely laminated blue-gray limestone, mostly planar though with some possible low-angle cross stratification. Near-horizontal bedding.
	Itacarambí 1	Ita1	Sete Lagoas/Middle	-15.07576	-44.16063	Planar-laminated and low-angle-cross-stratified pale dove-gray limestone. Near-horizontal bedding. Some small-scale quarternary speleothems and tufas grow on outcrop surfaces and are discernible in float. Some sparse tabular intraclast conglomerate.
17	Gruta do Janelão	GdJ	Sete Lagoas/Middle	-15.114	-44.242	Near-horizontally-bedded, laminated blue-gray lime grainstone with abundant tabular intraclast conglomerate and low-angle cross-stratification. In places, meters of planar laminated limestone, with isolated clumps of crystal fans, draped with finely laminated calcitic sediment.
18	Grutinha	Grutinha	Sete Lagoas/Middle	-15.146	-44.241	Near-horizontally-bedded, laminated blue-gray limestone with abundant tabular intraclast conglomerate and low-angle cross-stratification.
19	Levinópolis 1	Lev	Sete Lagoas/Middle	-15.25023	-44.29068	Creek bed exposure of near-horizontally bedded finely laminated and nodular dove-gray limestone. Some thin beds of tabular intraclast conglomerate visible.
	Januária Redemption Tour 1	JRT1	Sete Lagoas/Middle	-15.26228	-44.22683	Januária-area exposure of near-horizontally-bedded dark blue-gray limestone. Finely laminated. Ripple and low-angle cross-stratified. Abundant tabular intraclast conglomerate. Some plates of thin, mud-draped conglomerate beds in place and in float containing putative animal fossil fragments.
	Itacarambí 2	Ita2	Sete Lagoas/Middle	-15.26317	-44.24398	Quarry wall exposure of wrinkly-laminated, ripple- and

						low-angle-cross-stratified blue-gray limestone. In places, thinly bedded (recessive shale partings?).
	Levinópolis 2	Lev	Sete Lagoas/Middle	-15.26917	-44.27406	Cliff-side exposure of near-horizontally bedded finely laminated dove-gray limestone. Abundant tabular intraclast conglomerate, low-angle x-strat, and some possible nodular textures. Perhaps 30 m total of section.
20	Januária 10	Jan10	Sete Lagoas/Middle	-15.39659	-44.43865	Near-horizontally-bedded, laminated blue-gray limestone with abundant tabular intraclast conglomerate and low-angle cross-stratification.
21	Januária 4	Jan4	Sete Lagoas/Middle	-15.499	-44.457	Near-horizontally-bedded, laminated blue-gray limestone with abundant tabular intraclast conglomerate and low-angle cross-stratification.
	Januária Redemption Tour 2	JRT2	Sete Lagoas/Middle	-15.5871	-44.47456	Januária-area exposure of near-horizontally-bedded dark blue-gray limestone. Finely laminated. Ripple and low-angle cross-stratified. Abundant tabular intraclast conglomerate. Some plates of thin, mud-draped conglomerate beds in place and in float containing putative animal fossil fragments.
	Montes Claros 4	MC4	Lagoa do Jacaré	-16.6452	-43.89268	Lagoa do Jacaré formation. Nearly horizontally bedded blue-gray and tan-weathering limestone. Laminae, where visible, are wiggly and deformed as with early soft-sediment deformation or differential compaction. Sparse tabular intraclast conglomerate beds.
	Montes Claros 3	MC3	Lagoa do Jacaré	-16.65052	-43.8958	Lagoa do Jacaré formation. Accessible from protected shoulder of road between Montes Claros and Nova Esperança. Nearly horizontally bedded blue-gray and tan-weathering limestone. Laminae, where visible, are wiggly and deformed as with early soft-sediment deformation or differential compaction. Sparse tabular intraclast conglomerate beds. Some hairpin folding.
	Lapa Grande	LG	Sete Lagoas/Lower	-16.70686	-43.9403	Dark blue-gray limestone. Horizontally bedded, faintly planar laminated.
	Montes Claros 1	MC1	Lagoa do Jacaré	-16.75634	-43.90674	Lagoa do Jacaré formation. Nearly horizontally bedded blue-gray and tan-weathering limestone. Laminae, where visible, are wiggly and deformed as with early soft-sediment deformation or differential compaction. Sparse tabular intraclast conglomerate beds.

	Montes Claros 2	MC2	Lagoa do Jacaré	-16.7599	-43.91668	Lagoa do Jacaré formation. Nearly horizontally bedded blue-gray and tan-weathering limestone. Laminae, where visible, are wiggly and deformed as with early soft-sediment deformation or differential compaction. Sparse tabular intraclast conglomerate beds.
	Buenópolis D	BuenoD	Lagoa do Jacaré	-17.84878	-44.06735	Lagoa do Jacaré formation. Planar and wiggly laminated blue-gray limestone oriented 140/25 on eastern limb of Buenópolis syncline. Some tabular intraclast conglomerate beds visible, some possible low-angle cross-stratification.
	Buenópolis A	BuenoA	Serra do Saudade	-17.86459	-44.15657	Serra do Saudade or Lagoa do Jacaré formation roadcut on limb of syncline near Buenópolis town 80-90/30 beds of olive-green and rust-red finely planar laminated siliciclastic siltstone, with some decimeter-scale interbeds of blue-gray laminated, cross-stratified limestone.
	Buenópolis B	BuenoB	Serra do Saudade	-17.86763	-44.15816	Serra do Saudade or Lagoa do Jacaré formation roadcut on limb of syncline near Buenópolis town 80-90/30 beds of olive-green and rust-red finely planar laminated siliciclastic siltstone, with some decimeter-scale interbeds of blue-gray laminated, cross-stratified limestone.
	Buenópolis C	BuenoC	Serra do Saudade	-17.87388	-44.16089	Serra do Saudade or Lagoa do Jacaré formation roadcut on limb of syncline near Buenópolis town 80-90/30 beds of olive-green and rust-red finely planar laminated siliciclastic siltstone, with some decimeter-scale interbeds of blue-gray laminated, cross-stratified limestone.
	Buenópolis City Roadside	BuenoCity	Serra do Saudade	-17.8764	-44.17288	Lagoa do Jacaré or Serra do Saudade formation. Thinly bedded olive- and rust-colored shale/siliciclastic siltstone, near-horizontal beds. Perhaps 3 m exposure. Heavily foliated (10/70).
	Cedro do Abaeté 1	CdA1	Serra do Saudade	-19.15563	-45.70413	Serra do Saudade Formation. "Tiffany blue" or aqua-green-colored finely planar-laminated siltstone of a highly heterogeneous composition.
	Cedro do Abaeté 2	CdA2	Serra do Saudade	-19.21098	-45.76023	Serra do Saudade formation. "Tiffany blue" or aqua-green-colored, sometimes purple and blue, finely planar-laminated siltstone of a highly heterogeneous composition.
	Pave Sete	PS	Sete Lagoas/Lower	-19.39635	-44.42524	Large quarry exposure. 100+ meters of dove gray and tan limestone. Finely laminated,

						some visible ripples within otherwise planar laminated beds.
	Eucalyptus Fields	EF	Sete Lagoas/Middle	-19.39644	-44.4253	Finely laminated, low-angle cross-stratified dove gray limestone.
22	Riacho do Campo Paredão	RdC	Sete Lagoas/Lower	-19.42717	-44.37978	15-20 m roadside exposure; smooth, water saw cut surface with natural weathering surfaces at margins of wall. Entire outcrop dominated by centimeter- to decimeter-scale aragonite crystal fans (calcite pseudomorphs) growing on planar laminated carbonate muds and among some ripple-cross-stratified very fine grainstone. Fans stand out as dark purple-blue and white. Grainstone is somewhat peach-colored.
	Paraiso Mine	Paraiso	Sete Lagoas/Middle	-19.46247	-44.35608	Hundreds-of-meters quarry exposure of near-horizontally-bedded, planar laminated and low-angle-cross-stratified blue-gray limestone.
23	Sete Lagoas Polícia Rodoviária	SLPR	Sete Lagoas/Middle	-19.47492	-44.29178	7-10-m roadside exposure; heavily recrystallized dark blue-gray limestone. Can see columnar stromatolites growing in several-meter-scale mound. Individual stromatolites grow near-vertically relative to modern gravity and have diameters of several centimeter, though internal laminations are difficult to distinguish through alteration.
24	Sete Lagoas Two Towers	SLTT	Sete Lagoas/Middle	-19.49003	-44.27534	30-m exposure of medium blue-gray to dove gray limestone. Most massively bedded near base, thinning to half-m scale upsection. Near-horizontal bedding orientation. Finely laminated. Low angle cross-stratification and migrating tabular cross sets (3d bedforms) clearly visible. Some intervals coarser than others, and granule-scale intraclasts and several-centimeter-scale oncolites can be discerned. Occasional granule-to-pebble-scale tabular intraclast conglomerate.
25	Gruta do Baú	GdBau	Sete Lagoas/Middle	-19.548258	-43.988897	Extensive, hundred-m cliff exposure of near-horizontally-bedded, planar laminated and low-angle-cross-stratified blue-gray limestone.
	Lapinha	Lap	Sete Lagoas/Middle	-19.56149	-43.95958	Near-horizontally-bedded, laminated blue-gray limestone with abundant tabular intraclast conglomerate and low-angle cross-stratification.
	Lagoa Santo Antonio	LSA	Sete Lagoas/Middle	-19.57846	-44.01548	Near-horizontally-bedded, laminated blue-gray limestone with abundant tabular intraclast

						conglomerate and low-angle cross-stratification.
	Pitanguí limestone mine	PitMine	Sete Lagoas/Lower	-19.618	-44.86787	40-50-m exposure of horizontally-bedded yellow-tan and pale blue-gray limestone. Planar lamination.
	Pitanguí flats roadcut	PitR	Serra do Saudade	-19.64568	-44.85785	Serra do Saudade or Lagoa do Jacaré Formation? Dull pink/taupe-colored, finely planar laminated siliclastic siltstone, weathering to thin chips and powdery silt. Gently folded and faulted with centimeter-scale offsets. Bedding on-average close to horizontal.
	Lagoa dos Mares	LdM	Sete Lagoas/Middle	-19.668336	-43.995575	Steel blue limestone cliff. Faintly laminated, partially metamorphosed to featureless marble.
	Onça Pitanguí mountain roadside	OPRoad	Serra do Saudade	-19.68698	-44.74889	Serra do Saudade or Lagoa do Jacaré Formation? Dull pink/taupe-colored, finely planar laminated siliclastic siltstone. Bedding on-average close to horizontal.
	13 Quedas Hillside	13Q	Mesoproterozoic Basement	-19.69176	-44.79187	Metamorphic, crystalline basement.
	Onça Pitanguí Abandoned Quarry	OPQuarry	Neoproterozoic Metasediments	-19.69829	-44.74087	Heavily (possibly hydrothermally) altered very coarse quartz arenite and pebble-scale, matrix-supported quartz-rich conglomerate. Parts of outcrop appear schistose, with abundant platy micas. Possibly part of Neoproterozoic metasedimentary rocks of region.
	Cachoeira Serra dos Ferreira	SdF	Mesoproterozoic Basement	-19.71147	-44.72879	Massive greenschist, part of metamorphic crystalline basement.
	São Francisco Riverbank	SFR	Sete Lagoas/Middle	-19.773414	-45.478028	On the banks of the São Francisco River, a roughly 5-m high outcrop of horizontally-bedded tan and blue-gray limestone. Bottom and top thirds of outcrop are stromatolitic. Bottom third is comprised of irregular stromatolites, as though digitate stromatolites merged to form mounds and domes. Upper third is comprised of more regular, columnar stromatolites with diameters as large as 20 centimeters. Middle third is comprised of cross-stratified, oolitic lime grainstone. Cross-strat approaches swaley/hummocky habit and flow direction varies considerably.
	Butterfly Mine	BM	Sete Lagoas/Middle	-20.28257	-45.84119	Sete Lagoas Formation. Faintly laminated massively bedded dark blue-gray limestone. Mostly planar lamination, some possible low-angle cross-stratification. 130/65.

	Experimental Farm	ExpFarm	Sete Lagoas/Middle	-20.32644	-45.60524	50-80-m exposure of near-horizontally-bedded faintly laminated limestone.
	Corumbá Pains	CorPains	Sete Lagoas/Middle	-20.33695	-45.61893	5-100-centimeter-thick beds of faintly laminated limestone. Some tabular intraclast conglomerate. Faint cross-stratification.
	Costina Termite Farm	TerFarm	Sete Lagoas/Middle	-20.33989	-45.79238	Sete Lagoas: gently folded and tilted outcrops of planar and low-angle-cross-stratified laminated blue-gray limestone. Most extensive outcrop is oriented 152/35.
	Abandoned Farmhouse	AbanFarm	Sete Lagoas/Middle	-20.35954	-45.77149	Heavily folded and faulted outcrop of finely laminated dark blue-gray limestone.
	Pains Cattle Auction	PainsC	Sete Lagoas/Middle	-20.37901	-45.65108	Heavily folded and faulted blue-gray limestone. Where primary textures are visible, can discern 20-centimeter-scale trough cross stratification.
	Pains Roadcut	PainsR	Sete Lagoas/Middle	-20.39178	-45.55889	5-100-centimeter-thick beds of faintly laminated limestone. Some tabular intraclast conglomerate. Faint cross-stratification.

**Appendix Table 2.2.** Lithofacies names, descriptions, and interpreted depositional environments.

#) Lithofacies Name	Description	Depositional Environment
(1) Cross-stratified carbonate grainstone/rudstone	Fine to very coarse, well-rounded carbonate grains organized by oscillatory flows into ripple- and low-angle-cross-stratified structures. Grains are often oolitic, partially or completely micritized, or else peloids. Dominantly contain 3D bedforms, with indicators of flow direction changing frequently. This is the dominant facies in both the Salitre and Sete Lagoas formations, with other facies appearing in patches that are laterally discontinuous at meter-scales. See <b>Figs. 3a-c</b> and text.	Wave-swept shallow platform
(2) Tabular intraclast conglomerate	Poorly sorted intraclast conglomerate comprised primarily of round-edged, thin (centimeter-thickness) tablets of limestone or dolostone in a fine- to coarse-grained limestone or dolostone matrix, with occasional cobbles and boulders. Tablets are often imbricated or even vertical. Tend to occur as laterally discontinuous beds with flat bases and domed tops draped by finer sediment. See <b>Figs. 3d-e</b> and text.	Wave-swept shallow platform, intermittently affected by storms and gravitational failures of steep sides of microbial buildups
(3) Planar-laminated, very fine-grained limestone/dolostone	Planar laminated carbonate, both limestone and dolostone. Component grains are fine- and very fine-scale peloids. Sometimes laminae are not perfectly parallel, with millimeter and centimeter-scale variations in laminae thickness. See <b>Fig. 3f</b> .	Moderately deep platform, near the limits of fair-weather-wave-base
(4) Nodular limestone	Centimeter-scale nodules of fine, well-rounded carbonate sediment, predominately calcitic. Nodules are distinguished from matrix by subtle differences in primary grain size. Many nodules contain recrystallized silica botryoids near their cores, associated with iron oxide pseudomorphs after pyrite. See <b>Figs. 3g-h</b> and text.	Moderately deep platform, near the limits of fair-weather-wave-base
(5) Crinkly laminite	Laminated carbonate, both limestone and dolostone, where millimeter- to centimeter-scale laminae appear crinkly or undulating, at 1 centimeter or smaller irregular wavelengths. See text and lower half of <b>Fig. 3h</b> .	Moderately deep platform, near the limits of fair-weather-wave-base
(6) Digitate stromatolite buildups	Laterally discontinuous tabular and flat-bottomed, lens-shaped biostromes and bioherms comprised of branching and merging 1-2 centimeter diameter stromatolites. Stromatolites are often, though not always, comprised of finely crystalline CFA (carbonate fluorapatite) cement, interlaminated with calcitic peloids and amorphous organic material. Sometimes, digits merge without branching and form “cauliflower”-like heads and mounds that with less CFA. Interstromatolite fill is predominately well-rounded calcite grains (ooids and peloids) with some rare well-rounded phosphatic intraclasts. See <b>Fig. 4</b> and text.	Wave-swept shallow platform
(7) Columnar stromatolite buildups	2-10-meter-scale mounds of large (decimeter-scale) columnar and stratiform stromatolites. Comprised predominately of calcite and some later dolomite. Mounds often nucleate on and grow around pebble to boulder scale intraclast conglomerate. See <b>Fig. 5</b> and text.	Wave-swept shallow platform, intermittently affected by storms and gravitational failures of steep microbial reef slopes, where stromatolites near herm margins feel the strongest flows and shelter stromatolites in the inner herm, allowing more persistent vertical growth

<p>(8) Symmetric-wave-rippled limestone</p>	<p>Centimeter-scale laminae and fragmented laminae preserve symmetric peaks with decimeter-scale wavelengths. Peaks often characterized by overlapping or shingling laminae and some folded and fragmented laminae. Topographic lows between peaks filled with fine carbonate sediment, compensating relief of peaks before next generation of wave-rippled limestone. See <b>Fig. 7</b> and text.</p>	<p>Wave-swept shallow platform</p>
<p>(9) Crystal fans</p>	<p>Several-centimeter to decimeter-scale fans of blunt-ended, acicular crystals nucleating at a point on planes of finely laminated, very fine-grained carbonate sediment. Comprised of anhedral interlocking mosaic of calcite crystals. Sometimes isolated, surrounded by planar and ripple-cross-stratified very fine grainstones. Sometimes growing in laterally extensive "fields." See <b>Fig. 8</b> and text.</p>	<p>Moderately deep platform, near the limits of fair-weather-wave-base</p>

*Appendix B*PRELIMINARY EVALUATION OF CATION BRIDGING AS A  
MECHANISM OF ORGANIC MATTER PRESERVATION IN  
PHOSPHATIC MICROBIALITES OF THE SALITRE  
FORMATION, NORTHEASTERN BRAZILCecilia B. Sanders, Kelsey Moore, and John P. Grotzinger<sup>1</sup>*All you can do is make an ending.*— Terry Pratchett, *Witches Abroad***B.1 Abstract**

Well-preserved organic material and morphologically detailed macro- and micro-fossils have been observed in numerous phosphate-enriched sedimentary deposits (phosphorites) around the world, but style and quality of preservation vary widely according to the mechanism and timing of phosphate mineralization in a given setting. By analogy with microbial taphonomy in cherts, one possible mechanism is that of cation bridging between organic material and mineral precursors. In this study, we examine the evidence for this mechanism in Ediacaran phosphorite of the Salitre Formation in northeastern Brazil. In the Salitre Fm., phosphate mineralization occurs as carbonate-fluorapatite (CFA) cements in digitate stromatolite buildups within cross-stratified grainstone facies. In these buildups, CFA cements are intimately associated with primary organic material within stromatolitic laminae. We present new data in the form of polarized light microscopy and backscattered electron images, which allow for the characterization of the style and fossil preservation quality of phosphate mineralization in these rocks: precipitation of CFA from porewaters contemporaneous with the degradation of microbial biomass below the sediment chemocline, resulting in only rare, limited preservation of cell morphologies in the CFA cement matrix. We also present texture-specific X-Ray spectra measured via energy-dispersive spectrometry, which reveal apparent enrichment of Mg in organic material which cannot be explained by admixture with CFA cements alone. These data suggest that, like organic-rich cherts, cation-bridging via Mg

---

<sup>1</sup>Division of Geological and Planetary Sciences, California Institute of Technology, Pasadena, CA 91125, USA

may have occurred in sediment porewaters, lowering kinetic barriers to phosphate mineralization and preservation of organic matter in the Salitre phosphorite.

## **B.2 Introduction**

The preservation of microbial and animal body fossils through replacement or encasement by phosphate mineral cements is well-documented throughout Earth history and in modern phosphogenetic environments. However, there are myriad styles of phosphate mineral preservation, the conditions for which may depend on depositional environment, local biotic and abiotic influences on the chemistry of the fluid medium, and even the structure and composition of the fossil substrate. The style and quality of preservation of organic material in phosphate minerals in ancient rocks is thus a record of paleoenvironmental and paleoecological conditions, but a record whose interpretation requires a mechanistic understanding of the relationship between environment and early phosphate mineralization. The scientific community has approached this understanding by degrees, through the past 40 years of taphonomic experimentation and detailed description of sedimentary phosphate deposits around the world, Phanerozoic and Precambrian. Each sedimentary phosphate deposit represents a potential taphonomic window particular to a given time, place, and ecology, and presents a new opportunity to test different models of phosphate mineralization.

The Salitre Formation of eastern Brazil provides such an opportunity, its lowermost member containing phosphatic digitate stromatolite buildups (Caird et al., 2017; Kuchenbecker, Luis, and Galvão, 2011; Aroldo Misi and Veizer, 1998; C. Sanders and Grotzinger, 2021; Shiraishi et al., 2019) which formed in a persistently submerged, high wave energy setting (C. Sanders and Grotzinger, 2021). In these buildups, phosphate mineralization is spatially restricted to the interiors and nearest margins of digitate stromatolites and is closely associated with organic material, both diffuse and concentrated within filamentous microbial body fossils (C. Sanders, Eiler, and Grotzinger, 2022; C. Sanders and Grotzinger, 2021; Shiraishi et al., 2019). What processes facilitated the formation of phosphatic carbonate fluorapatite (CFA) cements in association with organic material? Did cells and extracellular organic secretions play a role in the nucleation and growth of CFA cements, through their metabolic influence on sediment porewater chemistry, as passive growth substrates whose surface properties lowered kinetic barriers to mineralization, or both?

One possible mechanism by which organic material may facilitate its preservation

through early mineralization is cation bridging, wherein negatively charged cell surfaces and/or extracellular polymeric substances (EPS) adsorb positively charged ions from the surrounding fluid medium, which in turn form complexes with and concentrate negatively charged ions. These complexes accumulating around organic matter can assemble as precursor phases to cement minerals, such that crystalline cements can nucleate around the organic material, precluding its further degradation by heterotrophic organisms and even the heat and pressure of burial. The cation bridging mechanism has been implicated in the early mineralization of cyanobacterial mats in silica-precipitating systems, wherein organic material accumulates Mg cations, which apparently forms complexes with dissolved silica anions ( $H_3SiO_4^-$ ), resulting in the rapid formation of  $SiO_2$  crystals around microbial cells even at dissolved silica concentrations well below saturation (Moore, Pajusalu, et al., 2020; Moore, Gong, et al., 2021).

Precursors to the phosphate mineral carbonate fluorapatite (CFA), which cements the Salitre Formation's phosphatic stromatolites, are formed by the complexing of dissolved phosphate anions and Ca cations. Cation bridging may theoretically occur between organic materials and phosphate anions, as between organic materials and silica anions, as a mechanism of phosphate mineralization and organic matter preservation which may have determined the style and extent of phosphogenesis. Cation enrichment of organic material surrounded by CFA cements, as has been observed in organic material surrounded by chert, may imply the role of cation bridging in the facilitation of early phosphate mineralization and organic matter preservation in phosphorite deposits of the Salitre Formation.

In this study, we examined phosphatic digitate stromatolites of the Salitre Formation using optical microscopy, scanning electron microscopy (SEM), and energy dispersive spectrometry (EDS) in order to (1) characterize the style and quality of preservation of primary organic material within phosphatic stromatolite laminae, and (2) determine whether that organic material is enriched with respect to Mg or other cations, such as might be observed if cation bridging was a mechanism in the early formation of phosphatic cements in the growing stromatolites.

### **B.3 Geologic context**

The Salitre Formation is part of the Una Group, a package of sedimentary rock which includes Marinoan-age glaciogenic diamictite and subsequent carbonate platform deposits, grading upwards into mixed carbonate and siliciclastic deposits (Guimarães

et al., 2011; Kuchenbecker, Luis, and Galvão, 2011; A. Misi and Kyle, 1994; Aroldo Misi and Veizer, 1998). The Una Group represents sedimentation in a foreland basin system, which formed during the downflexure of the São Francisco Craton's interior during its Neoproterozoic collision with the adjacent West Congo Craton. This tectonosedimentary environment is described in great detail in previous studies (Martins-Neto, Pedrosa-Soares, and Lima, 2001; Reis, Alkmim, et al., 2016; Reis, Suss, et al., 2017). The lowermost Nova America member of the Salitre Formation, roughly 50-100 meters in thickness, contains the sedimentary phosphorite deposits which are the subject of this study. These phosphorite deposits occur among extensive cross-stratified oolitic grainstone, with meter and decameter-scale lenses of coarser rudstone and tabular intraclast conglomerate, and laterally discontinuous intervals of crinkly to wavy laminated mudstone (Caird et al., 2017; A. Misi and Kyle, 1994; C. Sanders and Grotzinger, 2021).

Phosphate mineralization is spatially restricted to digitate stromatolite buildups, occurring in meter and decameter-scale mounds and tabular reefs with centimeters to meters of synoptic relief, interfingering with the cross-stratified grainstone facies (Caird et al., 2017; Delisle, 2015; C. Sanders and Grotzinger, 2021; Shiraishi et al., 2019). There are also buildups of non-phosphatic, carbonate-cemented stromatolites, though these tend to have domal and columnar morphologies, rather than digitate (Caird et al., 2017; Delisle, 2015; C. Sanders and Grotzinger, 2021). Disordered or transitional stromatolite morphologies also are observed, containing both carbonate and phosphatic cements (C. Sanders and Grotzinger, 2021). Often, phosphatic and non-phosphatic stromatolites co-occur within centimeters to meters of each other. Phosphate mineralization takes the form of micro- to cryptocrystalline carbonate fluorapatite (CFA) cements within stromatolites and at their immediate margins. It does not extend to the grainy, inter-stromatolite fill – which is carbonate cemented – nor the laterally adjacent cross-stratified grainstone and rudstone facies (C. Sanders and Grotzinger, 2021). Phosphatic intraclasts are rare, and where they occur they appear to be directly sourced from nearby CFA-cemented stromatolite buildups (C. Sanders and Grotzinger, 2021).

### **Depositional facies model**

Sedimentary and stratigraphic data from the phosphorite member of the Salitre Formation are consistent with deposition in a shallow, wave-dominated, persistently submerged carbonate platform environment. This depositional facies model is developed in our previous work (C. Sanders and Grotzinger, 2021). Both CFA-cemented

and carbonate-cemented stromatolites and associated microbially-influenced laminae occur within this depositional facies. The spatial distribution of CFA-cemented and carbonate-cemented stromatolite facies is not dependent on water depth or flow energy regime, but on highly local factors which may include microbial ecological structure of the stromatolite-forming microbial mats, or transient variations in the chemistry of porewaters and bottom waters associated with different microbial communities at the seafloor.

### **Paragenetic framework**

The paragenesis of the phosphatic digitate stromatolites of the Salitre formation has been established by through optical petrography at outcrop and hand-sample scales, and texture-specific analysis of carbon, oxygen, and sulfur isotope geochemistry (Caird et al., 2017; C. Sanders, Eiler, and Grotzinger, 2022; C. B. Sanders et al., 2022; C. Sanders and Grotzinger, 2021; Shiraishi et al., 2019). The paragenetic framework developed in these studies supports a scenario wherein phosphate mineralization – i.e., the saturation of porewaters with respect to carbonate-rich fluorapatite (CFA), and lowering of kinetic barriers to CFA nucleation and growth – occurred as a relatively early diagenetic process. Thus, abundance of trace elements incorporated into the CFA and carbonate cement matrix is likely to reflect processes in the pore fluids from which cements were first precipitated during earliest burial and lithification.

## **B.4 Methods**

### **Samples**

Structurally detailed microbial body fossils are rare in the Salitre Formation, but primary organic material – typically amorphous kerogen – is abundant, occurring as micrometer- and 10s-of-micrometer thick laminae and/or micrometer-scale rounded and filamentous inclusions embedded in the cryptocrystalline carbonate fluorapatite (CFA) matrix of the Salitre's digitate stromatolites. These inclusions were first identified via optical thin section petrography, and verified as organic in composition using the Renishaw InVia Confocal Raman Microscope with 514 nm laser, located in the Mineral Spectroscopy Lab in Caltech's Division of Geological and Planetary Science (GPS).

### **Scanning electron microscopy and energy dispersive spectrometry**

The abundance of cations in and around inclusions of primary organic material was measured relative to the abundance of cations in the associated CFA matrix and adjacent carbonate grains using the Zeiss 1550VP Field Emission SEM, located in the Analytical Facilities of Caltech's GPS Division. Backscattered electron images and energy spectra were collected using a 15-20 KeV electron beam, working in variable pressure (VP) mode with uncoated, isopropanol-cleansed petrographic thin sections. Organic matter inclusions embedded in the CFA cements were distinguished from any carbon-rich surface contamination by their apparent surface relief in backscattered electron images of the samples' surface.

The relative abundance of cations associated with organic matter compared to cations associated with the CFA matrix was assessed by comparison of the intensity of X-Rays at energies associated with the characteristic  $K\alpha$  emissions produced by displacement of inner-shell electrons of atoms and subsequent transfer of outer-shell electrons to this lower energy. The intensities of these  $K\alpha$  lines may be directly compared between energy spectra collected with the same operational parameters (accelerating voltage, detectors, etc.) during the same analytical session, are assumed to scale directly with the abundance of a given element in the analytical volume interrogated by the SEM's electron beam.

### **B.5 Results**

**Transmitted Light Optical Microscopy:** Using plane-polarized white light transmitted through petrographic thin sections, we captured photomicrographs of numerous examples of primary organic material preserved in the laminae of CFA-cemented digitate stromatolites from the Salitre Formation. In these photomicrographs, organic matter appears as diffuse, translucent to opaque tan and brown regions. Its spatial distribution and relationship to the mineral fabrics within the stromatolites follows several patterns: (1) concentrated in microbial body fossils, primarily in filaments with widths of 1-10  $\mu\text{m}$  and lengths of 10s to several 100s of  $\mu\text{m}$  (Fig. 1-a), (2) concentrated in bundles of filamentous body fossils oriented parallel to stromatolite laminae (Fig. 1-b), or (3) as diffuse inclusions in micro-to-cryptocrystalline CFA-cemented laminae bracketed above and below by laminae composed of carbonate ooids and peloids (Fig. 1-b, Fig. 2). In some CFA-cemented laminae with diffuse inclusions of organic material, there occur striations filled with inclusion-poor CFA cement which are sub-vertical/sub-perpendicular relative to laminae orientation, with widths of order 1-10  $\mu\text{m}$  and lengths of 10s to several 100s of  $\mu\text{m}$  (Fig. 2).

In the case of organic material associated with microbial body fossils, morphological characteristics beyond approximate size and distribution of filaments are only rarely observed – and when observed, provide only the suggestion of lengthwise septation. Ornaments, surface textures, and other subcellular details are apparently not preserved – either due to their absence, or due having a size smaller than that of enclosing cement crystals.

Scanning Electron Microscopy and Energy Dispersive Spectrometry: In backscattered electron images of uncoated thin sections of digitate stromatolite laminae from the Salitre Formation, organic matter is characterized by a dark, matte appearance relative to the surrounding CFA cement matrix, carbonate cement, carbonate peloids and ooids, and minor silica. CFA cements appear the brightest, likely due to the greater capacity of the CFA mineral lattice for substitution of trace heavy ions (e.g., REEs) compared to that of calcite, dolomite, or quartz/silica. EDS spectra of the CFA cement matrix were characterized by high intensities at 2.013 KeV (characteristic of the  $K\alpha_1$  emission of P), 3.690 KeV (Ca  $K\alpha_1$ ), and moderate intensities at 0.277 KeV (C  $K\alpha_1$ ) and 0.525 KeV (O  $K\alpha_1$ ), the relative intensities of these peaks being consistent with the expected abundance of the elements P, Ca, C, and O in the mineral CFA. High intensities at 3.690 KeV (Ca  $K\alpha_1$ ) and 1.253 KeV (Mg  $K\alpha_1$ ), and moderate intensities at 0.277 KeV (C  $K\alpha_1$ ) and 0.525 KeV (O  $K\alpha_1$ ) were characteristic of calcite and dolomite cements and allochemical grains, with the ratio of Mg  $K\alpha_1$  emission intensity to Ca  $K\alpha_1$  emission intensity being closer to 1 for dolomite compared to calcite. EDS spectra of organic material were characterized by high intensity emission peaks at 0.277 KeV (C  $K\alpha_1$ ), 2 or more orders of magnitude higher than that of the surrounding CFA and carbonate minerals. Organic matter is not intrinsically enriched with respect to metal cations, and so the presence of characteristic  $K\alpha$  peaks of Mg or Ca associated with organic matter may represent either (1) cation enrichment due to adsorption to cell surfaces and EPS, or (2) presence of mineral cements in the analytical volume interrogated by the electron beam due to small size/depth of the organic matter inclusions exposed at the surface of polished thin sections. Peaks associated with other cations such as Fe, Mn, and Na, were not observed in energy spectra of organic matter inclusions or surrounding minerals.

Within matter inclusions of the measured digitate stromatolite laminae, the only cations with significant characteristic peaks in the EDS spectra were magnesium and calcium. Since calcium is a major structural component of CFA, calcite, and

dolomite, the primary cement minerals, it may not be possible to distinguish Ca-enrichment of organic matter from Ca signals from the cement in which the organic matter is embedded. Magnesium is a major component of dolomite (molar ratio Mg/Ca = 1) and high-Mg calcite (Mg/Ca = 0.1-0.4); however, it is only a minor component of CFA, in which the molar ratio of Mg/Ca may only be on the order of 0.05 or less (McClellan, 1980). Thus, the presence of Mg peaks in the EDS spectra of organic matter inclusions which are surrounded by CFA rather than carbonate cements could be interpreted as contribution to the energy spectrum from minor magnesium substitutions within CFA included alongside the organic material in the analytical volume of the electron beam; but it may be possible that the Mg signal is indeed associated with the organic matter directly. These cases may be distinguished by the presence or absence of a dilution signal. If organic matter was truly not enriched in Mg, then the Mg  $K\alpha 1$  peak intensity in an EDS spectrum of organic matter mixed with CFA will be lower than the Mg peak intensity of CFA alone – due to the dilution of the emission signal CFA-bound Mg by Mg-poor organic matter. The spectra and corresponding backscattered electron images of 5 representative examples of organic matter surrounded by CFA and carbonate cements are presented in Figs. 3 and 4. General trends are summarized here.

In all measured cases, Ca  $K\alpha 1$  emissions for carbonate minerals and CFA were of similar intensity, to within an order of magnitude, consistent with expected Ca abundance in those minerals. Intensity of Ca  $K\alpha 1$  emission of organic material inclusions, however, was always an order of magnitude or below that of surrounding CFA cements. This is consistent with a scenario in which the analytical volume of the electron beam targeting organic material also contained some of the surrounding CFA cements, such that the Ca signal was diluted.

Mg  $K\alpha 1$  intensity was always observed to be 1 or more orders of magnitude greater for carbonate minerals (grains and cements) than in CFA consistent with expected Mg/Ca ratios of these minerals. The Mg  $K\alpha 1$  emission of organic material inclusions, however, was always roughly equal to that of the surrounding CFA cement. This is inconsistent with a scenario in which the emission signal from Mg substituted for Ca in the mineral lattice CFA was diluted by mixture with Mg-poor organic matter. It is more consistent with a scenario in which the organic matter itself was enriched with respect to Mg.

Maps of characteristic  $K\alpha$  emission intensities for major elements in a representative phosphatic digitate stromatolite laminae are presented in Figure 5. Mg enrichment

of organic material is difficult to confirm visually in these maps due to the high Mg  $K\alpha$  emission of Mg-rich phases such as dolomite and high-Mg calcite within the field of view. Nevertheless, these images highlight the intimate association between organic matter and CFA cements even at millimeter spatial scales.

## **B.6 Discussion and conclusions**

**Style and Timing of Phosphate Mineralization:** Digitate stromatolite buildups of the Salitre Formation in Northeastern Brazil represent a substantial episode of Neoproterozoic phosphorite mineralization. Previous studies have characterized the depositional environment of these digitate stromatolite buildups as a shallow, wave-swept carbonate platform deposited in a foreland basin based on the spatial distribution of sedimentary structures in outcrops and drill cores (Caird et al., 2017; A. Misi and Kyle, 1994; Aroldo Misi and Veizer, 1998; C. Sanders and Grotzinger, 2021). In this depositional setting, digitate stromatolite buildups interfingered at m- and cm-scales with wave-worked carbonate rudstone and grainstone, as well as non-digitate domal and columnar stromatolite buildups, and crinkly laminite. Elemental and mineralogical mapping at cm to  $\mu\text{m}$  scales, combined with texture-specific carbonate clumped isotope paleothermometry and carbon and oxygen isotopic measurements, constrained the paragenesis of the phosphatic and non-phosphatic stromatolites and grainy inter-stromatolite fill (C. Sanders, Eiler, and Grotzinger, 2022; C. Sanders and Grotzinger, 2021). This work inferred that phosphate enrichment in the Salitre Formation was exclusive to digitate stromatolites in the form of cryptocrystalline cements which were coeval with calcite cements precipitated in laterally adjacent grainstone.

Throughout the geologic record, early diagenetic phosphatic cements (mainly CFA) are observed to preserve microbial fossils and animal tissues with remarkable fidelity even at nm to  $\mu\text{m}$  spatial scales, leading to the impression of early phosphate mineralization as an important taphonomic window. However, there is considerable variation in the style of phosphatization across these fossiliferous sedimentary phosphorites with respect to depositional environment, relative timing of phosphatization and organic matter remineralization, and quality of organic matter preservation. In the Doushantuo Formation (600 Ma) in Southern China, phosphatized microbial fossils and putative embryonic animal fossils are abundant within rounded CFA grains and intraclasts in inner shelf sediments, implying authigenic phosphogenesis in an oxic water column and at the sediment-water interface (Bailey et al., 2007; Muscente, Hawkins, and Xiao, 2015; Xiao, Zhang, and Knoll, 1998). Similarly, in

the lower members of the Vindhyan Supergroup of Central India, intricately woven filamentous microfossils are preserved within rounded CFA grains. In Western and Northern Mongolia, partially and wholly CFA-mineralized body fossils of archaeocyathids and microscopic shelly fauna are observed in Lower Cambrian carbonate reefs and associated fossiliferous packstone (Demidenko et al., 2003; Pruss et al., 2019).

The digitate stromatolites of the Salitre Formation represent yet a different mode of phosphate mineralization than is represented in these Ediacaran and Lower Cambrian sedimentary phosphorite deposits. Rather than phosphatic casts or molds preserving subcellular structural detail, we observe that phosphatic stromatolites of the Salitre Formation contain mainly diffuse organic matter as inclusions in cryptocrystalline CFA cements, and occasionally filaments and bundles of filaments containing concentrated amorphous organic material – which are typically disrupted by fabric-destructive recrystallization of the surrounding CFA cement, or overgrowth of adjacent micritic calcite and dolomite grains. This style of phosphate mineralization of organic matter more closely resembles that described in digitate stromatolites of the Jhamarkotra Formation in the Lower Aravalli Supergroup of Northern India (Bengtson et al., 2017; Sallstedt et al., 2018). The Salitre, however, lacks the Jhamarkotra's distinctive assemblage of globular and filamentous structures and only preserves filaments, and those more diffusely distributed in the phosphatic laminae and without the Jhamarkotra filaments' close packing arrangement.

Another similarity between the Salitre Formation microbialites and those of the Jhamarkotra Formation, is the presence of sub-vertical striations within those stromatolitic laminae where inclusions of amorphous organic material are the most dense. These sub-vertical striations may be remnants of the interstices between bundles of filaments growing in near-vertical “tufts” relative to the paleo-seafloor, as are preserved in the Jhamarkotra stromatolites. Such structures indicate phosphate mineral growth around a microbial mat whose component cells grew upwards, likely as a phototropic response, suggesting that in these laminae mineralization of organic matter occurred relatively early before the degradation of the uppermost, photosynthetic microbial biomass. Conversely, the absence of sub-vertical striations and the appearance of less orderly, tangled filaments with random orientations may suggest precipitation of phosphate minerals from porewaters only after the degradation of phototrophic mats and during the burial of organic matter below the chemocline, where chemotrophic metabolisms dominated.

Role of Mg cation bridging in phosphate mineralization of organic matter: In samples of the Salitre Formation's phosphatic digitate stromatolites, we observed that the intensity of the Mg  $K\alpha 1$  peaks in EDS spectra of organic matter inclusions was typically equal to that of the surrounding CFA cements. It is possible that the Mg emission associated with the measured organic material results from the contribution of nearby Mg-containing CFA to the analytical volume interrogated by the electron beam. If this were the case, the signal from Mg in the CFA crystal lattice should be diluted by the presence of Mg-poor organic material. This dilution signal is indeed observed with Ca: intensity of the Mg  $K\alpha 1$  peaks in EDS spectra of organic matter inclusions was consistently about an order of magnitude lower than in CFA cements not associated with organic matter. The fact that Mg emission associated with organic material is roughly the same as that associated with CFA is consistent with a scenario in which the measured organic material is not actually Mg-poor. Rather, the organic material would have to be Mg-enriched.

Mg-enrichment of organic material surrounded by mineral cements has – in experimental studies and observations of ancient organic-rich cherts – been interpreted as evidence of the role of Mg cations in forming “bridges” between negatively-charged cell surfaces and silica anions during early diagenesis (2020; Moore, Gong, et al., 2021). Silica or chert is typically Mg-poor, and so the observation of Mg  $K\alpha$  emission in energy spectra of organic matter surrounded by chert is likely the result of Mg-enrichment of the organic material prior to or during silicification. As stated in “Results,” CFA can indeed accommodate Mg substitution for Ca in its mineral structure, with Mg/Ca molar ratios up to 0.05 (McClellan, 1980). Thus, depending on the spatial relationship at the molecular level between organic material and CFA at the time of cementation, it may be that CFA is so closely intermixed with organic material that it is impossible to resolve the emission of Mg which was adsorbed to organic material and the signal from Mg which was incorporated into the CFA mineral lattice. However, the fact that emission from Ca – a major structural component of CFA – is diminished in spectra collected from organic matter inclusions relative to surrounding CFA cement would require an explanation wherein the CFA closely associated with organic matter is somehow depleted in Ca. This, too, would imply some other mechanism by which the presence or absence of organic matter controlled the distribution of cations at some point in the diagenetic history of the rock.

If organic material generated by the stromatolite-forming microbial mats of the

Salitre paleobasin was enriched with respect to Mg early due to adsorption of soluble  $Mg^{2+}$  to the surface of cells or extracellular polymeric substance (cation bridging), it may have been possible for organic material to more easily adsorb phosphate anions. This could have lowered kinetic barriers to the precipitation of CFA precursor minerals around organic material by bringing the components necessary for the formation of precursors to cement minerals into close contact with one another – allowing phosphatic cements to form early in sediment pore spaces and preserve organic material against further degradation.

This possible role of cation bridging in early phosphogenesis, facilitated by mat-forming microorganisms, has implications for the paleoenvironmental and paleoecological interpretation of the Salitre phosphorite. The lowering of kinetic barriers to early diagenetic mineralization could allow cements to precipitate from porewaters that are actually undersaturated with respect to phosphate. It may be the case that certain organic compounds – such as occur in EPS, or on the cell walls of certain bacterial taxa – might result in more efficient or complete Mg adsorption than others, resulting in cation bridging and assembly of phosphate mineral precursors in some microbial mats and not others. Interestingly, high porewater concentration of Mg – resulting in high Mg/Ca ratios in non-phosphatic stromatolites relative to phosphatic stromatolites – has been proposed as a major inhibitor to phosphate mineralization among the Ediacaran stromatolites of the lower Aravalli Supergroup in Northern India near Udaipur (Sisodia and Chauhan, 1990). This argument is based on the experimental evidence that elevated Mg concentrations inhibit phosphate mineralization by preventing exchange of structural Mg for Ca during the early diagenetic transition from amorphous phosphatic precursors to apatite minerals (Martens and Harriss, 1970), as well as the observation of Sisodia and Chauhan, 1990 that non-phosphatic stromatolites were relegated to intertidal zone facies and phosphatic stromatolites to subtidal facies in the Udaipur area. The phosphatic stromatolites of the Salitre Formation, too, occur in subtidal depositional facies; but since the Salitre's non-phosphatic stromatolites also occur in subtidal depositional facies, Mg enrichment in intertidal flat environments cannot have determined the spatial distribution of phosphate mineralization.

To conclusively address the role of cations in early phosphate mineralization around organic matter, it will be necessary to undertake laboratory experiments analogous to those performed by previous workers for microbial mats in silica-precipitating systems (e.g., Moore et al., 2020) and for animal tissues in apatite-precipitating

systems (e.g., Briggs and Kear, 1993; Briggs and McMahon, 2016; Gueriau et al., 2020). However, in the phosphatic stromatolites of the Salitre Formation, it appears that enrichment of Mg could plausibly have facilitated nucleation and growth of CFA cements around organic material, though perhaps not early enough or extensively enough to preserve microbial fossils in significant detail.

## **B.7 Acknowledgements**

The authors would like to thank Ma Chi and George Rossman of the Caltech Division of Geological and Planetary Sciences Analytical Facility and Mineral Spectroscopy Laboratory for their assistance and guidance with the instruments utilized in this study. We also thank Andrew Knoll of Harvard University's Department of Earth and Planetary Sciences for the provision of fossiliferous chert samples, and valuable discussions on the taphonomy of microorganisms and soft-bodied animals.

We also express our deep gratitude for the students, professors, and researchers of the Laboratório de Análises de Minerais e Rochas (LAMIR) e Laboratório de Análises de Bacias (LABAP) da Universidade Federal do Paraná, as well as our collaborators from the Universidade Federal do Bahia, without whom we could not have collected our samples and immersed ourselves in the geology and culture of the studied region. We extend a heartfelt thanks, as well, to the farmers, miners, educators, and conservationists of the Chapada Diamantina and Cavernas do Peruaçu regions for their guidance and expertise.

We also wish to thank the reviewers, and to acknowledge that this work was supported by the National Science Foundation Graduate Research Fellowship Program (NSF GRFP), and the Simons Foundation. We thank the Simons Collaboration on the Origins of Life (SCOL) for funding and support.

Lastly, we humbly acknowledge the Xakriab´a, the communities of and surrounding the historic Quilombo da Gruta dos Brejões, as well as other indigenous peoples whose names and identities may have been lost to colonialism and occupation, on whose land this work relies.

## **References**

Bailey, Jake V. et al. (2007). "Evidence of giant sulphur bacteria in Neoproterozoic phosphorites". In: *Nature* 445.7124, pp. 198–201. ISSN: 14764687. DOI: 10.1038/nature05457.

- Bengtson, Stefan et al. (2017). “Three-dimensional preservation of cellular and subcellular structures suggests 1.6 billion-year-old crown-group red algae”. In: *PLoS Biology* 15.3, pp. 1–38. ISSN: 15457885. DOI: 10.1371/journal.pbio.2000735.
- Briggs, Derek E.G. and Amanda J. Kear (1993). “Fossilization of soft tissue in the laboratory”. In: *Science* 259.5100, pp. 1439–1442. ISSN: 00368075. DOI: 10.1126/science.259.5100.1439.
- Briggs, Derek E.G. and Sean McMahon (2016). “The role of experiments in investigating the taphonomy of exceptional preservation”. In: *Palaeontology* 59.1, pp. 1–11. ISSN: 14754983. DOI: 10.1111/pala.12219.
- Caird, R. A. et al. (2017). “Ediacaran stromatolites and intertidal phosphorite of the Salitre Formation, Brazil: Phosphogenesis during the Neoproterozoic Oxygenation Event”. In: *Sedimentary Geology* 350.January, pp. 55–71. ISSN: 00370738. DOI: 10.1016/j.sedgeo.2017.01.005. URL: <http://dx.doi.org/10.1016/j.sedgeo.2017.01.005>.
- Delisle, Renee Alayne (2015). “Phosphatic Peritidal Limestone of the Neoproterozoic Salitre Formation, Brazil, and Precambrian Economic Phosphorite”. PhD thesis. Acadia University, p. 141. URL: <http://openarchive.acadiau.ca/utills/getdownloaditem/collection/Theses/id/1019/filename/1033.pdf/mapsto/pdf>.
- Demidenko, Yu E. et al. (2003). “Age of phosphorites from the Khubsugul basin (Mongolia)”. In: *Doklady Earth Sciences* 389.3, pp. 317–321. ISSN: 1028334X.
- Gueriau, Pierre et al. (2020). “Oxidative conditions can lead to exceptional preservation through phosphatization”. In: *Geology* 48.12, pp. 1164–1168. ISSN: 19432682. DOI: 10.1130/G45924.1.
- Guimarães, J. T. et al. (2011). “The Bebedouro Formation, Una Group, Bahia (Brazil)”. In: *Geological Society Memoir* 36.1, pp. 503–508. ISSN: 04354052. DOI: 10.1144/M36.47.
- Kuchenbecker, Matheus, Humberto Luis, and Daniel Galvão (2011). “Caracterização estrutural e considerações sobre a evolução tectônica da Formação Salitre na porção central da Bacia de Irecê, norte do Cráton do”. In: *Geonomos* 19.2, pp. 42–49.
- Martens, Christopher S. and Robert C. Harriss (1970). “Inhibition of apatite precipitation in the marine environment by magnesium ions”. In: *Geochimica et Cosmochimica Acta* 34.5, pp. 621–625. ISSN: 00167037. DOI: 10.1016/0016-7037(70)90020-7.
- Martins-Neto, M. A., A. C. Pedrosa-Soares, and S. A.A. Lima (2001). “Tectono-sedimentary evolution of sedimentary basins from Late Paleoproterozoic to Late Neoproterozoic in the São Francisco craton and Araçuaí fold belt, Eastern Brazil”. In: *Sedimentary Geology* 141-142, pp. 343–370. ISSN: 00370738. DOI: 10.1016/S0037-0738(01)00082-3.

- McClellan, G. H. (1980). "Mineralogy of carbonate fluorapatites ( Francolites)." In: *Journal, Geological Society* 137.6, pp. 675–681.
- Misi, A. and J. R. Kyle (1994). "Upper Proterozoic carbonate stratigraphy, diagenesis, and stromatolitic phosphorite formation, Irece Basin, Bahia, Brazil". In: *Journal of Sedimentary Research A: Sedimentary Petrology and Processes* 64 A.2, pp. 299–310.
- Misi, Aroldo and Ján Veizer (1998). "Neoproterozoic carbonate sequences of the Una Group, Irecê Basin, Brazil: Chemostratigraphy, age and correlations". In: *Precambrian Research* 89.1-2, pp. 87–100. ISSN: 03019268.
- Moore, Kelsey R., Jian Gong, et al. (2021). "A new model for silicification of cyanobacteria in Proterozoic tidal flats". In: *Geobiology* 19.5, pp. 438–449. ISSN: 14724669. DOI: 10.1111/gbi.12447.
- Moore, Kelsey R., Mihkel Pajusalu, et al. (2020). "Biologically mediated silicification of marine cyanobacteria and implications for the Proterozoic fossil record". In: *Geology* 48.9, pp. 862–866. ISSN: 19432682. DOI: 10.1130/G47394.1.
- Muscente, A. D., Andrew D. Hawkins, and Shuhai Xiao (2015). "Fossil preservation through phosphatization and silicification in the Ediacaran Doushantuo Formation (South China): A comparative synthesis". In: *Palaeogeography, Palaeoclimatology, Palaeoecology* 434, pp. 46–62. ISSN: 00310182. DOI: 10.1016/j.palaeo.2014.10.013. URL: <http://dx.doi.org/10.1016/j.palaeo.2014.10.013>.
- Pruss, Sara B. et al. (2019). "Phosphatized early Cambrian archaeocyaths and small shelly fossils (SSFs) of southwestern Mongolia". In: *Palaeogeography, Palaeoclimatology, Palaeoecology* 513, pp. 166–177. ISSN: 00310182. DOI: 10.1016/j.palaeo.2017.07.002. URL: <https://doi.org/10.1016/j.palaeo.2017.07.002>.
- Reis, Humberto L.S., Fernando F. Alkmim, et al. (2016). "The São Francisco Basin". In: *The São Francisco Craton, Eastern Brazil: Tectonic Genealogy of a Miniature Continent*. Ed. by Monica Heilbron, Umberto G. Cordani, and Fernando F. Alkmim. 1st ed. August. Springer, pp. 117–143. ISBN: 9783319017150. DOI: 10.1007/978-3-319-01715-0.
- Reis, Humberto L.S., João F. Suss, et al. (2017). "Ediacaran forebulge grabens of the southern São Francisco basin, SE Brazil: Craton interior dynamics during West Gondwana assembly". In: *Precambrian Research* 302. September, pp. 150–170. ISSN: 03019268. DOI: 10.1016/j.precamres.2017.09.023. URL: <http://dx.doi.org/10.1016/j.precamres.2017.09.023>.
- Sallstedt, T. et al. (2018). "Evidence of oxygenic phototrophy in ancient phosphatic stromatolites from the Paleoproterozoic Vindhyan and Aravalli Supergroups, India". In: *Geobiology* 16.2, pp. 139–159. ISSN: 14724669. DOI: 10.1111/gbi.12274.

- Sanders, Cecilia, John Eiler, and John Grotzinger (2022). “Chapter 2: Paragenesis of an Ediacaran carbonate-platform phosphorite, Constraints from optical petrography and texture-specific clumped isotope paleothermometry”. PhD thesis. Caltech.
- Sanders, Cecilia and John Grotzinger (2021). “Sedimentological and stratigraphic constraints on depositional environment for Ediacaran carbonate rocks of the São Francisco Craton: Implications for phosphogenesis and paleoecology”. In: *Precambrian Research* 363, June, p. 106328. ISSN: 03019268. DOI: 10.1016/j.precamres.2021.106328. URL: <https://doi.org/10.1016/j.precamres.2021.106328>.
- Sanders, Cecilia B. et al. (2022). “Chapter 3: Sulfur geochemistry of the Salitre Formation phosphorites, Implications for the role of sulfur cycling in phosphogenesis on an Ediacaran carbonate platform”. PhD thesis. Caltech.
- Shiraishi, Fumito et al. (2019). “Potential photosynthetic impact on phosphate stromatolite formation after the Marinoan glaciation: Paleooceanographic implications”. In: *Sedimentary Geology* 380, pp. 65–82. ISSN: 00370738. DOI: 10.1016/j.sedgeo.2018.11.014. URL: <https://doi.org/10.1016/j.sedgeo.2018.11.014>.
- Sisodia, M. S. and D. S. Chauhan (1990). “The influence of magnesium ions during the formation of stromatolitic phosphorites of Udaipur, Rajasthan, India”. In: *Geological Society Special Publication* 52, pp. 313–320. ISSN: 03058719. DOI: 10.1144/GSL.SP.1990.052.01.23.
- Xiao, Shuhai, Yun Zhang, and Andrew H. Knoll (1998). “Three-dimensional preservation of algae and animal embryos in a neoproterozoic phosphorite”. In: *Nature* 391, pp. 553–558. ISSN: 00280836. DOI: 10.1038/35318.

## B.8 Figures

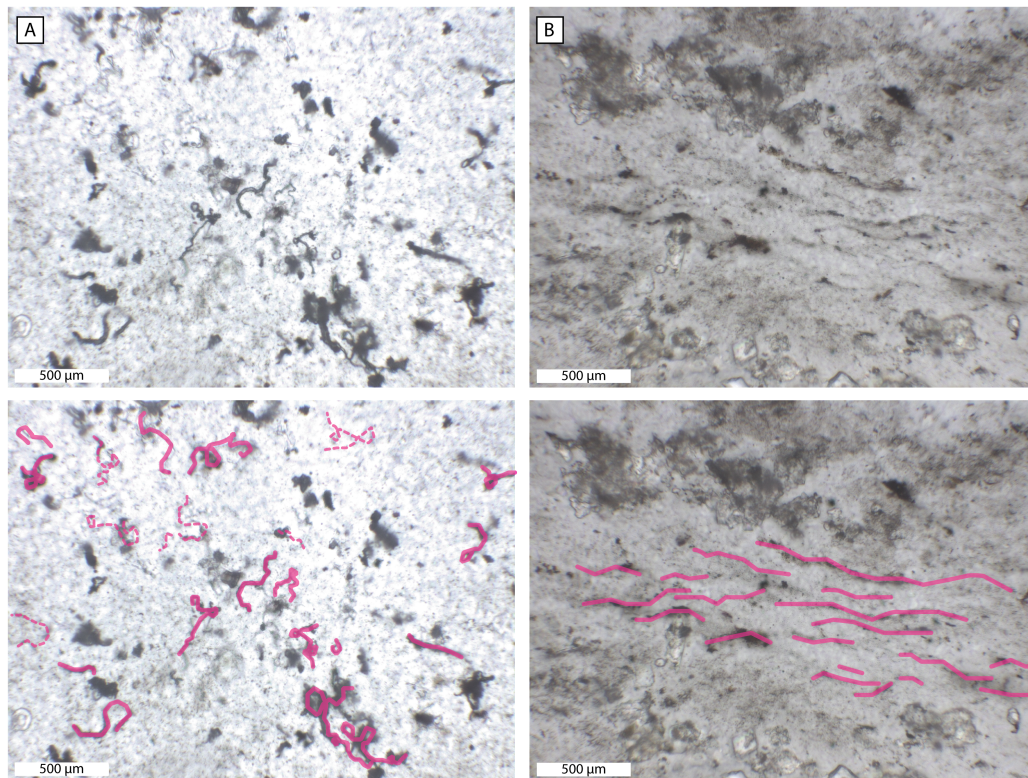


Figure B.1: Thin section photomicrographs with of CFA-cemented laminae in digitate stromatolites of the Salitre Formation, featuring organic matter concentrated in filamentous microfossils, with and without annotation. In annotated lower panels, pink lines indicate individual and bundled filamentous structures within the plane of focus. Dotted pink lines indicate filamentous structures outside of the plane of focus. (a) Randomly oriented filaments, folded back on themselves and tangled. (b) Filaments preferentially oriented parallel to stromatolite laminae.

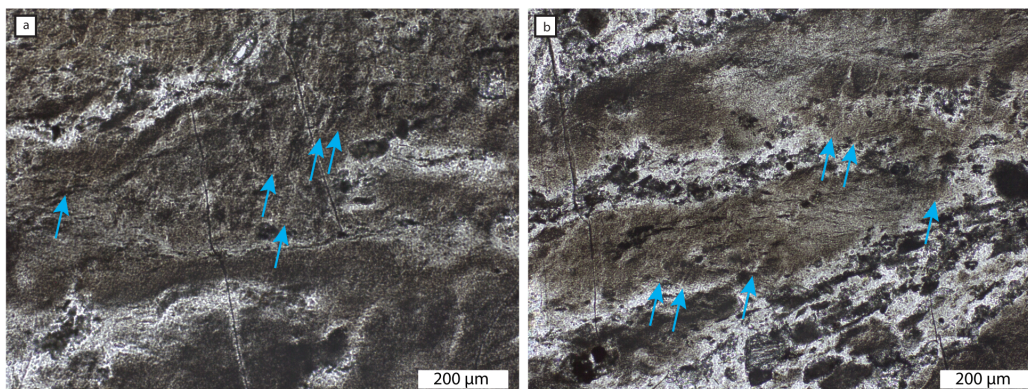


Figure B.2: Thin section photomicrographs of CFA-cemented laminae featuring diffuse inclusions of amorphous organic matter, with blue arrows indicating orientation of subvertical striations suggestive of microbial mat structure.

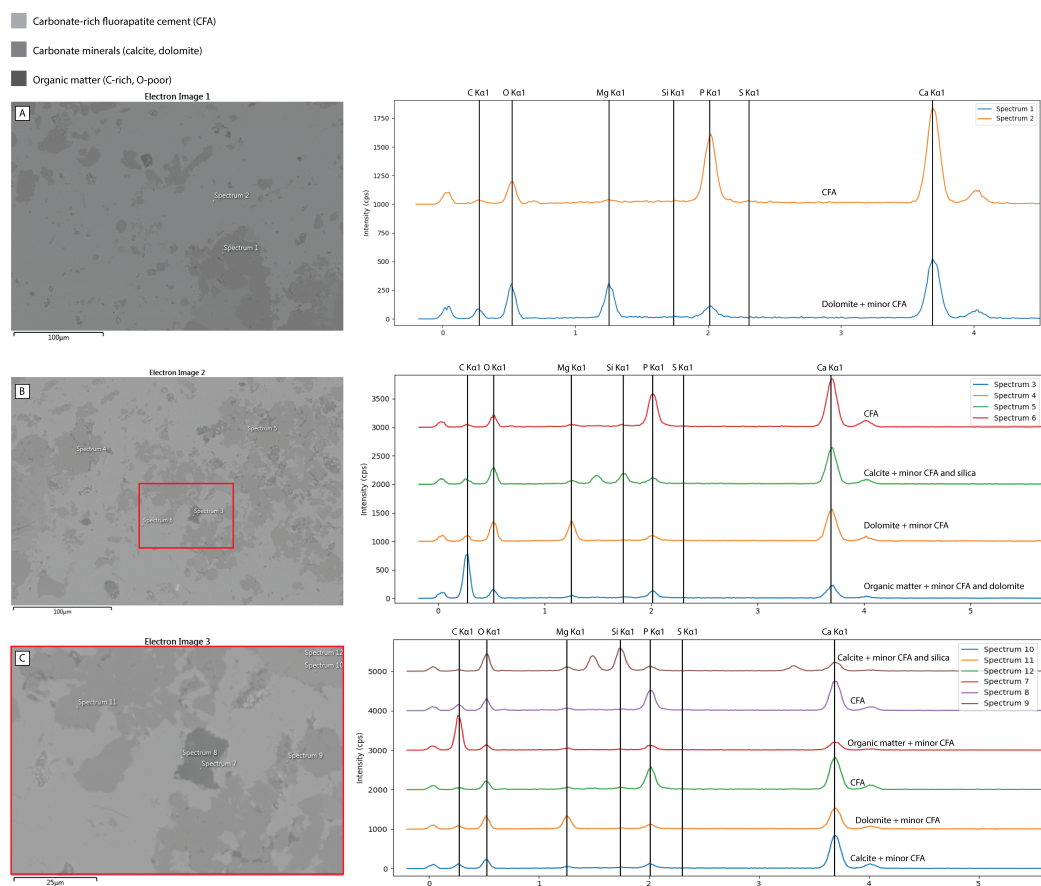


Figure B.3: Back-scattered electron images annotated with locations of point energy spectra (EDS), and plotted spectra. Energies of characteristic  $K\alpha$  X-Ray emission for major elements are indicated by vertical lines. (a-b) Representative images and spectra of digitate stromatolite laminae containing carbonate grains and minor carbonate cements in a cement matrix of carbonate fluorapatite (CFA). (c) Magnified inset from panel (b) and associated energy spectra. In all back-scattered electron images: lightest gray corresponds to cryptocrystalline CFA cement, medium gray corresponds to carbonate minerals including calcite and dolomite, and darkest gray/charcoal corresponds to native organic material.

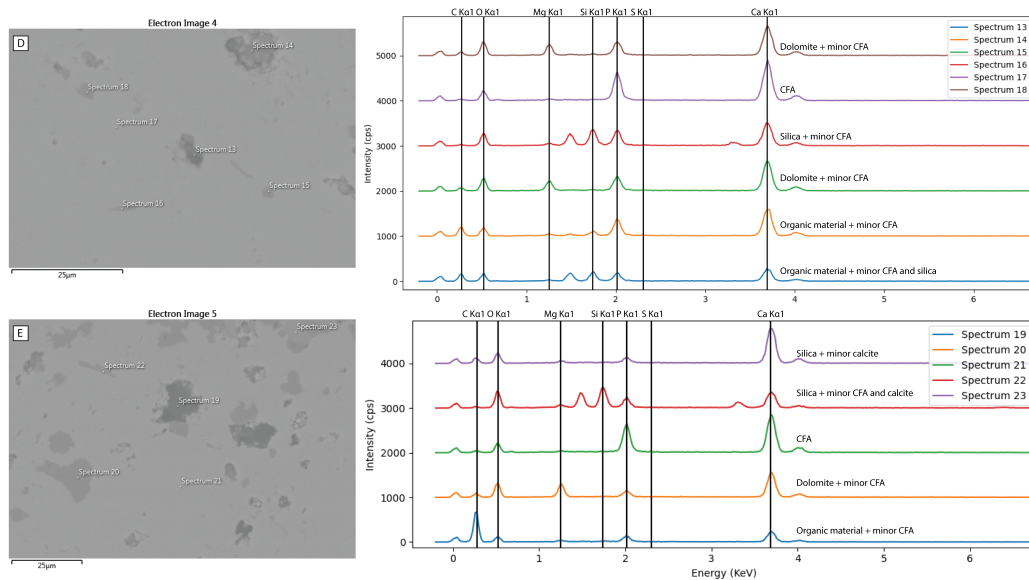


Figure B.4: Continuation of Fig. B.3. Back-scattered electron images annotated with locations of point energy spectra (EDS), and plotted spectra. Energies of characteristic  $K\alpha$  X-Ray emission for major elements are indicated by vertical lines. (d-e) Representative images and spectra of digitate stromatolite laminae containing carbonate grains and minor carbonate cements in a cement matrix of carbonate fluorapatite (CFA).

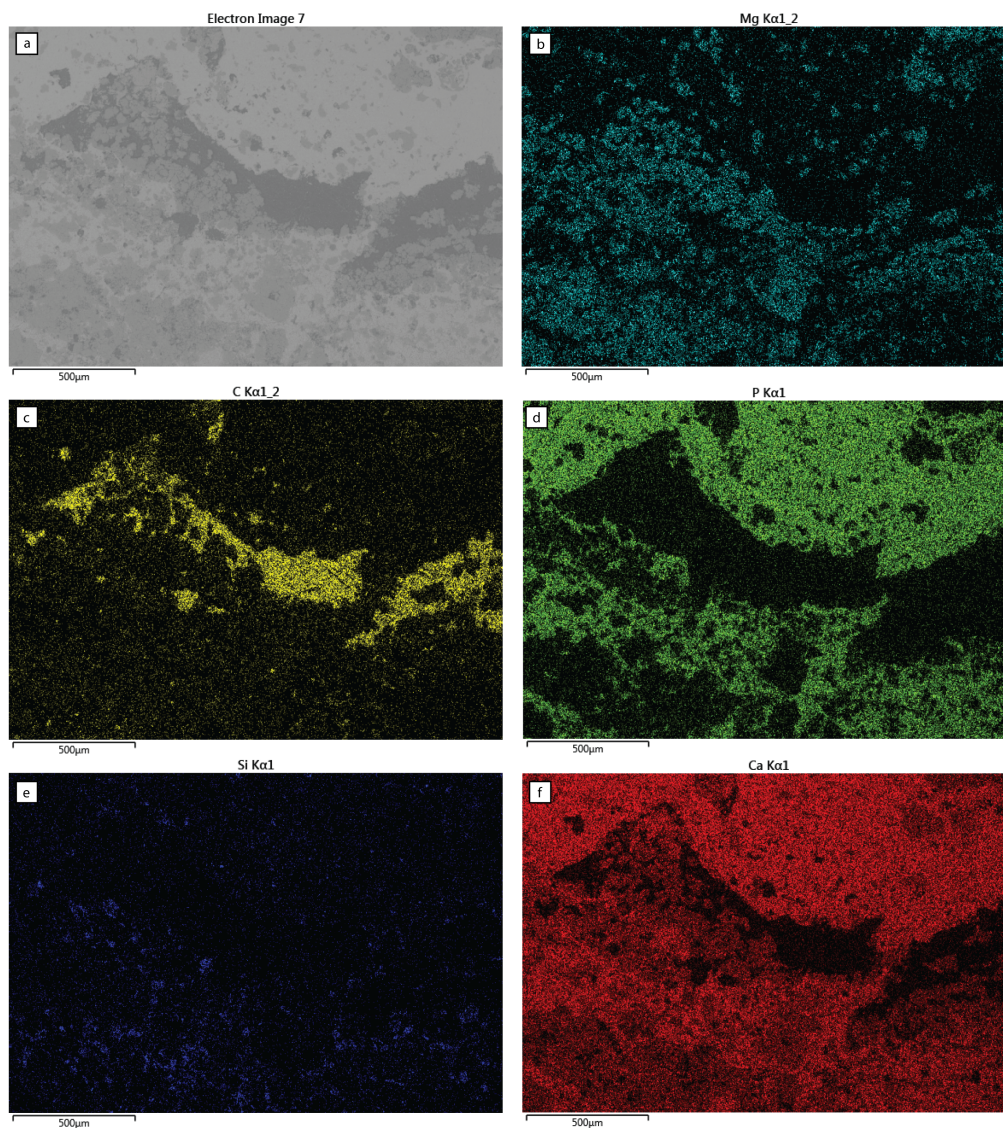


Figure B.5: (a) Back-scattered electron image and (b-f) corresponding maps of EDS spectra intensity for characteristic K $\alpha$  emissions of major elements, featuring organic matter, carbonate grains, and minor carbonate cements within CFA-cemented laminae of a phosphatic digitate stromatolite from the Salitre Formation.

*Appendix C*

QUESTIONNAIRE

*Appendix D*

CONSENT FORM